

**Photoluminescence Properties of Carbon Nanomaterials during Coronation
and Biodegradation**

by

Xiaoyun He

B.S., Wuhan University of Technology, 2013

M.S., University of Chinese Academy of Sciences, 2016

Submitted to the Graduate Faculty of the
Dietrich School of Arts and Sciences in partial fulfillment
of the requirements for the degree of
Doctor of Philosophy

University of Pittsburgh

2021

UNIVERSITY OF PITTSBURGH

DIETRICH SCHOOL OF ARTS AND SCIENCES

This dissertation was presented

by

Xiaoyun He

It was defended on

September 8, 2021

and approved by

Steve Weber, Ph.D., Professor, Department of Chemistry

Haitao Liu, Ph.D., Professor, Department of Chemistry

Michael R. Shurin, MD, Ph.D., Professor, Department of Pathology and Immunology

Dissertation Director: Alexander Star, Ph.D., Professor, Department of Chemistry and
Bioengineering

Copyright © by Xiaoyun He

2021

Photoluminescence Properties of Carbon Nanomaterials during Coronation and Biodegradation

Xiaoyun He, PhD

University of Pittsburgh, 2021

Carbon nanomaterials (CNMs) have been widely used in biomedical applications such as drug delivery, biosensing, and bioimaging. Due to their interactions with the biological systems in these applications, it is important to understand what happens to CNMs *in vivo*. Upon introduction into a biological environment, CNMs are rapidly coated with biomolecules (90% lipids) resulting in so-called ‘biocorona’. CNMs can also undergo additional bio-transformations including partial or complete biodegradation. This dissertation focuses on using fluorescence spectroscopy to study the chemical reactions between CNMs and different biomolecules upon coronation and biodegradation.

We first use fluorescence spectroscopy to study the reactions between the single-walled carbon nanotubes (SWCNTs) and the biologically important oxygenated lipid metabolites. A photoinduced cycloaddition reaction between metabolites bearing enone functional groups and SWCNTs is reported here. By creating covalent and tunable sp^3 defects in the sp^2 carbon lattice of SWCNTs through $[2\pi + 2\pi]$ photocycloaddition, a bright red-shifted photoluminescence (PL) was gradually generated. The mechanism of the photocycloaddition reaction was further investigated by comparing the reactivity with various organic molecules and computational calculations. The results of this study can enable engineering of the optical and electronic properties of semiconducting SWCNTs and provide understanding into their interactions with the lipid biocorona.

In addition to coronation, CNMs could induce a robust inflammatory response. Our research group has found that these effects can be mitigated by enzymatic biodegradation of CNMs through a peroxidase enzyme released by neutrophils during inflammation, myeloperoxidase (MPO). We performed PL studies on the MPO-catalyzed oxidation of graphene oxide (GO) and surfactant-coated SWCNTs. We further constructed two ratiometric sensors using SWCNT/GO nanoscrolls by incorporating surfactant-wrapped SWCNTs as the internal either turn-off or reference sensor. Our sensors show linear response to MPO oxidative machinery and hold the promise to be used as self-calibrating CNMs-based MPO activity indicators. Finally, the composition and structures of the fluorescent GO degradation products, in the form of polyaromatic hydrocarbons (PAHs), were analyzed using liquid chromatography–mass spectrometry and computational calculations. Our results indicated that structures with several conjugated benzene rings are likely to generate the observed PL.

Table of Contents

Table of Contents	vi
List of Tables	ix
List of Figures.....	xii
List of Schemes	xxvii
Preface.....	xxviii
1.0 Introduction.....	1
1.1 Carbon Nanomaterials (CNMs)	1
1.1.1 Carbon Nanotubes	2
1.1.2 Graphene Oxide	3
1.1.3 Nitrogen-doped Carbon Nanotubes Cups (NCNCs).....	7
1.2 Biological Interactions of Carbon Nanomaterials	8
1.2.1 Nano-Bio Interactions.....	8
1.2.2 CNMs Interactions with Lipids	10
1.2.3 Toxicity of Carbon Nanomaterials	11
1.2.4 Enzymatic Oxidative Degradation of CNMs	12
1.3 Fluorescence Spectroscopy	18
1.3.1 Fluorescence of Graphene Oxide and Graphene Quantum Dots	20
1.3.2 Fluorescence of Semiconducting Single-Walled Carbon Nanotubes	22
1.4 Mass Spectrometry	25
1.5 Transmission Electron Microscopy (TEM).....	26

2.0 $[2\pi + 2\pi]$ Photocycloaddition of Enones to Single-Walled Carbon Nanotubes

Creates Fluorescent Quantum Defects.....	29
2.1 Preface	29
2.2 Introduction	29
2.3 Materials and Methods	32
2.4 Results and Discussion	33
2.5 Conclusions	53

3.0 Photoluminescence Response in Carbon Nanomaterials to Enzymatic

Degradation	54
3.1 Preface	54
3.2 Introduction	54
3.3 Materials and Methods	56
3.4 Results and Discussion	59
3.5 Conclusions	75

4.0 Liquid Chromatography Mass Spectrometry Analysis in Carbon Nanomaterials

to Enzymatic Oxidation	77
4.1 Composition and Structure of Fluorescent Graphene Quantum Dots Generated by Enzymatic Degradation of Graphene Oxide.....	77
4.1.1 Preface.....	77
4.1.2 Introduction.....	77
4.1.3 Materials and Methods.....	79
4.1.4 Results and Discussion.....	81
4.1.5 Conclusions	96

4.2 Quantitative Analysis of Drug Loading and Release in Carbon Nanodelivery System	97
4.2.1 Preface.....	97
4.2.2 Introduction.....	97
4.2.3 Experimental	98
4.2.4 Results and Discussion.....	99
4.2.5 Conclusions	101
Appendix A Supporting Information.....	102
Appendix A.1 [2π + 2π] Photocycloaddition of Enones to Single-Walled Carbon Nanotubes Creates Fluorescent Quantum Dots.....	102
Appendix A.2 Photoluminescence Response in Carbon Nanomaterials to Enzymatic Degradation.....	131
Appendix A.3 Composition and Structure of Fluorescent Graphene Quantum Dots Generated by Enzymatic Degradation of Graphene Oxide.....	147
Appendix A.4 Quantitative Analysis of Drug Loading and Release in Carbon Nanodelivery System	185
Appendix B Publications	187
Bibliography	189

List of Tables

Table 2.1. Comparison between different compounds after 1 h reaction with SWCNTs under 566 nm illumination.	41
Table 2.2. Comparison between different compounds after 1 h reaction with SWCNTs.	44
Table 2.3. Gibbs free energies (ΔG) of different cycloaddition products between photoexcited (6,5) SWCNT (with 566 nm light) and different substrates.^a	46
Table 2.4. Reaction energies to form different cycloaddition products and reduction potential of substrates.	50
Table 4.1. Possible PAHs generated by MPO/H₂O₂/Cl⁻ oxidation of GO.	89
Table 4.2. Quantified amount of paclitaxel upon uncorking Au-NCNC.	100
Appendix Table 1. All compounds used for reaction with SWCNT.	102
Appendix Table 2. Reaction conditions and calculations for wavelength-dependence experiment.	113
Appendix Table 3. Computed reaction energies for different diastereomeric products of [2π + 2π] cycloaddition. All energies are Gibbs free energies (in kcal/mol) with respect to the photoexcited SWCNT with 566 nm light and the substrate ((3E,5Z)-undecadien-2-one). The most stable diastereomers in the reactions with each type of C=C bond on the SWCNT are shown in bold.	118
Appendix Table 4. Computed reaction energies for different diastereomeric products of [2π + 4π] cycloaddition. All energies are Gibbs free energies (in kcal/mol) with respect to the photoexcited SWCNT with 566 nm light and the substrate ((3E,5Z)-undecadien-	

2-one). The most stable diastereomers in the reactions with each type of C=C bond on the SWCNT are shown in bold.	119
Appendix Table 5. Computed reaction energies for different diastereomeric products of $[4\pi + 2\pi]$ cycloaddition. All energies are Gibbs free energies (in kcal/mol) with respect to the photoexcited SWCNT with 566 nm light and the substrate ((3E,5Z)-undecadien-	
2-one). The most stable diastereomers in the reactions with each type of C=C bond on the SWCNT are shown in bold.	120
Appendix Table 6. Comparison of Gibbs free energies of key cycloadducts using different level of theory for the single point calculation. All energies are in kcal/mol relative to (6,5)-SWCNT and (3E,5Z)-undecadien-2-one.	124
Appendix Table 7. Comparison of electronic energies of key cycloadducts using different nanotube length. All energies are in kcal/mol relative to (6,5)-SWCNT and (3E,5Z)-undecadien-2-one.	125
Appendix Table 8. Energies of all computed structures.	126
Appendix Table 9. Comparison of water Raman peaks.	137
Appendix Table 10. Potential PAHs generated by MPO/H₂O₂/Cl⁻ oxidation of GO (detected in the positive ionization mode).	149
Appendix Table 11. Potential PAHs generated by MPO/H₂O₂/Cl⁻ oxidation of GO (detected in the negative ionization mode).	153
Appendix Table 12. Comparison of PL emission under different excitations of GO after 5-day MPO-catalyzed degradation.	170
Appendix Table 13. The calculated set of vertical excitations and fluorescence energies (in nm units) obtained at CAM-B3LYP/6-311+G(2d,p) level of theory for the molecular	

systems decorated with ester, ether (epoxide), and/or carbonyl groups considered in this work under solvation (water) condition. The labels A and B refer to $C_{33}H_{18}O_3$ and $C_{25}H_{18}O_{10}$ stoichiometries, respectively. For absorption transitions selective excitations with oscillator strengths f larger than 0.01 are indicated, with excitations in the (325 ± 21) nm range indicated in bold 171

Appendix Table 14. The calculated set of vertical excitations and fluorescence energies (in nm units) obtained at CAM-B3LYP/6-311+G(2d,p) level of theory under solvation (water) condition for the case of structures decorated with OH and COOH groups. The labels C and D refer to $C_{33}H_{18}O_3$ and $C_{25}H_{18}O_{10}$ stoichiometries, respectively. For absorption transitions selective excitations with oscillator strengths f larger than 0.01 are indicated, with excitations in the (325 ± 21) nm range indicated in bold. 179

List of Figures

- Figure 1.1. Graphene as a 2D building block for other graphitic carbon materials including 0D fullerenes (left), 1D carbon nanotubes (middle), and 3D graphite (right). Reprinted with permission from ref¹. Copyright 2007 Nature Publishing Group. ... 1**
- Figure 1.2. The Raman spectrum of SWCNTs. The prominent bands highlighted bands provide vital insight into the properties and nature of the CNTs. Reprinted with permission from ref.⁴ Copyright 2007 John Wiley & Sons, Ltd..... 3**
- Figure 1.3. (a) Chemical structure and (b) 3D model of GO. Reprinted with permission from reference ⁵. Copyright 2012 American Chemical Society. (c) photograph of GO suspension in water, (d) TEM and (e) AFM images of GO single sheet. Reprinted with permission from ref. ⁷ Copyright 2008 American Chemical Society. 5**
- Figure 1.4. (a) UV-vis absorption, (b) Raman, and (c) high-resolution C_{1s} XPS spectra of pristine GO. Reprinted with permission from reference ¹¹. Copyright 2011 American Chemical Society. 6**
- Figure 1.5. (a) Solid-state ¹³C magic-angle spinning (MAS) NMR and (b) FTIR spectra of pristine GO. Reprinted with permission from references ^{12,21}. Copyright 2009 Nature Publishing Group and 2013 IOP Publishing Ltd. 7**
- Figure 1.6. Separation and corking of stacked nitrogen-doped carbon nanotube cups (NCNCs). Transmission electron microscopy images of (A) as-synthesized, stacked NCNCs, (B) oxidized NCNCs, (C) separated NCNCs, and (D) GNP-corked NCNCs. (E) schematic diagram for the preparation of corked NCNCs. Reprinted with permission from ref. ²⁵ Copyright 2015 by John Wiley & Sons, Inc. 8**

Figure 1.7. Size comparison between Carbon Nanomaterials and different molecules. Adapted with permission from ref.²⁹ and ref.³⁰. Copyright 2019 Springer International Publishing and 2021 Elsevier B.V..... 9

Figure 1.8. Computer modeling of SWCNTs binding with phospholipids and SP-D. The predicted binding pose of (A) lowest energy conformation of DPPC, (B) DPPC bound along the axis of SWCNT, lowest energy conformation of (C) PG, (D) PS, and (E) PE. (F) Lipid coating model generated using the PG-bound form of SWCNT shown in (C). Reprinted with permission from reference ³². Copyright 2012 American Chemical Society. 10

Figure 1.9. AFM images with section analysis of GO with HRP at (a) day 0 and (b) holey graphene oxide at day 10. Reprinted with permission from reference ⁴⁰. Copyright 2011 American Chemistry Society. 13

Figure 1.10. (a) Schematic diagram demonstrating the degradation of GO via the photo-Fenton reaction (b) AFM images of as-received GO after reaction with the Fenton reagent under UV irradiation for 0, 18, 36, and 54 h. All images were obtained in tapping mode, and the scale bars are 500 nm. (c) Fluorescence spectra of the GO solution after 0, 1, and 3 days of the photo-Fenton reaction. Reprinted with permission from reference ⁴². Copyright 2014 American Chemistry Society. 14

Figure 1.11. TEM images of MPO-mediated degradation of GO at three time points: (a) control (t = 0), (b) t = 15 h, and (c) t = 24 h. Reprinted with permission from reference ⁴³. Copyright 2015 Wiley-VCH Verlag GmbH & Co. KGaA, Weinheim..... 15

Figure 1.12. (a) Raman spectra of GO incubated with neutrophil extracellular traps (NETs) in the presence of NaCl and H₂O₂ for the indicated time-points. (b) Large (GO-L) and

small (GO-S) sheets were biodegraded by recombinant MPO in the presence of NaCl and H₂O₂ for 0-12 h, followed by treatment with catalase to quench the excess H₂O₂. Then, cell viability and genotoxicity assessment of the GO biodegradation products was performed using the human lung cell line BEAS-2B. Reprinted with permission from reference ⁴⁸. Copyright 2018 The Royal Society of Chemistry..... 16

Figure 1.13. a, Photograph of different short-cut nanotube suspensions after 24 h. b, Dynamic light scattering showing multiple smaller peaks corresponding to biodegraded nanotubes. c, Infrared spectra showing loss of M1 and S2 bands as nanotubes are degraded in the presence of hMPO and H₂O₂. OD, optical density. d, Raman spectra (excitation, 633 nm) of ethanol-dried nanotubes (black) and (hMPO and H₂O₂)-treated nanotubes, showing loss of the characteristic G-band, followed by appearance and decay of the D-band over time. Reprinted with permission from reference ⁴⁹. Copyright 2010 Nature Publishing Group..... 17

Figure 1.14. Scheme illustration of controlled opening and degradation of Au-NCNCs by MPO enzymatic oxidation system. Reprinted with permission from reference ⁵⁰. Copyright 2015 American Chemistry Society..... 18

Figure 1.15. Jablonski diagram. Reprinted with permission from reference ⁵¹. Copyright 2013 European Biophysical Societies' Association (EBSA). 19

Figure 1.16. Schematic diagram of a fluorescence spectrometer. Reprinted with permission from reference ⁵². Copyright 2015 Informa UK Limited. 20

Figure 1.17. (a) Schematic band structure of GO (pink and blue colors represent conduction and valence bands, respectively). (b) Calculated energy gap of $\pi-\pi^*$ transitions as a

function of the number of fused aromatic rings (N). Reprinted with permission from reference ⁶⁵. Copyright 2010 Wiley-VCH Verlag GmbH & Co. KGaA, Weinheim. 21

Figure 1.18. (a) The relation between SWCNT structure and graphene sheet roll-up. Structures shown with red labels are metallic or semimetallic; those with black labels are semiconducting. Reproduced with permission from reference ⁶⁷. Copyright 2009 Springer-Verlag. (b) A schematic illustration of the density of states of metallic (left) and semiconducting (right) SWCNTs. Reproduced with permission from reference ⁶⁸. Copyright 2011 Royal Society of Chemistry. (c) Optical absorption spectra of 15 types of single-chirality species. Reprinted with permission from reference ⁶⁹. Copyright 2021 The American Association for the Advancement of Science. (d) Excitation–emission profile of polymer-functionalized SWCNT suspension. Reprinted with permission from reference ⁷⁰. Copyright 2016 The Authors..... 23

Figure 1.19. (a) Covalent sidewall functionalization of (6,5)-SWCNTs with 4-nitrobenzenediazonium tetrafluoroborate gives rise to a new fluorescent peak, E_{11}^- , that is red-shifted by 181 meV and 8.4 times brighter (in integrated intensity) than the original E_{11} exciton photoluminescence. (b) Controlled sp^3 defects brighten dark excitons. Reprinted with permission from reference ⁷⁶. Copyright 2013 Nature Publishing Group..... 24

Figure 1.20. General scheme of a mass spectrometer. Reprinted with permission from reference ⁷⁷. Copyright 2017 Springer International Publishing AG. 25

Figure 1.21. Diagram of electrospray sources, using skimmers for ion focalization and a curtain of heated nitrogen gas for desolvation (top), or with a heated capillary for

desolvation (bottom). Reprinted with permission from reference ⁷⁸ . Copyright 2007 Wiley-VCH Verlag GmbH & Co. KGaA, Weinheim.....	26
Figure 1.22. Schematic diagram of TEM. Reprinted with permission from reference ⁸⁰. Copyright 2019 Cambridge University Press.....	27
Figure 2.1. EE maps of SWCNTs (a) before and after 1 h reaction with 9-KODE under 566 nm illumination. (b) Fluorescent emission spectra change over 1 h (spectra taken every 5 min with 566 nm excitation). (c) UV-vis-NIR absorption spectra of the reaction mixture at different time points; expanded insets show E₁₁ and E₂₂ absorption peaks. (d) Emission intensities of E₁₁, E₁₁⁻, and E₁₁[*] of SWCNTs (with 566 nm excitation) reacted with 9-KODE over 6 h.....	36
Figure 2.2. (a) Raman spectra of SWCNTs before and after reaction with 9-KODE under 6-h 566 nm and 285 nm illumination, respectively. (b) Normalized apparent quantum efficiency (AQE) of the reaction illuminated at different wavelengths (285, 345, 566, and 988 nm) for 1h. The emission spectra were recorded under 566 nm excitation before and after illumination.	38
Figure 2.3. EE maps of SWCNTs (a) before and after 1 h reaction with 3-decen-2-one under 566 nm illumination. (b) Fluorescent emission spectra change over 1 h (spectra taken every 5 min with 566 nm excitation). (c) UV-vis-NIR absorption spectra of the reaction mixture at different time points; expanded insets show E₁₁ and E₂₂ absorption features. (d) Emission intensities of E₁₁, E₁₁⁻, and E₁₁[*] of SWCNTs (with 566 nm excitation) reacted with 3-decen-2-one over 6 h.	42
Figure 2.4. Structures and energies of representative [2π + 2π] cycloaddition and Diels-Alder products. ^a Dispersion energies (ΔE_{disp}) between SWCNT and the substituents on the	

cycloadduct were calculated using Grimme's DFT-D3 method from the dispersion-free HF functional.¹⁴⁶ 49

Figure 3.1. (a) Catalytic peroxidase and halogenation cycles of MPO. Adapted with permission from ref. 35. Copyright 2012 American Chemical Society. (b) Schematic diagram illustrating the enzymatic degradation of SWCNTs and GO (carbon and oxygen atoms are shown in gray and red, respectively)..... 61

Figure 3.2. (a) UV-vis-NIR absorption spectra and (b) photoluminescence emission spectra of the MPO/H₂O₂/Cl⁻ degradation of SWCNTs (CMC wrapped) from day 0 to day 5. 63

Figure 3.3. (a) UV-vis-NIR spectra, (b) Raman spectra, (c, d) TEM images, (e) photoluminescence emission, and (f) excitation spectra of the 5-day MPO/H₂O₂/Cl⁻ degradation of GO. (*) is the water Raman peak. The PL emission spectra (e) were obtained with excitation at 325 nm. The excitation spectra (f) were obtained at an emission wavelength of 440 nm..... 66

Figure 3.4. Fluorescence emission spectra of the degradation of GO with neutrophil-like HL-60 cells under (a) 325 nm and (b) 300 nm excitation (cells were centrifuged down before taking the measurements). The insets show that the PL spectra of the samples containing GO after 24 h incubation with cells after background subtraction (samples containing cells only after 24 h incubation (dashed red lines) served as the background, as they show a flat line in the insets). (c) TEM image of the supernatant of the sample containing GO after 24 h incubation with cells. 69

Figure 3.5. (a) Diameter (by DLS) and zeta potential of different samples. TEM images of (b, d) SWCNT(SC)/GO or (c, e) SWCNT(CMC)/GO (b, c) before and (d, e) after the 5-day MPO/H₂O₂/Cl⁻ degradation..... 71

Figure 3.6. Photoluminescence spectra of the MPO/H₂O₂/Cl⁻ degradation of (a) SWCNT(SC)/GO or (b) SWCNT(CMC)/GO nanoscrolls from day 0 to day 5. The visible and NIR PL spectra were recorded under 325 nm and 566 nm excitation, respectively. (c) Schematic mechanism diagram illustrating the degradation of SWCNT/GO nanoscrolls (the oxygen-containing defect sites are shown in red)..... 73

Figure 3.7. (a, b) Changes in the SWCNT(SC)/GO or (c, d) SWCNT(CMC)/GO nanoscrolls. (a, c) Normalized photoluminescence intensity and (b, d) ratio of intensity (Ratio) over 5-day MPO/H₂O₂/Cl⁻ degradation. The error bars represent standard deviations based on three replicate measurements. 75

Figure 4.1. Schematic diagram illustrating the oxidative biodegradation of graphene oxide (GO) into polycyclic aromatic hydrocarbons (PAHs). 78

Figure 4.2. LC-MS total ion liquid chromatograms (TIC) in positive ionization mode of (a) pure methanol, (b) MPO control, and (c) after 5-day MPO/H₂O₂/Cl⁻ degradation of GO. Note: the red * symbol in panel (c) indicates the peak subjected to chemical formula screening..... 82

Figure 4.3. Workflow for chemical formula and structure screening of potential PAHs generated through enzymatic degradation of GO. 84

Figure 4.4. (a) LC-MS/MS product ion spectrum of the precursor ion m/z 485.11 in Table 1. (b) Tentative structure assignment..... 90

**Figure 4.5. (a) LC-MS/MS product ion spectrum of the precursor ion m/z 251.04 in Table 1.
 (b) Tentative structure assignment..... 90**

**Figure 4.6. Molecular configurations with (A) $C_{33}H_{18}O_3$ and (B) $C_{25}H_{18}O_{10}$ stoichiometries.
 For each system the corresponding absorption vertical excitations (in the range (325 ± 20) nm) and fluorescence energies are indicated. The color scheme corresponds to C (gray), H (white) and O (red). 95**

Appendix Figure 1. UV-vis absorption spectrum of 9-KODE in nanopure water. 104

Appendix Figure 2. The relation between I_0/I_{11^-} (with 566 nm excitation) and the reaction time of SWCNTs reacted with 9-KODE under 566 nm illumination. The fitted data (red line) was acquired by fitting the experimental data (black dots) with equation 1, where I_0 is the E_{11} intensity of pristine SWCNTs..... 105

Appendix Figure 3. Fluorescent emission spectra (with 566 nm excitation) of SWCNTs (no dopants compound) before and after 1 h 566 nm illumination. 107

Appendix Figure 4. PL emission spectra (with 566 nm excitation) of SWCNTs and 9-KODE reaction mixture pretreated with either 250 mM ascorbic acid (a) or 250 μ g/mL morin (b) before and after 1 h 566 nm illumination. 108

Appendix Figure 5. EE maps of SWCNTs (a) before and after 1 h reaction with 9-KODE under 285 nm illumination. (b) Fluorescent emission spectra change over 1 h (spectra taken every 5 min with 566 nm excitation). (c) UV-vis-NIR absorption spectra of the reaction mixture at different time points; expanded insets show E_{11} and E_{22} absorption peaks. (d) Emission intensities of E_{11} , E_{11^-} , and E_{11^*} of SWCNTs (with 566 nm excitation) reacted with 9-KODE over 6 h..... 109

Appendix Figure 6. PL emission spectra (with 566 nm excitation) of SWCNTs and 9-KODE reaction mixture pretreated with either 250 mM ascorbic acid (a) or 250 μg/mL morin (b) before and after 1 h 285 nm illumination.	111
Appendix Figure 7. Fluorescent emission spectra (with 566 nm excitation) of SWCNTs and 9-KODE before and after being stored in the dark for 1 h.....	112
Appendix Figure 8. Fluorescent emission spectra (with 566 nm excitation) of SWCNTs and different compounds before and after 566 nm illumination for 1 h.....	114
Appendix Figure 9. EE maps (a) and fluorescent emission spectra (b) of SWCNTs before and after 1 h reaction with 3-decen-2-one under 300 nm illumination. (c) UV-vis-NIR absorption spectra of the reaction mixture at different time points; expanded insets show E₁₁ absorption feature.....	115
Appendix Figure 10. Fluorescent emission spectra (with 566 nm excitation) of SWCNTs and 3-hepten-2-one before and after 566 nm illumination for 1 h.....	116
Appendix Figure 11. Three dimensional structures of different diastereomers in the [2π(a) + 2π(d)] (1) cycloaddition reaction with (3E,5Z)-undecadien-2-one.	117
Appendix Figure 12. Three dimensional structures of different diastereomers in [2π(a) + 4π(de)] (4) cycloaddition reaction with (3E,5Z)-undecadien-2-one.....	118
Appendix Figure 13. Three dimensional structures of different diastereomers in [4π(ab) + 2π(d)] (7) cycloaddition reaction with (3E,5Z)-undecadien-2-one.	119
Appendix Figure 14. Energies and 3D structures of [2π + 2π] cycloaddition of (3E,5Z)-undecadien-2-one to the SWCNT with other π bonds. All energies are in kcal/mol. All energies are Gibbs free energies (in kcal/mol) with respect to the photoexcited SWCNT with 566 nm light and the substrate ((3E,5Z)-undecadien-2-one).	121

Appendix Figure 15. UV-vis-NIR absorption spectra (a) and PL emission spectra (b) of MPO/H₂O₂/Cl⁻ degradation of SWCNT (SC) from Day 0 to Day 5..... 131

Appendix Figure 16. UV-vis-NIR absorption spectra (a) and PL emission spectra (b) of SWCNT(CMC) before and after dilution with H₂O..... 131

Appendix Figure 17. EE maps of SWCNT (CMC) before and after 5-day MPO/H₂O₂/Cl⁻ degradation..... 132

Appendix Figure 18. The normalized PL intensity of SWCNT(CMC) over 5-day MPO/H₂O₂/Cl⁻ degradation. The error bars represent standard deviations based on three replicate measurements..... 132

Appendix Figure 19. UV-vis-NIR absorption spectra (a) and PL emission spectra (b) of SWCNT(CMC) before and after 5-day MPO/H₂O₂/Cl⁻ degradation without MPO, H₂O₂, and Cl⁻, respectively..... 133

Appendix Figure 20. NIR PL emission spectra of MPO/H₂O₂/Cl⁻ degradation without SWCNTs from Day 0 to Day 5..... 133

Appendix Figure 21. Size distribution of GQDs for the sample shown in Figure 3d. Image J software was used to measure size distribution. 134

Appendix Figure 22. EE maps of GO before and after 5-day MPO/H₂O₂/Cl⁻ degradation. 134

Appendix Figure 23. PL emission spectra of MPO/ H₂O₂/Cl⁻ degradation of GO from Day 0 to Day 5 with different excitation wavelengths ranging from 275 to 375 nm other than 325 nm (Figure 2d). (*) is water Raman peak..... 135

Appendix Figure 24. PL emission spectra of GO after 5-Day degradation with different excitations. (*) is water Raman peak..... 136

Appendix Figure 25. The normalized PL intensity of GO over 5-day MPO/H₂O₂/Cl⁻ degradation. The error bars represent standard deviations based on three replicate measurements..... 138

Appendix Figure 26. UV-vis-NIR absorption spectra (a) and Raman spectra (b) of GO before and after 5-day MPO/H₂O₂/Cl⁻ degradation without MPO, H₂O₂, and Cl⁻, respectively. 138

Appendix Figure 27. TEM images of GO after 5-day degradation without MPO (a), H₂O₂ (b), and Cl⁻ (c), respectively. 139

Appendix Figure 28. PL emission (a) and excitation (b) spectra of 5-day MPO/H₂O₂/Cl⁻ degradation of GO without MPO, H₂O₂, and Cl⁻, respectively. The emission spectra in (a) were obtained with excitation at 325 nm. The excitation spectra in (b) were obtained at emission wavelength 440 nm..... 139

Appendix Figure 29. Visible PL emission (a, with 325 nm excitation) and excitation (b, at emission wavelength 400 nm) spectra of MPO/H₂O₂/Cl⁻ degradation without GO from Day 0 to Day 5. PL emission spectra (c) after 5-day MPO/H₂O₂/Cl⁻ degradation without GO with different excitation wavelengths ranging from 275 to 375 nm. (*) is water Raman peak. 140

Appendix Figure 30. PL emission spectra of MPO/H₂O₂/Cl⁻ degradation of GO after 5-day degradation (1), and control without GO (2). The emission spectra were obtained with excitation at 325 nm. Spectra were normalized based on the intensity of water Raman peaks. Spectrum 3 is the result after subtracting spectrum 2 from spectrum 1. 141

Appendix Figure 31. AFM images and line profiles of SWCNT(SC) (a) or SWCNT(CMC) (b) nanoscroll before degradation. 142

Appendix Figure 32. UV-vis-NIR absorption spectra of MPO/H₂O₂/Cl⁻ degradation of SWCNT(SC)/GO (a) or SWCNT(CMC)/GO (b) nanoscrolls from Day 0 to Day 5. 143

Appendix Figure 33. (a, b) Changes in the SWCNT(SC)/GO or (c, d) SWCNT(CMC)/GO nanoscrolls. (a, c) Normalized photoluminescence intensity and (b, d) ratio of intensity (Ratio) over 5-day MPO/H₂O₂/Cl⁻ degradation. The error bars represent standard deviations based on three replicate measurements..... 144

Appendix Figure 34. (a, b) Changes in the SWCNT(SC)/GO or (c, d) SWCNT(CMC)/GO nanoscrolls. (a, c) Normalized photoluminescence intensity and (b, d) ratio of intensity (Ratio) over 5-day MPO/H₂O₂/Cl⁻ degradation. The error bars represent standard deviations based on three replicate measurements..... 145

Appendix Figure 35. Ratio of intensity (Ratio) over 5-day MPO/H₂O₂/Cl⁻ degradation using either polynomial (a, c) or exponential (b, d) regression models..... 146

Appendix Figure 36. Positive-ion ESI mass spectra of chromatographic peaks at (a) 9.28 min, (b) 20.29 min, and (c) 26.35 min in Figure 4.2c..... 148

Appendix Figure 37. LC-MS total ion liquid chromatograms (TIC) in negative ionization mode of (a) pure methanol, (b) MPO control, and (c) after 5-day MPO/H₂O₂/Cl⁻ degradation of GO. Note: the red * symbol in panel (b) indicates the peak subjected to chemical formula screening. 151

Appendix Figure 38. Negative-ion ESI mass spectra of chromatographic peaks at (a) 7.63 min, (b) 20.24 min, and (c) 26.32 min in Appendix Figure 34c..... 152

Appendix Figure 39. TEM images of (a) GO and (b) GO after 5-day MPO/H₂O₂/Cl⁻ degradation. Adapted with permission from S1. Copyright 2020 American Chemical Society. 154

Appendix Figure 40. Raman spectra of GO in the initial state and after 5-day MPO/H₂O₂/Cl⁻ degradation. The expanded inset show the D and G peaks of GO degradation products. 155

Appendix Figure 41. (a) XPS survey, (b) high-resolution carbon 1s and (c) high-resolution oxygen 1s spectra of GO (top) and GO after 5-day MPO/H₂O₂/Cl⁻ degradation (bottom)..... 156

Appendix Figure 42. (a) LC-MS/MS ion chromatogram showing the product ion profile and (b) LC-MS/MS product ion spectrum of the precursor ion m/z 463.13 in Appendix Table 10..... 157

Appendix Figure 43. (a) LC-MS/MS ion chromatogram showing the product ion profile and (b) LC-MS/MS product spectrum of the precursor ion m/z 445.12 in Appendix Table 10..... 158

Appendix Figure 44. (a) LC-MS/MS ion chromatogram showing the product ion profile and (b) LC-MS/MS product spectrum of the precursor ion m/z 371.10 in Appendix Table 10..... 159

Appendix Figure 45. (a) LC-MS/MS ion chromatogram showing the product ion profile and (b) LC-MS/MS product spectrum of the precursor ion m/z 480.16 in Appendix Table 10..... 160

Appendix Figure 46. (a) LC-MS/MS ion chromatogram showing the product ion profile and (b) LC-MS/MS product spectrum of the precursor ion m/z 413.27 in Appendix Table 10.....	161
Appendix Figure 47. (a) LC-MS/MS ion chromatogram showing the product ion profile and (b) LC-MS/MS product spectrum of the precursor ion m/z 325.06 in Appendix Table 10.....	162
Appendix Figure 48. (a) LC-MS/MS ion chromatogram showing the product ion profile and (b) LC-MS/MS product spectrum of the precursor ion m/z 501.09 in Appendix Table 10.....	163
Appendix Figure 49. (a) LC-MS/MS ion chromatogram showing the product ion profile and (b) LC-MS/MS product spectrum of the precursor ion m/z 161.06 in Appendix Table 10.....	164
Appendix Figure 50. (a) LC-MS/MS ion chromatogram showing the product ion profile and (b) LC-MS/MS product spectrum of the precursor ion m/z 271.55 in Appendix Table 10.....	165
Appendix Figure 51. (a) LC-MS/MS ion chromatogram showing the product ion profile and (b) LC-MS/MS product spectrum of the precursor ion m/z 547.08 in Appendix Table 10.....	166
Appendix Figure 52. (a) LC-MS/MS ion chromatogram showing product the ion profile and (b) LC-MS/MS product spectrum of the precursor ion m/z 455.31 in Appendix Table 10.....	167

Appendix Figure 53. (a) LC-MS/MS ion chromatogram showing the product ion profile and (b) LC-MS/MS product spectrum of the precursor ion m/z 783.58 in Appendix Table 10..... 168

Appendix Figure 54. PL excitation (black line) and emission spectra (red line) of GO before (dashed line) and after (solid line) 5-day enzymatic degradation. The PL emission spectra were obtained with excitation at 325 nm. The excitation spectra were obtained at emission wavelength 440 nm..... 169

Appendix Figure 55. LC-MS chromatogram of paclitaxel and docetaxel with associated chemical structure and molecular weight..... 186

Appendix Figure 56. Calibration plot for the quantification of paclitaxel..... 186

List of Schemes

Scheme 1.1. Mechanism of CNTs induced pulmonary inflammation. Reprinted with permission from reference ³⁵. Copyright 2013 Elsevier B.V.....	12
Scheme 2.1. Proposed reaction mechanisms for generating different cycloaddition defects on (6,5) SWCNT.	45
Scheme 4.1. Schematic representation of the proposed mechanism for MPO/H₂O₂/Cl⁻ degradation of GO. The numbers indicated in red correspond to oxidation state of the carbon atoms.	88
Scheme 4.2. Illustration for the loading of NCNC with cargo and corking with gold nanoparticles, followed by release of cargo through incubation with enzymatic oxidation.....	98

Preface

I would like to first express my sincerest gratitude to my research advisor, Professor Alexander Star, from whom I have learned so much. His mentoring has been invaluable towards my intellectual growth. More importantly, the respect and enthusiasm he treated science, and his rigorousness, optimism, generosity, and calmness personality, both have a profound impact on me. Thank you for all the support and help he provided with me. It has been a true honor to know, work with and learn from him.

I would also like to express my appreciation to my committee members, Professor Steve Weber, Professor Haitao Liu, and Professor Michael R. Shurin. Their time and valuable advice towards the improvement of my research projects. Thank you.

Special thanks to all my collaborators, from whom I have learned a great deal of science through our efforts. I would like to thank Professor Valerian Kagan and Dr. Alexandr A. Kapralov for their knowledge in biochemistry and their assistance in performing cell studies. To Dr. Bo Wegge Laursen, for the thoughtful discussion about the fluorescence data. To Professor Peng Liu, Dr. Ilia Kevlishvili, Katherina Murcek and Dr. Dan C. Sorescu, for performing computation modeling.

Furthermore, I would like to thank my colleagues, former and current group members, Dr. Cheuk Fai Chiu, Dr. Seth C. Burkert, Dr. James Ellis, Dr. Sean I. Hwang, Michael Chido, Dr. David L. White, Dr. Wenting Shao, Long Bian, Zidao Zeng, Christian Gamboa, Zhengru Liu, and Rodrigo Silva Ferreira. Thank you for their challenging discussions and thoughtful encouragement. It has been a pleasure working with all of you and I wish you the best of luck with your future endeavors.

I would like to extend my gratitude to the faculty, staff, and students of the Department of Chemistry for their assistance throughout my time as a member of the University of Pittsburgh. I would like to thank Christie Hay, Mary Beth Conroy, LaShawn Youngblood and all the other second floor staff members for their assistance throughout the years. To Bhaskar Godugu, thank you for the help he provided about sample preparation and data analysis. To Dave Emala and the members of the electronic shop, thank you for your help towards instrument trouble-shooting to achieve my research goals. To Lori Neu for all my glass needs and her warm conversation. Much appreciation is owed to Tom Harper from the Department of Biological Science for his help with all of my electron microscopy questions and ideas. To Dr. Joel Gillespie for his training and valuable understanding of the many analytical techniques used within the department.

Thank you for the love of my family and friends accompanying me throughout this journey. Words could not express my feeling with all the priceless love and caring you gave to me. To my parents, thank you for giving me life and always being there for me. I wish I could be a better daughter by giving you more accompany and without letting you worry about me so much.

1.0 Introduction

1.1 Carbon Nanomaterials (CNMs)

Graphene, the parent of all graphitic forms of carbon,¹ is a two-dimensional (2D) sheet of sp^2 -hybridized carbon atoms arranged in a honeycomb lattice (Figure 1.1). Graphene serves as the building block for graphitic materials of other dimensionalities. It can be wrapped to form 0D fullerenes, rolled into 1D nanotubes, and/or stacked together to form graphite. Each carbon atom in the graphene lattice contributes a π orbital to form a delocalized network of electrons.

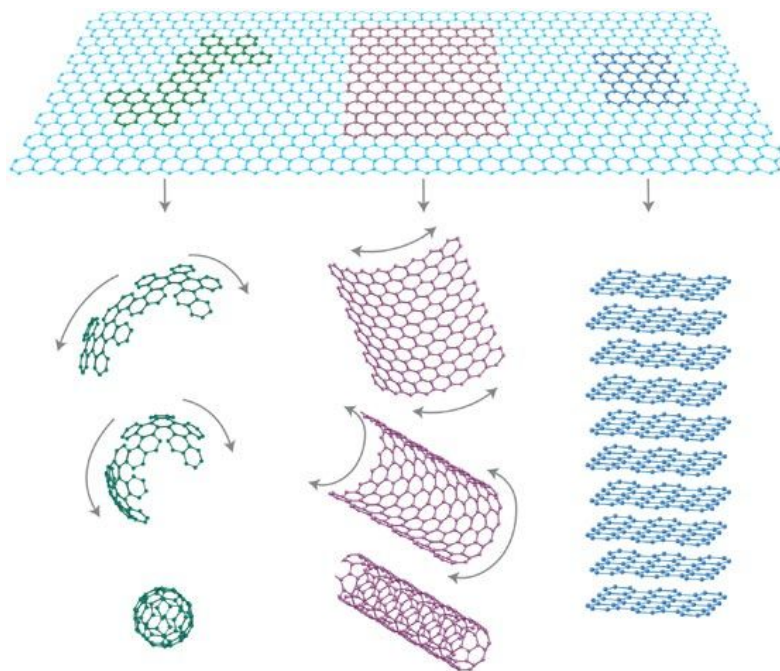


Figure 1.1. Graphene as a 2D building block for other graphitic carbon materials including 0D fullerenes (left), 1D carbon nanotubes (middle), and 3D graphite (right). Reprinted with permission from ref ¹.

Copyright 2007 Nature Publishing Group.

1.1.1 Carbon Nanotubes

Various methods have been developed for the synthesis of single-walled carbon nanotubes (SWCNTs). These include electric arc discharge, laser vaporization, and catalytic chemical vapor deposition (CVD). There are mainly two catalytic CVD methods have been developed, high-pressure carbon monoxide (HiPCO) process² and cobalt-molybdenum catalyst (CoMoCAT) process.³ Specifically, in HiPCO process, SWCNTs are produced through heating a mixture of carbon monoxide (CO) and a small amount of iron carbonyl ($\text{Fe}(\text{CO})_5$). The thermal decomposition of $\text{Fe}(\text{CO})_5$ produce iron nanoparticles in the gas phase. These iron clusters serve as the nucleation site for the transformation of CO into carbon during the growth of SWCNTs. In CoMoCAT process, SWCNTs are produced through the decomposition of CO on a silica supported cobalt-molybdenum bimetallic catalyst. CoMoCAT process could synthesize SWCNTs with narrow distribution of tube diameter and provide good chirality control during synthesis.

Raman spectra of SWCNTs (Figure 1.2) displayed two characteristic bands, D band and G band. Defect and sp^3 carbon atoms give rise to D band, and G band is associated with the sp^2 carbon atoms in the SWCNTs wall. The resonant G' band (sometimes called D* band) at $\sim 2600 \text{ cm}^{-1}$ occurs as an overtone of the D band. The position of the radial breathing mode (RBM) of SWCNTs is correlated with the individual chirality of the nanotubes. The intensity ratio between the D band and G band, or I_D/I_G , represent the increased sp^3 defects in SWCNTs.

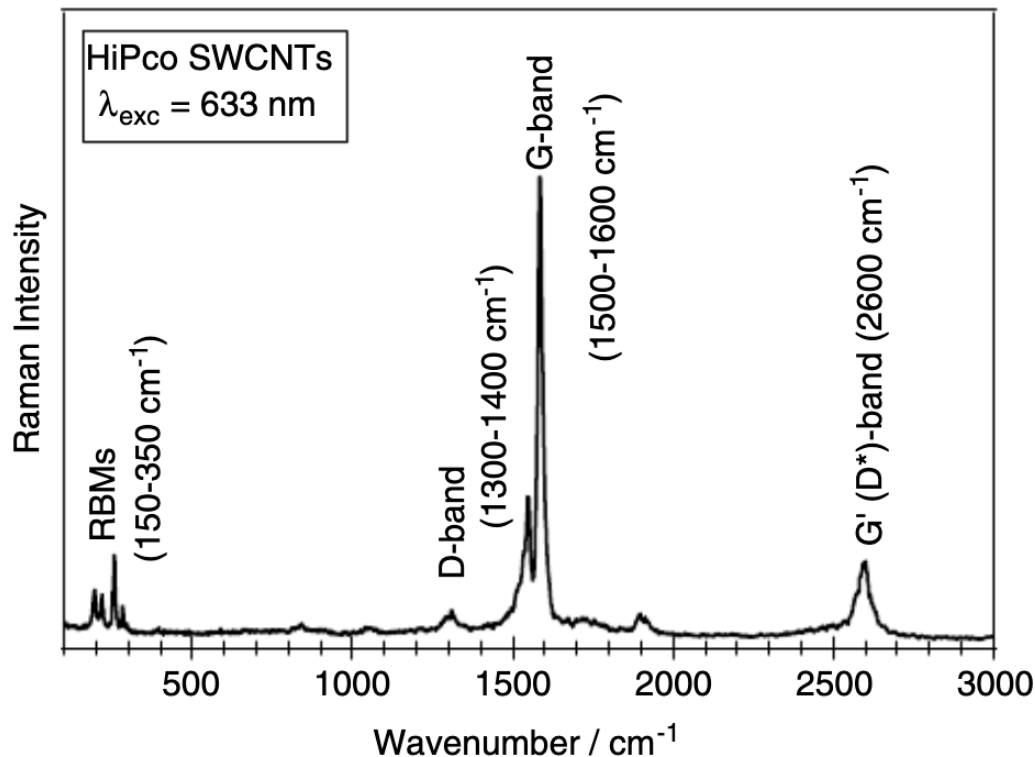


Figure 1.2. The Raman spectrum of SWCNTs. The prominent bands highlighted bands provide vital insight into the properties and nature of the CNTs. Reprinted with permission from ref.⁴ Copyright 2007 John Wiley & Sons, Ltd.

1.1.2 Graphene Oxide

Graphene oxide (GO), traditionally served as a precursor for chemically derived graphene (i.e., reduced graphene oxide), is a compound consisting of carbon, oxygen, and hydrogen atoms in variable ratios. It can be considered as graphene sheets further decorated with chemically bonded oxygen-containing functional groups, such as hydroxyl, epoxide, carbonyl, and carboxylic groups. Compared with pristine graphene, the presence of these functional groups give rise to remarkable structure defects, enables GO to be a composite containing both sp²- and sp³-hybridized carbon atoms. Due to the tunability of the chemical composition and the resulting

physicochemical properties of GO, through chemical, thermal, or electrochemical engineering of the defect sites, the scope of GO applications has been largely expanded.⁵

Hummer's method,⁶ a reliable solution-based process developed in 1958, has been one of the most widely-used synthesis techniques both in industrial and academic laboratories nowadays to produce single-layer graphene oxide. Briefly, synthesis of GO is achieved through oxidative treatment of graphite with strong oxidizers, addition of potassium permanganate to a solution of graphite, sodium nitrate, and sulfuric acid.

Figure 1.3a and 1.3b display the chemical structure and 3D structural model of GO bearing carboxylic acid groups at the edges, and phenol, hydroxyl, and epoxide groups mainly on the basal plane. As a result of oxygen-containing groups decoration, GO is hydrophilic, and soluble in water giving a yellowish-brown color, as shown in Figure 1.3c. Figure 1.3d and 1.3e show the transmission electron microscopy (TEM) and atomic force microscopy (AFM) images of GO, which indicate the size of GO sheet is in the micrometer scale and the thickness of a single sheet is around 1 nm.

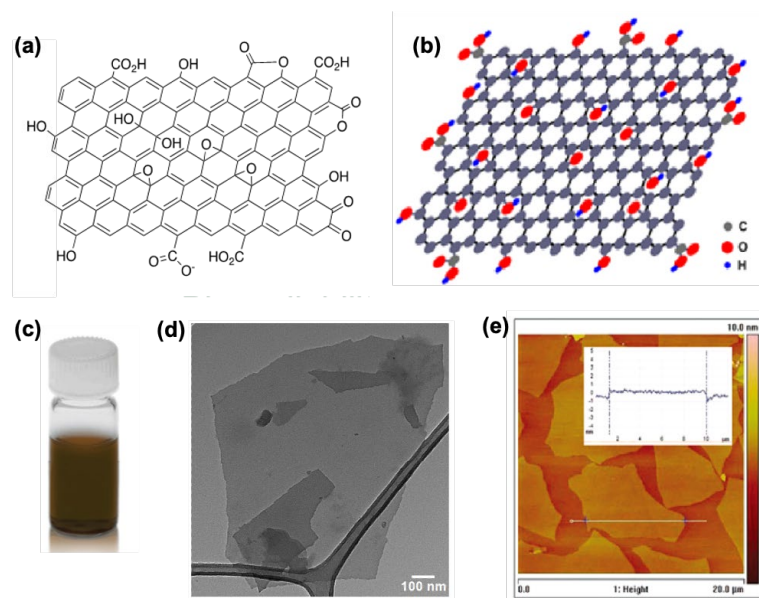


Figure 1.3. (a) Chemical structure and (b) 3D model of GO. Reprinted with permission from reference ⁵. Copyright 2012 American Chemical Society. (c) photograph of GO suspension in water, (d) TEM and (e) AFM images of GO single sheet. Reprinted with permission from ref. ⁷ Copyright 2008 American Chemical Society.

The chemical composition of GO and the presence of oxygen functional groups in GO have been identified using various spectroscopic techniques, including ultraviolet-visible absorption spectroscopy (UV-vis), Raman spectroscopy,⁸⁻¹¹ X-ray photoelectron spectroscopy (XPS),^{8, 11-15} solid-state nuclear magnetic resonance (SS-NMR),^{12, 16-18} and Fourier transform infrared spectroscopy (FTIR).^{14, 17, 19-21}

Figure 1.4a shows the UV-vis absorption spectrum of GO suspension in water. One main peak at ~ 230 nm originates from the π - π^* transition of aromatic C-C and C=C bonds in sp^2 hybrid regions and a shoulder peak at 300 nm which correspond to n - π^* transition of the C=O bonds in sp^3 hybrid regions, which confirmed the existence of carbonyl groups on the surface of GO.²² Similar to SWCNTs, Raman spectra of GO (Figure 1.4b) displayed two characteristic bands, D band, which measures the presence of disorder in sp^2 -hybridized carbon systems, and G band

evaluates stretching of C-C bonds in graphitic materials.²³ The I_D/I_G provides information about the disorder in the graphitic lattice of the GO sheets.²³

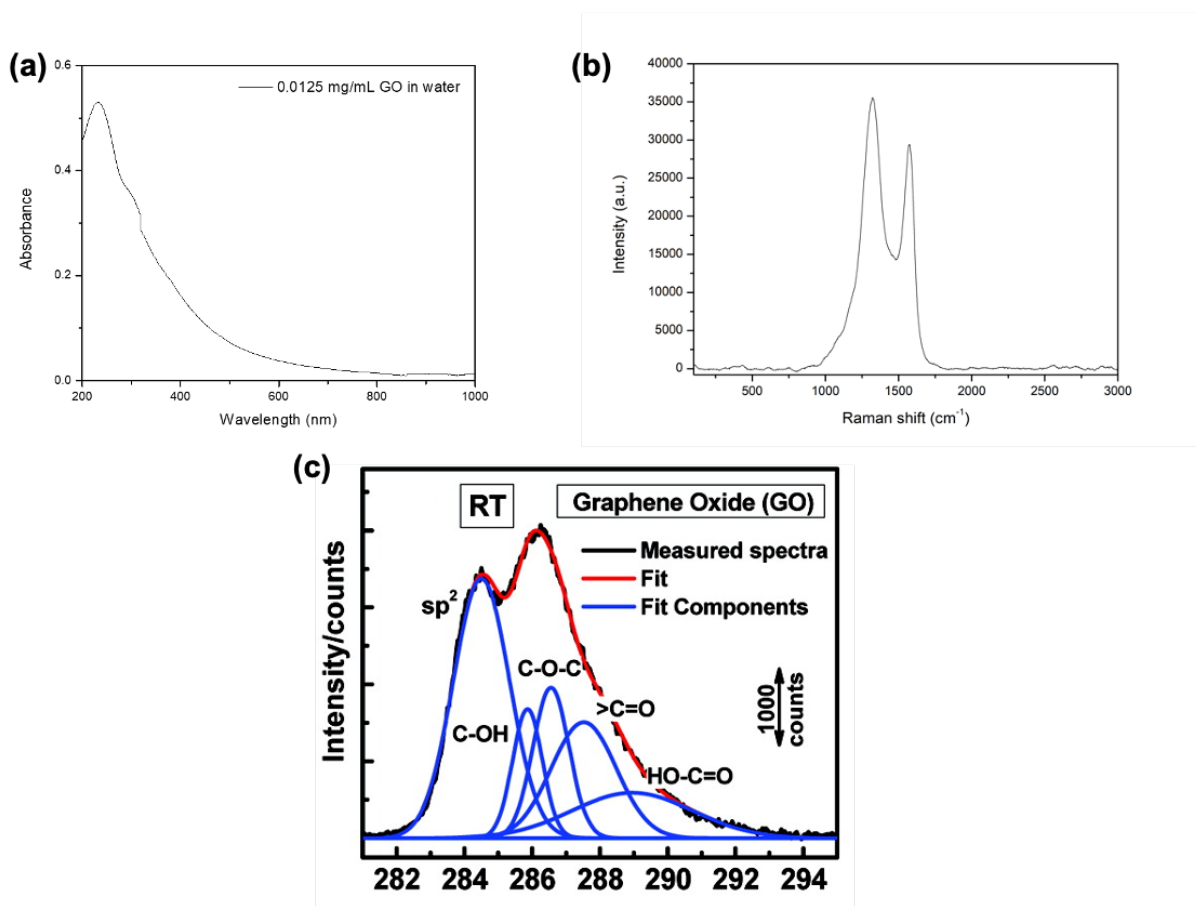


Figure 1.4. (a) UV-vis absorption, (b) Raman, and (c) high-resolution C_{1s} XPS spectra of pristine GO.

Reprinted with permission from reference ¹¹. Copyright 2011 American Chemical Society.

Three main peaks are revealed in the typical ^{13}C NMR spectrum of GO (Figure 1.5a). The peak at 60 ppm can be assigned to carbon atoms bonding to the epoxy group, the peak around 70 ppm corresponds to the hydroxyl group connected to the carbon atoms, and the peak around 130 ppm is ascribed to the graphitic sp^2 carbon.^{12, 16} In addition, in the high-resolution ^{13}C NMR spectrum another three small peaks were also found at about 101, 167, and 191 ppm. These three

weak peaks were tentatively assigned to lactol, the ester carbonyl, and the ketone groups, respectively.¹²

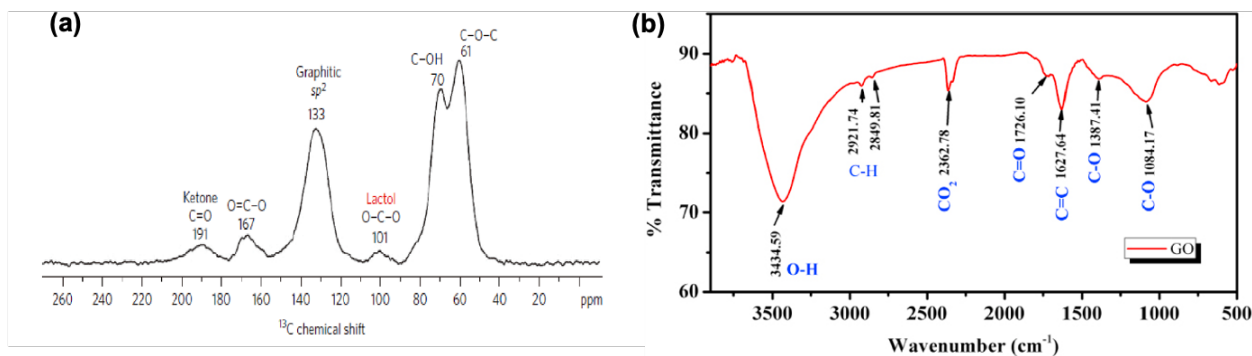


Figure 1.5. (a) Solid-state ^{13}C magic-angle spinning (MAS) NMR and (b) FTIR spectra of pristine GO.

Reprinted with permission from references ^{12, 21}. Copyright 2009 Nature Publishing Group and 2013 IOP Publishing Ltd.

1.1.3 Nitrogen-doped Carbon Nanotubes Cups (NCNCs)

By incorporating nitrogen-doping into the carbon lattice of CNTs during synthesis, unique, stacked-cups structures was formed (Figure 1.6a). Nitrogen-doped carbon nanotube cups (NCNC) synthesized from chemical vapor deposition (CVD) can be effectively separated into individual and short stack segments through oxidation in mineral acids and subsequent probe-tip sonication (Figure 1.6c). Our group have shown that these separated cups can be sealed with gold nanoparticles through a citrate reduction of chloroauric acid (Figure 1.6d), and therefore representing an attractive drug delivery nanocarrier.²⁴

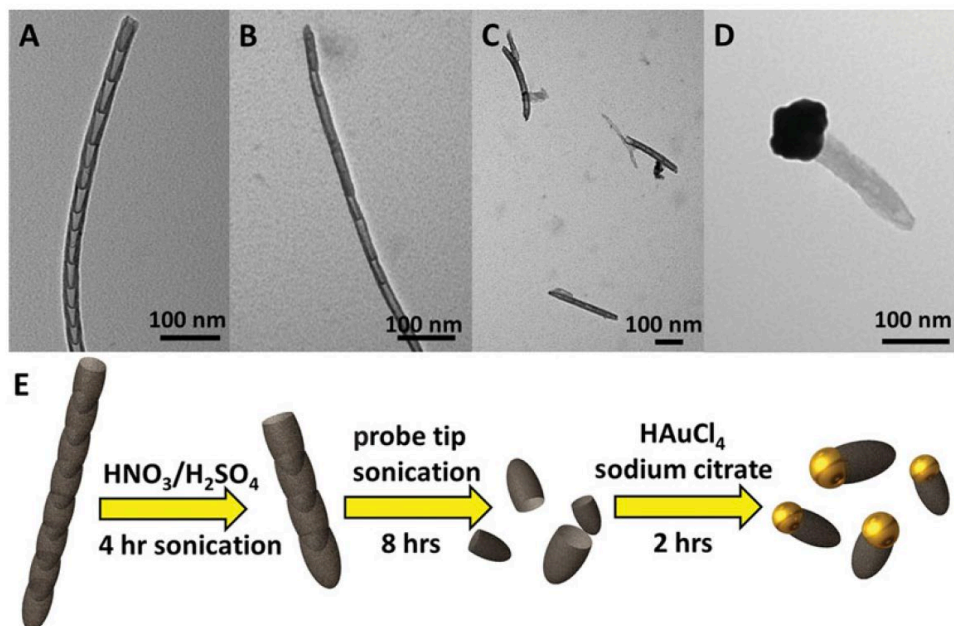


Figure 1.6. Separation and corking of stacked nitrogen-doped carbon nanotube cups (NCNCs). Transmission electron microscopy images of (A) as-synthesized, stacked NCNCs, (B) oxidized NCNCs, (C) separated NCNCs, and (D) GNP-corked NCNCs. (E) schematic diagram for the preparation of corked NCNCs. Reprinted with permission from ref. ²⁵

Copyright 2015 by John Wiley & Sons, Inc.

1.2 Biological Interactions of Carbon Nanomaterials

1.2.1 Nano-Bio Interactions

Nanotechnology is the engineering and manipulation of nanomaterials to design tools and devices. With the increasing improvement of the nanotechnology, understanding the interface between nanomaterials and biological systems becomes important.

CNMs are primarily in the range of 1 to 1000 nanometers. As shown in Figure 1.7, biological entities, such as proteins and viruses, are comparable in size to the engineering-inspired nanomaterials. Due to the above size match, a lot of research has been done to study the biotransformation of nanomaterials, and applied nanomaterials in the field of biosensing, drug delivery, bioimaging, and tissue engineering.²⁶⁻²⁸

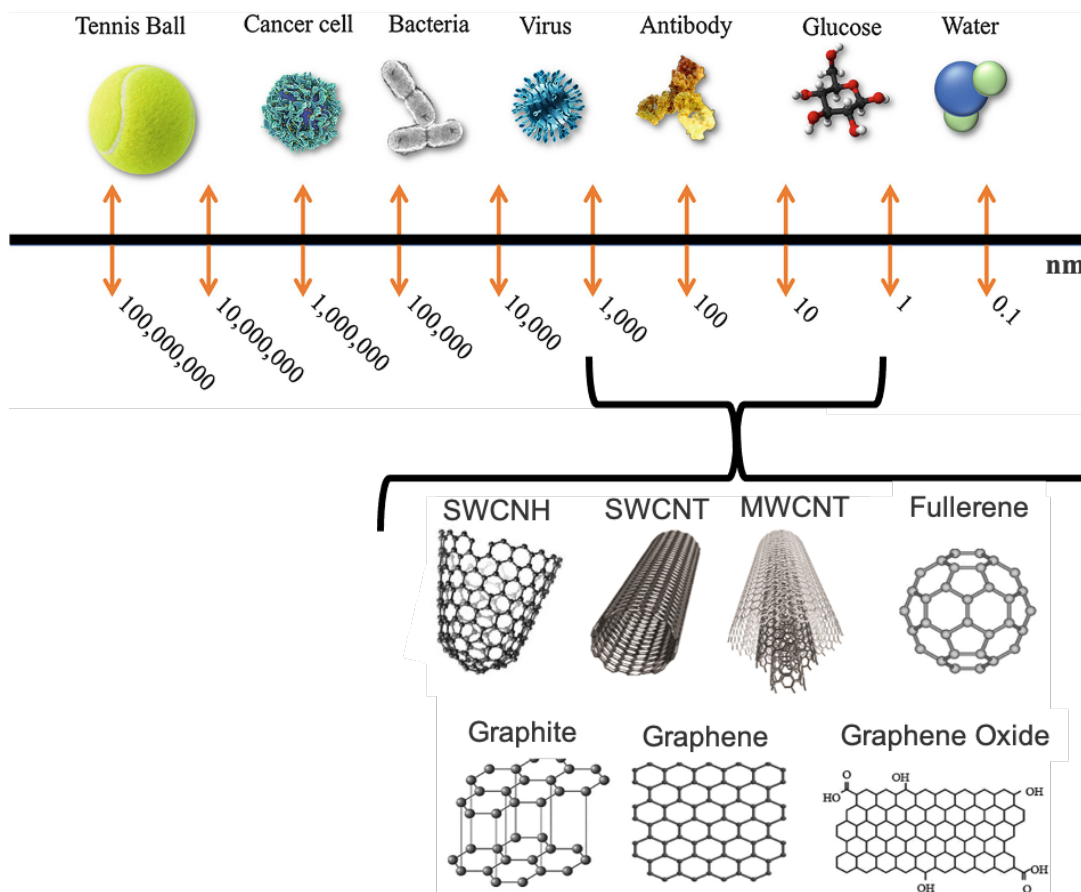


Figure 1.7. Size comparison between Carbon Nanomaterials and different molecules. Adapted with permission from ref.²⁹ and ref.³⁰. Copyright 2019 Springer International Publishing and 2021 Elsevier B.V..

1.2.2 CNMs Interactions with Lipids

The introduction of CNMs to body is mainly through pulmonary routes on inhalation. Previous research^{31, 32} have shown that foreign particles are rapidly coated with a corona of biomolecules, mainly lipids (90%) and protein (10%), upon inhalation, that may influence their cellular uptake and toxicity of nanomaterials, as shown in Figure 1.8.

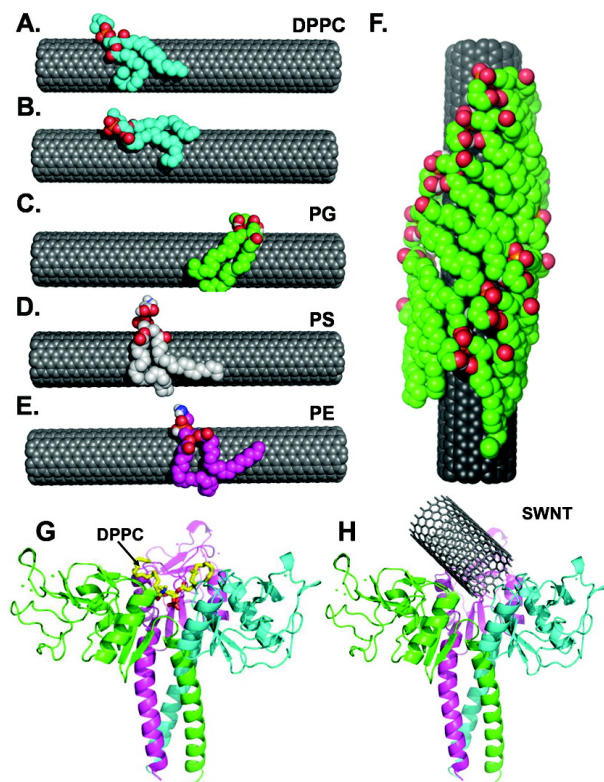


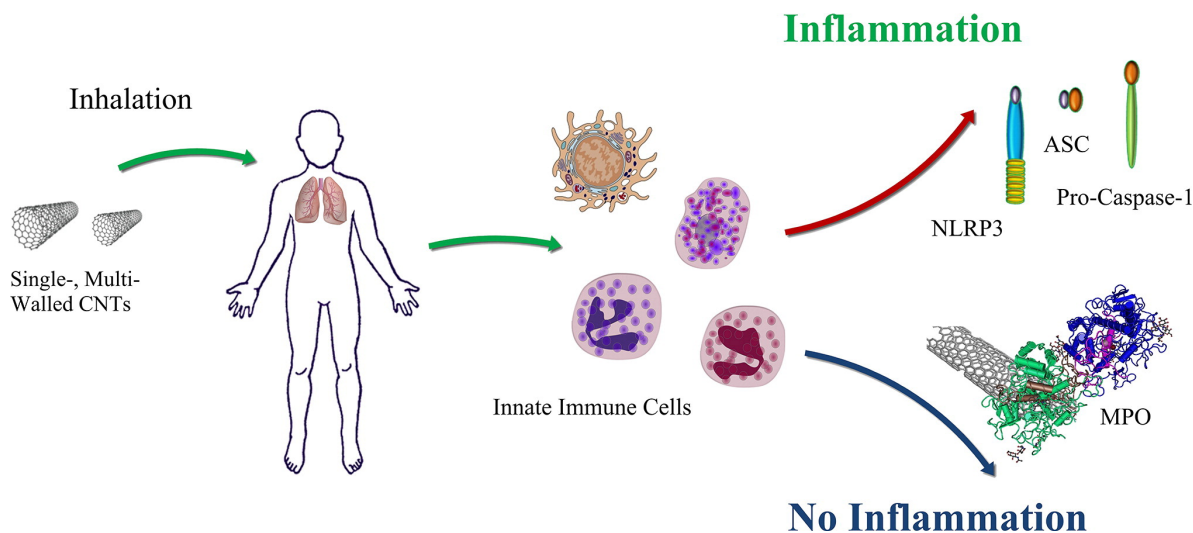
Figure 1.8. Computer modeling of SWCNTs binding with phospholipids and SP-D. The predicted binding pose of (A) lowest energy conformation of DPPC, (B) DPPC bound along the axis of SWCNT, lowest energy conformation of (C) PG, (D) PS, and (E) PE. (F) Lipid coating model generated using the PG-bound form of SWCNT shown in (C). Reprinted with permission from reference³². Copyright 2012 American Chemical Society.

Extensive investigations have undergone in order to determine how factors such as nanoparticle physico-chemical properties, biological media composition, and incubation time affect the identity and quantity of proteins in the biomolecule corona.^{33, 34} However, similar investigations into the factors which affect the lipid component of the biomolecule corona are lacking, and investigations which have been performed have not resulted in clear understanding of the factors influencing lipid corona formation. Herein, we propose to investigate how the aforementioned variables affect the lipid component of the biomolecule corona.

1.2.3 Toxicity of Carbon Nanomaterials

Previous research has shown that exposure to CNMs, especially CNTs, can result in pulmonary toxicity and cytotoxicity.^{35, 36} Scheme 1.1 illustrates the diagram of inflammatory process. Foreign inducers, such as CNTs, initiates a multidimensional response from the sensors, innate immune cells, such as macrophages, mast cells, eosinophils, neutrophils and so on. These cells could further produce soluble mediators leading to inflammation in target tissues.

Additionally, numerous reports have confirmed that GO can cause dose-, time-, thickness-, and size-dependent cytotoxicity including *in vivo* toxicity, platelet aggregation, pulmonary thromboembolism, granuloma formation, and it can also attenuate immune response.^{37, 38} Even similar graphene-based materials synthesized by different methods often exhibit different physicochemical properties,³⁹ leading to contradictory results on toxicity.^{38, 39} In view of these varied reports of toxicity induced by GO, exploring methods to alleviate or quell these effects seems to be prudent.



Scheme 1.1. Mechanism of CNTs induced pulmonary inflammation. Reprinted with permission from reference

³⁵. Copyright 2013 Elsevier B.V.

1.2.4 Enzymatic Oxidative Degradation of CNMs

Our group has demonstrated that GO can be biodegraded by horseradish peroxidase (HRP) over the course of 20 days when incubated with small, localized concentrations of hydrogen peroxide ($\sim 40 \mu\text{M}$).⁴⁰ Figure 1.9 shows that 10-day incubation resulted in the formation of holes on the basal plane. Holey graphene oxide has a sheet height of 1.10 nm, and the holes were authentic at a height of 0.01 nm.

In contrast, during the same period of analysis, HRP failed to oxidize chemically reduced graphene oxide (RGO). Computational analysis indicated that HRP was preferentially bound to the basal plane rather than the edge for both GO and RGO. Owing to the more dynamic nature of HRP on GO, the heme active site of HRP was in closer proximity to GO compared to RGO, thereby facilitating the oxidation of the basal plane of GO.

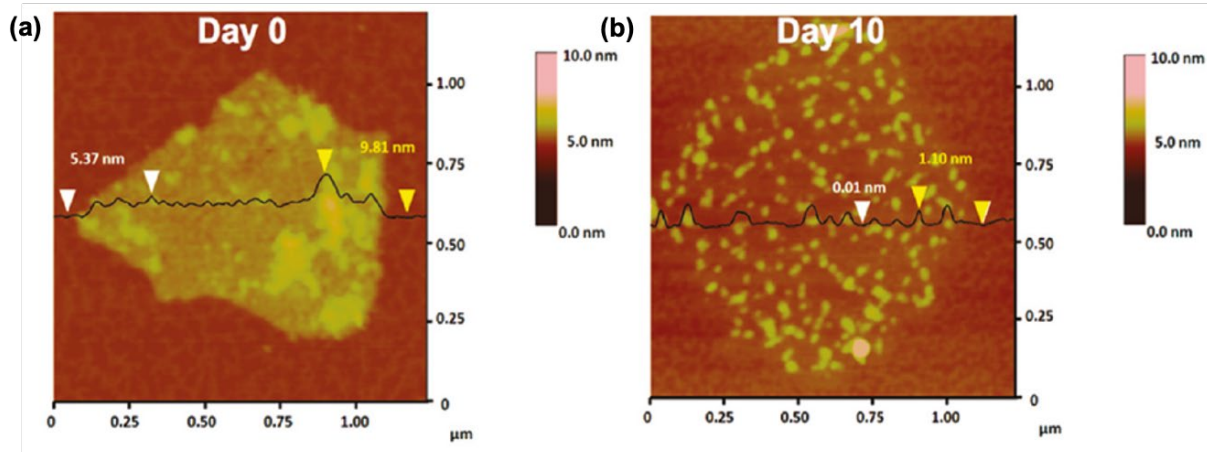


Figure 1.9. AFM images with section analysis of GO with HRP at (a) day 0 and (b) holey graphene oxide at day 10. Reprinted with permission from reference ⁴⁰. Copyright 2011 American Chemistry Society.

Moreover, in order to know the possible toxicological implication of those products formed during the degradation process, a mass spectrometry (MS)-friendly oxidation method, photo-Fenton reaction, to oxidize GO was performed.^{41, 42} On the basis of FTIR, MS, and NMR data, potential structures for these oxidation products, which consist of oxidized polycyclic aromatic hydrocarbons (o-PAH) intermediates, were identified and proposed.

Interestingly, strong fluorescence was observed after 3-day oxidation treatment (Figure 1.10c). Upon excitation at 325 nm, GO demonstrates a broad peak that is centered around 430 nm. By day 1, the fluorescent intensity increased 154% versus day 0, and its spectrum is both broad and centered on 430 nm. Finally, the fluorescence intensity on day 3 increases 1814 and 1175% versus day 0 and 1, and its sharp peak is centered at ~440 nm. This increase in fluorescence provides evidence that GO is broken down into conjugated products (e.g., oxidized PAHs and/or GQDs), which gradually becomes dominant in the system with longer reaction time (i.e., days 2 and 3).

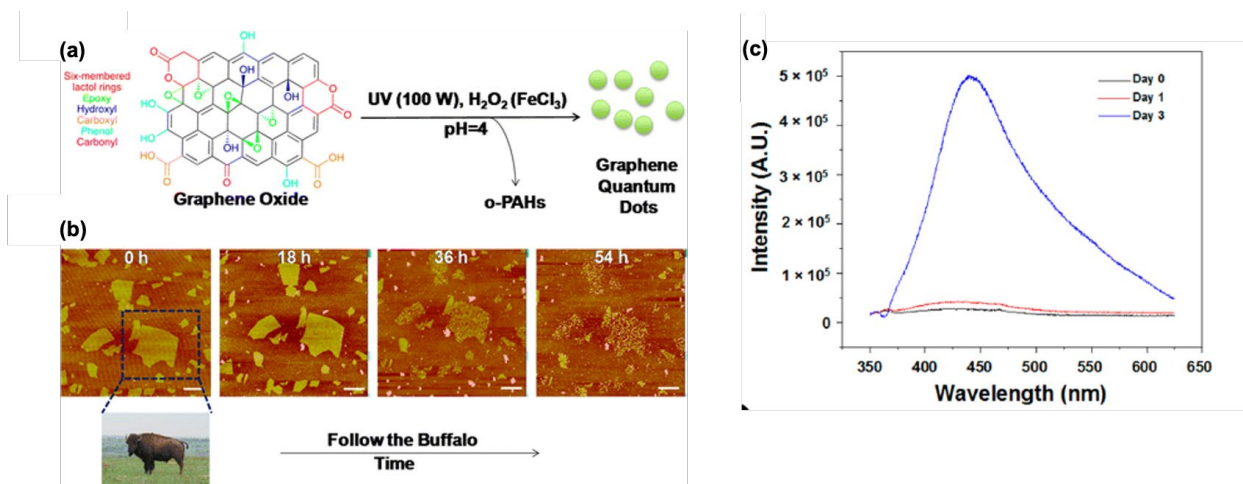


Figure 1.10. (a) Schematic diagram demonstrating the degradation of GO via the photo-Fenton reaction (b) AFM images of as-received GO after reaction with the Fenton reagent under UV irradiation for 0, 18, 36, and 54 h. All images were obtained in tapping mode, and the scale bars are 500 nm. (c) Fluorescence spectra of the GO solution after 0, 1, and 3 days of the photo-Fenton reaction. Reprinted with permission from reference ⁴². Copyright 2014 American Chemistry Society.

In 2015, the biodegradation of GO sheets was reported by using myeloperoxidase (MPO) derived from human neutrophils in the presence of a low concentration of H₂O₂.⁴³ Different from plant-derived enzyme HRP, MPO is a crucial peroxidase secreted by various primary phagocytic cells in the innate immune system.⁴⁴ In particular, MPO is the most abundantly expressed by neutrophils during the first phase of inflammation, which produces potential oxidants such as hypochlorous acid (HOCl) and reactive radical intermediates, essential to kill the pathogens or to eliminate endogenous molecules.⁴⁵ Moreover, MPO is also known to catalyze the production of the major oxidant, HOCl, from H₂O₂ and chloride anion (Cl⁻).^{46, 47}

After 15-hour incubation, the characteristic sheet shape and flat morphology of GO, observed in the control GO samples (Figure 1.11A) started to significantly disappear. Numerous damaged parts throughout the graphitic lattice of GO are visible, forming perforated GO, where

most of the holes were connected to each other. After 24 h, only a few visual fields showed evidence of residual carbonaceous material, while all GO sheets completely degraded (Figure 1.11 C) and the large GO sheets were no longer present. The holey GO sheets (15 h treated) lost their integrity as well.

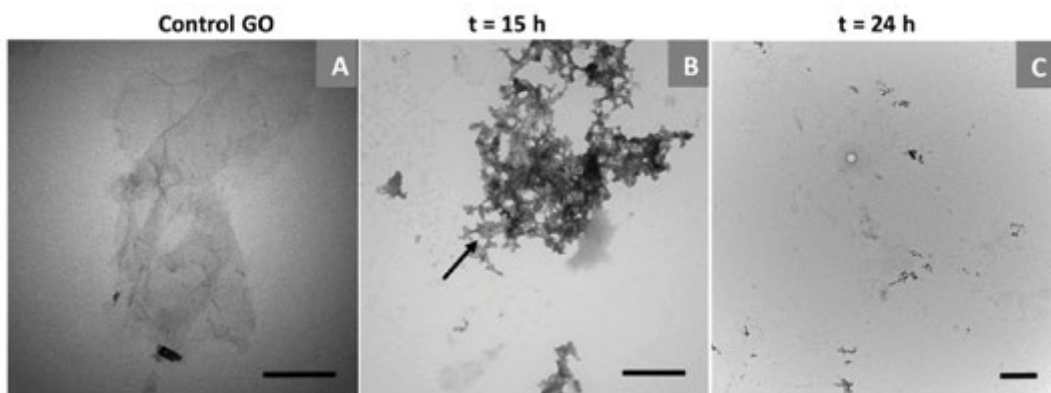


Figure 1.11. TEM images of MPO-mediated degradation of GO at three time points: (a) control ($t = 0$), (b) $t = 15$ h, and (c) $t = 24$ h. Reprinted with permission from reference ⁴³. Copyright 2015 Wiley-VCH Verlag GmbH & Co. KGaA, Weinheim.

Recently, Bengt Fadeel and co-workers further confirmed the successful degradation of GO by primary neutrophils.⁴⁸ Figure 1.12 clearly shows that both the D and G band intensities of GO were significantly reduced after 6 h and continued to decrease at 12 h of incubation with NETs in the presence of H_2O_2 . As the degradation products could have toxicological implications, they also evaluated the impact of degraded GO on the bronchial epithelial cell line BEAS-2B. MPO-degraded GO was found to be non-cytotoxic and did not elicit any DNA damage.

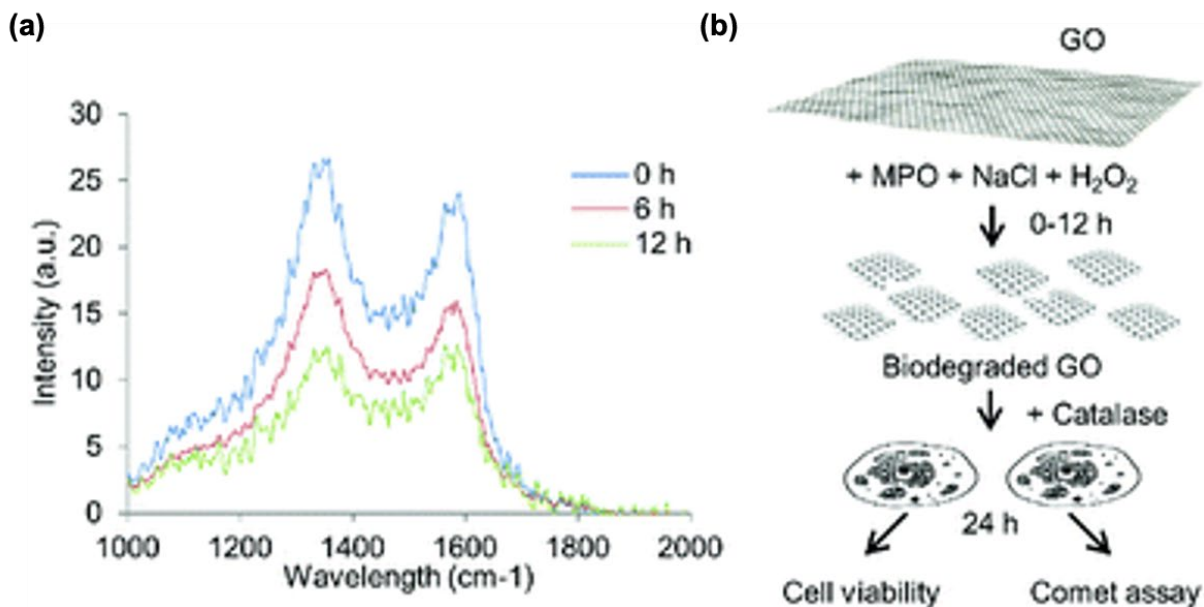


Figure 1.12. (a) Raman spectra of GO incubated with neutrophil extracellular traps (NETs) in the presence of NaCl and H₂O₂ for the indicated time-points. **(b)** Large (GO-L) and small (GO-S) sheets were biodegraded by recombinant MPO in the presence of NaCl and H₂O₂ for 0-12 h, followed by treatment with catalase to quench the excess H₂O₂. Then, cell viability and genotoxicity assessment of the GO biodegradation products was performed using the human lung cell line BEAS-2B. Reprinted with permission from reference ⁴⁸.

Copyright 2018 The Royal Society of Chemistry.

In addition to the GO, MPO/H₂O₂/Cl⁻ oxidation system have also been shown to effectively degrade SWCNTs⁴⁹ and NCNCs.⁵⁰ In 2010, Kagan *et al*⁴⁹ first reported the MPO-catalyzed degradation of SWCNTs, as shown in Figure 1.13. The biodegraded CNTs have been proved to be non-inflammatory in the lungs of mice. These findings give evidence for the development of the strategies mitigating the pulmonary side effects of the CNMs.

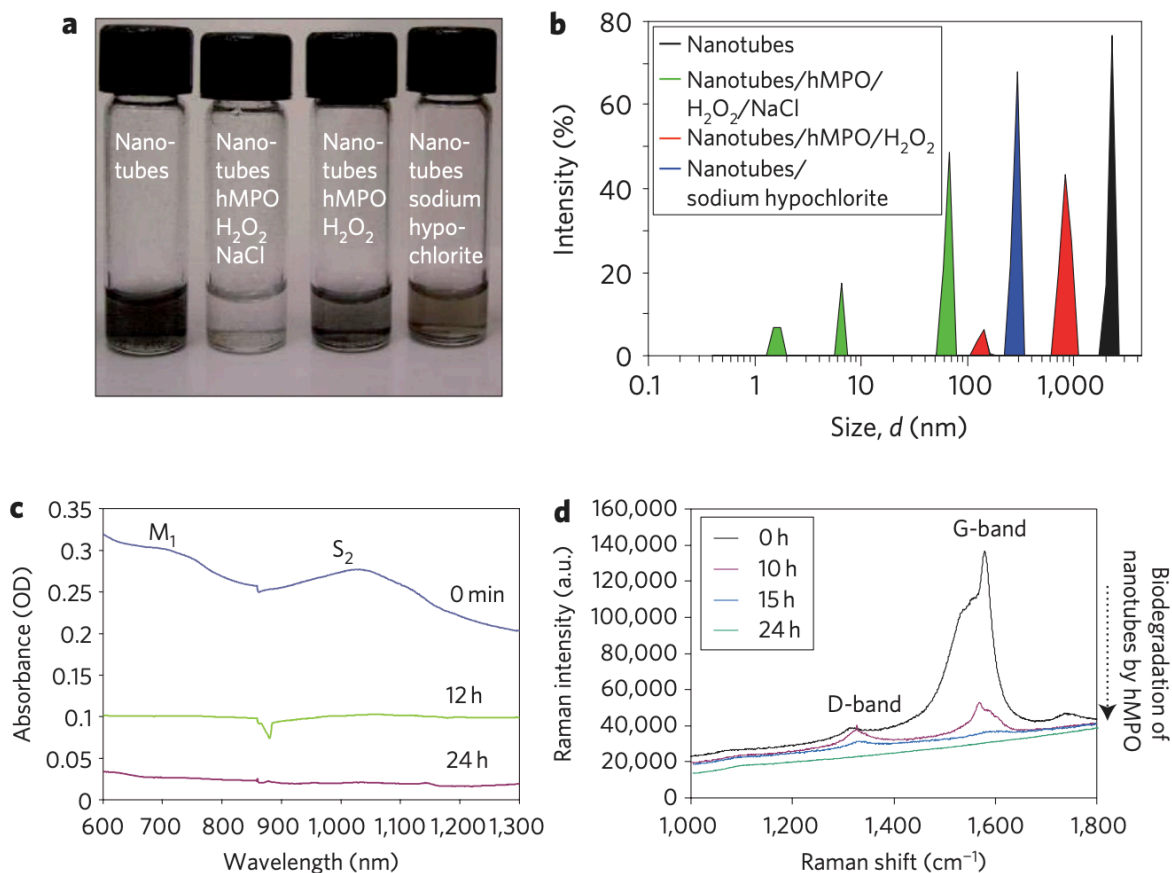


Figure 1.13. a, Photograph of different short-cut nanotube suspensions after 24 h. b, Dynamic light scattering showing multiple smaller peaks corresponding to biodegraded nanotubes. c, Infrared spectra showing loss of M1 and S2 bands as nanotubes are degraded in the presence of hMPO and H₂O₂. OD, optical density. d, Raman spectra (excitation, 633 nm) of ethanol-dried nanotubes (black) and (hMPO and H₂O₂)-treated nanotubes, showing loss of the characteristic G-band, followed by appearance and decay of the D-band over time. Reprinted with permission from reference ⁴⁹. Copyright 2010 Nature Publishing Group.

It has been found that the enzymatic degradation of gold-corked NCNCs (Au-NCNCs) would trigger the release of gold nanoparticles corks from the nanocups at the initial stage of degradation (Figure 1.14). This process enables the actively open of the cups before the complete degradation of NCNC shells within a course of 20 days. Such triggered opening and controlled degradation of Au-NCNCs makes them become ideal drug delivery carriers. Au-corked NCNCs

were demonstrated to be capable of effective (i) delivery of paclitaxel to tumor-associated myeloid-derived suppressor cells (MDSC), (ii) MPO-regulated release, and (iii) blockade of MDSC immunosuppressive potential.

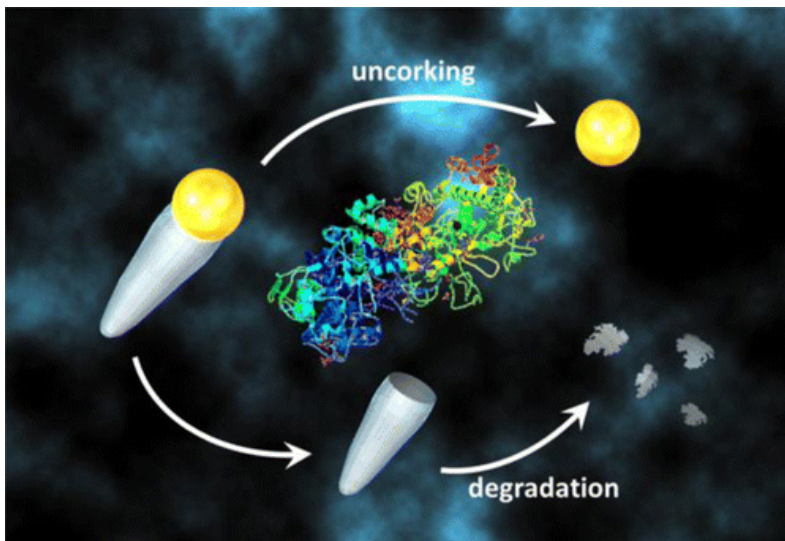


Figure 1.14. Scheme illustration of controlled opening and degradation of Au-NCNCs by MPO enzymatic oxidation system. Reprinted with permission from reference ⁵⁰. Copyright 2015 American Chemistry Society.

1.3 Fluorescence Spectroscopy

Fluorescence spectroscopy is a type of electromagnetic spectroscopy that analyzes fluorescence from a sample. It involves using a beam of light, usually ultraviolet light, that excites the electrons in molecules of certain compounds and causes them to emit light; typically, but not necessarily, visible light.

Jablonski diagram (Figure 1.15) clearly illustrates the mechanism of fluorescence. Prior to excitation, a fluorescent molecule is in the lowest vibrational level of the electronic ground state S_0 . Excitation by the absorption of light of an appropriate wavelength produces a change to an excited vibrational level of the first excited singlet state S_1 . After a very short time period (10^{-12} s)

the lowest vibrational level of S_1 is reached by a series of non-radiative energy transfer processes known as vibrational relaxation, in which the molecule collides with surrounding solvent molecules and loses energy as heat. The system remains at this level for a significantly longer period (10^{-9} s) before a transition occurs to the S_0 state with the emission of a photon. This process is known as fluorescence.

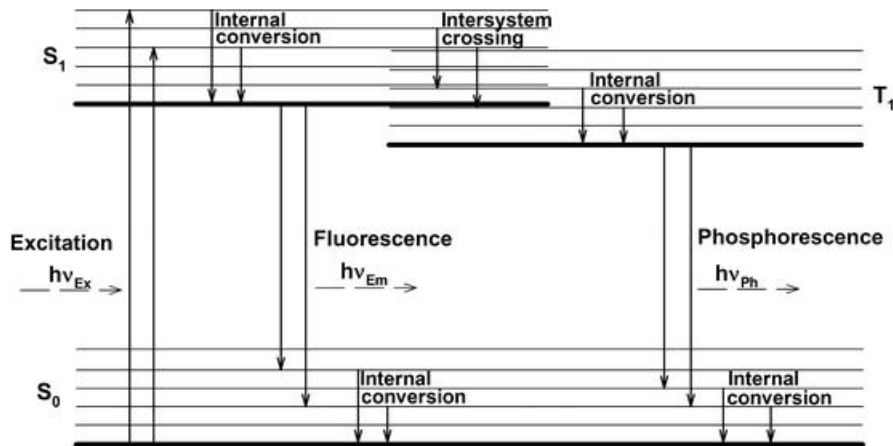


Figure 1.15. Jablonski diagram. Reprinted with permission from reference ⁵¹. Copyright 2013 European Biophysical Societies' Association (EBSA).

A simple spectrofluorometer consists of a source of excitation, which can be a lamp or laser (usually a xenon lamp), an excitation monochromator, a cuvette where the sample is placed, an emission monochromator (which allows to scan through the emitted wavelengths), a photon detector, and a recorder. In addition to a monochromator, filters are added that remove unwanted wavelengths in the excitation beam and unwanted scattered light from the emission channel.

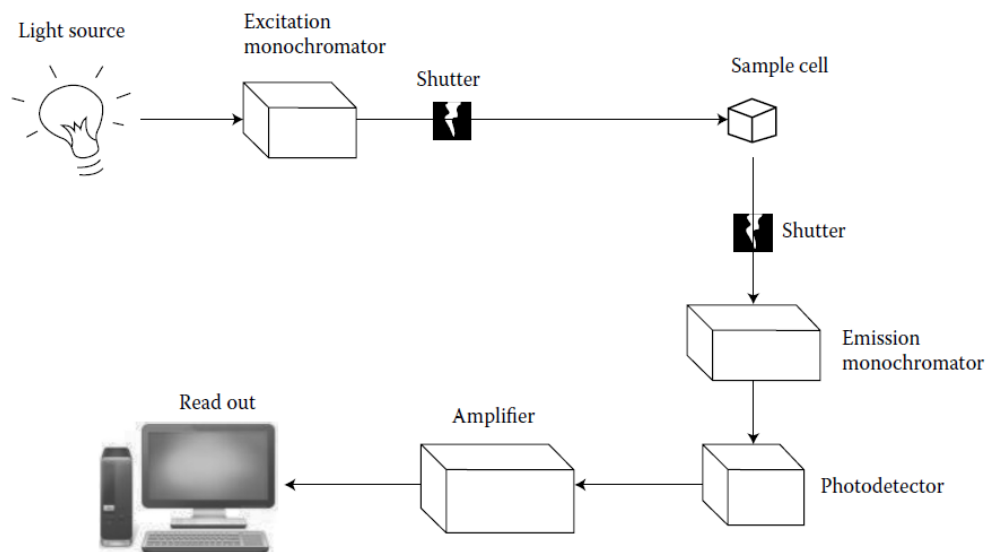


Figure 1.16. Schematic diagram of a fluorescence spectrometer. Reprinted with permission from reference ⁵².

Copyright 2015 Informa UK Limited.

Fluorescence can be measured as either the excitation or the emission spectra. The emission spectrum is obtained by recording the emission intensity as a function of the emission wavelength, λ_{em} , at a constant excitation wavelength, λ_{ex} . Conversely, the excitation spectrum is obtained by recording the excitation intensity as a function of the excitation wavelength as a constant emission wavelength.⁵³ If the emission spectra are recorded at different λ_{ex} , then a fluorescence excitation–emission results that is in the three-dimensional (3D) form.⁵⁴

1.3.1 Fluorescence of Graphene Oxide and Graphene Quantum Dots

Pristine graphene is characterized as a zero bandgap semiconductor or semimetal,¹ and could not generate fluorescence unless assisted by phonons owing to the absence of an energy gap.⁵⁵ However, with the incorporation of heterogeneous atoms, GO becomes an electronically hybrid carbon material containing a mixture of sp^2 and sp^3 bonding sites, whose opto-electronic

properties are determined by the π states of the sp^2 sites.⁵⁶ The presence of localized finite-sized molecular sp^2 clusters within a sp^3 matrix can lead to confinement of π - electrons in GO. The π and π^* electronic levels of the sp^2 clusters lie within the bandgap of s and s^* states of the sp^3 matrix and are strongly localized (Figure 1.17a).^{57, 58} The fluorescence in such carbon systems is a result of radiative recombination of localized electron–hole pairs in sp^2 clusters, which essentially behave as the luminescence centers or chromophores.⁵⁹ Since the local bandgap depends on the size, shape, and fraction of the sp^2 domains, tunable photoluminescence emission can be achieved by controlling the nature of sp^2 sites.

In principle, the bandgap of GO can be tuned from 0 eV to that of benzene by destroying the integrity of π system (Figure 1.17b). Smaller sp^2 domains have a larger energy gap due to a stronger confinement effect. One of the major methods to induce the band gap is to cut large GO sheets into graphene quantum dots (GQDs) through a chemical oxidation.⁶⁰⁻⁶⁴

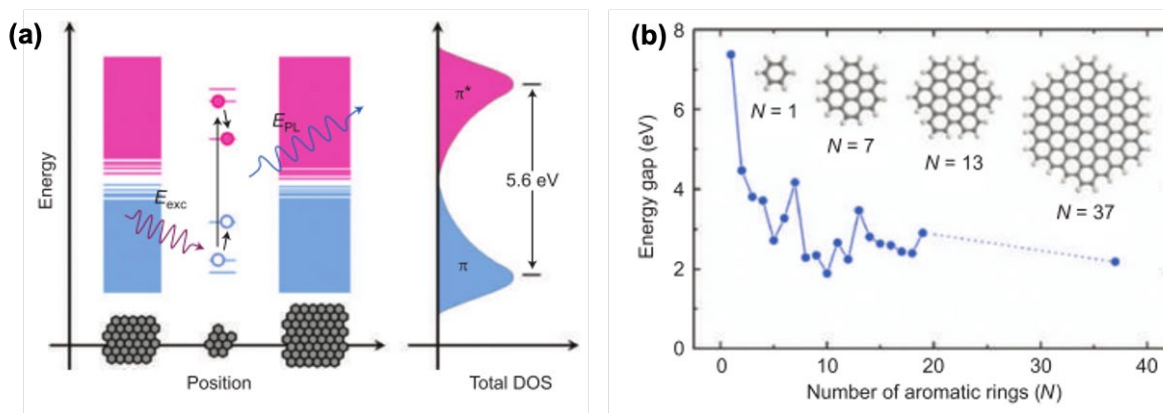


Figure 1.17. (a) Schematic band structure of GO (pink and blue colors represent conduction and valence bands, respectively). (b) Calculated energy gap of π – π^* transitions as a function of the number of fused aromatic rings (N). Reprinted with permission from reference ⁶⁵. Copyright 2010 Wiley-VCH Verlag GmbH & Co. KGaA, Weinheim.

1.3.2 Fluorescence of Semiconducting Single-Walled Carbon Nanotubes

Carbon nanotube can be viewed as a rolled-up graphene sheet (Figure 1.18a). Depending on the different roll-up vectors, each SWCNTs structure can be labeled by a pair of integers, (n,m), known as the chiral indices, which define its diameter and chiral angle. Particularly, the chiral angle of zigzag and armchair configuration is 0° and 30° , respectively. Nanotubes with $n-m=3i$ (i is an integer) is metallic in nature and the rest structures are semiconducting. The semiconducting SWCNTs give rise to a series of transitions, designated E_{11} or S_{11} , E_{22} or S_{22} , E_{33} or S_{33} , etc. as shown in their density of states (Figure 1.18b) whereas metallic SWCNTs mainly show their first M_1 transitions.

The bandgap fluorescence of individual single-walled carbon nanotubes (SWCNTs) was first reported by O'rell *et al.* The fluorescence of SWCNTs was observed at their E_{11} transition when being excited at their E_{22} (Figure 1.18b) or higher transitions (E_{33}). The optical transitions energies depend on the SWCNTs diameter and chiral angle. A typical semiconducting SWCNT displays a series of characteristic optical absorption peaks (Figure 1.18c) that fall in the near-IR (E_{11}), visible (E_{22}), and near-UV regions (E_{33}). Therefore, in the excitation-emission (EE) contour map of a mixture of different chirality SWCNTs, each major peak can be associated with a specific (n,m) species with the aid of tables of SWCNT spectral assignments.⁶⁶

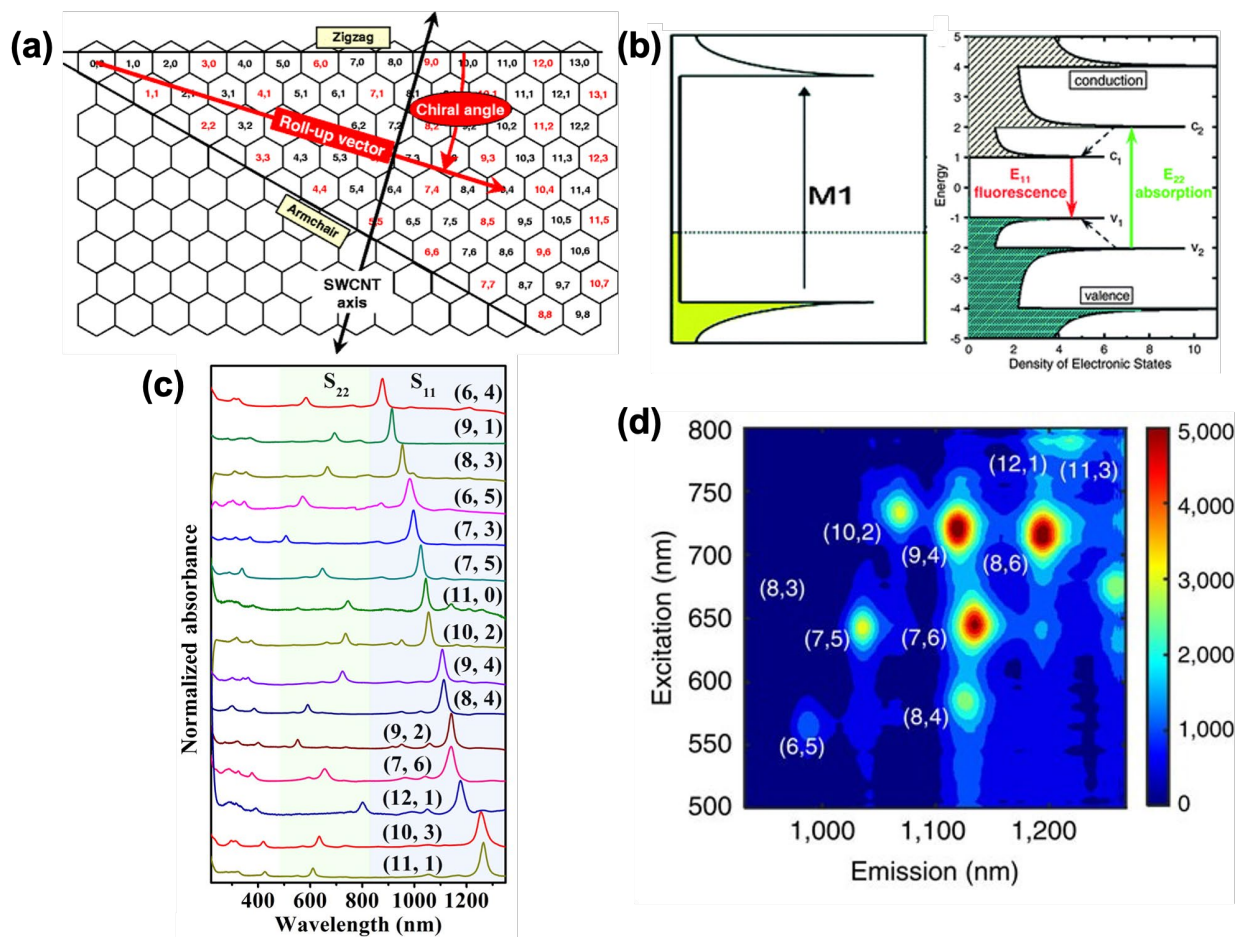


Figure 1.18. (a) The relation between SWCNT structure and graphene sheet roll-up. Structures shown with red labels are metallic or semimetallic; those with black labels are semiconducting. Reproduced with permission from reference ⁶⁷. Copyright 2009 Springer-Verlag. (b) A schematic illustration of the density of states of metallic (left) and semiconducting (right) SWCNTs. Reproduced with permission from reference ⁶⁸. Copyright 2011 Royal Society of Chemistry. (c) Optical absorption spectra of 15 types of single-chirality species. Reprinted with permission from reference ⁶⁹. Copyright 2021 The American Association for the Advancement of Science. (d) Excitation–emission profile of polymer-functionalized SWCNT suspension. Reprinted with permission from reference ⁷⁰. Copyright 2016 The Authors.

Recent studies in the photoluminescence of SWCNTs focus on the covalent functionalization to generate a newly red-shift sp^3 defect-induced E_{11}^- or E_{11}^* peak, as shown in Figure 1.19a. As this PL emission is much brighter than the original E_{11} emission and in the region

of second NIR window, which made the functionalized SWCNTs applicable in bioimaging⁷¹ and photoelectronic devices,⁷²⁻⁷⁴ it has been attracted wide interests since the first work reported by Ghosh in 2010.⁷⁵ Through covalent doping, the frontier orbitals (ground-state and excited-state) split into four distinct levels (Figure 1.19b). The optical transitions from the lower excited-state and the higher ground-state sublevels could therefore represented the newly red-shifted PL.

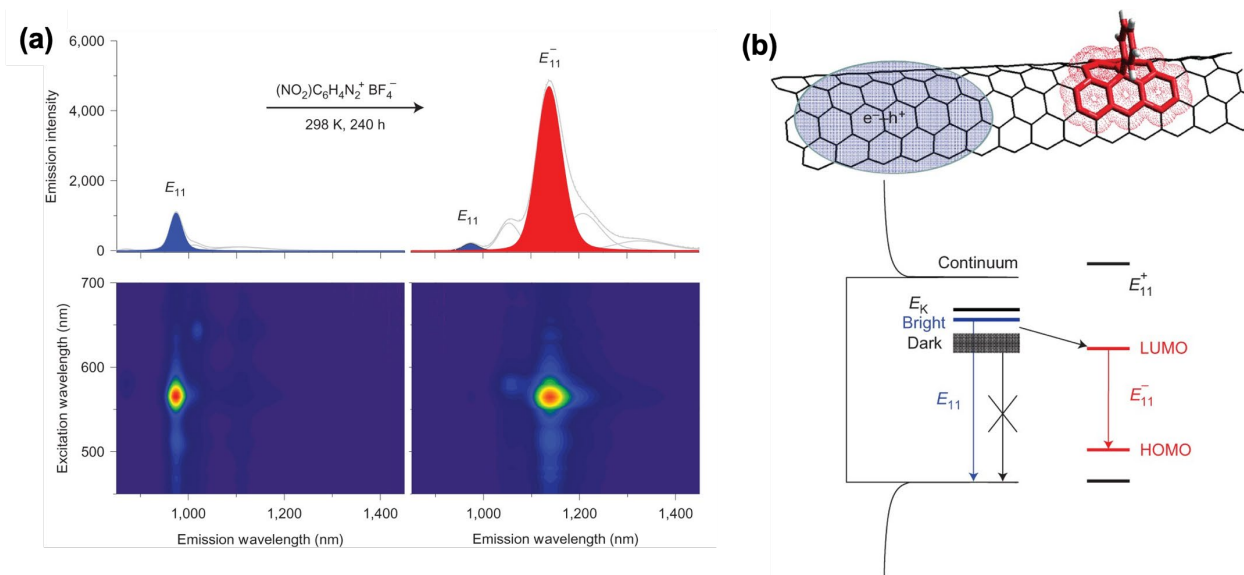


Figure 1.19. (a) Covalent sidewall functionalization of (6,5)-SWCNTs with 4-nitrobenzenediazonium tetrafluoroborate gives rise to a new fluorescent peak, E_{11}^- , that is red-shifted by 181 meV and 8.4 times brighter (in integrated intensity) than the original E_{11} exciton photoluminescence. (b) Controlled sp^3 defects brighten dark excitons. Reprinted with permission from reference ⁷⁶. Copyright 2013 Nature Publishing Group.

1.4 Mass Spectrometry

The basic concept of mass spectrometry (MS) is to first generate ions of the analyte compounds, to separate the ions based on their mass-to-charge ratio (m/z) and to detect them in terms of their respective m/z and abundance.⁷⁷

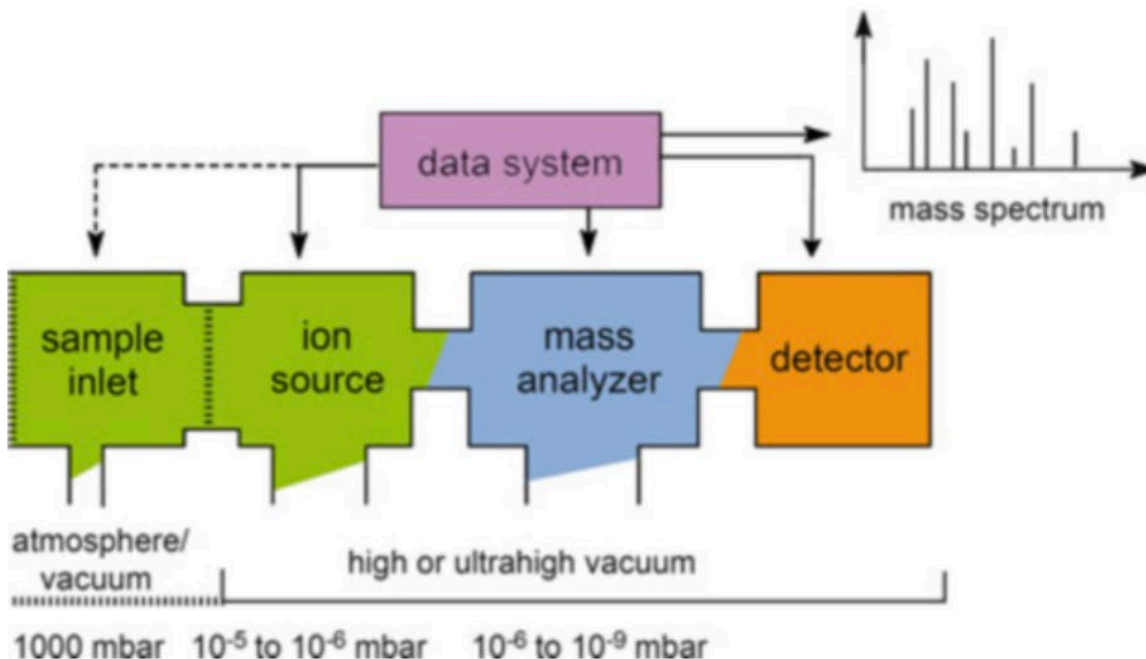


Figure 1.20. General scheme of a mass spectrometer. Reprinted with permission from reference ⁷⁷. Copyright 2017

Springer International Publishing AG.

To generate charged species, ions from atoms or molecule, different types of ionization techniques have been developed to achieve this goal for various analytes, electron ionization, chemical ionization, matrix-assisted laser desorption/ionization, electrospray ionization (ESI) and so on. ESI is a soft ionization technique that producing ion using electrospray in which high voltage is applied to the liquid samples to create aerosol. ESI is useful to analyze large, non-volatile, and thermally labile compounds such as proteins. One reason for the high-mass capability of ESI is a

result of the continuous ionization starting from atmospheric pressure and leading into the high vacuum mass analyzer. Another reason has been found in the characteristic generation of multiply charged ions in the ESI process.

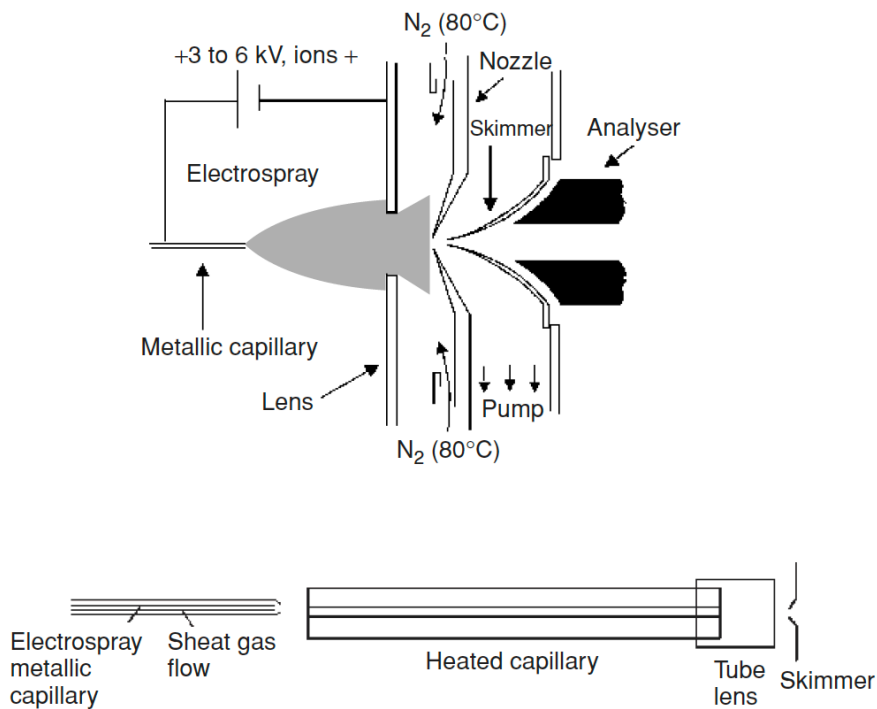


Figure 1.21. Diagram of electro spray sources, using skimmers for ion focalization and a curtain of heated nitrogen gas for desolvation (top), or with a heated capillary for desolvation (bottom). Reprinted with permission from reference ⁷⁸. Copyright 2007 Wiley-VCH Verlag GmbH & Co. KGaA, Weinheim.

1.5 Transmission Electron Microscopy (TEM)

Transmission electron microscopy (TEM) is a widely used high-resolution imaging technique in nanotechnology and nanomaterials analysis. A high-energy (80 keV or more) electron beam, fired from a tungsten filament, is focused by electromagnetic lenses on the ultra-thin solid

sample and then passes through it, as shown in Figure 1.22. An image is formed based on the electrons transmitted through the sample after passing through other lenses.

As the interaction between the electrons and specimen is impacted by the sample's thickness/density, composition, and crystallinity. The electrons that are transmitted through the specimen subsequently provide contrast in the resulting image. This allows the investigation of sample morphology and structure down to sub-nanometer scale scale to be carried out.⁷⁹ The high resolution of the TEM is a result of the small wavelength of the transmitted individual electron.

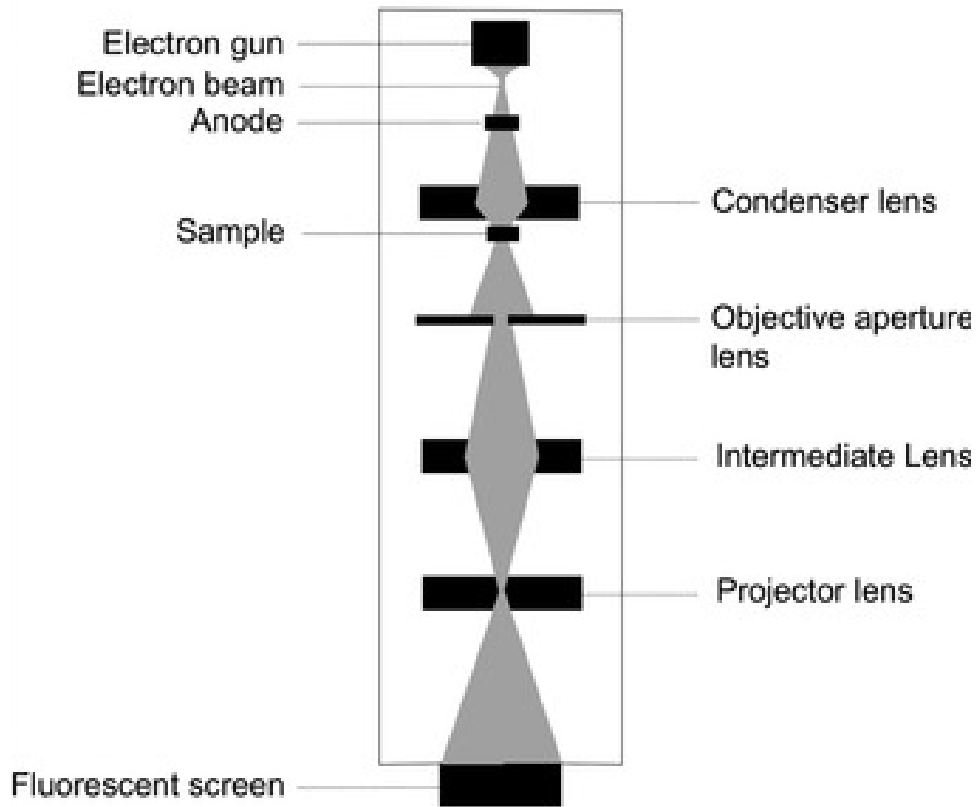


Figure 1.22. Schematic diagram of TEM. Reprinted with permission from reference ⁸⁰. Copyright 2019

Cambridge University Press.

SWCNTs was first being observed in fullerene soot by Sumio Iijima using TEM in 1991.⁸¹ Since then, TEM has been used as a very powerful tool to investigate the morphology, structure, and composition of SWCNTs.

2.0 $[2\pi + 2\pi]$ Photocycloaddition of Enones to Single-Walled Carbon Nanotubes Creates Fluorescent Quantum Defects

2.1 Preface

The material contained in the following Chapter was adapted with permission from *ACS Nano* 2021, 15, 4833-4844. Copyright 2021 American Chemical Society.

List of Authors: Xiaoyun He, Ilia Kevlishvili, Katherina Murcek, Peng Liu, and Alexander Star

Author Contributions: X.H. and A.S. designed the experiments. X.H. performed the experimental work. I.K., K.M. and P.L. performed the computational work. All authors contributed to the writing of the manuscript.

2.2 Introduction

Semiconducting single-walled carbon nanotubes (SWCNTs) exhibit chirality-dependent near-infrared (NIR) photoluminescence (PL) when their bundles are exfoliated by suspension using surfactants.^{82, 83} Each single-chirality semiconducting SWCNT displays characteristic E_{22} excitation – E_{11} emission peak, related to its optical transition between corresponding van Hove singularities. In addition to this band-gap fluorescence, the emergence of a red-shifted fluorescence emission, designated as E_{11}^- or E_{11}^* , was reported.⁸⁴⁻⁸⁶ The activation of the red-shifted PL has been achieved by reactions with ozone,^{84, 87} lipid hydroperoxide,⁸⁸ hypochlorite,⁸⁹ alkylation,^{85, 90-95} diazonium chemistry,^{86, 96, 97} guanine nucleobases,⁹⁸ and other chemical treatments.⁹⁹⁻¹⁰⁴ This

emission is a single-photon in nature,¹⁰⁵ can facilitate up-conversion¹⁰⁶ and be generated from trions trapped at chemical sites at room temperature.^{94, 95} These features enable the applications of functionalized-SWCNTs as promising fluorescent probes with excitation and emission in the NIR region well suited for noninvasive *in vivo* detection and bioimaging.⁸⁷ Additional applications include single-photon emission at room temperature in photonic devices,^{73, 74, 107} as well as chemical sensing.¹⁰⁸ However, even though the mechanism of this optical behavior has been extensively studied,^{109, 110} the chemical types of created quantum defects are still limited.^{103, 104} Beyond oxygen-containing defects on the SWCNTs,^{84, 87-89} alkyl^{85, 90-95} and aryl^{86, 96, 97, 99-102} groups have been also shown to generate E_{11}^- emission. Among them, only few studies^{91, 96, 99-101} reported the creation of the fluorescent quantum defects other than oxygen by means of photochemical reaction activated under either E_{22} transition of nanotubes or UV light.

Polyunsaturated fatty acids (PUFA) are one of the basic lipids composing microcellular membranes.¹¹¹ Oxidation of PUFA can yield an array of bioactive oxygenated lipid mediators such as octadecanoids, eicosanoids, docosanoids, and other lipid metabolites.¹¹² For example, oxidation of linoleic acid (LA) *via* the 15-lipoxygenase (15-LOX) or non-enzymatic pathway can produce two main classes of octadecanoids, hydroxy-octadecadienoic acid (HODE) and oxo-octadecadienoic acid (KODE).^{112, 113} Our group has previously demonstrated that the defect-induced PL in SWCNTs can be achieved through photo-oxidation by lipid hydroperoxides.⁸⁸ We hypothesized that lipid hydroperoxides can photochemically oxidize SWCNTs resulting in the formation of ether functional groups on the SWCNT sidewalls.⁸⁸

In this work, we investigated the interaction between SWCNTs and linoleic-acid-oxidative products, especially KODE and HODE. Compared to the previously reported linoleic acid hydroperoxides,⁸⁸ these compounds are not strong oxidants, thus rendering them unlikely to

generate similar oxygen-defects on the sidewalls of nanotubes. We found that these compounds can also photochemically react with SWCNTs through a $[2\pi + 2\pi]$ cycloaddition. The photochemical reaction results in a gradual increase of the red-shifted defect-induced PL (E_{11}^-) accompanied by the decrease of E_{11} under illumination. To further confirm the feasibility of proposed $[2\pi + 2\pi]$ cycloaddition doping in SWCNTs, we performed the reaction with shorter-chain commercially available organic compounds containing a carbonyl functional group with or without a conjugated carbon-carbon double bond. Our results indicate that 3-decen-2-one, potentially a class of α,β -unsaturated carbonyl compounds (enones), can effectively functionalize SWCNTs through $[2\pi + 2\pi]$ photocycloaddition. Density functional theory (DFT) calculations were performed to investigate the relative thermodynamic stability of a number of possible cycloadducts, including $[2\pi + 2\pi]$ and $[4\pi + 2\pi]$ products involving different C-C bonds on the chiral nanotube and products with different stereoselectivity. A detailed analysis on the steric repulsions and London dispersion interactions between the enone substrate and the SWCNT surface was performed to reveal factors that stabilize the $[2\pi + 2\pi]$ cycloadducts. While 1,3-dipolar and Diels-Alder cycloaddition reactions with carbon nanotubes and other carbon nanosurfaces have been studied extensively using computation to understand the origin of reactivity as well as regioselectivity of these transformations,¹¹⁴⁻¹¹⁷ $[2\pi + 2\pi]$ cycloadditions with SWCNTs are less explored computationally,^{118,119} because they are usually kinetically less accessible. Additionally, most of the computational efforts have involved smaller organic substrates, without alkyl chain substituents, and in turn, the substituent effect on the chemo- and regioselectivity has been overlooked. This photo-activated reaction gives a way to create fluorescent quantum defects in SWCNTs through a controllable, facile, and inexpensive synthetic route.

2.3 Materials and Methods

Cobalt-molybdenum-catalyzed (CoMoCAT) single-walled (6,5) carbon nanotubes were purchased from Sigma-Aldrich (SG65, 0.7-0.9 nm diameter) and used without further purification. Morin hydrate and ascorbic acid were also purchased from Sigma-Aldrich.

SWCNT suspensions were prepared at 0.5 mg/mL with 0.5 wt % sodium cholate (SC, Sigma-Aldrich) as a surfactant in nanopure water. The suspensions were sonicated for 1 h and centrifuged at 7000 rpm for 30 min (Centrifuge 5804, Eppendorf) to remove large SWCNT bundles. The top 90% of the supernatant was transferred to a separate container and used as stock.

The prepared surfactant-coated SWCNT stock solution was diluted 25 times, and mixed with either 170 μ M of a series of 18-carbon fatty acids (Appendix Table 2, No. 1–15) or 20 mM of each No. 16–20 compounds (Appendix Table 2). Samples were illuminated with 566 nm light at a power density of 6.13 mW/cm² for 60 min unless stated otherwise.

NIR photoluminescence measurements were performed on a Nanolog spectrofluorometer (HORIBA Jobin Yvon) equipped with a xenon lamp (400 W) light source, double excitation monochromators, and Symphony II InGaAs array (NIR) detector. Spectra were obtained using 566 nm excitation wavelength, which is in resonance with the first absorption band of the (6,5) SWCNTs. Slit widths were set at 10 nm for both excitation and emission. All measurements were obtained with an 830 nm long-pass filter at ambient temperature. Power density was measured independently with an optical power meter (Thorlabs PM200) and detector (Thorlabs S120VC). Power densities at different illumination wavelengths for the reactions are available in Appendix Table 3.

UV-vis-NIR absorption spectra were obtained using PerkinElmer Lambda 900 spectrophotometer over the wavelength range of 200–1200 nm.

Raman spectra were acquired on XploRA plus confocal Raman microscope (Horiba) with 638 nm laser (24 mW) operating at 10% power.

All the DFT calculations were carried out by using the GAUSSIAN 16 program.¹²⁰ Full geometry optimizations were performed with the PBE¹²¹ functional with Grimme's D3 dispersion correction¹²² and the split-valence 3-21G basis set. Single-point energy calculations on the PBE-D3-optimized geometries were performed in water using the SMD solvation model¹²³ at the PBE-D3/6-31G(d) level of theory, with thermal corrections to Gibbs free energies calculated by harmonic vibration frequency analysis at the PBE-D3/3-21G level of theory. A 15 angstrom nanotube was generated using Avogadro,^{124, 125} and terminal carbons were capped using hydrogens. To ensure 15 angstrom model was sufficient for this study, electronic energies of key structures were also calculated using longer (50 Å) nanotube model (Appendix Table 8). Single point energy calculations for reduction potentials were performed at the PBE-D3/6-311++G(d,p) level of theory in water using the SMD solvation model.

2.4 Results and Discussion

The photo-activated reaction between SWCNTs and 9-KODE was conducted by irradiating the reaction mixture under 566 nm light. This wavelength corresponds to E₂₂ electronic transition in (6,5)-SWCNTs.⁸² The selected wavelength is exclusive to SWCNTs, because 9-KODE does not absorb light at 566 nm, as shown by the absorption spectrum in Appendix Figure 1.

Figure 2.1a shows the excitation-emission (EE) maps of SWCNTs before and after reaction with 9-KODE for 1 h under illumination at 566 nm. Before the reaction (6,5)-SWCNTs displayed a characteristic bandgap E₁₁ emission at ~990 nm with 566 nm E₂₂ excitation, consistent with the

previously reported fluorescence of (6,5)-SWCNTs.⁸² The emission shoulders could be attributed to the photon sideband peak¹²⁶⁻¹²⁸ and the remaining impurity of other SWCNT chiralities.⁶⁶ After 1 h illumination by resonant light at nanotube E₂₂ transition (566 nm), E₁₁ peak faded away and a red shifted E₁₁⁻ peak, centered at ~1114 nm, appeared accompanied by weak tail PL at longer wavelengths. It should also be noted that an even brighter PL peak centered at ~1114 nm emerged corresponding to the excitation by NIR light at E₁₁ transition of SWCNTs (Figure 2.1a, right panel). The PL intensity excited at E₁₁ is significantly higher compared to that excited at E₂₂ is the result of higher E₁₁ absorption intensity of SWCNTs. However, this feature is less obvious in pristine nanotube due to the overlap with Rayleigh scattering (Figure 2.1a, left panel). The Rayleigh scattering (diagonal stripes on the upper-left corner of both EE maps in Figure 2.1a) is a result of the inherent optical filter configuration of the spectrofluorometer, the ineffectiveness of the equipped 830 nm long-pass filter to reject the scattered excitation light longer than 830 nm. Similar scattering effect has also been shown in the work using a 1150 nm long-pass filter.⁸⁹ Figure 2.1b shows the spectra changes over 1 h photoreaction under 566 nm illumination, revealing the disappearance in the original E₁₁ emission and gradual increase of two defect-induced PL peaks E₁₁⁻ and E₁₁^{*}, centered at ~1114 nm and ~1255 nm, respectively. The existence of the isoemissive point at ~1050 nm is indicative of the direct conversion of the E₁₁ emissive species to defect-induced emissive species, without the formation of an intermediate in the transition between them.¹²⁹⁻¹³¹

Figure 2.1c compares the UV-vis-NIR absorption spectra of reaction mixture at different time points under 566 nm irradiation. 9-KODE gives a characteristic absorption centered at 285 nm corresponding to the π to π^* transition of $\alpha,\beta,\gamma,\delta$ -dienone structure based on Woodward-Fieser rules.¹³²⁻¹³⁴ This peak decreased with the progress of the reaction and finally disappeared after 6 h

irradiation; simultaneously a peak has appeared at ~ 230 nm with extended 6 h illumination. The ~ 55 nm blue-shift of the absorption indicates the complete consumption of 9-KODE with the destruction of the acyclic dienone structure and the formation of cyclobutane and/or oxetane ring.¹³⁵⁻¹³⁸

The expanded inset in Figure 2.1c, showing vis-NIR absorbance of SWCNTs on a magnified scale, reveals E_{11} and E_{22} peaks drop by 21.1% and 3.7%, respectively, after treatment. The spectra change is analogous to those observed during oxygen⁸⁹ and alkyl⁸⁵ functionalization, which could be attributed to perturbations in the π -electron system from covalent doping. Besides, there is an obvious ~ 5 nm blue-shift at E_{11} transition after 6-h illumination. This observation can be correlated to the decreased length of the pristine, nonfunctionalized regions of SWCNTs as the reaction proceeds. When the defect-defect distance (Appendix Figure 2) shortens to sub-10 nm scale, this could cause increased quantum confinement effect along the SWCNTs.^{85, 139, 140} Figure 2.1d shows the changes of emission intensity of E_{11} , E_{11}^- , and E_{11}^* peaks over 6-h 566 nm irradiation. The E_{11} emission decreased monotonically within ~ 1 h of the reaction and then plateaued, while E_{11}^- intensity increased to a maximum after ~ 1 h and then subsequently decreased. The decline in E_{11}^- was caused by excessive functionalization after achieving optimal defect density on SWCNTs. The same observations were reported by Piao *et al*⁸⁶ with diazonium functionalization. Notably, the intensity of the second red-shifted emission band, E_{11}^* , concurrently changed at a rate slower than E_{11}^- . In contrast to the sharp drops of E_{11}^- by 63%, another defect-induced peak, E_{11}^* , only decreased by 23% after reaching its maximum. Here, similarly to previously reported dual red-shifted emissions with alkyl⁹⁴ and aryl¹⁰¹ group functionalization, we observed the finite initial slopes of the time-dependent kinetic curves for E_{11}^- and E_{11}^* and significant slower decay rate of E_{11}^* compared to E_{11}^- . The above kinetic features of

E_{11}^- and E_{11}^* more closely related to that of the parallel reactions than to the consecutive reactions.¹⁴¹ Specifically, if E_{11}^- is an intermediate species and E_{11}^* is the final product, the kinetic curve of E_{11}^* would continue to increase after E_{11}^- species reaches its maximum at around 60 min. It could be thus inferred that E_{11}^* emissive species, with a binding energy as high as ~ 260 meV, were formed in parallel processes to E_{11}^- emissive species rather than through sequential conversion of E_{11}^- sites into E_{11}^* emitters.¹⁰¹

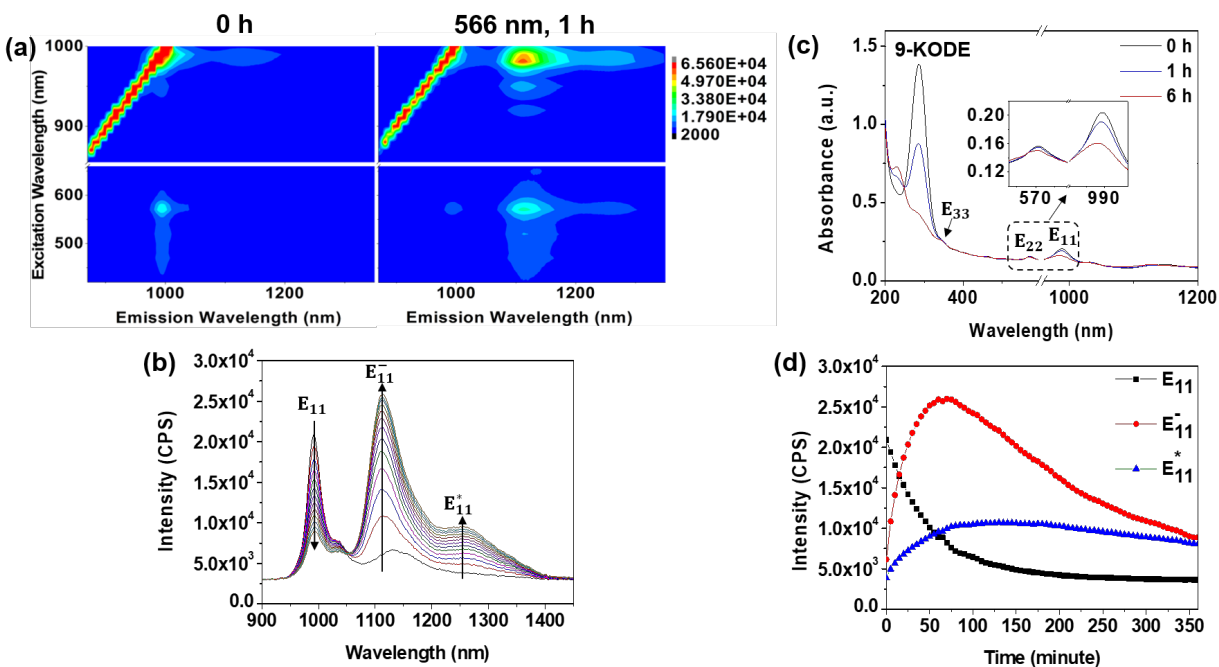


Figure 2.1. EE maps of SWCNTs (a) before and after 1 h reaction with 9-KODE under 566 nm illumination. (b) Fluorescent emission spectra change over 1 h (spectra taken every 5 min with 566 nm excitation). (c) UV-vis-NIR absorption spectra of the reaction mixture at different time points; expanded insets show E_{11} and E_{22} absorption peaks. (d) Emission intensities of E_{11} , E_{11}^- , and E_{11}^* of SWCNTs (with 566 nm excitation) reacted with 9-KODE over 6 h.

To ensure the observed effects were caused by the reaction between SWCNTs and 9-KODE, one control experiment was conducted without the addition of 9-KODE. As shown in Appendix Figure 3, after 1 h 566 nm irradiation, neither obvious E_{11} decline nor evolution of both

defect peaks (E_{11}^- and E_{11}^*) was observed. To confirm the doping was achieved through radical reactions, another control experiment was performed with radical scavengers, morin or ascorbic acid. When the reaction mixture was pretreated with radical scavenger to terminate any radical reactions, no enhancement of E_{11}^- and E_{11}^* emission was observed (Appendix Figure 4). Moreover, saturated steric acid (18:0) without dienone functional group did not produce any spectra changes as well.⁸⁸ Thus, it could be concluded that the produced red-shifted PL peaks were induced by photoinitiated radical reaction between SWCNTs and dienone structure in 9-KODE. Similar radical reaction mechanism has been proposed for other photochemical reactions aimed to generate the defects in SWCNTs.^{88, 96, 100, 101} In addition to 566 nm light activation, we also conducted the reaction under 285 nm illumination, resonant light to π to π^* transition in 9-KODE (Appendix Figure 1). In this reaction, the photoexcited species are 9-KODE instead of SWCNTs. 285 nm is beyond the E_{44} transition (~ 300 nm) of (6,5)-SWCNTs,¹²⁶ at which the molar extinction coefficient of SWCNTs is order of magnitude lower than that of 9-KODE.¹⁴²⁻¹⁴⁴ Similar approaches have been reported using UV light to excite only the dopants not the SWCNTs.^{89, 101} Interestingly, we observed the emergence of the same defect-induced PL under 1h 285 nm illumination (Appendix Figure 5). The generated defect peaks, together with the corresponding energy shift, well matched those created under 1 h 566 nm illumination treatment (Table 2.1).

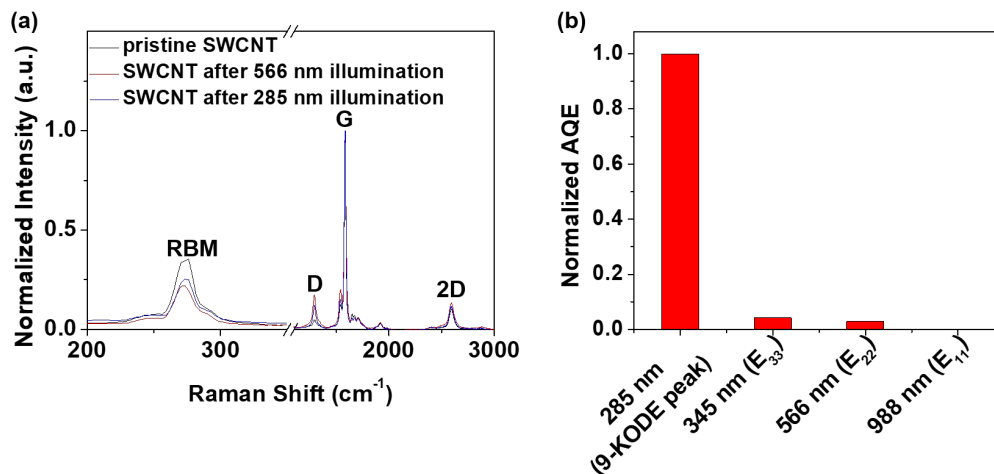


Figure 2.2. (a) Raman spectra of SWCNTs before and after reaction with 9-KODE under 6-h 566 nm and 285 nm illumination, respectively. (b) Normalized apparent quantum efficiency (AQE) of the reaction illuminated at different wavelengths (285, 345, 566, and 988 nm) for 1h. The emission spectra were recorded under 566 nm excitation before and after illumination.

The successful defect formation under both 566 nm and 285 nm illumination was further confirmed by Raman spectroscopy. Figure 2.2a shows the Raman spectra of SWCNTs with an increase of D/G ratio from 0.05 to 0.17 and 0.12 after 6-h reaction under 566 nm and 285 nm illumination, respectively. The rise in D/G ratio indicates the increased defect density of SWCNTs after reactions. The comparatively higher defect density after 566 nm irradiation, compared to 285 nm irradiation, is consistent with both PL emission and UV-vis-NIR absorption spectra (Figure 2.1 and Appendix Figure 5) due to more doping under 566 nm irradiation. The aforementioned results suggest that the mechanism of the reaction involves the excited state of either SWCNTs or 9-KODE as demonstrated by the effective E₁₁⁻ formation at 566 nm and 285 nm excitation, respectively. Prior reports of light-assisted creation of fluorescent defects in SWCNTs involved the excitation of either nanotubes^{84, 88, 91, 96, 100} or dopants.^{87, 89, 101} Our light-driven

functionalization of SWCNTs can be triggered *via* dual pathways under resonant excitation of both dopants and SWCNTs.

To further investigate the photochemical nature of the reaction between SWCNTs and 9-KODE, the reaction mixture was stored in dark for 1h. As shown in Appendix Figure 7, without irradiation, no evolution of any defect PL peaks was observed. Besides, the action spectrum (Figure 2.2b) displaying the reaction efficiency at various illumination wavelength (285, 345, 566, and 988 nm) was also provided. Interestingly, we observed the highest reaction efficiency under 285 nm irradiation, the wavelength which matches the absorption band of 9-KODE (Appendix Figure 1), followed by the 345 nm illumination. This result further indicates that the doping reaction can be induced by direct excitation of either SWCNTs (E_{22} and E_{33} transitions) or 9-KODE. The mechanism of the reaction involves the excited states of both SWCNTs and 9-KODE. Notably, under excitation energy corresponding to E_{11} transition (988 nm) of (6,5)-SWCNTs, almost no defect PL evolved. The molar extinction coefficient of (6,5)-SWCNTs is the highest at 988 nm compared to 345 nm and 566 nm. The photon flux at 988 nm illumination is of the same order of magnitude as that at 566 nm illumination, and even orders of magnitude higher than that at 345 nm and 285 nm illumination (Appendix Table 2). However, the calculated apparent quantum efficiency (AQE) under 988 illumination is still three orders of magnitude lower compared to the highest AQE at 285 nm illumination (Appendix Table 2), which leads us to conclude that the photochemical reaction scarcely occurred at 988 illumination. The lack of functionalization under 988 nm was assumed to be a result of insufficient photon energy to overcome the reaction barrier.¹⁰⁰

Here, in order to further explore the mechanism of observed photochemical reaction, we also performed similar photo-reaction under 1 h 566 nm illumination between SWCNTs and other

14 commercially available octadecanoids (Appendix Table 1). The ratio of the intensity of the defect-induced E_{11}^- peak (I_{11}^-) with respect to E_{11} peak (I_{11}), together with the energy shifts (ΔE) are shown in Table 4.1. 9-oxoODA and 13-KODE, similar to 9-KODE, have a diene structure conjugated to a carbonyl functional group. Thus, similar doping chemistry with ~ 135 meV energy shift was observed. The relative lower reaction efficiency of 9-oxoODA with respect to 9-KODE could be a result of the E-Z isomerization of diene functional group.¹⁴⁵

The second group of compounds, HODE, compared with KODE group displayed a significant 10 meV higher energy shift with 145 meV, the defect PL further shifted to ~ 1120 nm. Besides, we also investigated the role of chirality on the reaction efficiency by testing both R- and S-HODE compounds (Appendix Table 1, data not shown). Our results indicated that the chirality of hydroxyl functional group did not affect the cycloaddition reaction with SWCNTs in terms of similar defect PL energy shifts and reaction efficiency.

The third group compounds, 10E,12Z-CLA and 9Z,11E-CLA, though remained the dienes functional group as those with HODE, missing the conjugated hydroxyl group. Compared with HODE, similar energy shift at ~ 145 meV was observed, indicative of same type of cyclobutene ring formation with respect to HODE. However, the reaction between CLA and SWCNTs proceed at a much slower rate as shown by the low intensity ratio of 0.6 (Table 2.1). The less effective functionalization can be further confirmed by compared the intensity ratio with that before the reaction, namely for pristine SWCNTs, which is ~ 0.3 . A similar effect has also been reported by Kwon *et al.*, who observed the dependence of E_{11}^- emission wavelengths and I_{11}^-/I_{11} ratios on different substituted (fluoro)alkyl/aryl sp^3 -defects.⁹¹ Linoleic acid oxidative products containing only one carbonyl group (3-oxo-stearic acid), or conjugated triene or tetraene groups (Appendix

Table 1, No. 11-15) were also tested for reaction with SWCNTs under 1 h 566 illumination. As shown in Appendix Figure 8, no defect PL was observed.

Table 2.1. Comparison between different compounds after 1 h reaction with SWCNTs under 566 nm illumination.

Compound name	Skeletal structure	E ₁₁ (nm)	E ₁₁ ⁻ (nm)	ΔE (meV)	I ₁₁ ⁻ /I ₁₁
9-KODE		993	1114	135	3.2
9-KODE (285 nm illumination for 1 h)		993	1112	134	0.9
9-oxoODA		991	1109	133	1.5
13-KODE		993	1114	135	2.5
9R-HODE		991	1121	145	1.0
13R-HODE		990	1120	145	1.4
10E,12Z-CLA		991	1120	143	0.6
9Z,11E-CLA		991	1121	145	0.6

Furthermore, we tested this reaction with other commercial enone compounds. Compared with PUFA compounds, these commercial enones are less expensive thus enabling potentially to scale up the synthesis of SWCNTs with quantum defects. Figure 2.3a shows the EE maps of SWCNTs before and after 1 h photoreaction with 3-decen-2-one under 566 nm illumination. A bright red-shifted PL peak centered at ~1126 nm with as high as 151 meV energy shift (Table 2.2)

was appeared. Figure 2.3b showed the progressive spectra within 1 h reaction, which further confirmed the gradual increase of two defect-induced PL accompanied by the decrease of original E_{11} peak. Figure 2.3c displayed the change of the UV-vis-NIR spectra over 6 h reaction. Consistent with previous results (Figure 2.1c), SWCNTs absorption peaks, especially at E_{11} transition, decreased progressively, demonstrating the successful functionalization of the SWCNTs. Besides, the shrinkage of the absorption peak at 300 nm due to n to π^* transition of enone functional group of 3-decen-2-one were indicative of the consumption of 3-decen-2-one in the process. Kinetics curve (Figure 2.3d) showed the change of PL emission peak intensity over 6 h reaction. With the continuous decrease of the original E_{11} peak, two defect-induced PL peaks (E_{11}^- and E_{11}^*) gradually increased and then plateaued. Furthermore, reaction under illumination with 300 nm light, resonant with n to π^* transition of 3-decen-2-one absorption instead of SWCNTs, was performed. As shown in Appendix Figure 9 and Table 2.2, same defect-induced E_{11}^- peak centered at ~ 1127 nm with 154 meV energy shift appeared.

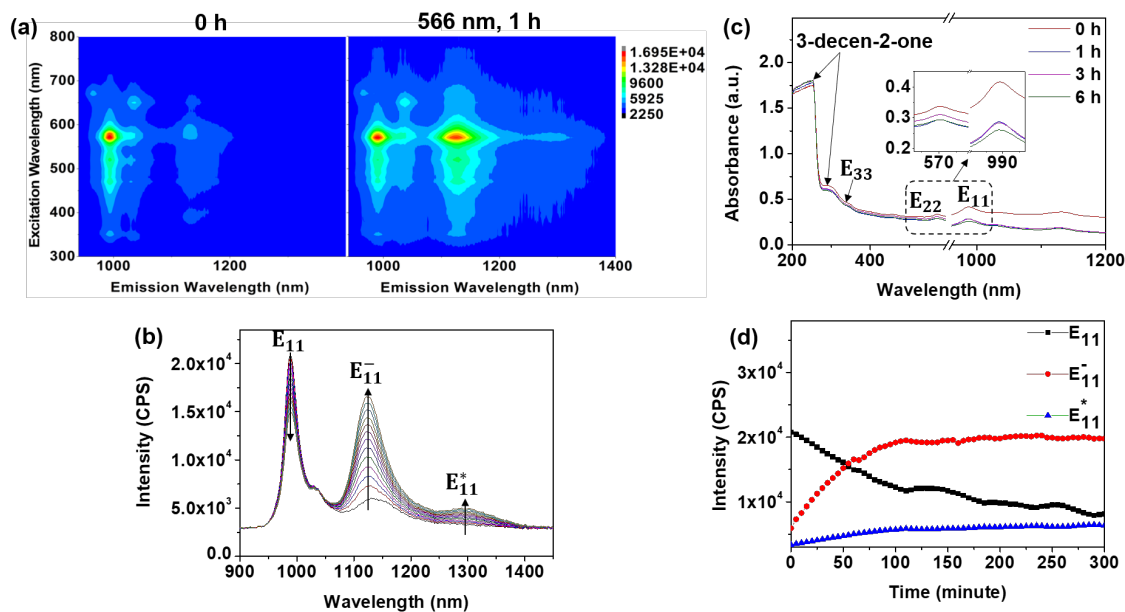


Figure 2.3. EE maps of SWCNTs (a) before and after 1 h reaction with 3-decen-2-one under 566 nm illumination. (b) Fluorescent emission spectra change over 1 h (spectra taken every 5 min with 566 nm

excitation). (c) UV-vis-NIR absorption spectra of the reaction mixture at different time points; expanded insets show E_{11} and E_{22} absorption features. (d) Emission intensities of E_{11} , E_{11}^- , and E_{11}^* of SWCNTs (with 566 nm excitation) reacted with 3-decen-2-one over 6 h.

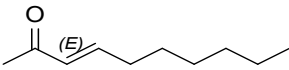

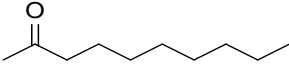
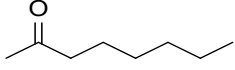
We also compared 3-decen-2-one with other similar structure compounds (Appendix Table 1, No. 17-20) by their photo-induced reactivity with SWCNTs. As shown in Table 2.2, across all the tested compounds, 3-decen-2-one was the best in the emergence of the defect-induced PL as indicated by the highest I_{11}^-/I_{11} ratio of 1.1.

The reaction between SWCNTs and 3-octen-2-one, an organic molecule containing same enone functional group as 3-decen-2-one though with shorter 8-carbon chain length, proceeded at a very low efficiency. The intensity ratio I_{11}^-/I_{11} was only 0.39, barely increased compared with 0.3 for pristine SWCNTs. Furthermore, the reaction with another even shorter molecule 3-hepten-2-one under 1 h 566 nm irradiation did not induce any defect PL (Appendix Figure 10). Here, we believe the length of carbon chain played a determining role on the reaction efficiency with SWCNTs. Longer chain organic molecules have more favorable interactions with the hydrophobic surface of the nanotubes. Besides, when the reaction was initiated with the light that is resonant with the n to π^* of corresponding organic molecules, a radical of the organic molecules is formed. As the lifetime of radicals is usually very short, longer chain molecules are more likely to react with the surfactant-wrapped SWCNTs more quickly before the radicals are quenched.

Two more compounds containing only keto functional groups, 2-decanone and 2-octanone, have been tested as well. As shown in Table 2.2, the reaction between SWCNTs and both molecules were slow under 566 nm illumination with intensity ratio of 0.49 and 0.46, respectively. This indicates that carbon-carbon double bonds can form four-membered ring structure with

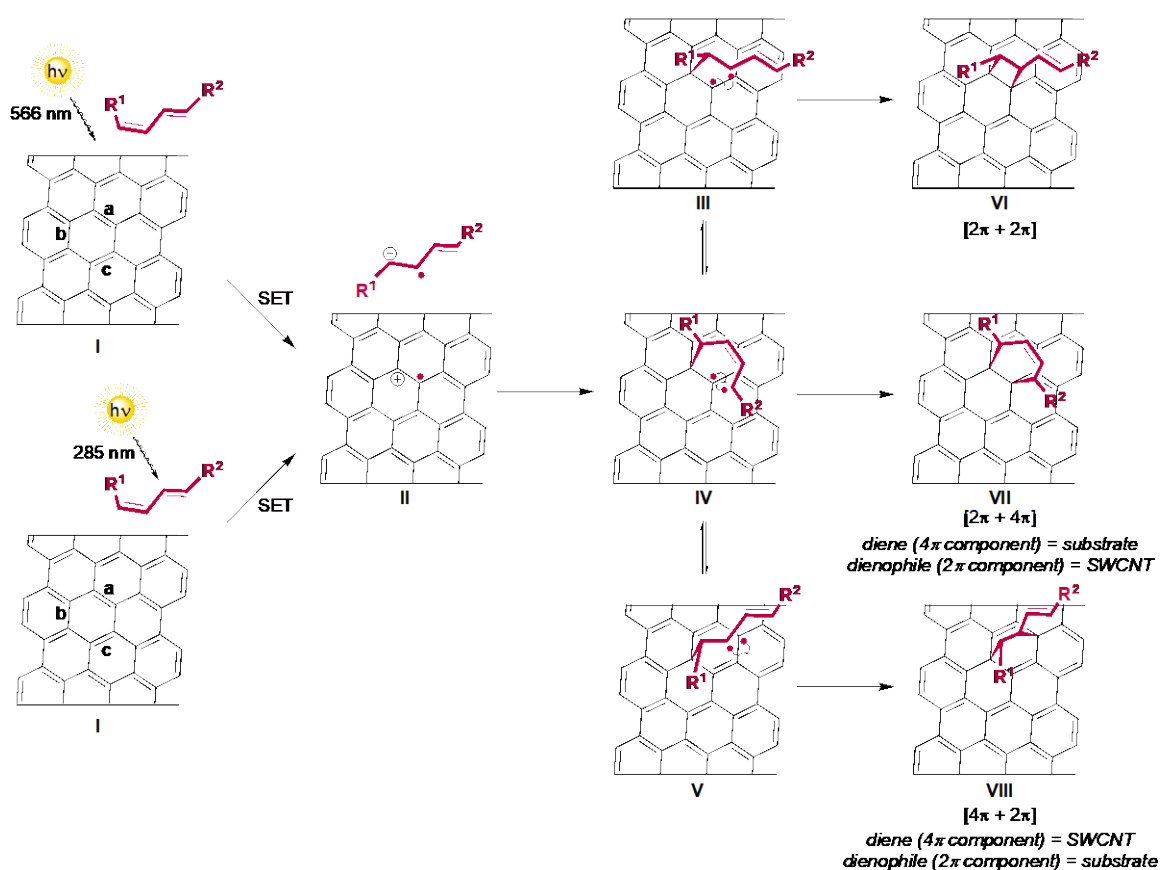
double bonds of SWCNTs more effectively than carbonyl groups through $[2\pi + 2\pi]$ photocycloaddition.

Table 2.2. Comparison between different compounds after 1 h reaction with SWCNTs.

Compound name	Skeletal structure	# of carbon	Illumination wavelength	E_{11} (nm)	E_{11}^- (nm)	ΔE (meV)	I_{11}^-/I_{11}
3-decen-2-one		10	566	990	1126	151	1.1
			300	988	1127	154	0.82
3-octen-2-one		8	566	988	1130	157	0.39
			296	988	1130	157	0.39
2-decanone		10	566	988	1120	147	0.49
2-octanone		8	566	987	1121	150	0.46

Based on the experimental findings where the reaction was not observed under thermal conditions, as well as past studies on photo-functionalization of SWCNTs,^{91, 100} we propose a reaction mechanism (Scheme 2.1) that involves initial single electron transfer (SET) from the photo-excited SWCNT to the enone substrate, or, alternatively, SET from SWCNT to the photo-excited enone, to generate a radical anion (**II**). The radical anion is rapidly trapped onto the SWCNT surface to form a C–C bond in a diradical intermediate (**III**, **IV**, or **V**). The subsequent C–C bond formation from the diradical intermediate may lead to several possible cycloaddition products, including the four-membered ring product (**VI**) *via* $[2\pi + 2\pi]$ cycloaddition and six-membered ring products (**VII** and **VIII**) *via* Diels-Alder ($[2\pi + 4\pi]$ or $[4\pi + 2\pi]$) cycloadditions where the substrate serves as the diene and the dienophile component, respectively. These stepwise

cycloadditions are not expected to be stereospecific. Thus, either cis or trans stereoisomer may be formed in each pathway. Because different cycloaddition products (VI, VII, and VIII) are all formed *via* diradical intermediates (III, IV, and V) that are under rapid equilibrium, we expect that the product ratio is thermodynamically controlled and the relative energies of the cycloaddition products can be used to predict the major defect formed on the SWCNT surface.

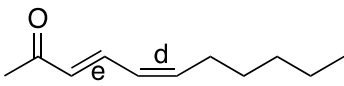


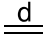
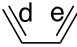
Scheme 2.1. Proposed reaction mechanisms for generating different cycloaddition defects on (6,5) SWCNT.

We performed density functional theory (DFT) calculations to investigate the Gibbs free energies (ΔG) of the $[2\pi + 2\pi]$, $[2\pi + 4\pi]$ (substrate as diene), and $[4\pi + 2\pi]$ (substrate as dienophile) photocycloaddition products in the reaction between (6,5) SWCNT and (3E,5Z)-

undecadiene-2-one (Table 2.3). Because there are three distinct types of C–C bonds on the SWCNT (bonds a-c, Scheme 1), cycloaddition products involving each of the three types of C–C bonds were calculated. Here, we define bond (a) and (c) as the C–C bonds relatively parallel to the axis of the nanotube and bond (b) as the C–C bonds nearly perpendicular to the axis. Furthermore, both cis and trans stereoisomers of the cycloaddition products and the diastereomers formed *via* addition of either of the prochiral faces of the alkene substrate were also considered (Appendix Table 4-6). Our DFT calculations indicate that the $[2\pi + 2\pi]$ cycloaddition products are thermodynamically much more stable than the Diels-Alder products. The two most favorable products (**1** and **3**, Table 2.3) are formed *via* $[2\pi + 2\pi]$ cycloaddition with bonds (a) and (c) on the SWCNT, which are relatively parallel to the axis of the nanotube.

Table 2.3. Gibbs free energies (ΔG) of different cycloaddition products between photoexcited (6,5) SWCNT (with 566 nm light) and different substrates.^a

Substrate name	Substrate skeletal structure	Cycloaddition product ^b	ΔG (kcal/mol)
(3E,5Z)-undecadiene-2-one		$[2\pi(a) + 2\pi(d)]$ (1)	-19.5
		$[2\pi(b) + 2\pi(d)]$ (2)	-16.0
		$[2\pi(c) + 2\pi(d)]$ (3)	-18.4
		$[2\pi(a) + 4\pi(de)]$ (4)	-9.6
		$[2\pi(b) + 4\pi(de)]$ (5)	-11.3
		$[2\pi(c) + 4\pi(de)]$ (6)	-7.8

		$[4\pi(ab) + 2\pi(d)]$ (7)	-9.6
		$[4\pi(ac) + 2\pi(d)]$ (8)	50.2
		$[4\pi(bc) + 2\pi(d)]$ (9)	-2.3
<hr/>			
		$[2\pi(a) + 2\pi(d)]$ (10)	-25.6
ethylene		$[2\pi(b) + 2\pi(d)]$ (11)	-25.8
<hr/>			
		$[2\pi(a) + 4\pi(de)]$ (12)	-27.5
1,3-butadiene		$[2\pi(b) + 4\pi(de)]$ (13)	-25.7

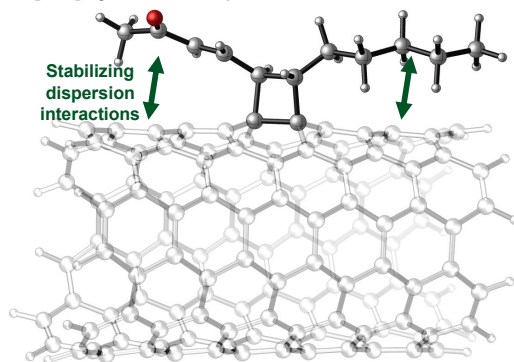
^a See Appendix Tables 4-6 for energies of the less stable stereoisomers in each reaction pathway.

^b See Scheme 1 for the three different types of C-C bonds (a-c) on the SWCNT surfaces involved in the cycloadditions.

Analysis of the steric repulsion and attractive London-dispersion interactions between the substrate and the nanotube surface revealed multiple factors that affect the stability of the $[2\pi + 2\pi]$ and Diels-Alder products. In the most stable $[2\pi + 2\pi]$ cycloaddition products (**1** and **3**, Table 2.3) the alkenyl and alkyl substituents on the four-membered ring can align along with the axis of the nanotube and are stabilized by London-dispersion interactions (Figure 2.4A). The addition to the perpendicular bond on SWCNT (*i.e.* product **2**, Figure 4.4B) places the alkenyl and alkyl substituents further away from the SWCNT surface due to the perpendicular alignment, leading

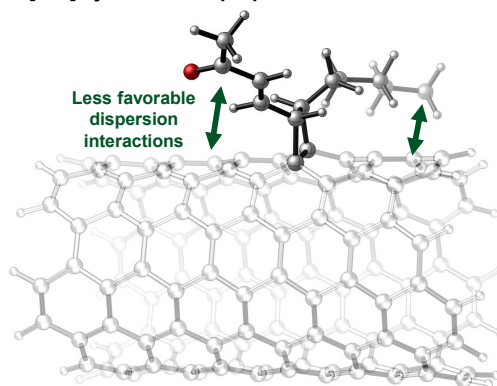
to decrease in the favorable dispersion interactions between the nanotube and the substrate. Furthermore, all Diels-Alder adducts are sterically more demanding, due to the formation of a six-membered ring, as opposed to a smaller four-membered ring. The Diels-Alder adducts are destabilized due to steric repulsions between the alkenyl and acyl substituents and the SWCNT surface.

A. [2+2] cycloaddition parallel to the axis of nanotube



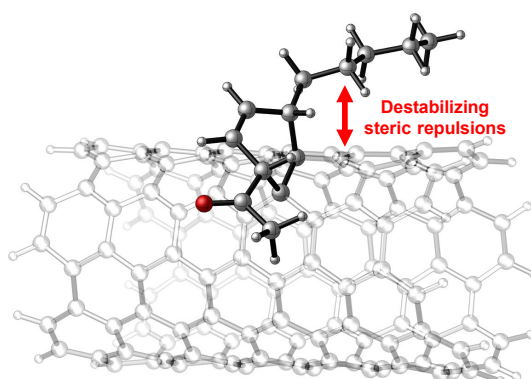
1
 $\Delta G = -19.5$ kcal/mol
 $\Delta E_{\text{disp}}^a = -23.6$ kcal/mol

B. [2+2] cycloaddition perpendicular to the axis of nanotube



2
 $\Delta G = -16.0$ kcal/mol
 $\Delta E_{\text{disp}}^a = -19.7$ kcal/mol

C. Most favorable Diels-Alder cycloaddition product



5
 $\Delta G = -11.3$ kcal/mol
 $\Delta E_{\text{disp}}^a = -23.6$ kcal/mol

Figure 2.4. Structures and energies of representative $[2\pi + 2\pi]$ cycloaddition and Diels-Alder products. ^a

Dispersion energies (ΔE_{disp}) between SWCNT and the substituents on the cycloadduct were calculated using

Grimme's DFT-D3 method from the dispersion-free HF functional.¹⁴⁶

The analysis above suggests that the $[2\pi + 2\pi]$ cycloadducts **1** and **3** are stabilized due to attractive dispersion interactions with the substituents on the four-membered ring, while the Diels-Alder adducts are destabilized by steric repulsions with the substituents. To further test this hypothesis and elucidate substituent effects on product stability, we compared the reaction energies of model $[2\pi + 2\pi]$ cycloadditions with an unsubstituted ethylene and Diels-Alder reactions with 1,3-butadiene (Table 2.3). Our results indicate that the two $[2\pi + 2\pi]$ cycloadducts with ethylene added to either bond (a) (**10**, Table 2.3) or bond (b) (**11**, Table 2.3) on SWCNT have similar energies ($\Delta G = -25.6$ and -25.8 kcal/mol, respectively). These results highlight the significance of the substituents on the olefin to stabilize regioisomers **1** and **3** as compared to **2** (Table 2.3). To further understand the origin of this difference, we computed the attractive dispersion interaction energies between the alkyl and alkenyl substituents on the cyclobutane and the nanotube. Adduct **1** has substantially larger dispersion interactions between the nanotube and the substituents than adduct **2** ($\Delta\Delta E_{\text{disp}} = -3.9$ kcal/mol) (Figure 2.4). This difference is consistent with the relative stabilities between these two product isomers ($\Delta\Delta G = -3.5$ kcal/mol, Table 2.3). The Diels-Alder cycloaddition of unsubstituted butadiene and SWCNT is slightly more exergonic than the $[2\pi + 2\pi]$ cycloaddition with ethylene. These results suggest that the lower stability of Diels-Alder adducts **4-6** as compared to $[2\pi + 2\pi]$ adducts (**1** and **3**) are due to substituent effects that lead to greater steric repulsions with the SWCNT and the loss of enone conjugation in the Diels-Alder adducts **4-6**.

Table 2.4. Reaction energies to form different cycloaddition products and reduction potential of substrates.

Substrate	Substrate	ΔG (kcal/mol)
-----------	-----------	-----------------------

name	skeletal structure	Most		Substrate
		favorable	Diradical	reduction
		[2 π + 2 π]	intermediate	potential ^a
		product		(V vs SCE)
(3E,5Z)- undecadiene-2-one		-19.5 ^b	-10.9	-1.58
2-hydroxy- (3E,5Z)- undecadiene		-23.1 ^b	-9.8	-2.68
(3E,5Z)- undecadiene		-22.1 ^b	-10.4	-2.92
2-undecanone		-1.6 ^c	6.1	-2.85

^a See SI for computational details of the reduction potential calculations. Single point energy calculations for reduction potentials were performed at the PBE-D3-6-311++G(d,p)/SMD(water) level of theory. ^b Cycloaddition between Z alkene and bond **a** on SWCNT. ^c Cycloaddition between carbonyl and bond **c** on SWCNT.

With the understanding of the [2 π + 2 π] cycloadducts as the major product of the photocycloaddition, we investigated factors that may contribute to the observed reactivity trend of different substrates. Based on the experimental intensity ratios (I_{11^-}/I_{11} , Table 2.1), it was apparent that dienone (KODEs) was more reactive than α -hydroxy-diene (HODEs), which was more reactive than unsubstituted diene (CLAs). To investigate the origin of the reactivity, we calculated

the energies of $[2\pi + 2\pi]$ cycloadducts and diradical intermediates (ref. ¹⁴⁷) in reactions with substrates (3E,5Z)-undecadiene-2-one, 2-hydroxy-(3E,5Z)-undecadiene, (3E,5Z)-undecadiene, and 2-undecanone (Table 2.4). In reactions with (3E,5Z)-undecadiene-2-one, 2-hydroxy-(3E,5Z)-undecadiene, and (3E,5Z)-undecadiene, formation of both the cycloadduct and the diradical intermediate are highly exergonic, and experimental reactivity trends do not correlate with the exergonicity. On the other hand, the computed reduction potentials of these substrates have good correlation with the observed reactivity trend. The reduction of dienone, (3E,5Z)-undecadiene-2-one, was significantly more favorable than the reduction of α -hydroxy-diene, 2-hydroxy-(3E,5Z)-undecadiene. The reduction of unsubstituted diene, (3E,5Z)-undecadiene, is the least favorable. The difference in reduction potential can be attributed to the relative stability of the radical anion, where the anion in dienone is better stabilized by resonance resulting in a large difference in reduction potential and reactivity. On the other hand, the difference between diene and α -hydroxy-diene is less significant, and the difference can be attributed to the stabilization of the negative charge by an inductive effect with an electron withdrawing hydroxy group on the α carbon. These results suggest that the rates of these reactions are affected by the initial single electron transfer to the substrate. Finally, we investigated the addition of 2-undecanone to SWCNT. This reaction is much less exergonic and involves a less stable diradical intermediate than the reactions with dienone, (3E,5Z)-undecadiene-2-one (Table 4.4). Therefore, the low reactivity of 2-decanone and 2-octanone (Table 4.2) can be attributed to the thermodynamically disfavored formation of the oxetane product.

2.5 Conclusions

We demonstrated that oxidative products of linoleic acid, particularly KODE and HODE, can efficiently functionalize the sp^2 carbon lattice of SWCNTs at ambient conditions through $[2\pi + 2\pi]$ photocycloaddition. The reaction occurs in aqueous solution at room temperature upon mixing the compounds with nanotubes in the presence of light. Notably, the sidewall cycloaddition can occur through two-sided photo excitation, with resonant excitation of either the nanotubes with visible light or the compounds with UV light. The aqueous medium also allows for *in situ* probing the evolution of the sidewall cycloaddition and provides a molecular level control. The observed chemistry of molecular engineering the surface of SWCNTs provides understanding of the reaction between SWCNTs and lipids, and can be potentially applied to *in vivo* lipid detection.

More importantly, this exciton-tailoring chemistry is not limited to 18-carbon fatty acid but also applicable to shorter enone-containing organic molecules with only 10-carbon length. The reaction efficiency largely depends on the chain length, while remains low with molecules containing only keto functional group. These findings provide a more economical and potentially scalable way to synthesize SWCNTs as being single-photon emitters.

Our computational results further supported the above proposed $[2\pi + 2\pi]$ photocycloaddition mechanism by comparing the stability of the products with those through $[2\pi + 4\pi]$ photocycloaddition. Additionally, dispersion interactions and steric effects were found to play key role in determining chemo- and regioselectivity of the reaction with SWCNTs. Products involved C=C pointing along the axis of SWCNTs are more favorable compared with those pointing perpendicular to the axis.

3.0 Photoluminescence Response in Carbon Nanomaterials to Enzymatic Degradation

3.1 Preface

The material contained in the following Chapter was adapted with permission from *Analytical Chemistry* 2020, 92, 12880-12890. Copyright 2020 American Chemical Society.

List of Authors: Xiaoyun He, David L. White, Alexandr A. Kapralov, Valerian E. Kagan, and Alexander Star

Author Contributions: X.H., D.L.W. and A.S. designed the experiments. D.L.W. synthesized the nanoscrolls and collected the AFM images. A.A.K. performed the cellular degradation experiments. X.H. performed all other experimental work. All authors contributed to the writing of the manuscript.

3.2 Introduction

Myeloperoxidase (MPO) is a crucial peroxidase secreted by various primary phagocytic cells of the innate immune system.⁴⁴ In particular, MPO is most abundantly expressed by neutrophils during the first phase of inflammation. MPO produces potent oxidants such as hypochlorous acid (HOCl) and other reactive intermediates that are essential to destroy pathogens.⁴⁵⁻⁴⁷ MPO enzymatic oxidative degradation of carbon nanomaterials has been previously demonstrated both *in vitro* and *in vivo*.^{148, 149} In particular, Kagan *et al.*⁴⁶ reported that,

on incubation with MPO, H₂O₂, and Cl⁻, carboxylated single-walled carbon nanotubes (SWCNTs) can be degraded into a series of carbonaceous byproducts including but not limited to CO, CO₂, and a range of hydrocarbons. The enzymatic oxidation of gold nanoparticle-corked nitrogen-doped carbon nanotube cups (NCNCs) has also been recently proposed as a drug delivery mechanism.⁵⁰ The enhanced enzymatic oxidation activity in the tumor microenvironment was utilized as a trigger to open the gold-corked NCNCs, representing a novel cancer immunotherapy approach using NCNCs as effective drug nanocarriers for the delivery of paclitaxel.¹⁵⁰ In addition to carbon nanotubes, Kurapati *et al.*⁴³ have reported the biodegradation of graphene oxide (GO) sheets by MPO in the presence of 200 μM H₂O₂. *In vitro* oxidation of GO by neutrophils and generated degradation products have also been demonstrated to be non-genotoxic.⁴⁸

Although there have been numerous studies¹⁵¹ of the biodegradation of carbon-based nanomaterials, the utilization of fluorescence spectroscopy to characterize carbon nanomaterials and monitor their chemical changes during enzymatic oxidation has not been investigated. The photoluminescence (PL) properties of carbon nanomaterials are closely related to their size, morphology, and the existence of defect sites.^{103, 152} PL spectroscopy provides opportunities to elucidate the mechanism of biodegradation and also serve as an analytical tool to measure the underlying MPO activity. We had previously concluded that MPO/H₂O₂/Cl⁻ enzymatic degradation was a relatively complete oxidation process for oxidized HiPco SWCNTs based on PL measurements. This is in contrast to the milder oxidation catalyzed by a plant-based enzyme, horseradish peroxidase (HRP).¹⁵³ We also investigated the role of different surfactants in the MPO-catalyzed degradation of pristine SWCNTs.¹⁵⁴ The band gap emissions of sodium cholate-, DNA-, and albumin-coated nanotubes (SC/DNA/BSA-SWCNTs) were quenched in a diameter-dependent fashion.

Commercial probes for detecting MPO activity measure reactive oxygen species (ROS), important antimicrobial agents generated by MPO during the immune response.¹⁵⁵ Such sensors have been validated by electron paramagnetic resonance spectroscopy, photoluminescence spectroscopy, magnetic resonance imaging,¹⁵⁶⁻¹⁵⁸ and electrochemical methods.¹⁵⁹⁻¹⁶¹ Carbon nanodots,¹⁶²⁻¹⁶⁴ SWCNTs,^{165, 166} GO,¹⁶⁷ and reduced GO (rGO)^{168, 169} have recently been explored as sensor candidates for the detection of MPO activity in both *in vitro* and *in vivo* environments. The complexity of MPO/H₂O₂/Cl⁻ oxidative machinery makes targeting one or several MPO-generated oxidants less representative of the overall MPO activity. Most of the current generations of carbon nanomaterials-based fluorescent sensors are based on a single fluorophore. In comparison, ratiometric sensors utilize two different fluorescence signals as internal references for each other. Ratiometric sensors provide a built-in correction for environmental interference, improve the signal-to-noise ratio, and broaden the linear range.¹⁷⁰

In this work, to address the above concerns, we systematically investigated the enzymatic degradation mechanism of SWCNTs and GO *via* photoluminescence. Based on our findings of the PL progression during MPO/H₂O₂/Cl⁻ oxidation, we constructed two ratiometric fluorescent sensors as sacrificial MPO indicators for *in vitro* environments.

3.3 Materials and Methods

Cobalt-molybdenum-catalyzed (CoMoCAT) single-walled (6,5) carbon nanotubes were purchased from Sigma-Aldrich and used without further purification. Aqueous SWCNT suspensions were initially prepared at 1 mg/mL with either 1 wt% sodium cholate (SC, Sigma-Aldrich) or 0.5 wt% sodium carboxymethylcellulose (CMC, Sigma-Aldrich) as a surfactant. The

suspensions were sonicated for 1 h and centrifuged to remove large SWCNT bundles. The top 90% of the supernatant was transferred to a separate container and used as a stock solution. GO aqueous solution (5 mg/mL) was purchased from Graphene Supermarket. SWCNT/GO nanoscrolls were synthesized by sonicating a mixture of 0.5 mg/mL of surfactant-coated SWCNTs and 1 mg/mL GO for 1 h.

For MPO enzymatic degradation experiments, six vials were prepared by adding 446 μL of 1 \times phosphate-buffered saline (PBS) (Sigma-Aldrich, 0.01 M phosphate buffer, 0.0027 M potassium chloride and 0.137 M sodium chloride, pH 7.4, at 25°C) and 50 μL of each sample (1 mg/mL GO, 0.5 mg/mL SWCNT, and GO/SWCNT). Lyophilized MPO (Athens Research & Technology, Inc.) was dissolved in 1 \times PBS with a final concentration of 2.5 $\mu\text{g}/\mu\text{L}$ and added to all six vials at a volume of 2 μL . The MPO/H₂O₂/Cl⁻ degradation was activated by adding 2 μL of 25 mM H₂O₂ (Fisher Scientific) every hour with total seven additions per day for 5 days. MPO (2 μL) was replenished daily to compensate for the loss. For control experiments without (i) carbon nanomaterials, (ii) MPO, (iii) H₂O₂, and (iv) Cl⁻, equal volumes of (i) nanopure H₂O, (ii) PBS, (iii) nanopure H₂O, and (iv) 1 \times phosphate-buffered solution were added to the degradation system at indicated time-points as a substitute for (i) carbon nanomaterials, (ii) MPO, (iii) H₂O₂, and (iv) PBS, respectively.

For cellular degradation of GO, human myeloid leukemia HL-60 cells were chosen and induced to differentiate into neutrophil-like cells by the addition of 1.5% dimethyl sulfoxide (DMSO) for 6 days. The differentiated cells were suspended in RPMI 1640 media without phenol red and seeded in six-well plates with a volume of 2 mL in each well. GO was added in a concentration of 0.035 mg/mL and incubated in the presence of N-formyl-methionyl-leucyl-phenylalanine (fMLP, 100 nM) and cytochalasin B (CyB, 5 $\mu\text{g}/\text{mL}$). After 24-h incubation, the

samples were centrifuged at 700 g for 5 min and the supernatant was taken for fluorescence and TEM measurements. The 0 h control sample, GO (0 h), was prepared by dissolving GO in RPMI 1640 media (without phenol red) at a concentration of 0.035 mg/mL, and centrifuged immediately after dissolving. For experiments without GO, the cells incubated with fMLP and CyB were centrifuged at either 0 h or 24 h, respectively, and the supernatant was collected for fluorescence measurements.

UV-vis-NIR absorption spectra were collected using a PerkinElmer Lambda 900 spectrophotometer over the wavelength range of 200 – 1200 nm. Raman spectra were acquired on an XploRA plus confocal Raman microscope (Horiba) with 638 nm laser (24mW) operating at 10% power.

Visible photoluminescence spectra were obtained using a Fluoromax-3 spectrometer (HORIBA Jobin Yvon) equipped with a xenon lamp light source and a photomultiplier tube detector. All visible emission spectra were recorded with 325 nm excitation unless otherwise stated. The slit widths were set at 10 nm and 3 nm for measurements of all MPO/H₂O₂/Cl⁻ and HL-60 cell degradation experiments, respectively.

NIR photoluminescence measurements were performed on a Nanolog spectrofluorometer (HORIBA Jobin Yvon) equipped with a xenon lamp (400 W) light source, double excitation monochromators, and a Symphony II InGaAs array (NIR) detector. Spectra were obtained using 566 nm excitation wavelength, which is in resonance with the first absorption band of the (6,5) SWCNTs. The slit widths were set at 10 nm for both excitation and emission. All measurements were obtained with an 830 nm long-pass filter at ambient temperature.

Transmission Electron Microscopy (TEM, FEI Morgagni, 80 keV) samples were prepared by dropcasting 6 μL of 100x diluted solution on a lacey carbon grid and dried under ambient conditions overnight.

The hydrodynamic diameter (by dynamic light scattering (DLS)) and zeta-potential of the samples in nanopore water were obtained using a Zetasizer Nano ZS90 (Malvern Panalytical Ltd). DLS was carried out with 1 mL samples under 633 nm laser irradiation. Each measurement was performed in triplicate. The zeta-potential measurements were conducted in the phase analysis light scattering (PALS) mode following the solution equilibration at 25°C. Each sample was measured three times and the average data was taken.

Atomic Force Microscopy (AFM) was taken using a Bruker multimode 8 system utilizing a Veeco Nanoscope IIIa controller in the tapping mode. An AppNano ACST-SS probes having a nominal radius of 1–2 nm was operated at a frequency of 160–225 kHz, an amplitude set point of 1.70–1.75 V, and a drive amplitude of 100–300 mV. Samples were prepared by dropcasting 10 μL of 10 times diluted respective nanoscroll solution onto freshly cleaved mica and left to dry under vacuum for at least two hours. SWCNTs(CMC)/GO nanoscrolls were additionally subjected to a 24-hour dialysis procedure using a 90 kDa filter before dropcasting to make identification of one-dimensional structures easier. All images were processed in Gwyddon.

3.4 Results and Discussion

The mechanisms of the MPO enzymatic oxidative machinery, peroxidase cycle and halogenation cycle, are summarized in Figure 3.1a. MPO is a heme-containing protein with Fe(III)-protoporphyrin IX as its active site. Initially, MPO is inactive and its heme group is in the

ferric resting state. Its interaction with hydrogen peroxide (H_2O_2) induces the active center to produce the oxidative ferryl oxo iron ($\text{Fe}^{4+}=\text{O}$), and the porphyrin (Por) π radical cation, collectively known as compound I, through a protein-assisted conversion. The generated oxidant can return to the resting state via two pathways. It can be reduced directly to the resting state by the conversion of Cl^- to hypochlorous acid in the acidic environment of neutrophils (red path). Otherwise, the reduction occurs in two sequential one-electron transfer steps. Compound I is reduced to compound II and then to the resting state, as the substrates (GO, SWCNTs, and/or SWCNT/GO nanoscrolls) are oxidized accordingly and form radical oxidative products.

The defect sites of carbon nanomaterials, such as pre-existing oxygen-containing functional groups in GO or hypochlorite (ClO^-) generated oxidative defects on the surface of SWCNTs,^{171, 172} serve as the initiation centers of MPO-catalyzed biodegradation.^{173, 174} The interactions between the defect sites of carbon nanomaterials and strong oxidants, ClO^- and compound I, facilitate the degradation of the structure of the material. As shown in Figure 3.1b, oxidative damage of SWCNTs results in shortened tubes with a variety of oxygen-containing defects, such as hydroxyl, ether, epoxide, and carboxyl groups on the surface. In contrast, holes gradually appear in the GO sheets resulting in the formation of graphene quantum dots (GQDs).^{42,}
⁴³ The ultimate shape and size of the resulting GQDs is dictated by the pre-existing pristine sp^2 domains in GO sheets. Although GO transitions from the two-dimensional morphology to zero-dimensional morphology,^{42, 43} SWCNTs retain their characteristic one-dimensional nanotube structures after MPO/ H_2O_2 / Cl^- treatment.⁴⁶ The less effective degradation can be attributed to the lack of the pre-existing oxygen-containing defect sites in pristine SWCNTs with respect to GO.⁴⁶

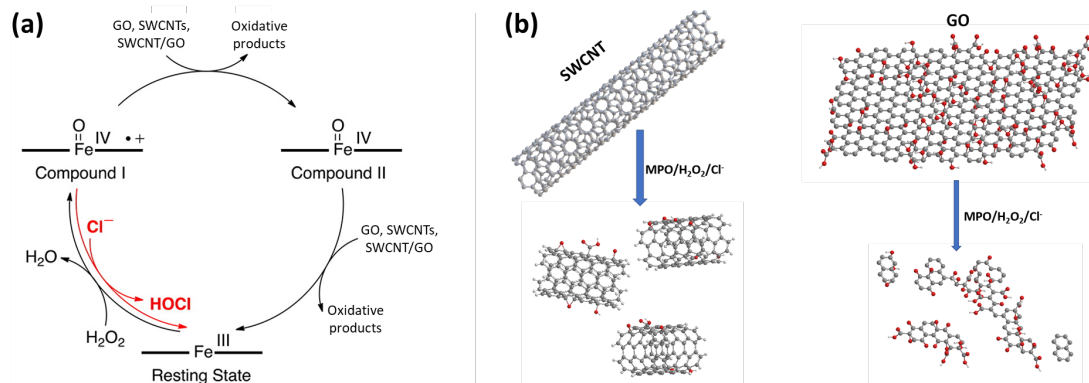


Figure 3.1. (a) Catalytic peroxidase and halogenation cycles of MPO. Adapted with permission from ref. 35. Copyright 2012 American Chemical Society. (b) Schematic diagram illustrating the enzymatic degradation of SWCNTs and GO (carbon and oxygen atoms are shown in gray and red, respectively).

Our previous results indicate that using sodium cholate (SC) as a surfactant, the NIR fluorescence of pristine SWCNTs is suppressed following the introduction of defects on the sidewalls of SWCNTs.^{153, 154} As shown in Appendix Figure 15, SC-wrapped SWCNTs displayed a gradual decrease in both the absorbance and PL intensity over the 5-day MPO/H₂O₂/Cl⁻ degradation. In this study, we tested another surfactant, carboxymethylcellulose (CMC), because of its favorable biocompatibility^{175, 176} and its potential as an ideal matrix of thin-film sensors.^{177, 178} Figure 3.2a displays the UV-vis-NIR spectra of CMC-coated SWCNTs over the 5-day oxidation. Although there was a small gradual decrease in the absorbance of day 5 sample, the day 5 spectrum retained the three absorption peaks centered at around 1000 nm, 575 nm, and 345 nm corresponding to the characteristic E₁₁, E₂₂, and E₃₃ excitonic transitions of (6,5)-SWCNTs.¹⁷⁹ The small decrease in the absorbance can be the result of the reaction mixture dilution by continuously replenishing H₂O₂ and MPO over the 5-day degradation process (Appendix Figure 16), the slight degradation of SWCNTs in response to MPO oxidative machinery, and experimental variations. However, in contrast to SC (Appendix Figure 15a), the retained absorption behavior of CMC

wrapped SWCNTs indicates the inhibition of the previously observed MPO degradation of SWCNTs using other surfactants.^{153, 154} The progressive PL intensity of the CMC-wrapped SWCNTs in Figure 3.2b showed slight decreases in the process of 5-day oxidative degradation, while remaining the characteristic E₁₁ emission peak of SWCNTs in day 5 sample. The excitation-emission (EE) maps in Appendix Figure 17 further confirmed the retained characteristic E₁₁ emission peak after 5-day degradation with little peak shift. The consistency of the PL intensity is indicative of the lack of defect sites formed on the surface of the exposed bare SWCNTs after the CMC wrapping. The observed surfactant-dependent reactivity¹⁸⁰ implies that, compared with SC, CMC protects the surface of SWCNTs through a higher surface coverage. With the less bare SWCNTs surface exposed to the strong oxidants generated in the MPO peroxidase and halogenation cycles (Figure 3.1a), fewer oxygen-containing defects will be generated. As these defects serve as the initiation centers of degradation,^{173, 174} fewer generated defect sites will make CMC-wrapped SWCNTs less susceptible to the MPO oxidative machinery, and thus exhibiting diminished reactivity as compared to the SWCNT(SC). The PL consistency of the SWCNT(CMC) over 5-day degradation was demonstrated by triplicate measurements (Appendix Figure 18), indicating its potential as being a reference sensor for MPO oxidative machinery.

To further confirm the factors affecting the change in the PL intensity, three control experiments were performed without the addition of MPO, H₂O₂, and Cl⁻, respectively. As shown in Appendix Figure 5a, similar to complete degradation systems, characteristic E₁₁, E₂₂, and E₃₃ excitonic transitions of (6,5)-SWCNTs remained in all three samples after 5-day degradation. Consistently, the PL intensity (Appendix Figure 19b) of three controls after 5-day oxidation displayed comparable intensity to that under complete MPO/H₂O₂/Cl⁻ degradation systems. This result revealed that the slight decrease in the PL intensity shown in Figure 3.2b is a combined

effect of the solution dilution, experimental variance, and modest SWCNT oxidation. The fluorescence background in the absence of SWCNTs was also being tested to exclude its contribution to the observed PL. As shown in Appendix Figure 20, the background PL at the SWCNT E₁₁ emission across 5-day oxidation is negligible and the change in the intensity is minimal compared to the samples with SWCNTs (Figure 3.2b).

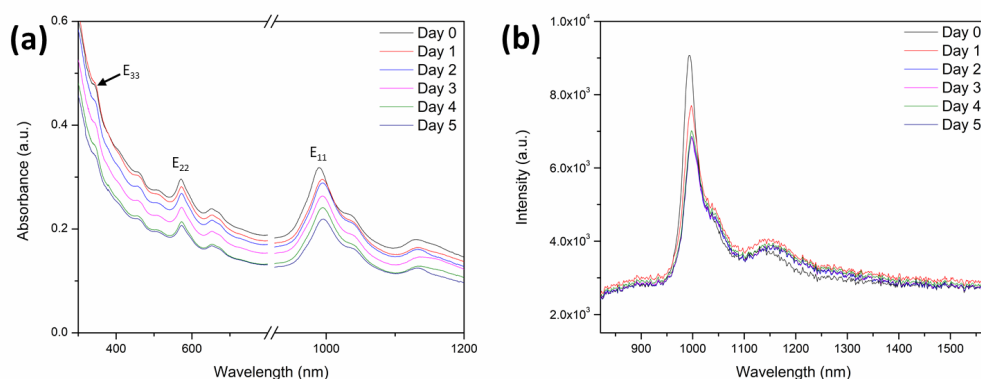


Figure 3.2. (a) UV-vis-NIR absorption spectra and (b) photoluminescence emission spectra of the MPO/H₂O₂/Cl⁻ degradation of SWCNTs (CMC wrapped) from day 0 to day 5.

The progressive spectra of GO substrates were also measured. Prior to the oxidation, the UV-vis-NIR absorption spectrum of pristine GO (Figure 3.3a) displayed one peak centered at 230 nm related to the π - π^* transition of the aromatic C-C bond, and another shoulder peak at around 300 nm corresponding to the n- π^* of the C=O bond transition. These two prominent features were gradually attenuated as a result of the 5-day oxidation treatment, demonstrating the degradation of the chemical structure of GO. Consistent with previous studies,^{40, 43, 48} the characteristic D (~ 1320 cm⁻¹) and G (~ 1570 cm⁻¹) bands of GO in the Raman spectra (Figure 3.3b) disappeared after a 5-day MPO/H₂O₂/Cl⁻ degradation. Transmission electron microscopy (TEM) reveals structural changes in GO before and after the 5-day MPO/H₂O₂/Cl⁻ oxidation (Figure 3.3c and 3.3d). In

contrast to the micrometer-sized GO single-layer sheet initially present, small GQDs with a diameter at around 20 nm (Appendix Figure 21) were observed after 5 days of oxidation.

The progression of MPO catalyzed oxidation of GO over 5 days was monitored using fluorescence spectroscopy. Interestingly, a broad emission peak centered at 440 nm (Figure 3.3e, Appendix Figure 22b), with an excitation peak centered at 325 nm (Figure 3.3f), gradually appeared over the 5-day degradation. Similar blue-luminescent GQDs have been previously observed during a photo-Fenton oxidation reaction of GO^{41, 42} while having never been reported in the context of the biodegradation system.¹⁵¹ The peak evolution had monotonic increases under different excitation wavelengths ranging from 275 to 375 nm over the time course (Appendix Figure 23). The oxidation-generated photoluminescence exhibited an excitation wavelength dependence (Appendix Figure 24). The emission peak position was located at 440 nm under the 300 nm excitation, and red-shifted 10-20 nm under either higher (275 nm) or lower excitation energies (350 and 375 nm). The highest intensity PL emission was observed under the 325 nm excitation, approximately 1.5 times higher than the second most intense peak under the 350 nm excitation. The PL emission spectra of GO features a minor peak at 367 nm that can be assigned as the water Raman peak. The water Raman peaks were also observed across different excitation wavelengths (Appendix Figure 24), and their positions agreed well with the calculated values (Appendix Table 9). Since the focus of this work is the PL evolution due to the GO degradation products, the solvent Raman peak intensity should be minimal. Under different excitations, GQD PL peaks are all well-resolved from the water Raman peaks (Figure 3.3e and Appendix Figure 24). Thus, the interference and possible distortion of the fluorescence spectra due to the solvent Raman peak are negligible. Since the 325 nm excitation gave rise to the highest relative intensity of the PL peak of the degradation product (at 440 nm) to the water Raman peak, it was selected for further

use in MPO-secreting cell degradation experiments and the dual-emission ratiometric sensors due to the brightness of the emission as compared to matrix effects. Furthermore, the standard deviation of the normalized PL intensity was as low as 0.12 for three replicate measurements (Appendix Figure 25), which indicates the favorable reproducibility of the GO substrate being a turn-on sensor for MPO oxidative machinery.

In order to confirm the necessity of the complete MPO/H₂O₂/Cl⁻ oxidation system for the degradation of GO, three control experiments were performed by removing MPO, H₂O₂, and Cl⁻, respectively. As compared to the complete disappearance of the characteristic GO peaks in the complete oxidation system, the UV-vis-NIR spectra of all three control samples (Appendix Figure 26a) still exhibited strong absorbance in the UV range (200-300 nm) with a minor degree of attenuation. The integrity of GO was further confirmed *via* Raman spectroscopy as the characteristic D and G bands of GO were still present in all three controls after the 5-day oxidation (Appendix Figure 26b). The Raman and UV-vis-NIR absorption results both indicate that the biodegradation of GO was markedly suppressed in all of three controls. Further evidence was obtained by TEM (Appendix Figure 27) as intact single-layer GO sheets were still present in all three 5-day degradation samples. The PL spectra of all three controls displayed negligible increases of the PL emission centered at 440 nm (Appendix Figure 28a) and excitation centered at 325 nm (Appendix Figure 28b). These results are consistent with previous studies where carbon nanotubes were shown to undergo incomplete MPO catalyzed degradation in the absence of chloride.⁴⁶ Missing one or more components in the peroxidase and halogenation cycles (Figure 3.1a) weakens the overall oxidation potential resulting in the less efficient degradation of GO.

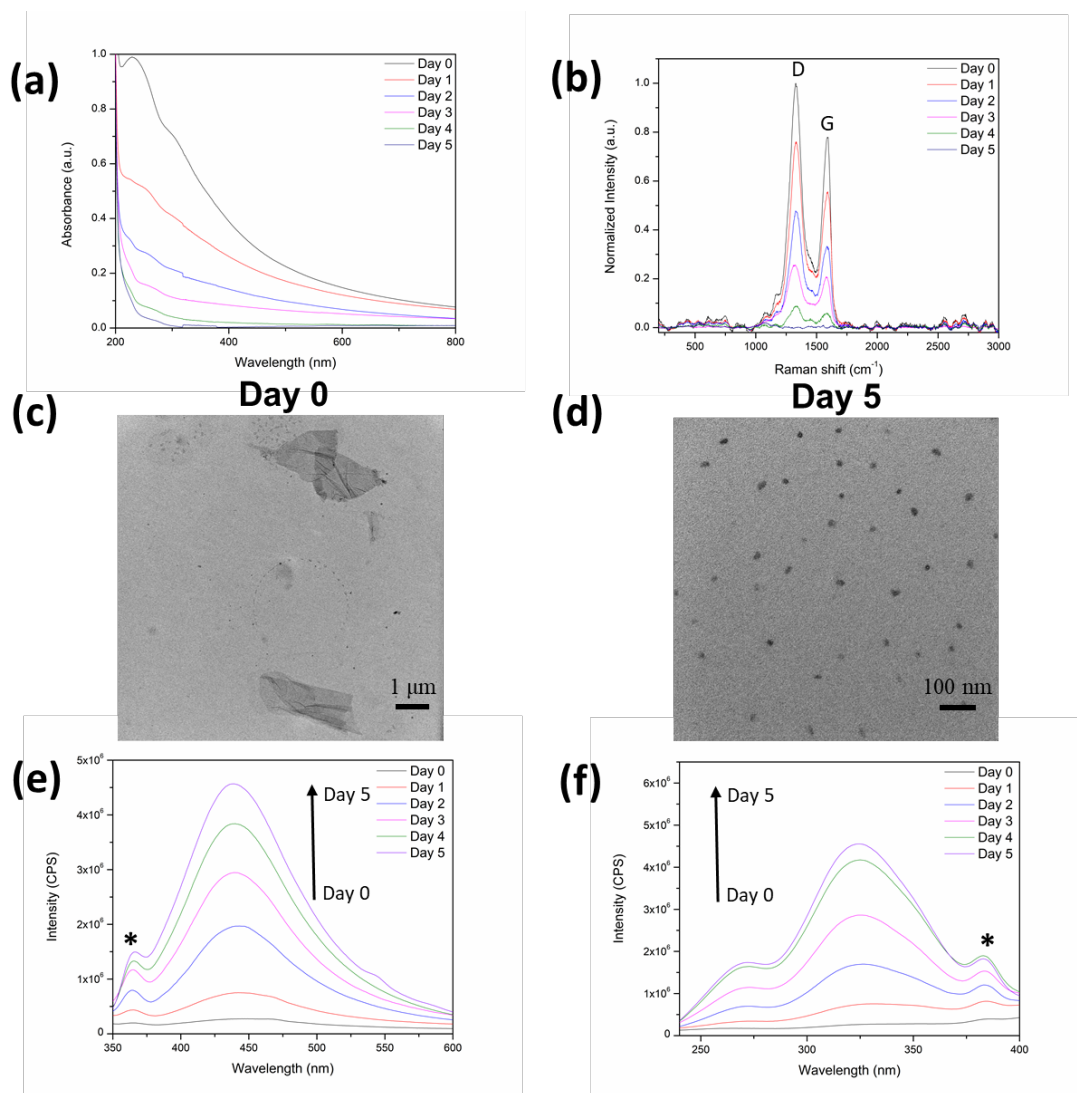


Figure 3.3. (a) UV-vis-NIR spectra, (b) Raman spectra, (c, d) TEM images, (e) photoluminescence emission, and (f) excitation spectra of the 5-day MPO/H₂O₂/Cl⁻ degradation of GO. (*) is the water Raman peak. The PL emission spectra (e) were obtained with excitation at 325 nm. The excitation spectra (f) were obtained at an emission wavelength of 440 nm.

To exclude the possibility that the background fluorescence was the primary contributor to increased PL, a control experiment was performed in the absence of GO. As shown in Appendix Figure 29a and 29b, different from the GO-based observations (Figure 3.3e and 3.3f), one emission peak centered at 400 nm was observed with an excitation peak at 290 nm, attributed to the

formation of the fluorescent compound dityrosine.^{181, 182} Furthermore, background subtraction was performed on the PL spectrum of the 5-day GO degradation sample. As shown in Appendix Figure 30, one peak centered at around 445 nm remained after the background subtraction, and was assigned to the formation of GO degradation products.

The PL studies of SWCNT degradation by neutrophils have been previously reported by our group.¹⁵⁴ A more efficient PL quenching was observed when incubating with neutrophils as compared to MPO alone. Previous studies also indicate the ability of neutrophils to extracellularly degrade GO *in vitro* through an MPO-catalyzed mechanism by Raman spectroscopy.⁴⁸ Thus, in this work, we proceeded to apply fluorescence spectroscopy to study the degradation of GO by MPO-secreting cells. Figure 3.4a,b shows the fluorescence emission spectra under different excitation wavelengths. The RPMI 1640 media (dashed lines) displayed a strong background fluorescence centered at 410 nm and 350 nm which is attributed to the combined effect of autofluorescence components such as tryptophan¹⁸³ and folic acid.¹⁸⁴ As the media itself contains L-tyrosine which is convertible into dityrosine, an intensely fluorescent compound, under the oxidative environment, the small decrease in the background fluorescence (Figure 3.4a and 3.4b, dashed black line vs. dashed red line) under both the excitation indicates that the formation of dityrosine is actually negligible under our experimental condition without the presence of GO. The main contributor of the background fluorescence remains to be its autofluorescence without the presence of GO. Although the media did increase the background fluorescence, the samples with GO after the 24 h incubation (solid red lines) displayed an increase in the fluorescence emission with respect to the corresponding 0 h samples (solid black lines) as well as higher intensity than the 24 h background (dashed red lines). Interestingly, under 300 nm excitation, one broad emission peak at 400-450 nm was formed exclusively with the sample containing GO after

incubating with the cells after 24 h (Figure 3.4b, red line). This additional shoulder peak is not observed under 325 nm excitation and unique with respect to all other samples under 300 nm excitation; thus it could serve as a direct clue indicating the possible formation of GO degradation products. Distinguishable fluorescent features stem from the GO oxidative products as evidenced by the dark dots in TEM images (Figure 3.4c). The background subtraction of PL emission under both excitation conditions reveals a peak centered at around 410 nm (Figure 3.4a and 3.4b insets), similar to the spectra of dityrosine.^{181, 182} We reasoned that, while the dityrosine formation is negligible in the absence of GO, the conversion could be increased with the existence of GO. It has been reported¹⁸⁵ that carbon nanomaterials could elicit a specific immune response pathway. The increased generation of oxidants will thus lead to more dityrosine formation. Second, compared with the direct addition of MPO in the MPO/H₂O₂/Cl⁻ oxidation, the existence of micrometer-sized cells¹⁸⁶ could interfere with the interaction between the secreted MPO and GO, and lead to the higher production of the byproduct, dityrosine. Consequently, the strong fluorescence of dityrosine may mask the fluorescence of GO degradation products. Although this result is limited to the detection of GO oxidative products over the dityrosine background in terms of PL, it shows that fluorescence spectroscopy can be applied as an analytical tool to study GO biodegradation as it shows distinguishable PL response between sample containing GO degradation products and other control samples based on either the peak intensity or the peak position. As for the further improvement of the detectability of GO degradation products versus dityrosine, the time-resolved photoluminescence technique could be a good candidate with regard to the possible different decay profiles of these two species,¹⁸⁷⁻¹⁹⁰ although it is beyond the scope of this work.

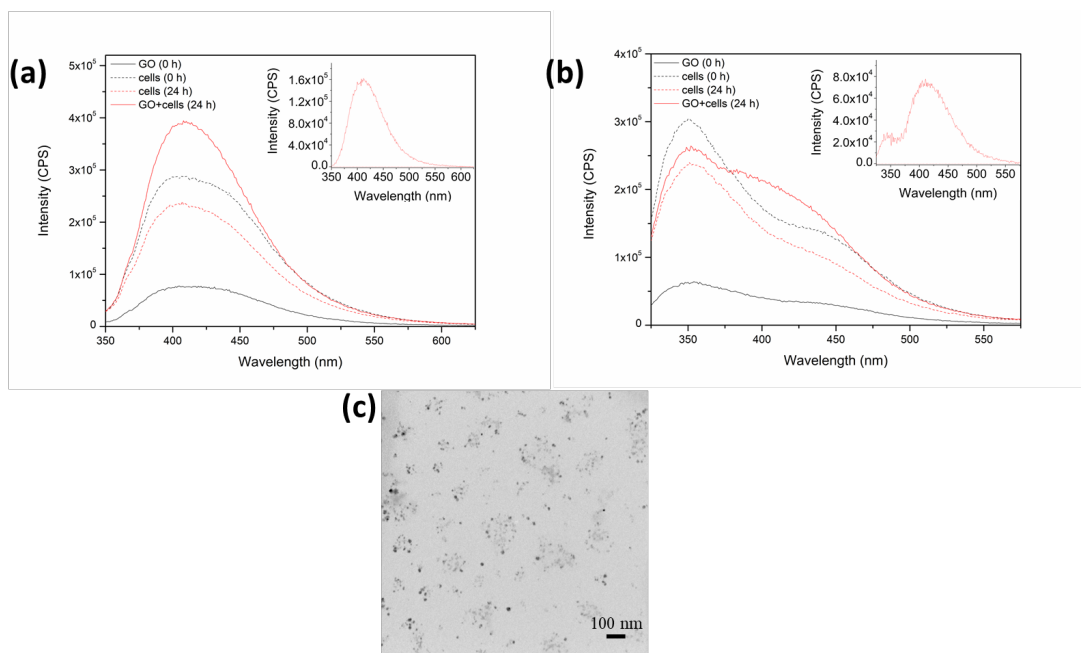


Figure 3.4. Fluorescence emission spectra of the degradation of GO with neutrophil-like HL-60 cells under (a) 325 nm and (b) 300 nm excitation (cells were centrifuged down before taking the measurements). The insets show that the PL spectra of the samples containing GO after 24 h incubation with cells after background subtraction (samples containing cells only after 24 h incubation (dashed red lines) served as the background, as they show a flat line in the insets). (c) TEM image of the supernatant of the sample containing GO after 24 h incubation with cells.

In the interest of developing sensors that can be calibrated in complex backgrounds, we combined the insights regarding GO and SWCNTs in the presence of MPO degradation to develop two dual emission ratiometric sensors with SC-coated or CMC-coated SWCNTs wrapped in GO (nanoscrolls). Although there is minimal PL background in the NIR range (Appendix Figure 20), the ratiometric strategy, as shown previously,¹⁹¹⁻¹⁹³ could overcome the limitations of the relative strong visible PL background (Appendix Figure 30 and 31). The GO-wrapped SWCNT nanoscrolls were synthesized according to the published sonication procedure.¹⁹⁴ The spontaneous formation of the core-shell structure is a result of the strong hydrogen bonding between the

hydrophilic surface of both GO^{195,196} and surfactant-coated SWCNTs. Additionally, the strong π - π stacking non-covalent interaction between the GO and the exposed bare CNT surface provides another driving force for wrapping.¹⁹⁴⁻¹⁹⁷ The zeta-potential values of these two types of nanoscrolls (Figure 3.5a) are representative of the magnitude of electrostatic interactions between colloidal particles and indicative of their colloidal stability. Both systems exhibited relatively large zeta potentials (-34.8 ± 13.9 and -41.5 ± 9.0 mV for SWCNT(SC)/GO and SWCNT(CMC)/GO, respectively), suggestive of the long-term suspendability from the electrostatic considerations. However, both hybrids exhibited lower zeta-potentials than the corresponding SWCNT precursors (-39.8 ± 8.62 and -53.2 ± 7.47 mV for SWCNT(SC) and SWCNT(CMC), respectively), highlighting differential charge density present in the surfactant-wrapped SWCNTs¹⁹⁸ as opposed to the complete composites. It should be noted that DLS measures the hydrodynamic radii of spherical particles, thus the absolute values (Figure 3.5a) may not reflect the actual sizes of GO, SWCNTs, and SWCNT/GO. However, complementary to location-specific TEM characterization, DLS data confirms the relatively narrow size distribution across each sample as they were obtained by analyzing the bulk sample as a whole. More importantly, the relative 60-100 nm increases and significant decreases of both nanoscrolls (222 ± 78 and 349 ± 182 nm for SWCNT(SC)/GO and SWCNT(CMC)/GO, respectively) with respect to their corresponding SWCNT precursors (120 ± 84 and 285 ± 111 nm for SWCNT(SC) and SWCNT(CMC), respectively) and GO (2400 ± 691 nm) precursors, respectively, further support the success of SWCNT wrapping and the conformational change of GO. This conclusion is consistent with both the previously published work¹⁹⁹ and the TEM results (Figure 3.5b and 3.5c). Figure 3.5b,c shows the TEM images of the synthesized nanoscrolls, revealing that the GO sheets were successfully wrapped around the nanotubes. AFM images and line profiles of both nanoscrolls are shown in Appendix Figure 31.

The SC- and CMC-wrapped nanotubes displayed the diameters of approximately 0.8 – 1.4 nm (Appendix Figure 31a) and 2 – 4 nm (Appendix Figure 31b), respectively, in accordance with previous work.^{200, 201} The line profiles also showed a maximum of ~ 2.5 nm (Appendix Figure 31a, Trace 2) and ~ 12 nm (Appendix Figure 31b, Trace 1) in diameter of SWCNT(SC) and SWCNT(CMC), respectively, which are greater than that of the correspondingly surfactant-wrapped nanotubes. This observation further demonstrated the successful formation of nanoscrolls through the wrapping of GO on the surface of SWCNTs.

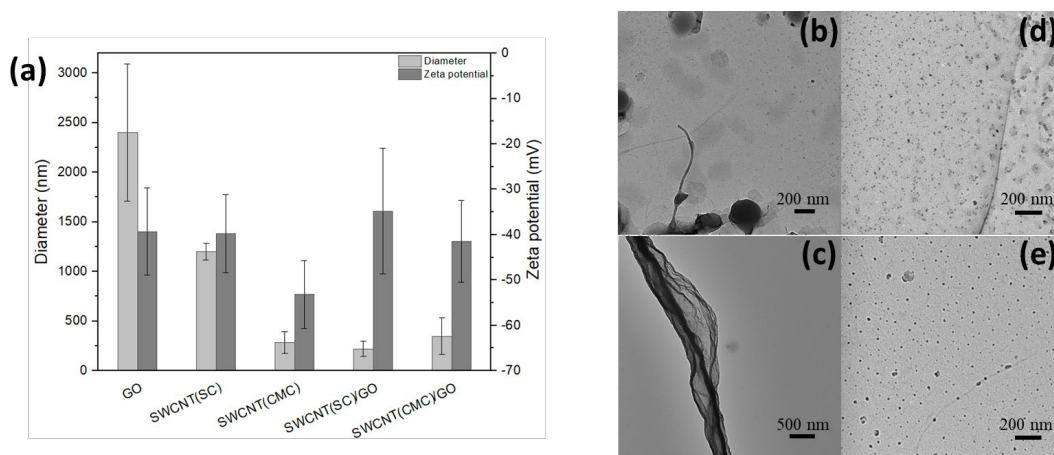


Figure 3.5. (a) Diameter (by DLS) and zeta potential of different samples. TEM images of (b, d) SWCNT(SC)/GO or (c, e) SWCNT(CMC)/GO (b, c) before and (d, e) after the 5-day MPO/H₂O₂/Cl⁻ degradation.

After degradation, TEM images illustrate that GO was preferentially degraded resulting in the formation of GQDs, while SWCNTs were still observable in both 5-day oxidation samples (Figure 3.5d and 3.5e). Appendix Figure 18 shows the UV-vis-NIR spectra of the two nanoscroll systems during the MPO-mediated degradation. Before oxidation, both nanoscrolls displayed characteristic absorption peaks of both GO (around 230 nm) and SWCNTs (~990 nm for the first (E₁₁) and ~570 nm for the second (E₂₂) excitonic transitions), which indicates the successful

construction of both nanoscrolls. Analogous to the individual oxidation of GO (Figure 3.3a), after the 5-day degradation, the characteristic GO peaks disappeared completely in both nanoscroll systems, demonstrating the complete degradation of GO. After 5 days of the MPO-driven degradation, the characteristic absorption and NIR fluorescent peaks of SWCNTs remained for both samples (Appendix Figure 32 and Figure 3.6), consistent with the TEM results (Figure 3.5d and 3.5e). SWCNT(CMC)/GO composites showed less degradation than the SWCNT(SC)/GO composites. This determination was made by the degree of decrease from day 0 to day 5 in both UV-vis-NIR (Appendix Figure 32) and NIR fluorescence spectra (Figure 3.6). The surfactant-dependent oxidation was also consistent with the individual CMC-SWCNTs (Figure 3.2) or SC-SWCNTs¹⁵⁴ (Appendix Figure 15) subjected to enzymatic degradation.

Figure 3.6 shows the change in the fluorescence intensity of two types of SWCNT/GO nanoscrolls during the 5-day enzymatic oxidation. An increasing fluorescence emission centered at 420 nm for SWCNT(SC)/GO and 430 nm for SWCNT(CMC)/GO was observed. We attributed this emission to the oxidation of wrapped GO sheets on the outer side of the nanoscroll core/shell structures (Figure 3.6c). This result was in accordance with the degradation occurring on the GO sheets individually (Figure 3.3e). The blue shifted emission can be accounted for by solvatochromism,^{202, 203} induced by incorporating surfactant-coated SWCNTs. The SWCNT NIR bandgap emission slowly decreased for SWCNT(SC)/GO nanoscrolls (Figure 3.6a) upon the generation of the defect sites on the surface of SWCNTs (Figure 2.6c). SWCNT(CMC)/GO nanoscrolls (Figure 3.6b) demonstrated less decrease due to the better surface-protection of SWCNTs by wrapped CMC.

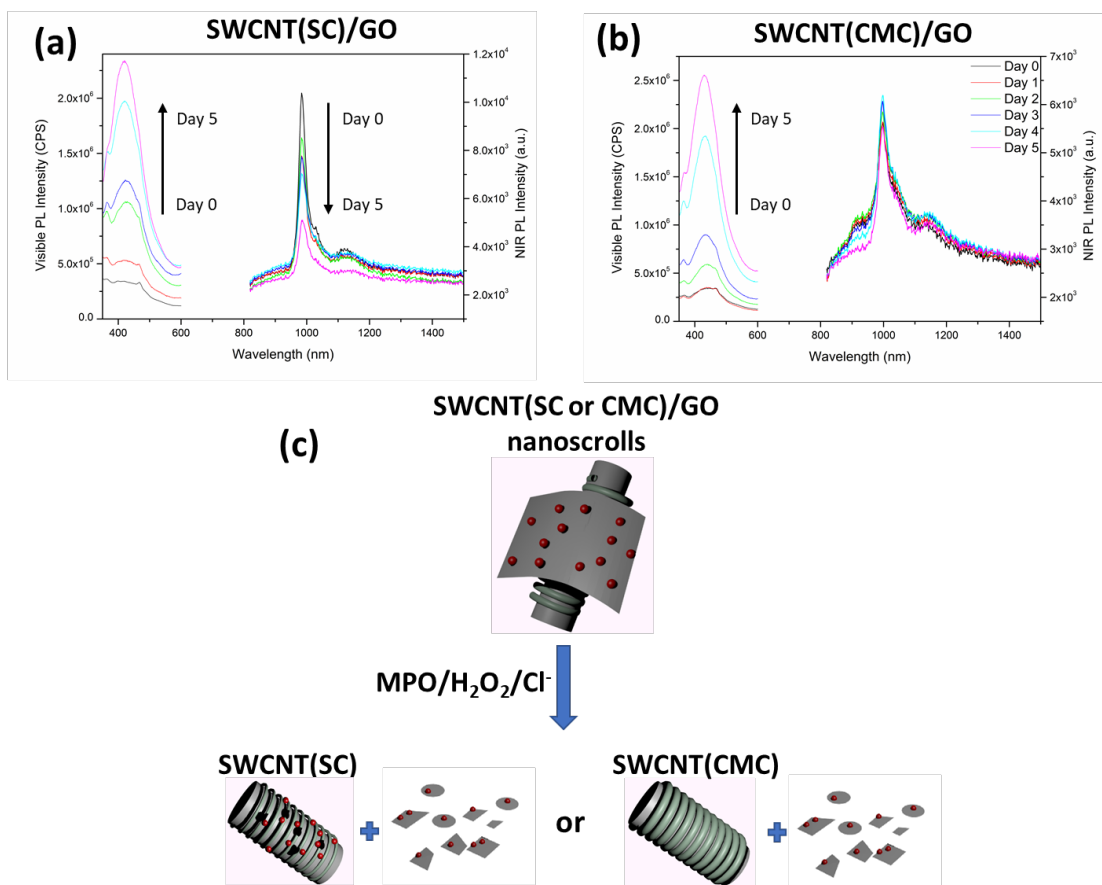


Figure 3.6. Photoluminescence spectra of the MPO/H₂O₂/Cl⁻ degradation of (a) SWCNT(SC)/GO or (b) SWCNT(CMC)/GO nanoscrolls from day 0 to day 5. The visible and NIR PL spectra were recorded under 325 nm and 566 nm excitation, respectively. (c) Schematic mechanism diagram illustrating the degradation of SWCNT/GO nanoscrolls (the oxygen-containing defect sites are shown in red).

Adopting a method similar to previously reported NIR ratiometric sensor systems,²⁰⁴ we normalized the visible and NIR signals of both nanoscrolls systems. We plotted the relationship between the ratio of intensity (Ratio) over time based on the fitted linear correlation of both emission signals with time (t). Detailed definitions are as follows:

$$I_{GO}^{normalized}(t) = \frac{I_{GO}(t)}{I_{GO}(5)} \quad (1)$$

$$I_{SWCNT}^{normalized}(t) = \frac{I_{SWCNT}(t)}{I_{SWCNT}(0)} \quad (2)$$

$$Ratio(t) = \frac{I_{GO}^{fitted}(t)}{I_{SWCNT}^{fitted}(t)} \quad (3)$$

Figure 3.7a,c shows the normalized fluorescence intensity (Eq. 1 and 2) for both visible GO and NIR SWCNT signals as a function of time. The fitted linear regression lines exhibited a minimum R² value of 0.87 for the visible signals of both nanoscrolls. The NIR signals of the SWCNT(SC)/GO sensor expressed a less rigorous correlation. The R² value of the NIR signal of SWCNT(CMC)/GO nanoscrolls was close to zero, which further confirmed that the NIR emission of CMC-wrapped remained invariant during the enzymatic oxidation. Figure 3.7b,d shows the dependence of *Ratio*(t) as a function of time for the MPO-catalyzed degradation. The result is the intensity of a pair of emission wavelengths that are representative of the oxidative stress in the MPO/H₂O₂/Cl⁻ system independent of the absolute intensity. The *Ratio*(t) values monotonically increased with time from Day 0 to Day 5. The quality of correlation proves that *Ratio*(t) is a valuable method to monitor the oxidative stress caused by the MPO/H₂O₂/Cl⁻ system in both SWCNT(SC)/GO and SWCNT(CMC)/GO nanoscrolls. More regression analysis was included in the Appendix A.2 (Appendix Figures 33-35). Looking forward, it would be interesting to visualize the degradation of nanoscrolls in terms of fluorescence microscopy. Applications can be made using fluorescence imaging technique to *in-situ* detect oxidative burst produced by MPO-secreting cells.

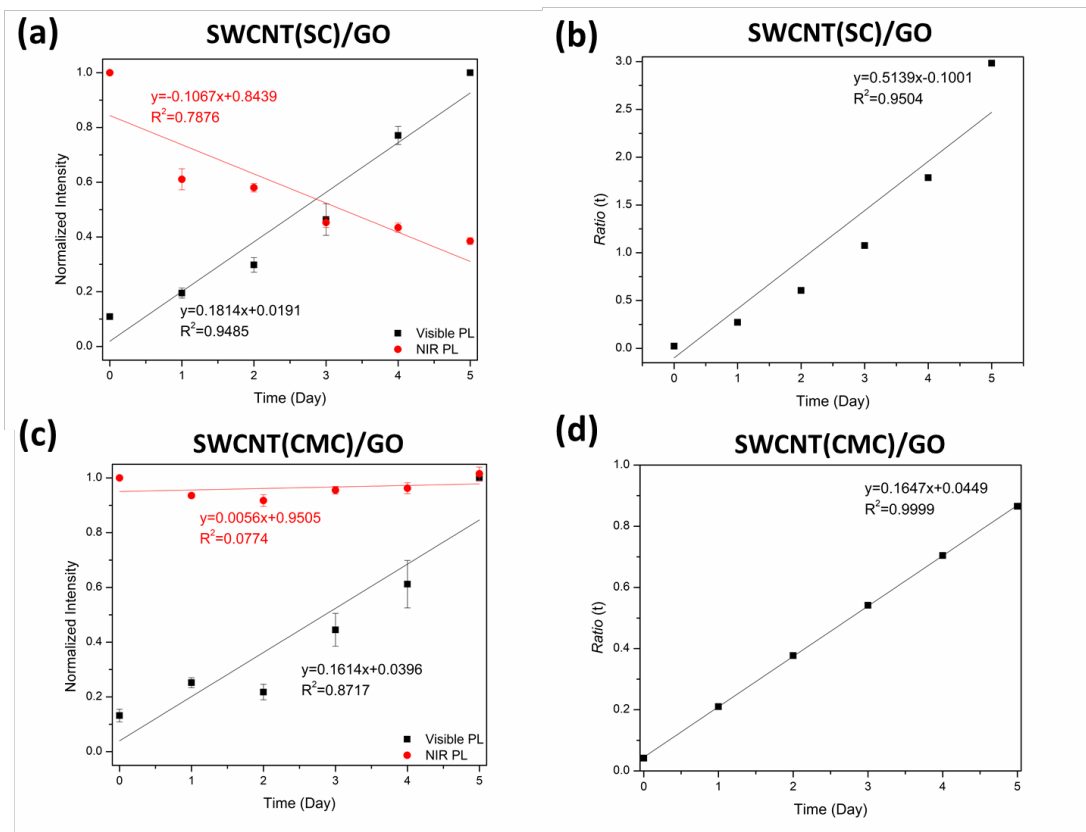


Figure 3.7. (a, b) Changes in the SWCNT(SC)/GO or (c, d) SWCNT(CMC)/GO nanoscrolls. (a, c) Normalized photoluminescence intensity and (b, d) ratio of intensity (Ratio) over 5-day MPO/H₂O₂/Cl⁻ degradation. The error bars represent standard deviations based on three replicate measurements.

3.5 Conclusions

In summary, we demonstrated, for the first time, the PL evolution during the MPO degradation of GO and SWCNTs. Increased fluorescence emission at around 440 nm was observed with the progression of enzymatic oxidation of GO as a result of the formation of GQDs. The GO fluorescence was also used for monitoring MPO activity in neutrophil-like HL-60 cells. In contrast,

the NIR E₁₁ fluorescence of surfactant-coated SWCNTs was either quenched (with SC) or remained almost unchanged (with CMC) during the 5-day degradation. The differences in surfactant coverage affected the ease of introducing defect sites on the sidewalls of SWCNTs. The two different PL systems were combined into a ratiometric fluorescence sensor, which can be self-calibrated regardless of environmental noise. SWCNT/GO nanoscrolls have been demonstrated to be sensitive to the MPO-dependent oxidative inflammatory response. The increased PL of GO in the visible range acts as a turn-on sensor and the NIR PL signal from SWCNTs is used either as the turn-off or reference sensor. For both fluorescence ratiometers, the ratio of the fluorescence intensity changed linearly with the progression of the bio-oxidation process. This ratiometric optical sensing platform is applicable in complex environments such as strongly scattering media and biological tissues. In particular, as the SWCNT(CMC)/GO system has the potential to be designed into a thin film sensor, our findings pave the way for the future development of the fluorescent sacrificial non-toxic solid state MPO activity indicators.

4.0 Liquid Chromatography Mass Spectrometry Analysis in Carbon Nanomaterials to Enzymatic Oxidation

4.1 Composition and Structure of Fluorescent Graphene Quantum Dots Generated by Enzymatic Degradation of Graphene Oxide

4.1.1 Preface

The material contained in the following Chapter was adapted with permission from *Journal of Physical Chemistry C* 2021, 125, 13361-13369. Copyright 2021 American Chemical Society.

List of Authors: Xiaoyun He, Dan C. Sorescu and Alexander Star

Author Contributions: X.H. and A.S. designed the experiments. X.H. performed the experimental work. D.C.C. performed the computational work. All authors contributed to the writing of the manuscript.

4.1.2 Introduction

Carbon nanomaterials (CNMs) such as carbon nanotubes and graphene have attracted tremendous attention for various applications in multiple fields including energy conversion and storage,^{205, 206} chemical sensors, and biomedicine.²⁰⁷ However, increasing use of CNMs also necessitates careful scrutiny of their impact on biological systems and human health. Understanding their interactions with cells of the innate immune system is of particular importance.²⁰⁸⁻²¹⁰ Myeloperoxidase (MPO), a key enzyme released by neutrophils during

inflammation, has been shown to catalyze the biodegradation of carbon nanomaterials both *in vitro* and *in vivo*.^{211, 212} Specifically, Kagan *et al.*⁴⁹ reported that incubation of carboxylated single-walled carbon nanotubes (SWCNTs) with MPO, H₂O₂, and Cl⁻ results in degradation into a series of carbonaceous by-products including but not limited to CO, CO₂, and a range of hydrocarbons. Kurapati *et al.*²¹³ have reported biodegradation of graphene oxide (GO) sheets by MPO in the presence of 200 μM H₂O₂. *In vitro* oxidation of GO by neutrophils has also been investigated and the generated degradation products have been found to be non-genotoxic.⁴⁸ However, the intermediate degradation products were hypothesized to be polycyclic aromatic hydrocarbons (PAHs) (Figure 4.1) with well-documented toxicity on their own.²¹⁴ Therefore, investigation of the oxidative biodegradation of CNMs and identification of their degradation products is of utmost importance to biological health.

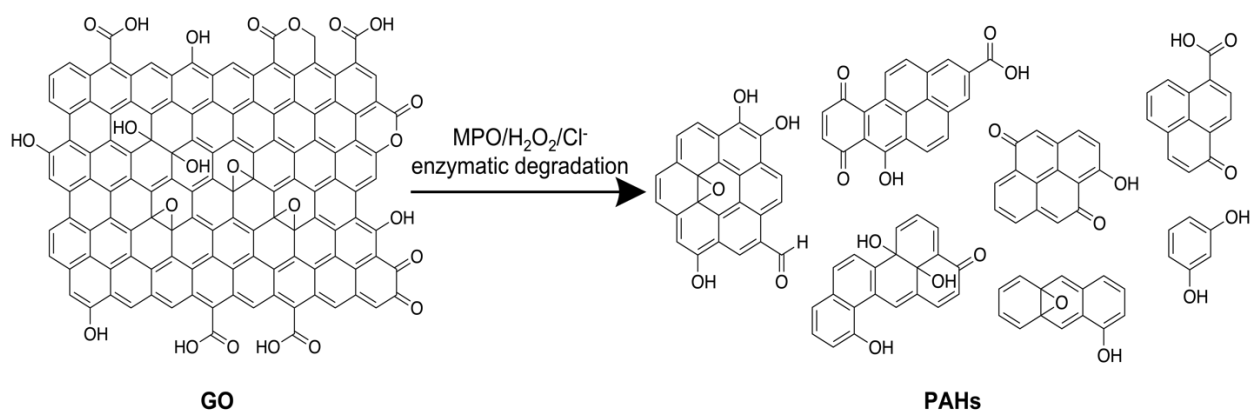


Figure 4.1. Schematic diagram illustrating the oxidative biodegradation of graphene oxide (GO) into polycyclic aromatic hydrocarbons (PAHs).

We have recently reported the observation of gradually increased photoluminescence (PL) of GO during MPO-catalyzed enzymatic degradation.²¹⁵ We attributed the observed fluorescence to the formation of the fluorescent degradation products, graphene quantum dots (GQDs)^{216, 217} or

carbon quantum dots,²¹⁸ which are presumably PAHs with specific molecular structures. Similar blue-luminescent GQDs have also been previously generated through a photo-Fenton oxidation reaction of GO.^{216, 219} Although some of the CNMs oxidative products generated through both enzymatic degradation^{49, 220} and photo-Fenton reaction^{216, 219} have been identified, the assigned products were found to be non-fluorescent in nature. The newly demonstrated PL property of the degradation products provide spectroscopic information that can help into structure assignment, as it implies certain energy bandgap between the highest occupied molecular orbital (HOMO) and the lowest unoccupied molecular orbital (LUMO). Therefore, in this work, we performed a composition and structure screening of the formed fluorescent PAHs by liquid chromatography-mass spectrometry (LC-MS) and density functional theory (DFT) calculations. By correlating the assigned products to the observed blue PL, our results would be helpful to understand the origin of fluorescent GO degradation products and contribute to future applications of GO in PL bio-imaging.

4.1.3 Materials and Methods

Similar to the reported MPO-catalyzed oxidation of CNMs,^{48, 49} MPO enzymatic degradation of GO was conducted as described previously.²¹⁵ Samples were prepared by adding 446 μL 1 \times phosphate buffer saline (PBS) (Sigma-Aldrich, 0.01 M phosphate buffer, 0.0027 M potassium chloride and 0.137 M sodium chloride, pH 7.4, at 25°C) and 50 μL of 1 mg/mL GO. Lyophilized MPO (Athens Research & Technology, Inc.) was dissolved in 1 \times PBS with a final concentration of 2.5 $\mu\text{g}/\mu\text{L}$ and added to all six vials at a volume of 2 μL . MPO/H₂O₂/Cl⁻ degradation was activated by adding 2 μL 25 mM H₂O₂ (Fisher Scientific) every hour, for a total of seven additions per day for 5 days. 2 μL MPO were replenished daily to compensate for the

loss. For control MPO experiments without GO, equal volumes of nanopure H₂O were added to the reaction mixture as a substitute for GO. It should be noted that as the MPO will gradually deactivate during incubation and H₂O₂ additions; seven additions of H₂O₂ were considered within 6 hours to ensure an efficient oxidation. Besides, as higher concentrations of H₂O₂ will deactivate MPO faster,²²¹ H₂O₂ was added in the seven aliquots instead of one addition. It has also been previously reported that the acidification of the reaction mixture upon H₂O₂ addition is compatible with the enzyme activity during proposed degradation procedures.⁴⁸

The oxidized products were collected by dichloromethane (DCM) extraction. After the DCM extraction, the solvent was evaporated and the resulting residue was resuspended in 500 μ L of methanol for injection into the LC-MS column. It could be reasoned that GO degradation products, in the form of PAHs with extended π -conjugated systems, are preferably present in the organic DCM layer instead of the aqueous layer as a result of the difference in solubility.^{217, 222} A similar extraction method has been used to analyze the enzymatic degradation products of SWCNTs.²²⁰

Liquid chromatography (LC) was performed using a Dionex-Ultimate 3000 (Thermo Fisher Scientific). The column employed was a Hypersil Gold C18, 100 \times 2.1 mm length and 1.9 μ m particle size from Thermo Fisher Scientific. The mobile phases used were 0.1% formic acid in water (mp1) and 0.1% formic acid in acetonitrile (mp2). An isocratic program with 30% mp1 and 70% mp2 was used. The flow rate was held constant at 200 μ L min⁻¹ with an injection volume of 5 μ L.

The LC effluent was pumped into a Q Exactive benchtop Orbitrap-based mass spectrometer (Thermo Fisher Scientific) with electrospray ionization (ESI) held at either positive or negative polarity. Nitrogen sheath gas and auxiliary gas flow rate were set up at 35 and 10

(arbitrary units), respectively. The capillary temperature was set at 250°C, the spray voltage was 3.5 kV and the S-lens voltage was set to 60 V. The instrument was operated at 70,000 resolving power and the automatic gain control (AGC) target was 1×10^6 .

MS/MS (MS^2) spectra were acquired by data dependent MS^2 experiments with an applied fragmentation energy of 30 eV. The experiments were operated at 35,000 resolving power. The AGC target and the maximum ion injection time (IT) were set to 1E5 and 50 ms.

The absorption and emission spectra of molecular systems of interest were calculated using time-dependent DFT²²³⁻²²⁵ for the ground and excited states as implemented in Gaussian 16 package.²²⁶ Calculations were performed at CAM-B3LYP/6-311+G(2d,p) level of theory.²²⁷ The effect of bulk solvent (water) on molecular configurations and on the corresponding vertical excitation and emission energies was considered by means of a polarizable continuum model^{228, 229} with inclusion of state-specific solvation for absorption or emission. An ultrafine integration grid with 99 radial shells and 590 angular points per shell was used in all calculations.

4.1.4 Results and Discussion

Figure 4.2 displays the LC-MS total ion chromatogram (TIC) profile in positive ionization mode of three different samples corresponding to pure methanol, MPO control, and degradation products after 5-day MPO/H₂O₂/Cl⁻ oxidation of GO. Similar chromatography peaks at retention time ~1 min appeared across all three samples, showing the background chromatographic peak. In contrast to the first two samples (Figures 4.2a and 4.2b), the chromatograph of the third sample (Figure 4.2c) displayed additional late-eluted chromatography peaks, indicating that these peaks could be a result of the formed GO degraded products. It can be reasoned that compared with solvent (methanol) and non-GO related products, such as dityrosine,^{230, 231} formed in the MPO

control sample, GO oxidative products with original π -conjugated systems would exhibit higher hydrophobicity and would have longer retention time.

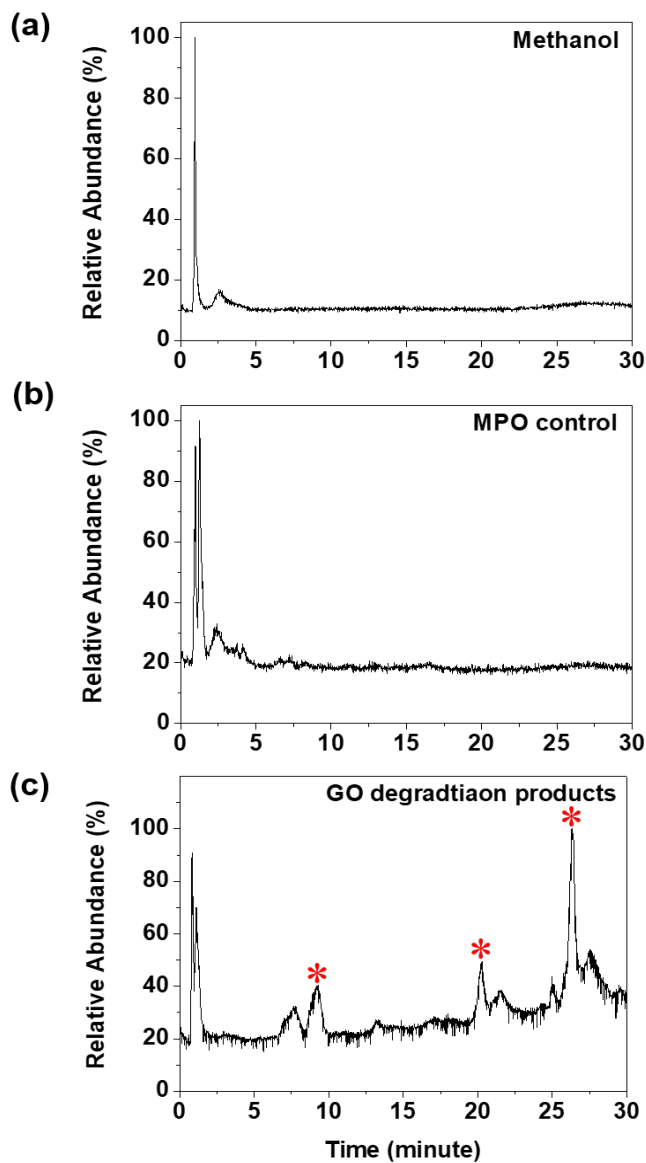


Figure 4.2. LC-MS total ion liquid chromatograms (TIC) in positive ionization mode of (a) pure methanol, (b) MPO control, and (c) after 5-day MPO/H₂O₂/Cl⁻ degradation of GO. Note: the red * symbol in panel (c) indicates the peak subjected to chemical formula screening.

In order to search for the potential molecular ion peaks correlated with GQDs, *i.e.*, the generated PAHs degradation products, we focused on three fractions eluted at 9.28 min, 20.29 min, and 26.35 min (denoted using a red * symbol in Figure 4.2c). Appendix Figure 36 displays the positive ion electrospray ionization (ESI) mass spectra obtained for the selected peaks. Here, a non-target screening workflow (Figure 4.3) was developed to filter out the chemical composition for the tentative GQDs, which are in the form of PAHs, in the degradation products. First, only the molecular ion peaks with relative intensities higher than 1% were chosen for analysis (Step I). At the same time, the relative intensity of the selected molecular ion peaks should be less than 1% in both pure methanol and in MPO control samples, as potential contributions from degradation products should not be present in both samples. After filtering out potential molecular ion peaks based on the 1% threshold cutoff, the following criteria were implemented to assign possible chemical compositions for each selected peak. Limit the number and type of elements (Step II) to ^{12}C (up to 100), ^1H (up to 100), ^{16}O (up to 100), ^{23}Na , ^{39}K , and ^{14}N (one ^{23}Na , ^{39}K , and ^{14}N for a singly charged peak, two ^{23}Na , ^{39}K , and ^{14}N for a doubly charged peak, and so forth). Also, the ideal composition candidates must contain at least three elements, *i.e.*, C, H and O. Different from laser desorption ionization (LDI) and/or matrix-assisted laser desorption ionization (MALDI) ionization methods, which produce primarily singly charged ions,²³²⁻²³⁵ ESI could generate a range of multiply charged species²³⁶ for each molecule: +2, +3, +4 and so on. Moreover, as ESI is one of the softest ionization techniques, detectability of some adducts during the ESI process depends on the availability of the small ions in the analytical process.^{237, 238} For example, sodium is one of the most common impurity, which could arise from multiple sources such as mobile phase additives, solvents, glassware, and so on.^{239, 240} Therefore, sodium adducts could be formed during the MS analysis. Here, four types of cationic adducts, namely $[\text{M} + n\text{H}]^{n+}$, $[\text{M} + n\text{Na}]^{n+}$, $[\text{M} +$

$nK]^{n+}$, and $[M + nNH_4]^{n+}$, were taken into consideration, where M represents the volatile analyte neutral molecules. The mass errors of the generated composition candidates for each molecular ion peak should be within ± 5 ppm (Step III). The ring double bond (RDB) value in the molecular candidates should be ≥ 4 to ensure the presence of at least one benzene ring in the structures (Step IV). The difference between experimental and theoretical intensity ratio of M+1(0.5) (isotope peak, 1 and 0.5 are the isotopic spacing for singly and doubly charged base peak, respectively) and M (base peak) should be within $\pm 10\%$ (Step V).

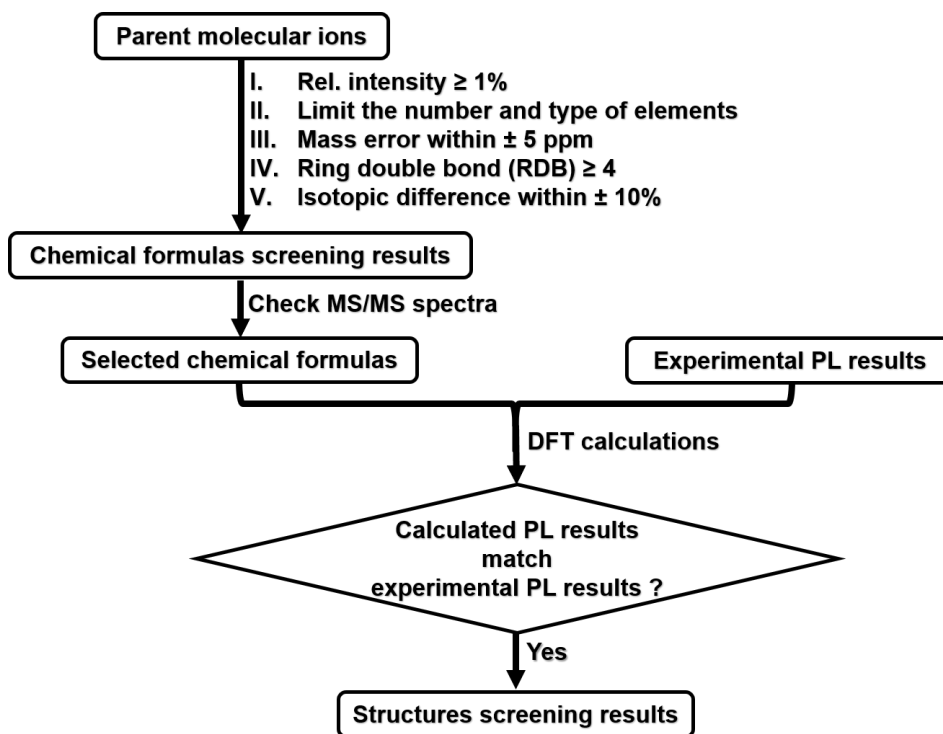


Figure 4.3. Workflow for chemical formula and structure screening of potential PAHs generated through enzymatic degradation of GO.

All the peaks that met the aforementioned criteria are summarized in Appendix Table 10. Four types of oxygen functionalities are known to exist in the GO: epoxide, hydroxyl, carbonyl,

and carboxyl groups.²⁴¹ While epoxide and carbonyl groups are expected to be detected in the positive ESI mode, hydroxyl and carboxyl groups are less sensitively detected in this positive mode.^{242, 243} Therefore, a chemical formula screening for the peaks detected in negative ionization mode (Appendix Figures 37 and 38) has also been performed using a procedure similar to that described in Figure 4.3 and the corresponding results are summarized in Appendix Table 11. In the negative-ion mode, deprotonated $[M - H]^-$ and $[M + Cl]^-$ adducts were taken into consideration. Therefore, in Step II, four types of elements, ^{12}C , 1H , ^{16}O and ^{35}Cl , were allowed. The maximum number of ^{12}C , 1H , and ^{16}O atoms remained 100, respectively, while the upper limit for maximum number of ^{35}Cl is one for a singly charged peak, two for a doubly charged peak, and so forth. Taken together the chemical formula screening results obtained in both positive and negative ionization modes are presented in Appendix Tables 10 and 11, respectively. The molecular weight of all the filtered GO biodegradation products ranged from ~150 to ~780 Da. They contained 7 to 50 carbon atoms, 4 to 80 hydrogen atoms, and 1 to 13 oxygen atoms. The carbon to oxygen (C/O) ratio varied from 1.4 to 25, comparable to the reported values of graphene-based material with different extent of oxidation.²⁴⁴⁻²⁴⁶

On the basis of the above chemical formula screening results, we proposed a mechanism of the MPO/H₂O₂/Cl⁻ enzymatic degradation of GO and generation of PAHs as described in Scheme 4.1. Here, hypochlorite (ClO⁻) and reactive radical intermediates of MPO are the two oxidants involved in biodegradation of GO.^{49, 215, 247} These two strong oxidants could play a similar role as the one reported for hydroxyl radicals.²¹⁶ They start attacking the defect sites in GO, namely those sp³ carbon atoms connected with hydroxyl and epoxide groups on the basal planes to break the C-C/C=C bonds apart (Scheme 4.1). Epoxide groups present on the basal planes of GO are particular unstable due to the unfavorable ring strain.²⁴⁸ Additionally, carbonyl groups can also

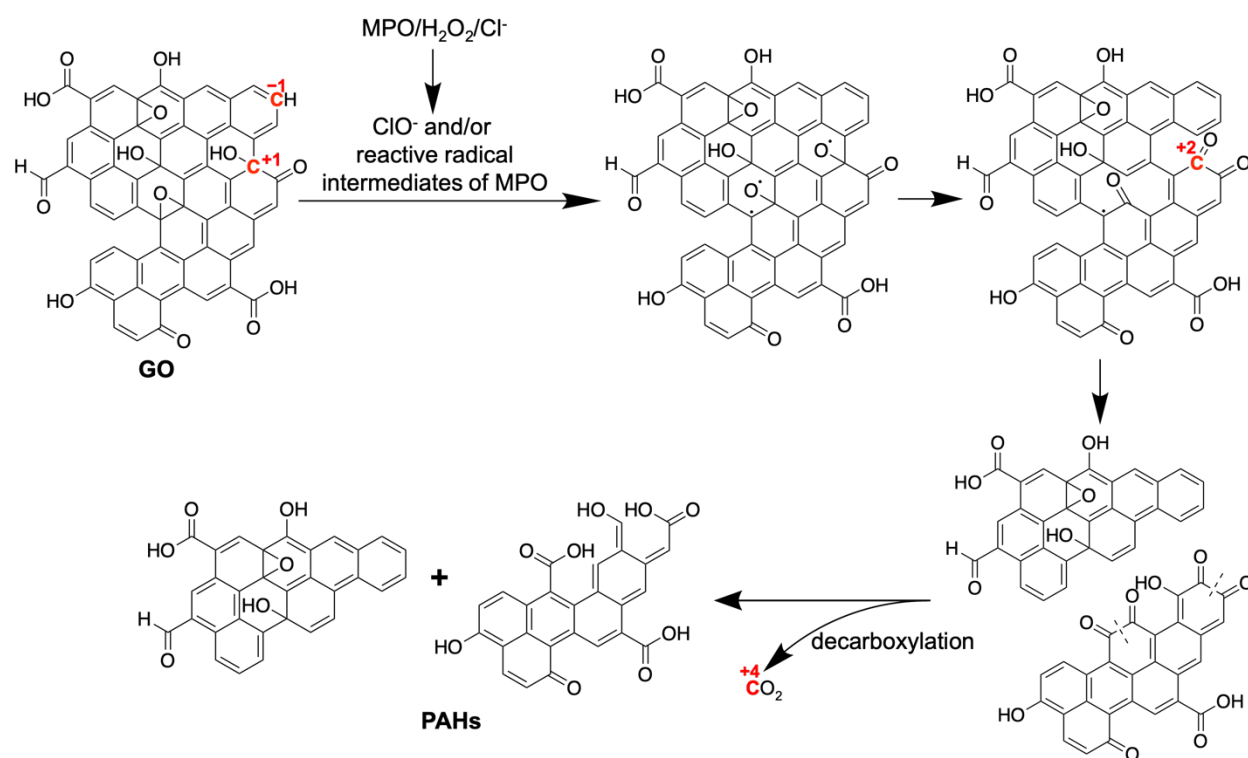
interact with ClO^- .²⁴⁷ The oxidation procedure is evidenced by an increase in the oxidation state of carbon atoms (highlighted in red in Scheme 4.1). Specifically, in the starting GO structures, the oxidation state of the hydrogenated sp^2 edge carbon atom is -1 , while the oxidation state of the in-plane sp^3 carbon connected with hydroxyl group is $+1$. During the enzymatic oxidation, the oxygen-containing functional groups can undergo further oxidation, such that the oxidation state of the carbon atom increases to $+2$, and further to $+4$ in the case of CO_2 . In these processes, different carbon-carbon bonds break thus effectively generating small sp^2 conjugated domains (usually less than 100 nm in size) in the form of PAHs that are free to fluoresce. The edges of the generated aromatic molecules should be either (partially or fully) hydrogenated or contain some oxygen functional groups. In addition, the following two processes are expected to happen during the entire degradation. First, similar to the case of carbon nanotubes,^{249, 250} it is anticipated that ClO^- could generate carboxyl and hydroxyl groups on the GO, which may serve as new degradation active sites, or ClO^- can form epoxides from terminal olefins.²⁵¹ Second, it is assumed that decarboxylation of carboxylic acid groups with formation of CO_2 could take place throughout the enzymatic oxidation.²⁴⁷

The proposed structural changes (Scheme 4.1) occurring during the enzymatic reaction have been evidenced by transmission electron microscopy (TEM, Appendix Figure 39) and Raman spectroscopy (Appendix Figure 40). Micrometer-sized GO completely disappeared after 5-days of enzymatic oxidation treatment leading to nanometer-sized degradation products (Appendix Figure 39b). The Raman spectrum of the pristine GO displays two characteristic D and G peaks, which are assigned to the sp^3 and sp^2 bonding states, respectively.²⁵² Both peaks significantly decreased after 5-day enzymatic oxidation confirming the degradation of GO. The D- to G-band intensities ratio, I_D/I_G , increases from 1.18 for pristine GO to 1.51 after enzymatic oxidation, indicating an

increased disorder in the graphitic carbon lattice. It could be reasoned that while most of the oxygenated groups are removed during the degradation, the generation of the holes within the basal planes of GO leads to discontinuity of its long-range sp^2 domains and a corresponding increase in the I_D/I_G .²⁵³

The proposed mechanism can be further supported by X-ray photoelectron spectroscopy (XPS) results (Appendix Figure 41). The quantified carbon-to-oxygen (C/O) atomic ratio was calculated based on XPS survey scan shown in Appendix Figure 41a. The increase of C/O atomic ratio from 1.94 in GO to 5.39 after 5-day degradation confirms the consumption of the oxygen-containing functional groups during the enzymatic degradation. This result is in accordance with our assumption that the oxygen-containing functional groups serve as the initial reactive sites being attacked and leading to the break of their surrounding C-C/C=C bonds. It should be noted that during the enzymatic degradation process the products are inevitably subject to different degrees of oxidation, which would consequently lead to an inhomogeneous nature of the degradation products and various C/O ratios (Appendix Tables 10 and 11). While the C/O ratio of 5.39 for the degradation products acquired using XPS characterization was obtained under the assumption of homogeneous products, the obtained value is within the range of C/O ratios obtained based on composition screening results (Appendix Tables 10 and 11) as found in LC-MS measurements and thus could represent the averaged composition property of the products. High-resolution C 1s spectra (Appendix Figure 41b) were deconvoluted into four peaks with varied proportions, corresponding to C-C/C=C in aromatic rings, C-O groups, C=O groups, and π to π^* satellite peak. After 5-day degradation, a decrease in peaks associated with oxygenated carbon was observed. The increased contribution of C-C/C=C species, compared to oxygenated carbon species as seen in C 1s spectra is also consistent with the increase of C/O atomic ratio, demonstrating that the

degraded products are less oxidized. The π - π^* satellite peak has been noticed for different chemically reduced GOs evolved upon chemical reduction of GO.^{12, 19} The appearance of π - π^* satellite contribution in the 5-day degradation products implies that the delocalized π -conjugated system was restored during the enzymatic degradation process.



Scheme 4.1. Schematic representation of the proposed mechanism for MPO/H₂O₂/Cl⁻ degradation of GO. The numbers indicated in red correspond to oxidation state of the carbon atoms.

Next, we focused on a more in-depth characterization of the obtained PAHs systems in terms of the chemical formula screening results (Appendix Tables 10 and 11). For this purpose, we have considered the case of molecular ions with specific mass-to-charge ratios m/z of 485.11 and 251.04 (Table 4.1), eluted at a retention time of 26.35 min in the positive-ion mode. In contrast to other ions that can be fragmented and can lead to diverse fragmentation patterns (Appendix Figures S42-S53, data for other peaks were not shown), the two molecular ions indicated above

can be hardly fragmented during ionization process as shown in LC-MS/MS product ion spectra (Figures 4.4a and 4.5a). As a result, it can be assumed that these two molecular ions have relative compact structures and contain extended conjugated π systems (Figure 4.4b and 4.5b), making them less susceptible to fragmentation. For these two ions, chemical formulas with the lowest mass error (Table 4.1), namely $C_{33}H_{18}O_3$ and $C_{25}H_{18}O_{10}$, were chosen. It should be noted that neither the extra hydrogen nor the sodium atoms (Figures 4.4b and 4.5b) attached to the proposed structures (with formula $C_{33}H_{18}O_3$ and $C_{25}H_{18}O_{10}$) are from the degradation product sample itself. The formation of either hydrogen or sodium cation adducts during the LC-MS analysis is due to the soft ESI ionization process as aforementioned.

Table 4.1. Possible PAHs generated by MPO/H₂O₂/Cl⁻ oxidation of GO.

Mass to charge ratio (m/z)	Experimental M+1(0.5)/M (%)	Charge (z)	Chemical formula	RDB ^a	Mass error (ppm)	Theoretical M+1(0.5)/M (%)
485.11378	39.93	1	$[C_{33}H_{18}O_3 + Na]^+$	25	-2.13	35.69
			$[C_{30}H_{22}O_4 + K]^+$	20	-2.45	32.45
251.04363	36.14	2	$[C_{25}H_{18}O_{10} + H + Na]^{2+}$	17	1.52	27.04
			$[C_{27}H_{16}O_{10} + 2H]^{2+}$	20	-3.27	29.2

^a RDB = ring double bond.

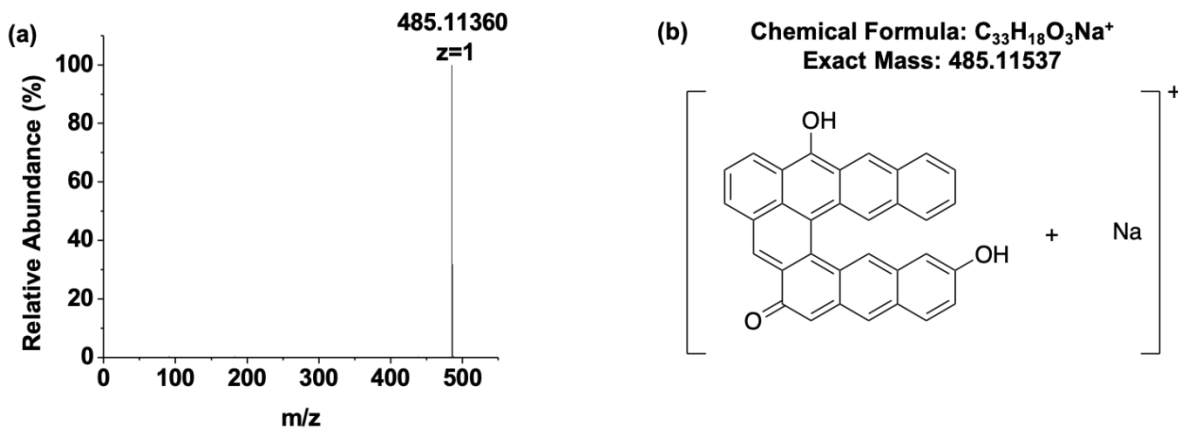


Figure 4.4. (a) LC-MS/MS product ion spectrum of the precursor ion m/z 485.11 in Table 1. (b) Tentative structure assignment.

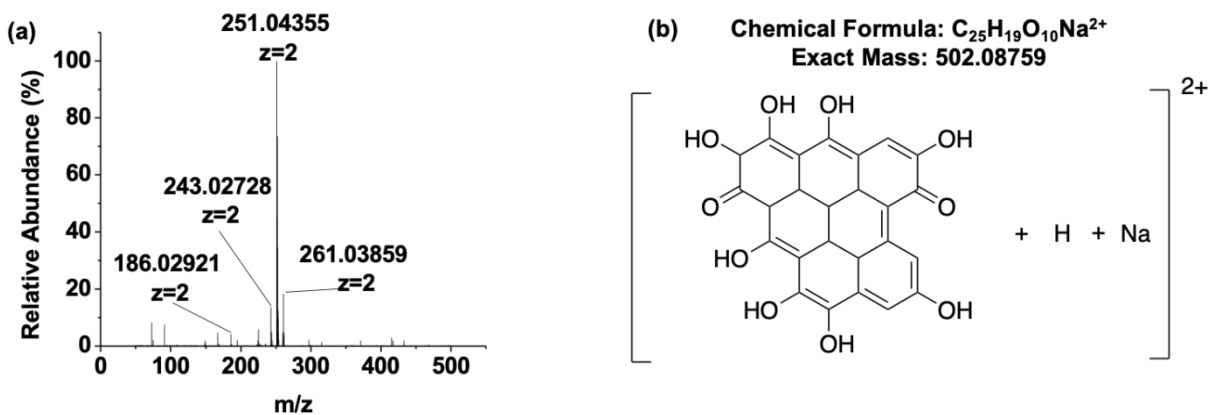


Figure 4.5. (a) LC-MS/MS product ion spectrum of the precursor ion m/z 251.04 in Table 1. (b) Tentative structure assignment.

For the resulted GO enzymatic degraded products, we have also performed an analysis of their fluorescence properties. Specifically, we found²¹⁵ that under 325 nm excitation, the degradation products have a blue fluorescence emission at 440 nm as shown in Appendix Figure

54. These spectroscopic findings impose additional electronic requirements that can be used in a structural screening process.

The information obtained from LC-MS and photoluminescence experiments has been further used to perform a theoretical screening of different molecular structures. The fundamental objective of this screening stage was to investigate if molecular systems having the same stoichiometries as those obtained in LC-MS experiments can be also responsible for the observed photoluminescence, showing in particular a blue photoluminescence in the 440 nm region under a 325 nm excitation. The structural screening has been initiated starting from the two stoichiometries $C_{33}H_{18}O_3$ and $C_{25}H_{18}O_{10}$, hereafter denoted as A and B, identified in our LC-MS experiments. Despite the apparent simplicity of these two sets of compounds, the associated chemical space of possible structural forms having these two stoichiometries is very large. In order to reduce the range of possibilities we followed a procedure consistent to the one described above for analysis of LC-MS data. Specifically, for the two A and B sets, we analyzed only the case of compact structures composed primarily from aromatic carbon rings with a high fraction of sp^2 hybridized carbon atoms. One might assume that upon enzymatic degradation, the resulted graphitic structures are primarily composed of 6-membered carbon rings but we included also the possibility that the resulted polycyclic aromatic systems can contain at most one 5- or 7-membered ring. Consistent to experimental findings, the edges of the structures are hydrogenated or contain oxygen functional groups consistent to those observed experimentally and satisfy the requirement to present ionization in a positive-ion mode. For the structures tested we have performed optimizations of the ground and electronic excited states under solvation conditions and determined the associated excitation and luminescence energies. The final selected molecular configurations have the experimentally derived stoichiometries and present UV absorption in the energy range (325 ± 20)

nm and blue luminescence in the spectral range (440 ± 20) nm, consistent to our experimental results. The ± 20 nm spread range for either absorption or emission is somewhat arbitrary and represents an estimated uncertainty interval motivated both by errors inherent to our PL experiments, for example due to selection of a 10 nm slit width, as well as by differences in spectral deviations related to the phosphate buffer saline solvent used in our experiments vs a pure water solvent used in computations. We also note that the solvent has been described in our theoretical analysis using of a polarizable continuum model^{228, 229} and such a description might not fully incorporate the complexity of real solvent clusters that might be formed at the interface with various functional oxygen groups decorating the PAHs structures.

In Figure 4.6 we summarize molecular configurations for compounds with A and B stoichiometries having absorption and fluorescence lines in the spectral ranges of interest. Additional details related to the specific electronic transitions involved in each case are detailed in Appendix Table 13. In Figure 4.6, A1-A3 and B1-B3 compounds represent systems which satisfy the general requirements imposed based on our experimental data in terms of compound stoichiometry, namely the need to be formed exclusively from 6-membered rings, to have a compact structure less susceptible to fragmentation, to have the expected oxygen or hydrogen functional groups decorating the edge carbon sites and to be characterized by optical absorption and emission energies consistent to our experimental PL measurements. Beside these systems we show that other type of molecular structures are also possible, for example compounds composed primarily from 6-membered carbon rings with one additional 5-membered ring (A4-A6, A8, A9) or a 7-membered ring (A7). Moreover, in addition to hydroxyl functional group, the systems can be decorated with ester, ether (epoxide), and/or carbonyl groups. A full list of the set of molecular configurations identified containing these groups are provided in Appendix Table 13. In addition,

in Appendix Table 14 we indicate structures containing purely hydroxyl or a mixture of hydroxyl and carboxylic groups, while satisfying the same spectroscopic limitations. Though hydroxyl and carboxyl groups are less sensitive, compared to the epoxide and carbonyl groups, to be detected in the positive ionization mode, the proposed structures shown in Appendix Table 14 are still of interest as hydroxyl and carboxyl groups could be major components in some of the degradation PAHs products.

Overall, the above results demonstrate that within the two general stoichiometries A ($C_{33}H_{18}O_3$) and B ($C_{25}H_{18}O_{10}$) identified by LC-MS measurements in the enzymatic degradation of GO, several different types of polycyclic hydrocarbon compounds having a high fraction of sp^2/sp^3 hybridized carbon and emitting blue light when excited with UV radiation can be identified, consistent to experimental results performed in this study.

A similar blue PL to the one found in this study has been reported previously in the case of chemically derived graphene oxide using hydrazine as a reducing agent.²⁵⁴ In that study, the absorbance was found to increase with hydrazine exposure time, leading to a PL intensity correlated to the amount of small sp^2 clusters formed. In particular, it was suggested²⁵⁴ that very small clusters containing only few aromatic rings should be responsible for the observed blue PL. The results reported in the current work as indicated in Figure 6 fully support these previous expectations and demonstrate that indeed, small sp^2 clusters containing only several (<10) aromatic rings, can present blue emission as observed experimentally. In contrast, based on the fact that the width of benzene is $\sim 2.8 \text{ \AA}$,²⁵⁵ the nm-sized degradation products observed under transmission electron microscopy (TEM, Appendix Figure 39b) could consist ~ 8000 benzene rings (for a ~ 20 nm particle), which make them less likely be responsible for the blue PL. In addition, using computational calculations, it was observed that in general the band gap of PAHs decreased as the

particle size increased.^{218, 256, 257} The energy gap is ~ 7 eV for a single benzene molecule and decreases to about 2 eV for systems containing about 20 aromatic rings.^{254, 258} Therefore, given the size of the observed carbonaceous degradation products, the corresponding gap is estimated to be too small to generate blue PL.

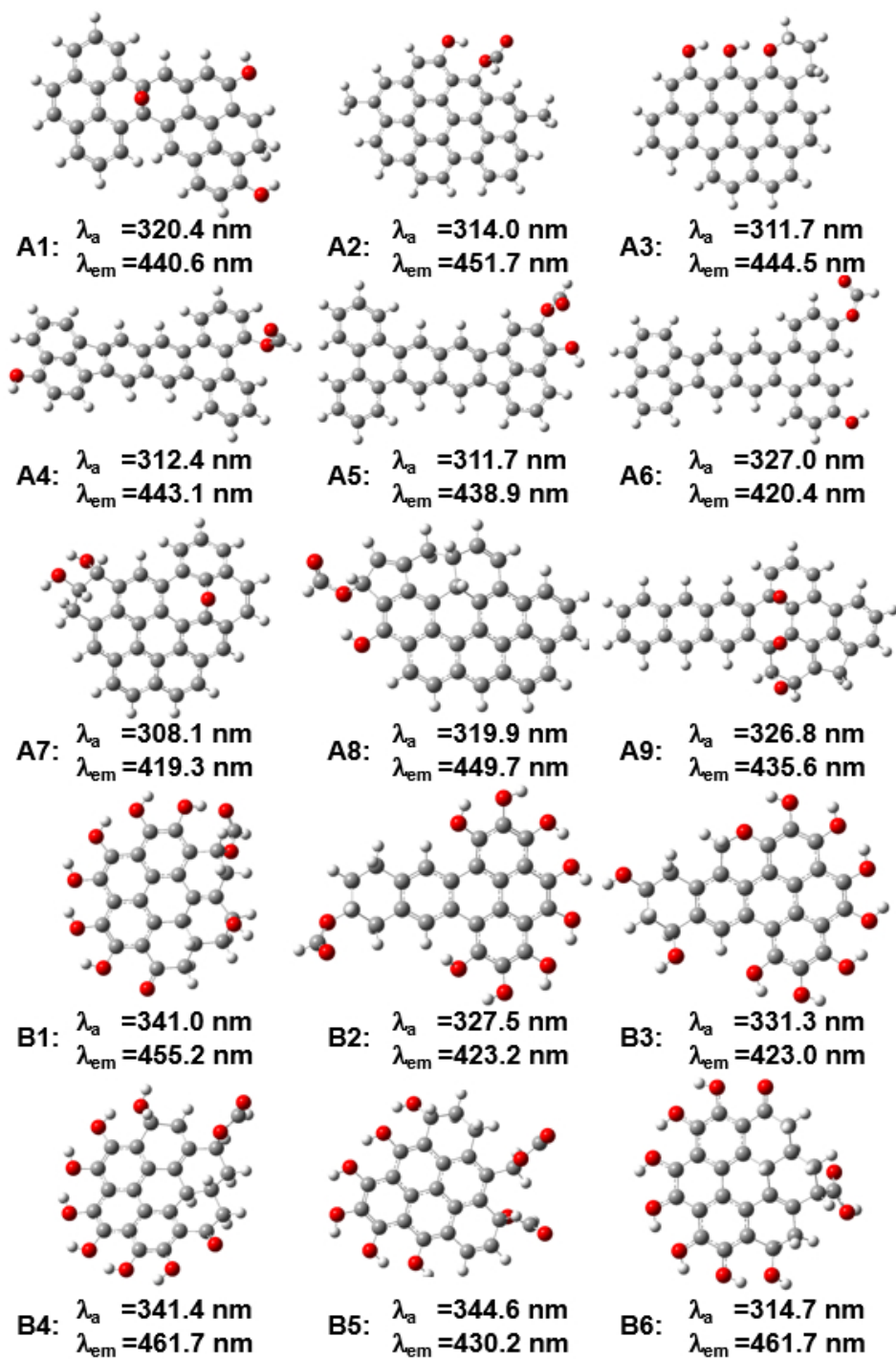


Figure 4.6. Molecular configurations with (A) $C_{33}H_{18}O_3$ and (B) $C_{25}H_{18}O_{10}$ stoichiometries. For each system the corresponding absorption vertical excitations (in the range (325 ± 20) nm) and fluorescence energies are indicated. The color scheme corresponds to C (gray), H (white) and O (red).

Compared with low-molecular-weight PAHs containing two or three rings which occur in the atmosphere, predominantly in the vapor phase, the above identified fluorescent products in the form of multi-ringed PAHs (containing more than four rings) could largely bound to particles and are in particulate phase.²⁵⁹ As majority of the high-molecular-weight PAHs are identified as carcinogenic,^{260, 261} similar to the reported DNA damage effect in the lung carcinoma cells of the enzyme-oxidized SWCNTs,²⁶² the bioaccumulation of the proposed fluorescent products from enzymatic degradation of GO could have potential toxicological concerns. Even though the GO oxidative products have been found to be non-genotoxic on bronchial epithelia cell line BEAS-2B,⁴⁸ other studies have shown that the toxicology of PAHs can depend on several factors including its functional groups,²⁶³ size,²¹⁴ dose,²⁶⁴ and metabolic activation.^{265, 266, 267}

4.1.5 Conclusions

In this work, we investigated the chemical compositions of the enzymatic oxidative products of GO, using LC-ESI-Orbitrap MS with up to 70,000 resolving power. A non-target screening workflow was developed to filter out the specific chemical formulas for the tentative PAHs products. The structures of the PAHs were proposed based on a combined use of experimental fluorescence measurements and DFT calculations. We demonstrated that polycyclic aromatic structures containing few conjugated repeating benzene units could be responsible for the observed blue PL emission. These results provide additional insight into the origin of fluorescence in GO enzymatic degradation, and can be used also as a practical method for tracking GO degradation products in biosensing and fluorescence tagging applications. The developed chemical composition and structure screening workflow could also be applicable to investigate the

fluorescence origins of GQDs generated through other oxidation methods than the enzymatic degradation considered in this work.

4.2 Quantitative Analysis of Drug Loading and Release in Carbon Nanodelivery System

4.2.1 Preface

Part of the material contained in the following Chapter was adapted with permission from *Nanoscale* 2018, 10, 17990-18000. Copyright 2018 Royal Society of Chemistry.

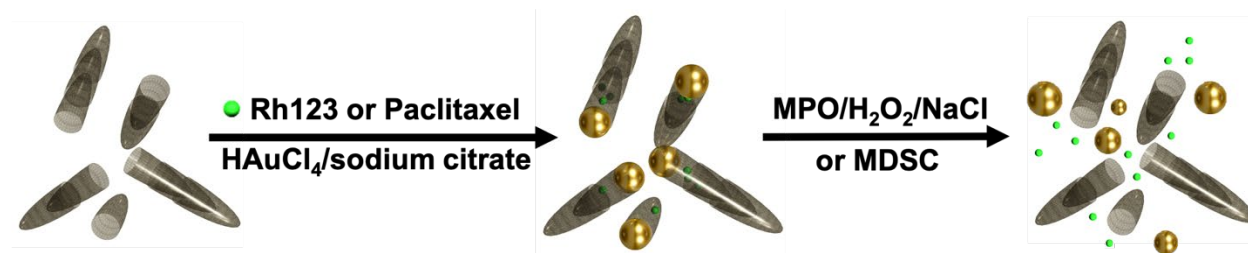
List of Authors: Seth C. Burkert, Galina V. Shurin, David L. White, Xiaoyun He, Alexandr A. Kapralov, Valerian E. Kagan, Michael R. Shurin, and Alexander Star

Authors Contributions: All authors contributed to the design of experiments and writing of the paper. S.C.B. carried out the corking and loading experiments and Au-NCNC characterization. D.L.W. performed high-resolution TEM. X.H. performed MS quantification of paclitaxel. A.A.K. and V.E.K. quantified MPO activity and peroxynitrite activity. G.V.S. and M.R.S. performed *in vivo* experiments.

4.2.2 Introduction

In response to MPO/H₂O₂/Cl⁻ enzymatic oxidation environment or myeloid-derived suppressor cells (MDSC), it has been demonstrated that gold corked NCNC (Au-NCNC) loaded with paclitaxel, a widely used chemotherapeutic, can be uncorked (Scheme 4.2) and release the drug in a controlled manner.⁵⁰ However, the drug loading and release profile in this system remains

unclear. Therefore, developing an effectively method to quantify the drug load and release would be important for the future application of Au-NCNs as an drug nanocarrier system.



Scheme 4.2. Illustration for the loading of NCNC with cargo and corking with gold nanoparticles, followed by release of cargo through incubation with enzymatic oxidation.

4.2.3 Experimental

Paclitaxel loaded Au-NCNC were suspended in 446 μL of PBS and 50 μL of water, additions of 2 μL of 2.5 g L^{-1} MPO every 6 hours and 2 μL of 25 mM H₂O₂ every hour with 12 additions a day. The samples were incubated at 37 °C for 48 hours. The resulting solutions were centrifuged at 1300g for 30 min with the supernatant (top 400 μL) being taken and the paclitaxel collected by dichloromethane (DCM) extraction. After the DCM extraction, the solvent was evaporated and the resulting residue was resuspended in 500 μL of methanol for injection into the LC-MS column. For quantification analysis, 20 μL of 0.5 mg mL^{-1} docetaxel was added as an internal standard.

Liquid chromatography was performed using a Dionex-Ultimate 3000 (Thermo Fisher Scientific). The column employed was a Luna-C18(2), 100 \times 2.0 mm length and 3 μm particle size from Phenomenex. The mobile phases used were 0.1% formic acid in water (A) and 0.1% formic acid in acetonitrile (B). An isocratic program with 50% A and 50% B was used. The flow rate was held constant at 200 $\mu\text{L min}^{-1}$ with an injection volume of 5 μL .

The LC effluent was pumped into a Q-Exactive benchtop Orbitrap-based mass spectrometer (Thermo Fisher Scientific) with electrospray ionization (ESI) held at a positive polarity. Nitrogen sheath gas and auxiliary gas flow rate were set up at 35 and 10 (arbitrary units), respectively. The capillary temperature was set at 250 °C, spray voltage was 3.5 kV and S-lens voltage set to 60 V. The instrument was operated in targeted single ion monitoring (t-SIM) by selecting the targeted compound (m/z , 854, $[M + H]^+$ for paclitaxel) and the internal standard (m/z 808, $[M + H]^+$ for docetaxel) at 70 000 resolving power and the AGC target was 1×10^6 .

4.2.4 Results and Discussion

Liquid chromatography and mass spectrometry (LC-MS) was used in order to track paclitaxel for two goals: (1) establish that paclitaxel is loaded within the interior of Au-NCNCs and is released upon incubation with MPO/H₂O₂/Cl⁻ and (2) determine the amount of the loaded paclitaxel. Successful observation of paclitaxel by LC-MS enabled quantification through comparing to an internal standard, docetaxel, and creating a calibration curve of the area ratios between the two molecules. LC-MS chromatograms of both paclitaxel and docetaxel can be seen in Appendix Figure 55. A calibration curve for quantifying paclitaxel in the $\mu\text{g mL}^{-1}$ range was constructed as observed in Appendix Figure 56. The supernatant of the corking solution after centrifugation and the resulting washes were analyzed by LC-MS to determine the amount of paclitaxel remaining in solution after the corking reaction. The initial corking solution had 100 μg of paclitaxel and the remaining supernatant and washing solutions had $64 \mu\text{g} \pm 23 \mu\text{g}$. Therefore, the amount of loaded paclitaxel to the interior of Au-NCNC is $36 \mu\text{g} \pm 23 \mu\text{g}$ resulting in a roughly 36% loading efficiency which correlates with our previously reported corking efficiency based on TEM.⁵⁰ Paclitaxel loaded Au-NCNC were incubated with MPO and H₂O₂ in PBS buffer for 0, 24,

and 48 hours. Upon completion of the MPO uncorking of the paclitaxel loaded Au-NCNC, the solution was centrifuged and the supernatant collected for paclitaxel extraction. DCM extraction was performed to collect any released paclitaxel resulting from uncorking. As a control, an empty Au-NCNC sample was also incubated with MPO and H₂O₂ for 48 hours with the same extraction performed. The amount of paclitaxel in these samples was quantified through LC-MS and the constructed calibration curve as seen in Table 4.2. At 0 hours, the area ratio of the paclitaxel is low enough that it can be assumed no paclitaxel is present. After 24 and 48 hours of incubation with MPO and H₂O₂ paclitaxel begins to be released from the cups as the released mass of paclitaxel in the solution is 0.302 µg and 0.910 µg respectively as shown in Table 4.2. The empty control sample does not show any paclitaxel indicating that no by-products of the MPO oxidation of Au-NCNC interfere with the paclitaxel quantification. These results demonstrate that paclitaxel is released slowly over time as only 3% of the loaded paclitaxel has been released after 48 hours of incubation with MPO. The hydrophobic interaction of paclitaxel with the interior of the NCNC is strong enough to require complete degradation of the NCNC for total release of paclitaxel despite the uncorking of gold occurring after 24 hours. We hypothesize that this strong interaction promotes a slow delivery of the therapeutic agent.

Table 4.2. Quantified amount of paclitaxel upon uncorking Au-NCNC.

Sample	Area ratio	Taxol release (ug)
0 hour	0.010	-
24 hours	0.088	0.302
48 hours	0.265	0.910
48 hours control	0.009	-

4.2.5 Conclusions

A quantification method using LC-MS has been developed to quantify the release of paclitaxel in NCNCs nanocarrier in response to MPO/H₂O₂/Cl⁻ enzymatic oxidative machinery. Quantified results showed that 36 µg ± 23 µg paclitaxel has been loaded into the Au-NCNC carrier with ~ 36% loading efficiency. 0.302 µg and 0.910 µg paclitaxel gradually released from the nanocarrier after 24- and 48-hours incubation, respectively. Therefore, only 3% of the loaded paclitaxel has been release after 48 hours MPO-catalyzed enzymatic oxidation.

Appendix A Supporting Information

Appendix A.1 [2 π + 2 π] Photocycloaddition of Enones to Single-Walled Carbon Nanotubes Creates Fluorescent Quantum Dots

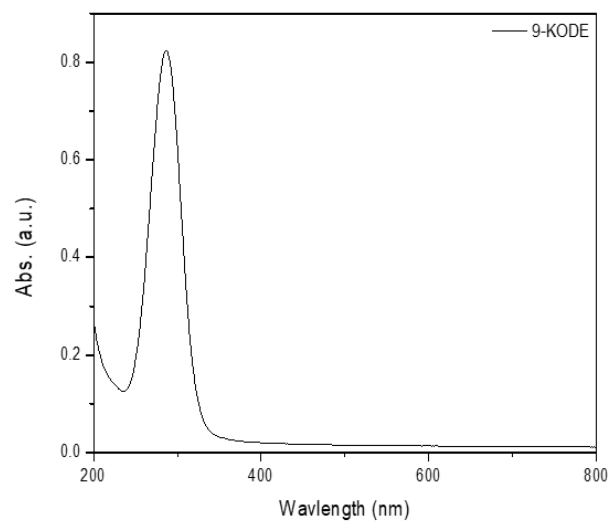
This section contains supporting information for Chapter 2.

Appendix Table 1. All compounds used for reaction with SWCNT.

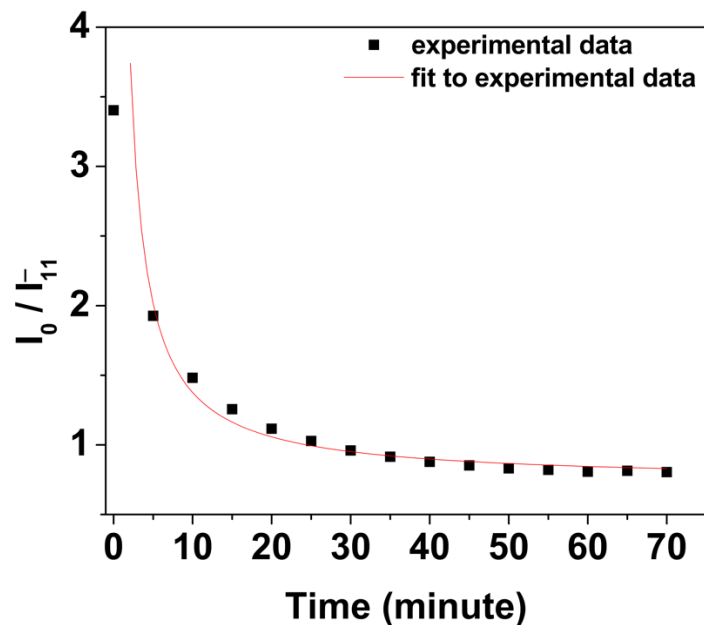
	Compound name		Molecular formula	LogP ¹	Manufacture
	IUPAC name	Synonym			
1	9-oxo-(10E,12Z)-octadecadienoic acid	9-KODE	C ₁₈ H ₃₀ O ₃	5.2	Cayman Chemical
2	9-oxo-(10E,12E)-octadecadienoic acid	9-oxoODA			
3	13-oxo-(9Z,11E)-octadecadienoic acid	13-KODE			
4	9(R)-hydroxy-(10E,12Z)-octadecadienoic acid	9R-HODE	C ₁₈ H ₃₂ O ₃	5.3	
5	9(S)-hydroxy-(10E,12Z)-octadecadienoic acid	9S-HODE			
6	13(R)-hydroxy-(9Z,11E)-octadecadienoic acid	13R-HODE			
7	13(S)-hydroxy-(9Z,11E)-octadecadienoic acid	13S-HODE			
8	(10E,12Z)-octadecadienoic acid	10E,12Z-CLA	C ₁₈ H ₃₂ O ₂	7.1	Sigma-Aldrich
9	(9Z,11E)-octadecadienoic acid	9Z,11E-CLA			
10	3-oxo-octadecanoic acid	3-oxo-stearic acid	C ₁₈ H ₃₄ O ₃	7	Cayman Chemical
11	(8Z,10E,12Z)-octadecatrienoic acid	8Z,10E,12Z-OTE	C ₁₈ H ₃₀ O ₂	6.7	
12	(9Z,11E,13E)-octadecatrienoic acid	9Z,11E,13E-OTE		6.7	
13	(9Z,11E,13Z)-octadecatrienoic acid	9Z,11E,13Z-OTE		6.4	

14	(9E,11E,13E)- octadecatrienoic acid	9E,11E,13E- OTE		6.4	
15	(9Z,11E,13E,15Z)- octadecatetraenoic acid	cis-parinaric acid	C ₁₈ H ₂₈ O ₂	5.9	
16	3-decen-2-one	-	C ₁₀ H ₁₈ O	3.4	Sigma- Aldrich
17	3-octen-2-one		C ₈ H ₁₄ O	2.3	
18	3-hepten-2-one		C ₇ H ₁₂ O	1.7	
19	2-decanone		C ₁₀ H ₂₀ O	3.7	
20	2-octanone		C ₈ H ₁₆ O	2.4	

¹ P is the octanol/water coefficient adopted from <https://pubchem.ncbi.nlm.nih.gov/>.



Appendix Figure 1. UV-vis absorption spectrum of 9-KODE in nanopure water.



Appendix Figure 2. The relation between I_0/I_{11}^- (with 566 nm excitation) and the reaction time of SWCNTs reacted with 9-KODE under 566 nm illumination. The fitted data (red line) was acquired by fitting the experimental data (black dots) with equation 1, where I_0 is the E_{11} intensity of pristine SWCNTs.

Based on a diffusion-limited exciton contact-quenching model,^{S1} following relationship has been derived,^{S2}

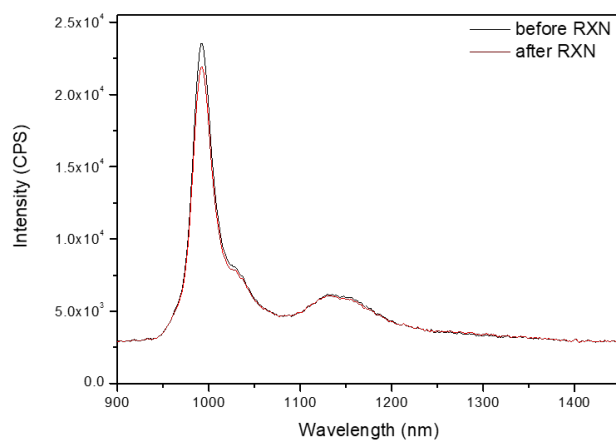
$$\frac{I_0}{I_{11}^-} = \frac{\eta_{11}}{\eta_{11}^-} \left(\frac{n_q}{k_c} \frac{1}{t} + \frac{k_p}{k_c} + 1 \right) \quad (1)$$

where I_0 and I_{11}^- are the emission intensities of unfunctionalized pristine SWCNTs E_{11} peak and functionalized SWCNTs E_{11}^- peak, respectively, η_{11} and η_{11}^- are the photoluminescence quantum yields of an exciton in the E_{11} (non-doped) and E_{11}^- states, respectively, n_q is the number of defects on the SWCNTs induced by intrinsic quenching sites, k_c is the rate constant of the light-induced reaction, t is the reaction time, and k_p is the rate constant of 9-KODE physisorption to the SWCNTs side wall.

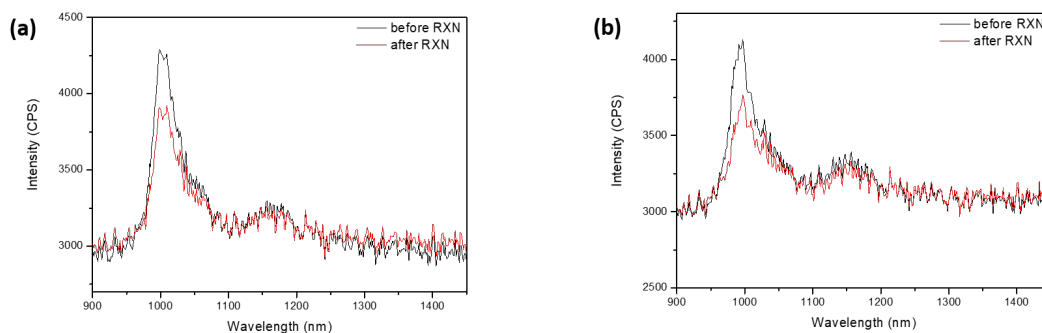
By fitting the experimental data with eq 1, the derived $\frac{\eta_{11}}{\eta_{11}} * \frac{n_q}{k_c}$ is ~ 6.4 and $\frac{\eta_{11}}{\eta_{11}} \left(\frac{k_p}{k_c} + 1 \right)$ is ~ 0.74 . The literature value of $\frac{\eta_{11}}{\eta_{11}}$ could range from smaller than $\frac{1}{18}$ S¹ to 1, S³ and n_q could range from one defect per 90 to 610 nm along SWCNTs. S⁴

Therefore, it's possible that the calculated k_c is larger than 0.28 defect/ $\mu\text{m}/\text{min}$, which result in more than 100 defects/ μm after 6-h reaction. As a result, the defect-defect distance could be sub-10 nm scale after 6-h reaction, comparable to the size of E₁₁ exciton. S⁵

This estimate would be more reliable than defect-defect distance calculations based on the experimental doping concentration of the dopant used in this study, because 9-KODE is light- and oxygen-sensitive, as well as hygroscopic. S⁶

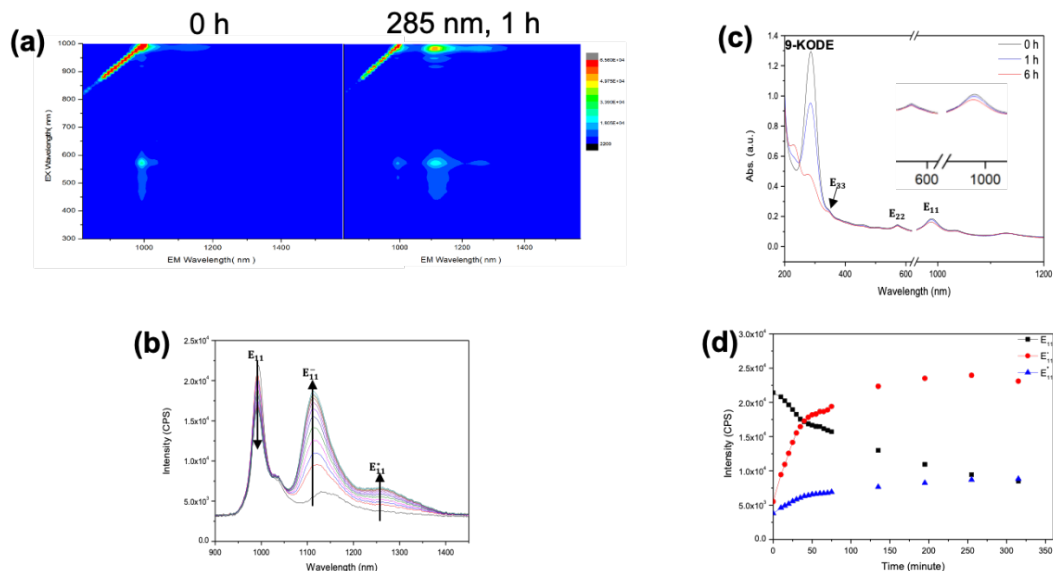


Appendix Figure 3. Fluorescent emission spectra (with 566 nm excitation) of SWCNTs (no dopants compound) before and after 1 h 566 nm illumination.



Appendix Figure 4. PL emission spectra (with 566 nm excitation) of SWCNTs and 9-KODE reaction mixture pretreated with either 250 mM ascorbic acid (a) or 250 µg/mL morin (b) before and after 1 h 566 nm illumination.

The diminished PL intensity (Appendix Figure 4) after the addition of the radical scavengers could be a result of the pH change of the reaction mixture,^{S7} which would in turn lead to the low PL quantum yield.^{S8}



Appendix Figure 5. EE maps of SWCNTs (a) before and after 1 h reaction with 9-KODE under 285 nm illumination. (b) Fluorescent emission spectra change over 1 h (spectra taken every 5 min with 566 nm excitation). (c) UV-vis-NIR absorption spectra of the reaction mixture at different time points; expanded insets show E_{11} and E_{22} absorption peaks. (d) Emission intensities of E_{11} , E_{11}^- , and E_{11}^* of SWCNTs (with 566 nm excitation) reacted with 9-KODE over 6 h.

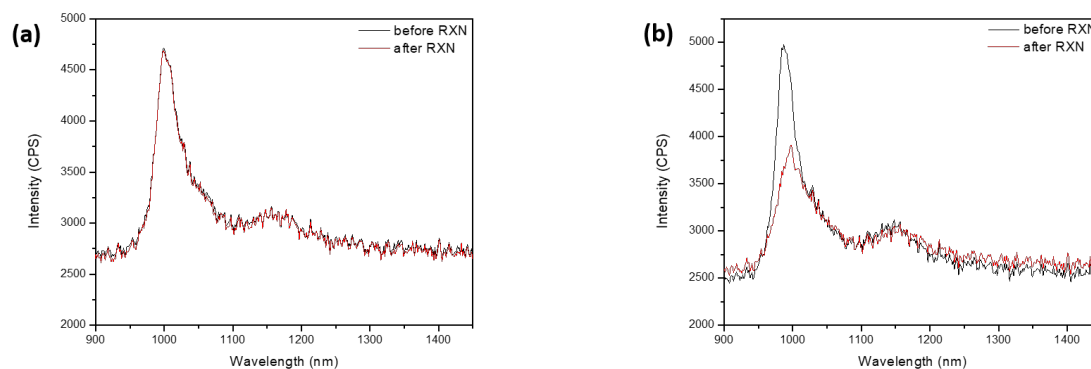
Two bright red-shifted defect-induced PL peaks, E_{11}^- at ~ 1112 nm and E_{11}^* at ~ 1255 nm, with relatively weak tails gradually appeared (Appendix Figure 5b) in the EE map (Appendix Figure 5a) after the reaction under both E_{22} and E_{11} excitation. The decline and blue-shifted UV-vis-NIR absorption peaks of 9-KODE, E_{11} , E_{22} , and E_{33} transitions of the SWCNTs further confirmed the same surface functionalization in nanotubes (Appendix Figure 5c). Kinetics studies (Appendix Figure 5d) also revealed similar trend of the evolution of the native E_{11} PL and both defect PL.

Here, though the reaction occurred in the same manner under both 566 nm and 285 nm illumination, the doping reaction proceeded at a lower rate under 285 nm irradiation. The extent

of functionalization under 285 nm at ~6 h (Appendix Figure 5d) is similar to that at ~1 h under 566 nm (Figure 2.1d).

As shown in Table 4.1, the ratio of the intensity of E_{11}^- peak with E_{11} peak after 1 h reaction was only 0.9, significantly lower than the reaction under 1 h 566 nm illumination. Besides, the characteristic absorption peak of 9-KODE at 285 nm remained after 6 h reaction (Appendix Figure 5c, red line), indicating the incomplete consumption of 9-KODE. Time-dependent evolution in Appendix Figure 5d showed that the functionalization reached optimal degree after 6-h reaction with 285 nm illumination, while SWCNTs would suffer from over-functionalization with 6-h 566 nm illumination.

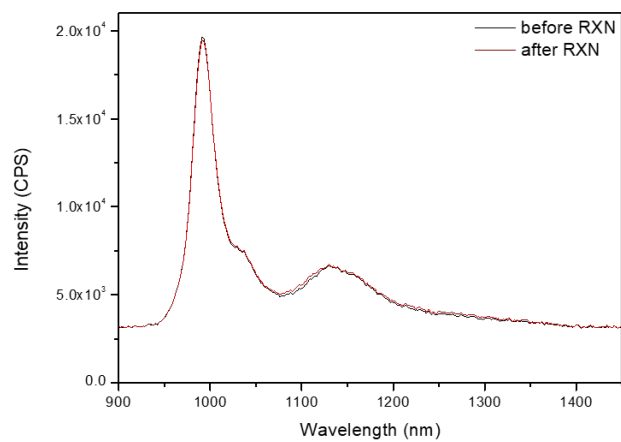
The slower reaction is a result of the lower power density (Appendix Table 2) with 285 nm illumination. Longer reaction time is needed to achieve the same extent of functionalization.



Appendix Figure 6. PL emission spectra (with 566 nm excitation) of SWCNTs and 9-KODE reaction mixture pretreated with either 250 mM ascorbic acid (a) or 250 µg/mL morin (b) before and after 1 h 285 nm illumination.

While the results in Appendix Figure 4 lead to the conclusion that the photochemical reaction is through a radical mechanism, we can not rule out the possibility that the absence of defect-induced PL could be partially due to the short-lived excited electronic states of the pH-doped SWCNTs.^{S9, S10}

Therefore, the experiments were reproduced under 1h 285 illumination as it could induce a more efficient reaction pathway (Figure 2.2b). As shown in Appendix Figure 6, no defect-PL have been evolved using both radical scavengers. These results further confirm the radical mechanism of the photochemical reaction between SWCNTs and 9-KODE.

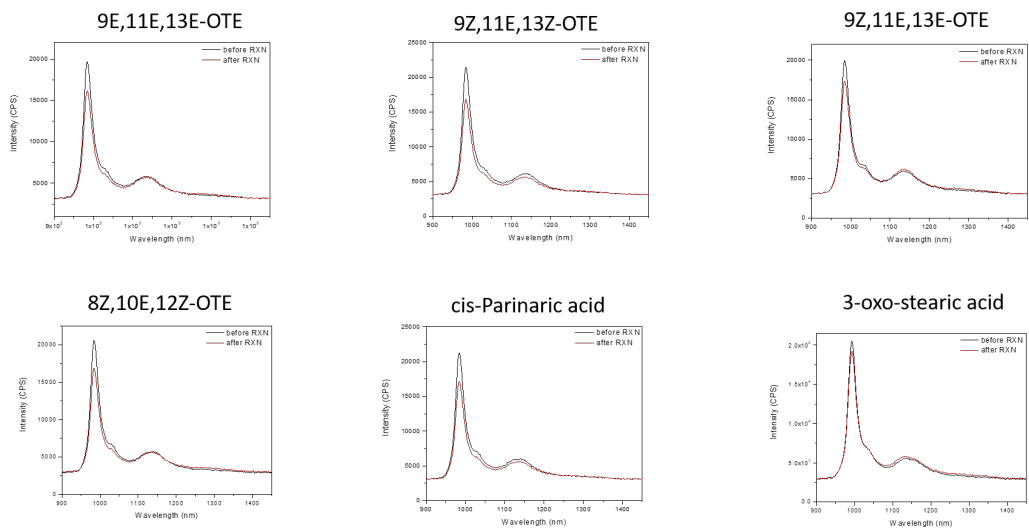


Appendix Figure 7. Fluorescent emission spectra (with 566 nm excitation) of SWCNTs and 9-KODE before and after being stored in the dark for 1 h.

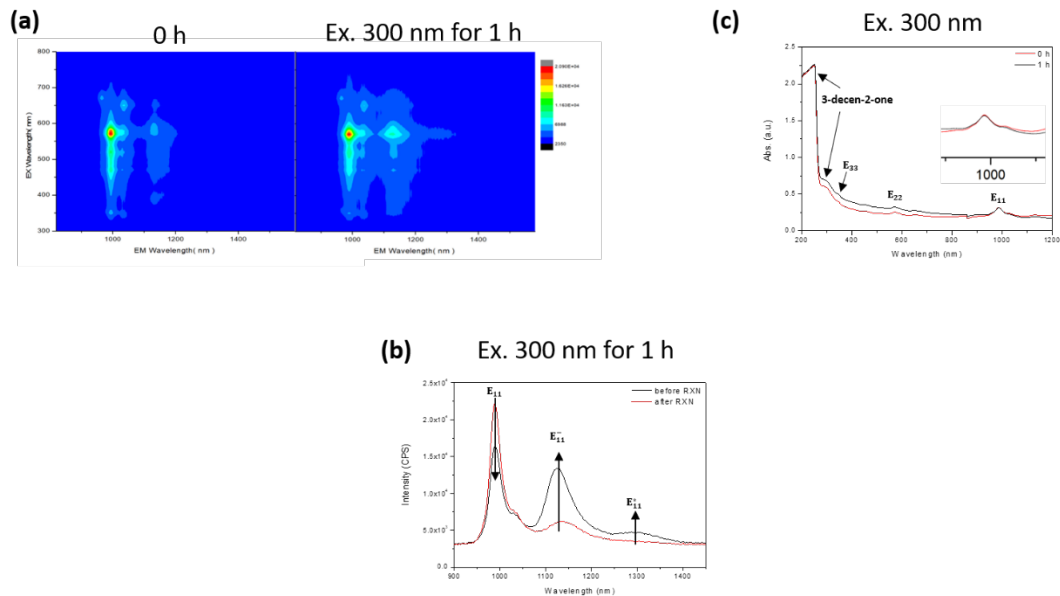
Appendix Table 2. Reaction conditions and calculations for wavelength-dependence experiment.

Wavelength (nm)	Power density (mW/cm ²)	Photon flux (# of photons per second per unit area)	ΔI_{11^-} (CPS)	Apparent quantum efficiency (AQE)	Normalized AQE ¹
285	0.12	1.72379E+18	13128	7.61578E-15	1
345	2.08	3.61694E+19	9620	2.65971E-16	0.042276051
566	6.13	1.74878E+20	19758	1.12982E-16	0.029462201
988	4.75	2.36542E+20	934	3.94855E-18	0.001797364

¹The apparent quantum efficiency (AQE) was calculated based on the change of the first defect-induced PL (ΔI_{11^-}) intensity corrected by the photon flux of the corresponding wavelength.^{S11}

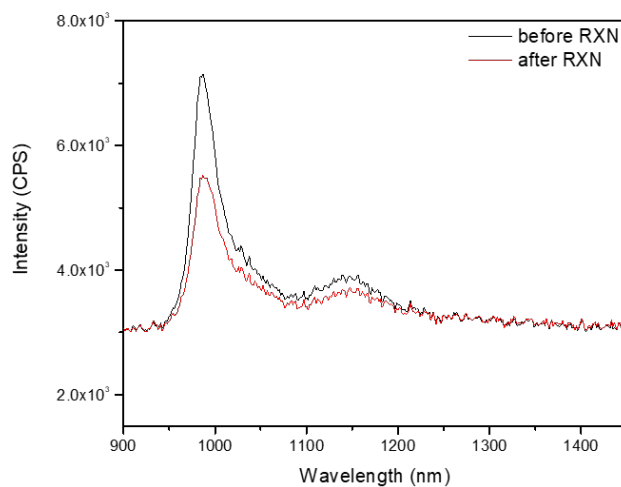


Appendix Figure 8. Fluorescent emission spectra (with 566 nm excitation) of SWCNTs and different compounds before and after 566 nm illumination for 1 h.



Appendix Figure 9. EE maps (a) and fluorescent emission spectra (b) of SWCNTs before and after 1 h reaction with 3-decen-2-one under 300 nm illumination. (c) UV-vis-NIR absorption spectra of the reaction mixture at different time points; expanded insets show E_{11} absorption feature.

Based on the similarity of PL feature of E_{11}^- peak between the 566 nm and 300 nm illumination treatment (Table 2.2), we believe the same type of defect sites formed under both conditions. However, as the energy shift does not match those generated with KODE and HODE compounds (Table 2.1), the sp^3 defects types are supposed to be different.



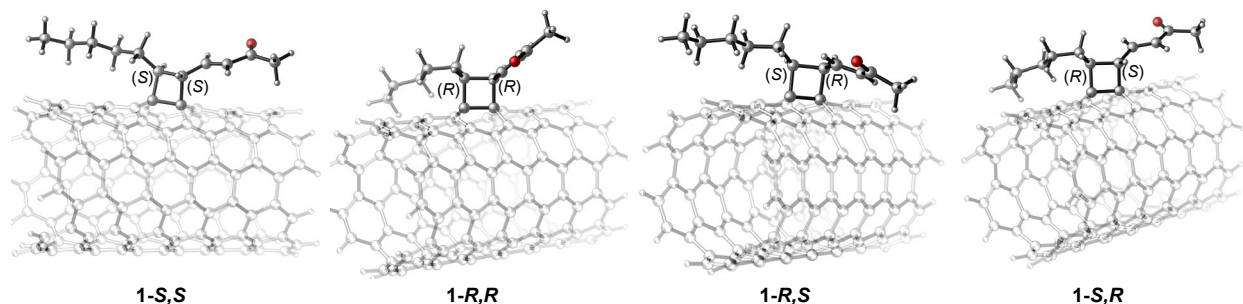
Appendix Figure 10. Fluorescent emission spectra (with 566 nm excitation) of SWCNTs and 3-hepten-2-one before and after 566 nm illumination for 1 h.

Both 3-octen-2-one and 3-hepten-2-one are more hydrophilic than 3-decen-2-one as shown by the octanol/water coefficient in Appendix Table 2, the observed lower reactivity (Table 2.2) seems contradictory with the trend shown with 18-carbon LA oxidative products (Table 2.1 and Appendix Table 1). Here, compared with hydrophilicity nature of the molecules, we believe the length of carbon chain played a more determining role on the reaction efficiency with SWCNTs.

Computational Studies

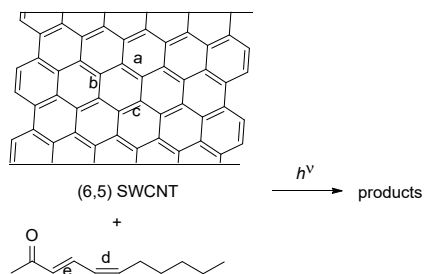
Stereoisomers of the Cycloaddition Products

Due to the inherent chirality of the (6,5) SWCNT, each $[2\pi + 2\pi]$ and $[4\pi + 2\pi]$ cycloaddition reaction can lead to the formation of 4 different stereoisomers, arising from 2 stereocenters at each newly formed carbon-carbon bond (Appendix Figures S11-S13). The reaction energy for the formation of each diastereomer was calculated using DFT, and the most stable stereoisomers were presented in Table 2.3 in the main text. The reaction energies for the less stable stereoisomers are listed in Appendix Tables 3-5.

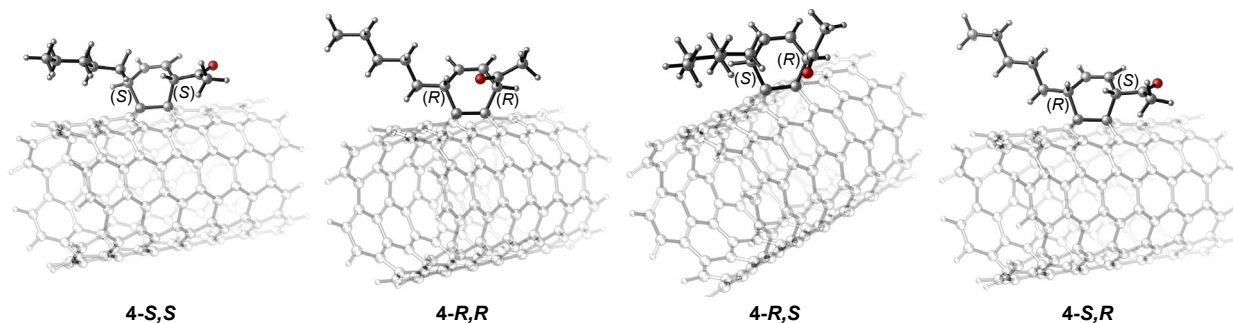


Appendix Figure 11. Three dimensional structures of different diastereomers in the $[2\pi(a) + 2\pi(d)]$ (1) cycloaddition reaction with (3E,5Z)-undecadien-2-one.

Appendix Table 3. Computed reaction energies for different diastereomeric products of $[2\pi + 2\pi]$ cycloaddition. All energies are Gibbs free energies (in kcal/mol) with respect to the photoexcited SWCNT with 566 nm light and the substrate ((3E,5Z)-undecadien-2-one). The most stable diastereomers in the reactions with each type of C=C bond on the SWCNT are shown in bold.



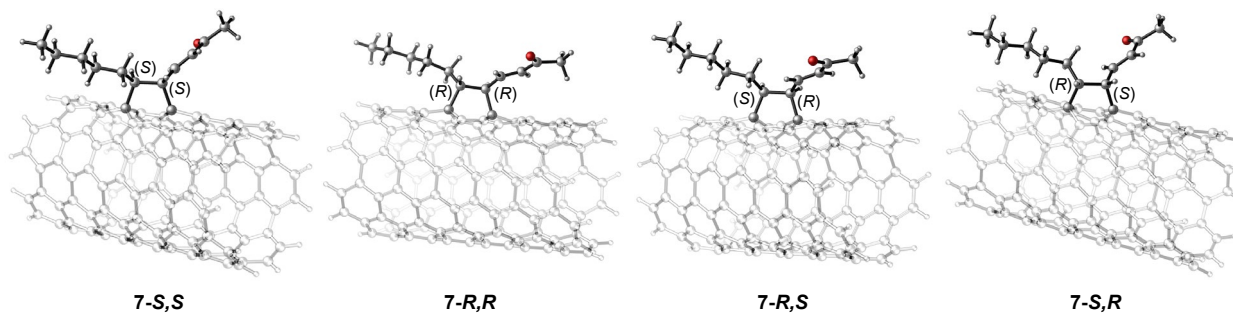
	C5-(<i>S</i>)/C6-(<i>S</i>)	C5-(<i>R</i>)/C6-(<i>R</i>)	C5-(<i>S</i>)/C6-(<i>R</i>)	C5-(<i>R</i>)/C6-(<i>S</i>)
$[2\pi(a) + 2\pi(d)]$ (1)	-19.5 (1-SS)	-14.9 (1-RR)	-14.6	-16.2
$[2\pi(b) + 2\pi(d)]$ (2)	-15.5	-16.0	-14.1	-12.8
$[2\pi(c) + 2\pi(d)]$ (3)	-13.2	-18.4	-16.3	-13.9



Appendix Figure 12. Three dimensional structures of different diastereomers in $[2\pi(a) + 4\pi(de)]$ (4) cycloaddition reaction with (3E,5Z)-undecadien-2-one.

Appendix Table 4. Computed reaction energies for different diastereomeric products of $[2\pi + 4\pi]$ cycloaddition. All energies are Gibbs free energies (in kcal/mol) with respect to the photoexcited SWCNT with 566 nm light and the substrate ((3E,5Z)-undecadien-2-one). The most stable diastereomers in the reactions with each type of C=C bond on the SWCNT are shown in bold.

	C3-(<i>S</i>)/C6-(<i>S</i>)	C3-(<i>R</i>)/C6-(<i>R</i>)	C3-(<i>S</i>)/C6-(<i>R</i>)	C3-(<i>R</i>)/C6-(<i>S</i>)
$[2\pi(a) + 4\pi(de)]$ (4)	-9.6	-9.1	-9.2	-8.7
$[2\pi(b) + 4\pi(de)]$ (5)	-8.8	-8.2	-3.8	-11.3
$[2\pi(c) + 4\pi(de)]$ (6)	-7.8	-5.4	-7.6	-4.5



Appendix Figure 13. Three dimensional structures of different diastereomers in $[4\pi(ab) + 2\pi(d)]$ (7) cycloaddition reaction with (3E,5Z)-undecadien-2-one.

Appendix Table 5. Computed reaction energies for different diastereomeric products of $[4\pi + 2\pi]$ cycloaddition. All energies are Gibbs free energies (in kcal/mol) with respect to the photoexcited SWCNT with 566 nm light and the substrate ((3E,5Z)-undecadien-2-one). The most stable diastereomers in the reactions with each type of C=C bond on the SWCNT are shown in bold.

	C5-(<i>S</i>)/C6-(<i>S</i>)	C5-(<i>R</i>)/C6-(<i>R</i>)	C5-(<i>S</i>)/C6-(<i>R</i>)	C5-(<i>R</i>)/C6-(<i>S</i>)
$[4\pi(ab) + 2\pi(d)]$ (7)	-9.6	-8.4	-7.2	-7.1
$[4\pi(ac) + 2\pi(d)]$ (8)	50.2	N/A ^a	N/A ^a	N/A ^a
$[4\pi(bc) + 2\pi(d)]$ (9)	-1.4	-2.3	-0.2	0.5

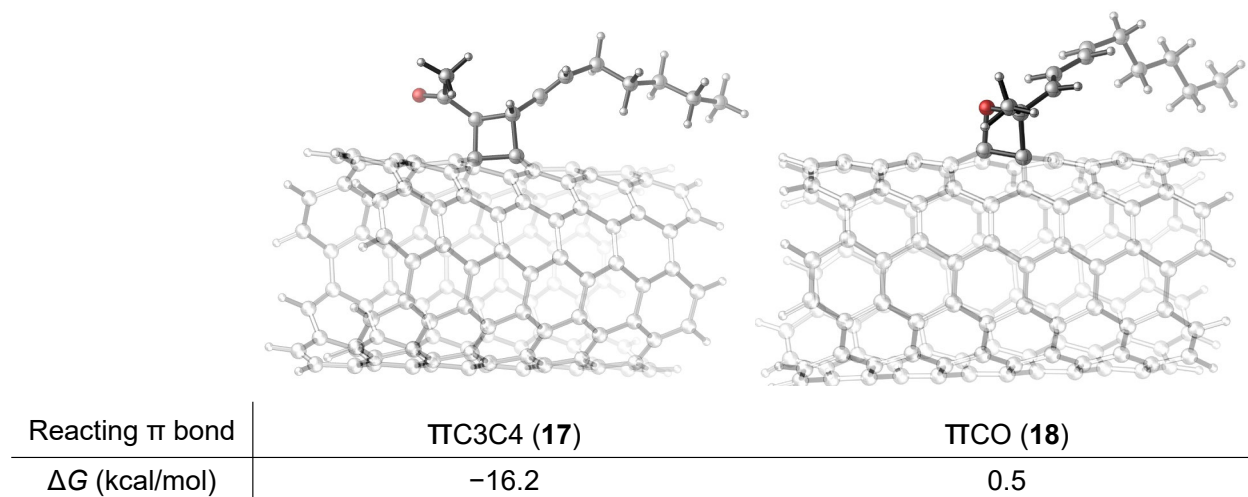
^a The product could not be optimized.

To better understand the origin of the differences in the stability of different stereoisomers, we farther analyzed the relative stabilities of products **1-SS** and **1-RR** (Appendix Table 3). Both addition products are trans stereoisomers, therefore, their relative stabilities should be attributed to the substrate-nanotube interactions and not steric repulsions between the alkenyl and alkyl substituents on the four-membered ring. In **1-SS**, the alkenyl and alkyl substituent groups both align parallel to the axis of the nanotube (Appendix Figure 11), which leads to the improved dispersion interactions between the nanotube and the substituents on the substrate. On the other hand, the substituents in **1-RR** are positioned perpendicular to the nanotube axis (Appendix Figure 11). Therefore, the favorable dispersion interactions are diminished in this product. To support this hypothesis, we calculated the dispersion interactions between the substituents and the nanotube in **1-RR** ($\Delta E_{\text{disp}} = -20.8$ kcal/mol), which is 2.7 kcal/mol lower than the dispersion interaction between the substituents and the nanotube in **1-SS** ($\Delta E_{\text{disp}} = -23.6$ kcal/mol, Figure 4.4) and mostly accounts for the difference in the stability of these two products. Additional source of the

difference could be accounted to the curvature of the alkyl chain in **1-RR** around the nanotube, whereas alkyl chain in **1-SS** has a more linear structure.

Substrate Regioselectivity

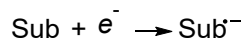
(3E,5Z)-undecadien-2-one has three distinct π bonds that could engage in cycloaddition. Therefore, $[2\pi + 2\pi]$ cycloaddition products with the internal alkene and the carbonyl group were also calculated (Appendix Figure 12). Our calculations indicate that the most favorable addition occurs with the terminal C5=C6 double bond. The addition to the internal π bond (**17**, $\Delta G = -16.2$ kcal/mol) is disfavored by 3.3 kcal/mol when compared to the most favorable product **1-SS** ($\Delta G = -19.5$ kcal/mol), which corresponds to the energy of the broken enone conjugation. The addition of the carbonyl (**18**, $\Delta G = 0.5$ kcal/mol) is disfavored by 20.0 kcal/mol, which can be attributed to the less favorable cleavage of the carbonyl π bond, relative to a weaker C=C π bond.^{S12}



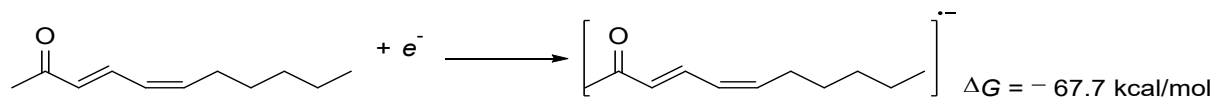
Appendix Figure 14. Energies and 3D structures of $[2\pi + 2\pi]$ cycloaddition of (3E,5Z)-undecadien-2-one to the SWCNT with other π bonds. All energies are in kcal/mol. All energies are Gibbs free energies (in kcal/mol) with respect to the photoexcited SWCNT with 566 nm light and the substrate ((3E,5Z)-undecadien-2-one).

Reduction Potential Calculation

The reduction potential of the substrates in Table 2.4 were calculated from the reaction Gibbs free energies of the following reduction half-reaction:



For example, to calculate the reduction of (3E,5Z)-undecadien-2-one, the reaction Gibbs free energy of the following half reaction was calculated from DFT-computed Gibbs free energies of the substrate and the corresponding radical anion at the PBE-D3/6-311++G(d,p)/SMD(water)//PBE-D3/3-21G level of theory, and the Gibbs free energy of an electron (-0.867 kcal/mol).^{S13}



With

$$\Delta G = -nFE$$

Gibbs free energy can be converted to the absolute standard reduction potential

$$E = 2.94 \text{ V}$$

Then the standard potential referenced to the SCE can be calculated from the following equation:^{S14}

$$E_{\text{solvent}}^{\ominus, \text{SCE}} = E_{\text{solvent}}^{\ominus, \text{abs}} - E_{\text{SCE, aq}}^{\text{abs}} = 2.94 - 4.522 = -1.58 \text{ V}$$

where $E_{SCE,aq}^{abs}$ is the absolute standard potential for the aqueous saturated calomel electrode (4.522 V).

Appendix Table 6. Comparison of Gibbs free energies of key cycloadducts using different level of theory for the single point calculation. All energies are in kcal/mol relative to (6,5)-SWCNT and (3E,5Z)-undecadien-2-one.

Structure	Method for Single Point Energy Calculation	
	PBE-D3/6-31G(d)	B3LYP-D3/6-31G(d)
(6,5)-SWCNT	0.0	0.0
1-SS	-19.5	-14.0
2-RR	-16.0	-9.5
5-RS	-11.3	-5.0

Both PBE-D3 and B3LYP-D3 were used for single point energy calculations of several [2+2] and [4+2] cycloaddition products. These results show that while the B3LYP-D3 method systematically underestimates the exergonicity of the reaction by a few kcal/mol, the relative energies between the [2+2] and [4+2] products remain unchanged. The [2+2] cycloadduct (**1-SS**) is still the most stable in terms of Gibbs free energies. Therefore, the conclusions drawn from the calculations are not affected by the choice of the functional. A pure DFT functional PBE-D3 was used to for the rest of the study, because of the better efficiency.

Appendix Table 7. Comparison of electronic energies of key cycloadducts using different nanotube length. All energies are in kcal/mol relative to (6,5)-SWCNT and (3E,5Z)-undecadien-2-one.

Structure	Modeled nanotube length	
	15 Å	50 Å
(6,5)-SWCNT	0.0	0.0
1-SS	-37.2	-40.5
2-RR	-33.4	-35.8
5-RS	-30.3	-32.5

To evaluate whether the use of a 15 Å model nanotube would affect the computed reaction energies, we compared the reaction electronic energies (ΔE) of several key [2+2] and [4+2] cycloaddition products computed using both 15 Å and 50 Å length nanotubes in geometry optimization and single point energy calculations (Appendix Table 7). The reaction Gibbs free energies could not be obtained with the larger 50 Å model because the vibrational frequency calculations become too expensive. These results show that while the use of shorter nanotube systematically underestimates the exothermicity of the reaction by 2-3 kcal/mol, the relative energies between the [2+2] and [4+2] products remain unchanged. The [2+2] cycloadduct (**1-SS**) is still the most stable in terms of electronic energies. Therefore, the conclusions drawn from the calculations are not affected by the choice of the length of the nanotube model.

Energies of All Computed Structures

Cartesian coordinates of all computed structures (ref. S15) are provided in a separate file in .xyz format.

Appendix Table 8. Energies of all computed structures.

	PBE-D3/6-31G(d)-SMD(H ₂ O)//PBE-D3/3-21G		
	E (a.u.)	H (a.u.)	G (a.u.)
10	-5192.654024	-5191.49039	-5191.640763
11	-5192.653337	-5191.490274	-5191.640964
12	-5269.964481	-5268.764992	-5268.918662
13	-5269.961552	-5268.762302	-5268.915838
14	-5619.915776	-5618.5073	-5618.687284
15	-5544.768494	-5543.364277	-5543.543211
16	-5621.133959	-5619.700378	-5619.880696
17	-5618.725532	-5617.340343	-5617.520437
18	-5618.697966	-5617.313473	-5617.493827
1-RR	-5618.722507	-5617.336635	-5617.518313
1-RS	-5618.722979	-5617.337238	-5617.517937
1-SR	-5618.725279	-5617.339749	-5617.520459
1-SS	-5618.730077	-5617.344613	-5617.525615
2-RR	-5618.724135	-5617.338829	-5617.520146
2-RS	-5618.719209	-5617.33411	-5617.514998
2-SR	-5618.720884	-5617.335559	-5617.517149

2-SS	-5618.722967	-5617.337637	-5617.519301
2-undecanone	-506.9746047	-506.6503284	-506.7139984
3-RR	-5618.728507	-5617.343074	-5617.523902
3-RS	-5618.724921	-5617.339253	-5617.52065
3-SR	-5618.722258	-5617.336505	-5617.516828
3-SS	-5618.719914	-5617.334429	-5617.515721
4-RR	-5618.715938	-5617.329553	-5617.509138
4-RS	-5618.717161	-5617.331043	-5617.508499
4-SR	-5618.716343	-5617.33052	-5617.50933
4-SS	-5618.719184	-5617.333146	-5617.509956
5-RR	-5618.717347	-5617.331433	-5617.508615
5-RS	-5618.720386	-5617.334753	-5617.512564
5-SR	-5618.709836	-5617.323665	-5617.500595
5-SS	-5618.716355	-5617.330274	-5617.507626
(6,5)-SWCNT	-5114.203681	-5113.098152	-5113.244697
6-RR	-5618.716199	-5617.330194	-5617.507056
6-RS	-5618.710952	-5617.325204	-5617.501732
6-SR	-5618.715941	-5617.329762	-5617.506776
6-SS	-5618.712122	-5617.325856	-5617.503276
7-RR	-5618.715013	-5617.328839	-5617.508035
7-RS	-5618.710823	-5617.324687	-5617.505907
7-SR	-5618.711997	-5617.32567	-5617.506027
7-SS	-5618.713013	-5617.326753	-5617.509914

8	-5618.618947	-5617.234021	-5617.414597
9-RR	-5618.700756	-5617.314827	-5617.498204
9-RS	-5618.699397	-5617.313268	-5617.493798
9-SR	-5618.698946	-5617.313122	-5617.49501
9-SS	-5618.70276	-5617.316868	-5617.496875
2-hydroxy-(3E,5Z)- undecadiene	-505.7248725	-505.4251141	-505.4862091
(3E,5Z)-undecadiene	-430.580825	-430.285185	-430.34385
(3E,5Z)-undecadien-2-one	-504.5476608	-504.2703743	-504.3303943
(6,5)-SWCNT (50 Å)	- 16992.192938		
1-SS (50 Å)	- 17496.724688		
2-RR (50 Å)	- 17496.717157		
5-RS (50 Å)	- 17496.711954		

References

S1. Miyauchi, Y.; Iwamura, M.; Mouri, S.; Kawazoe, T.; Ohtsu, M.; Matsuda, K. Brightening of Excitons in Carbon Nanotubes on Dimensionality Modification. *Nat. Photonics* **2013**, *7*, 715-719.

- S2. Wu, X.; Kim, M.; Kwon, H.; Wang, Y. Photochemical Creation of Fluorescent Quantum Defects in Semiconducting Carbon Nanotube Hosts. *Angew. Chem. Int. Ed.* **2018**, *57*, 648-653.
- S3. Piao, Y.; Meany, B.; Powell, L. R.; Valley, N.; Kwon, H.; Schatz, G. C.; Wang, Y. Brightening of Carbon Nanotube Photoluminescence through the Incorporation of sp^3 Defects. *Nat. Chem.* **2013**, *5*, 840-845.
- S4. Hertel, T.; Himmelein, S.; Ackermann, T.; Stich, D.; Crochet, J. Diffusion Limited Photoluminescence Quantum Yields in 1-D Semiconductors: Single-Wall Carbon Nanotubes. *ACS Nano* **2010**, *4*, 7161-7168.
- S5. Lüer, L.; Hoseinkhani, S.; Polli, D.; Crochet, J.; Hertel, T.; Lanzani, G. Size and Mobility of Excitons in (6, 5) Carbon Nanotubes. *Nat. Phys.* **2009**, *5*, 54-58.
- S6. Cayman Chemical. 9-OxoODE. <https://www.caymanchem.com/product/38420/9-oxoode>. (accessed January 05, 2021)
- S7. Strano, M. S.; Huffman, C. B.; Moore, V. C.; O'Connell, M. J.; Haroz, E. H.; Hubbard, J.; Miller, M.; Rialon, K.; Kittrell, C.; Ramesh, S.; Hauge, R. H.; Smalley, R. E. Reversible, Band-Gap-Selective Protonation of Single-Walled Carbon Nanotubes in Solution. *J. Phys. Chem. B* **2003**, *107*, 6979-6985.
- S8. Larsen, B. A.; Deria, P.; Holt, J. M.; Stanton, I. N.; Heben, M. J.; Therien, M. J.; Blackburn, J. L. Effect of Solvent Polarity and Electrophilicity on Quantum Yields and Solvatochromic Shifts of Single-Walled Carbon Nanotube Photoluminescence. *J. Am. Chem. Soc.* **2012**, *134*, 12485-12491.
- S9. O'Connell, M. J.; Bachilo, S. M.; Huffman, C. B.; Moore, V. C.; Strano, M. S.; Haroz, E. H.; Rialon, K. L.; Boul, P. J.; Noon, W. H.; Kittrell, C.; Ma, J.; Hauge, R. H.; Weisman, R. B.; Smalley,

R. E. Band Gap Fluorescence from Individual Single-Walled Carbon Nanotubes. *Science* **2002**, *297*, 593-596.

S10. Dukovic, G.; White, B. E.; Zhou, Z.; Wang, F.; Jockusch, S.; Steigerwald, M. L.; Brus, L. E. Reversible Surface Oxidation and Efficient Luminescence Quenching in Semiconductor Single-Wall Carbon Nanotubes. *J. Am. Chem. Soc.* **2004**, *126*, 15269-15276.

S11. Powell, L. R.; Piao, Y.; Wang, Y. Optical Excitation of Carbon Nanotubes Drives Localized Diazonium Reactions. *J. Phys. Chem. Lett.* **2016**, *7*, 3690-3694.

S12. Dean, J. A. Lange's Handbook of Chemistry. McGraw-Hill, New York, 1998.

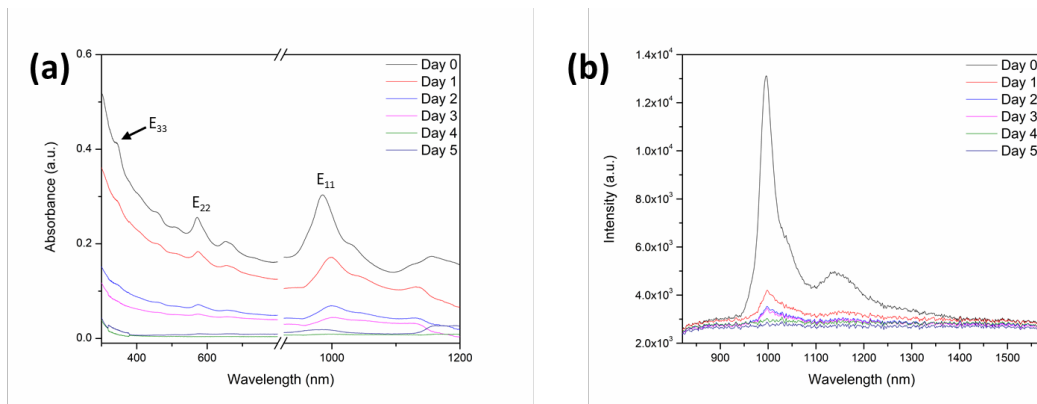
S13. Bartmess, J. E. Thermodynamics of the Electron and the Proton. *J. Phys. Chem.* **1994**, *98*, 6420-6424.

S14. Isse, A. A.; Gennaro, A. Absolute Potential of the Standard Hydrogen Electrode and the Problem of Interconversion of Potentials in Different Solvents. *J. Phys. Chem. B* **2010**, *114*, 7894-7899.

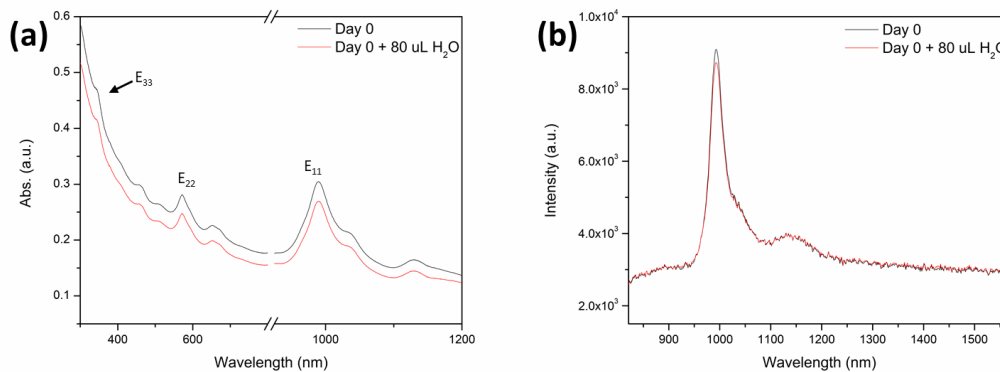
S15. Calculated coordinates are included seperately.

Appendix A.2 Photoluminescence Response in Carbon Nanomaterials to Enzymatic Degradation

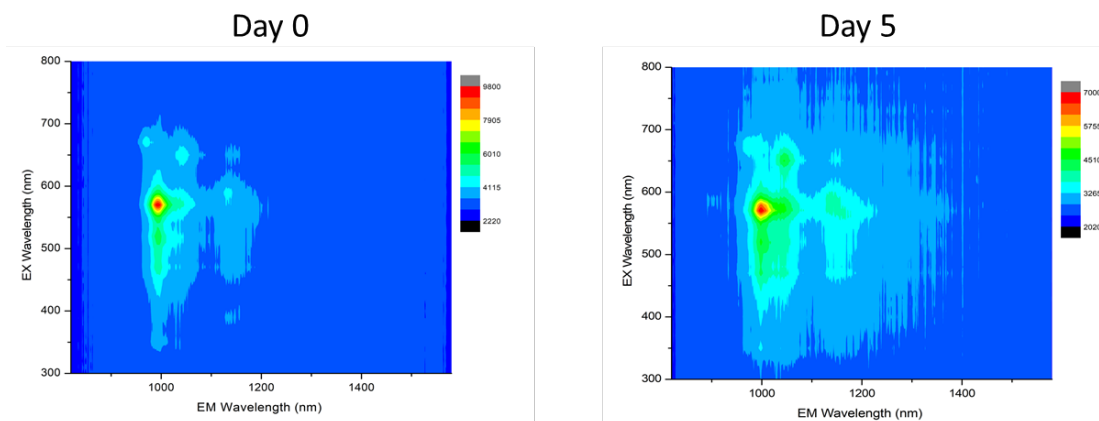
This section contains supporting information for Chapter 3.



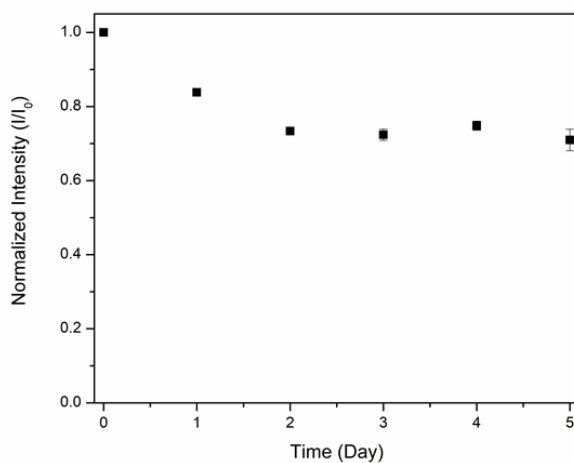
Appendix Figure 15. UV-vis-NIR absorption spectra (a) and PL emission spectra (b) of MPO/H₂O₂/Cl⁻ degradation of SWCNT (SC) from Day 0 to Day 5.



Appendix Figure 16. UV-vis-NIR absorption spectra (a) and PL emission spectra (b) of SWCNT(CMC) before and after dilution with H₂O.

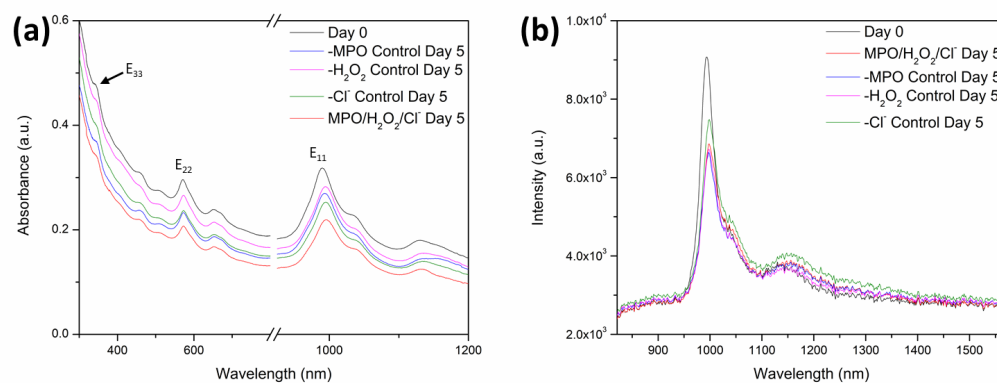


Appendix Figure 17. EE maps of SWCNT (CMC) before and after 5-day MPO/H₂O₂/Cl⁻ degradation.

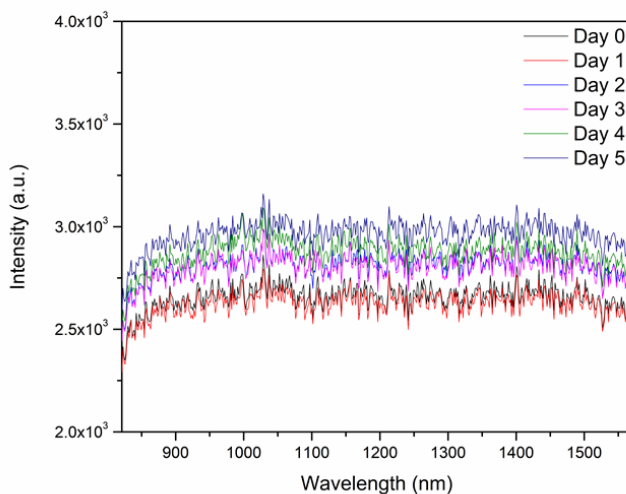


Appendix Figure 18. The normalized PL intensity of SWCNT(CMC) over 5-day MPO/H₂O₂/Cl⁻ degradation.

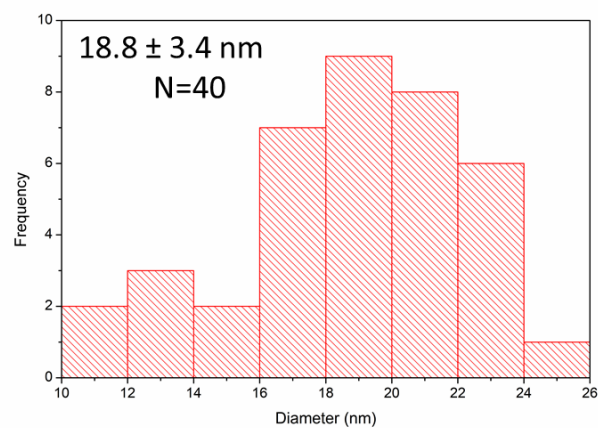
The error bars represent standard deviations based on three replicate measurements.



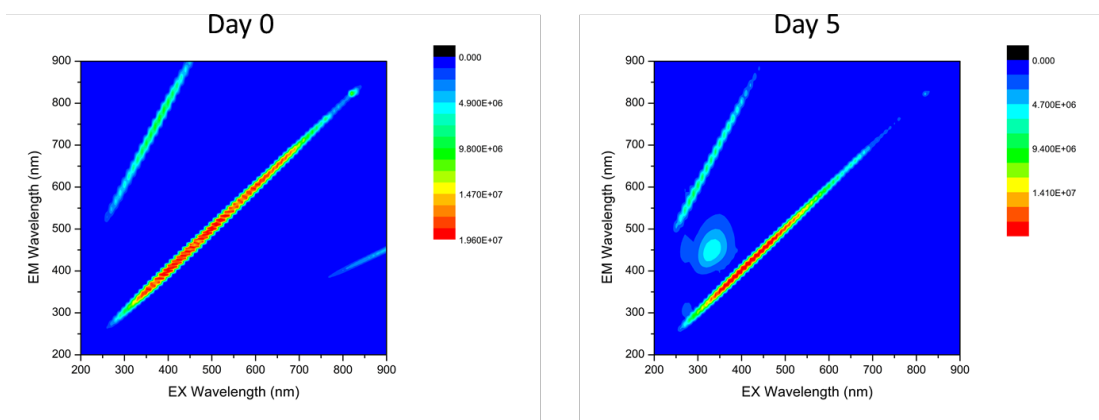
Appendix Figure 19. UV-vis-NIR absorption spectra (a) and PL emission spectra (b) of SWCNT(CMC) before and after 5-day MPO/H₂O₂/Cl⁻ degradation without MPO, H₂O₂, and Cl⁻, respectively.



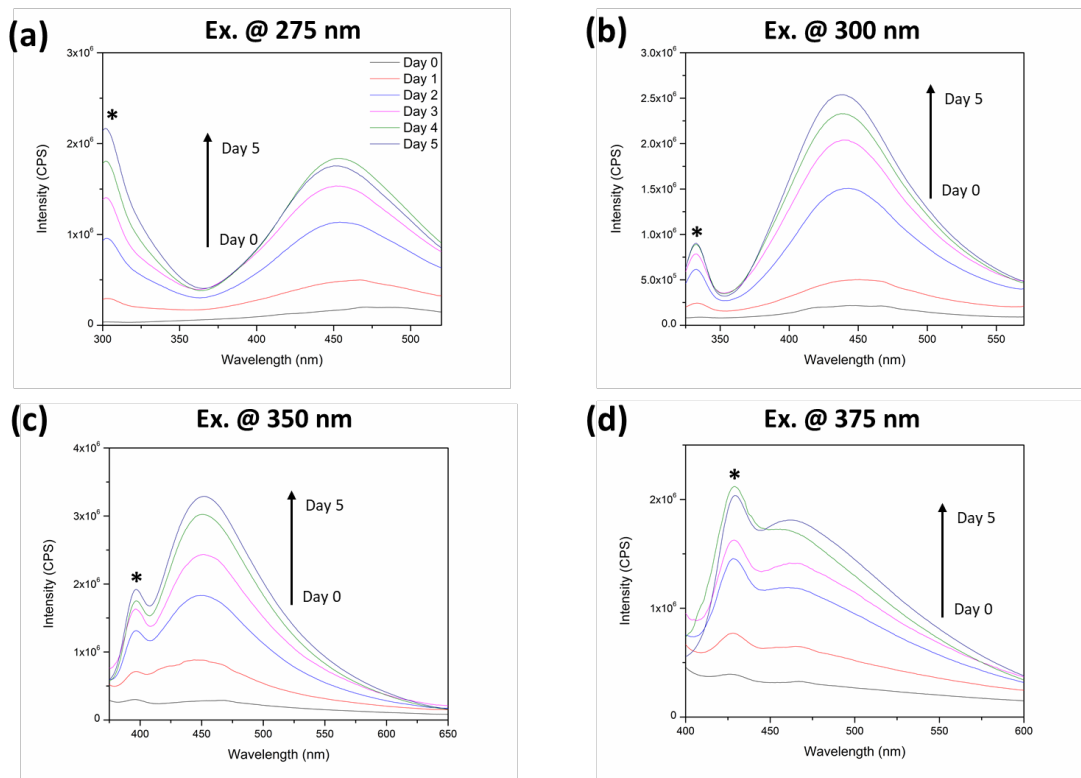
Appendix Figure 20. NIR PL emission spectra of MPO/H₂O₂/Cl⁻ degradation without SWCNTs from Day 0 to Day 5.



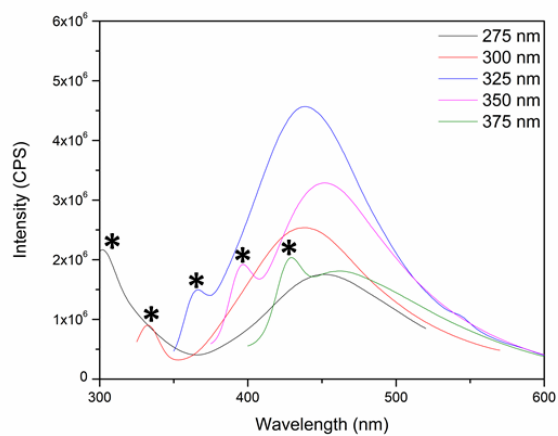
Appendix Figure 21. Size distribution of GQDs for the sample shown in Figure 3d. Image J software was used to measure size distribution.



Appendix Figure 22. EE maps of GO before and after 5-day MPO/H₂O₂/Cl⁻ degradation.



Appendix Figure 23. PL emission spectra of MPO/ H₂O₂/Cl⁻ degradation of GO from Day 0 to Day 5 with different excitation wavelengths ranging from 275 to 375 nm other than 325 nm (Figure 2d). (*) is water Raman peak.



Appendix Figure 24. PL emission spectra of GO after 5-Day degradation with different excitations. (*) is water Raman peak.

Appendix Table 9. Comparison of water Raman peaks.

Excitation wavelength (nm)	Theoretical peak position ^a (nm)	Experimental peak position ^b (nm)
275	304	302
300	335	333
325	367	367
350	399	397
375	432	429

Table notes:

a. Calculated according to equation as follows:¹

$$\lambda = \frac{1}{\frac{1}{\lambda_{ex}} - \bar{\nu} \cdot 10^{-7}}$$

Where:

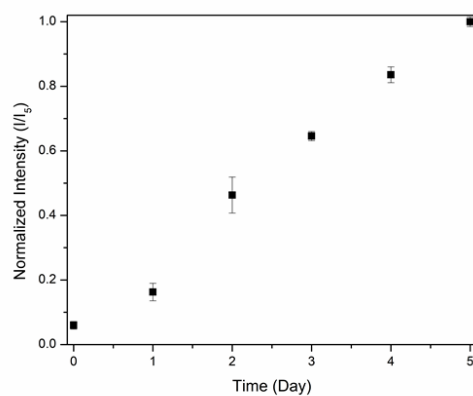
λ is the wavelength of the Raman scatter, nm

λ_{ex} is the excitation wavelength, nm

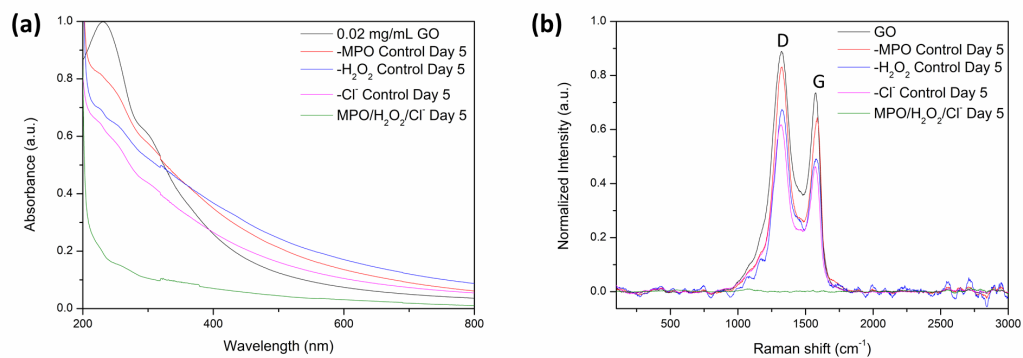
$\bar{\nu}$ is the Raman shift of water, which is around 3400-3600 cm^{-1} , 3500 cm^{-1} is assigned to $\bar{\nu}$ in the calculation

b. Based on Figure 2.3e and Appendix Figure 3.

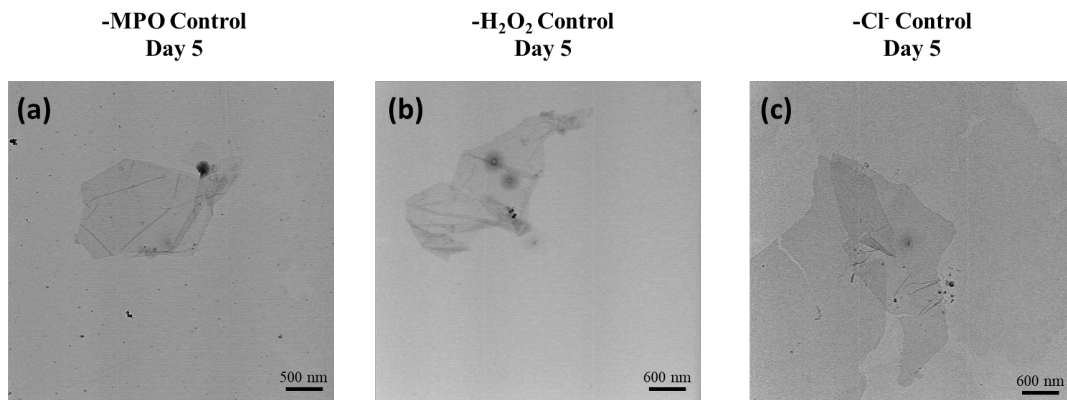
1. *Instrumentation for Fluorescence Spectroscopy*, in *Principles of Fluorescence Spectroscopy*, J.R. Lakowicz, Editor. 2006, Springer US: Boston, MA. p. 27-61.



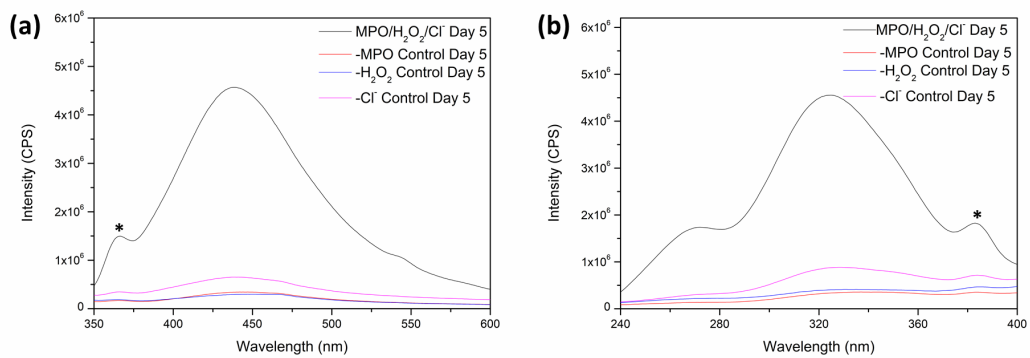
Appendix Figure 25. The normalized PL intensity of GO over 5-day MPO/H₂O₂/Cl⁻ degradation. The error bars represent standard deviations based on three replicate measurements.



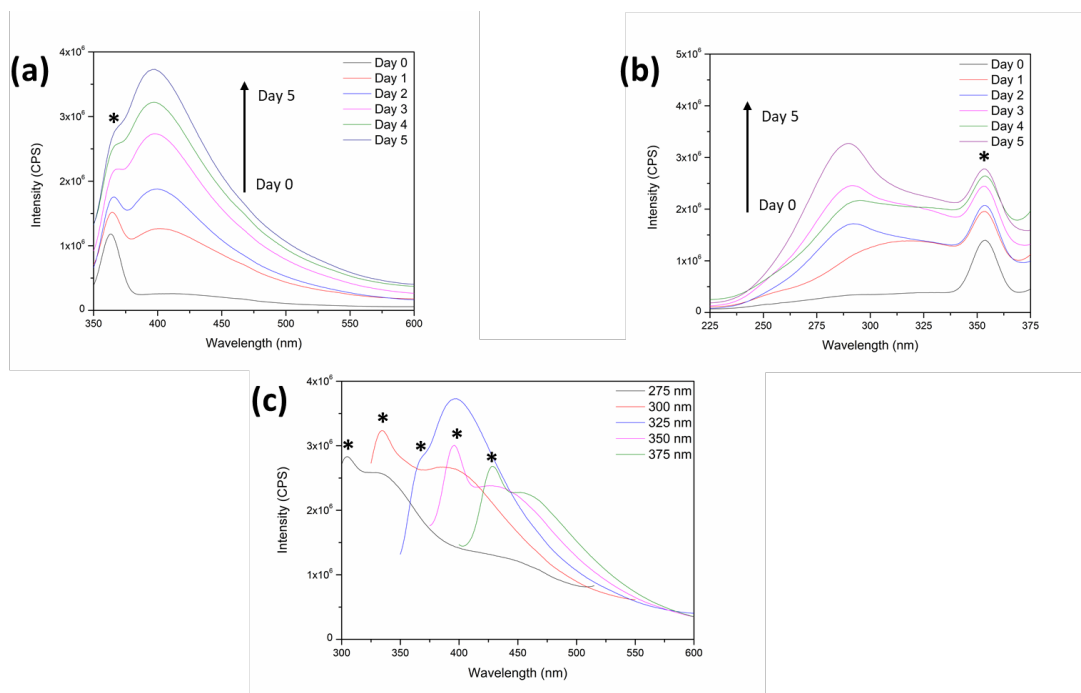
Appendix Figure 26. UV-vis-NIR absorption spectra (a) and Raman spectra (b) of GO before and after 5-day MPO/H₂O₂/Cl⁻ degradation without MPO, H₂O₂, and Cl⁻, respectively.



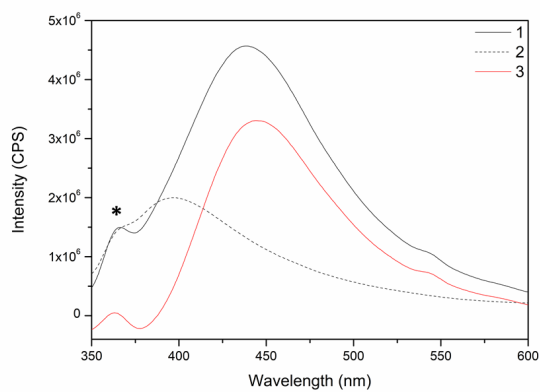
Appendix Figure 27. TEM images of GO after 5-day degradation without MPO (a), H₂O₂ (b), and Cl⁻ (c), respectively.



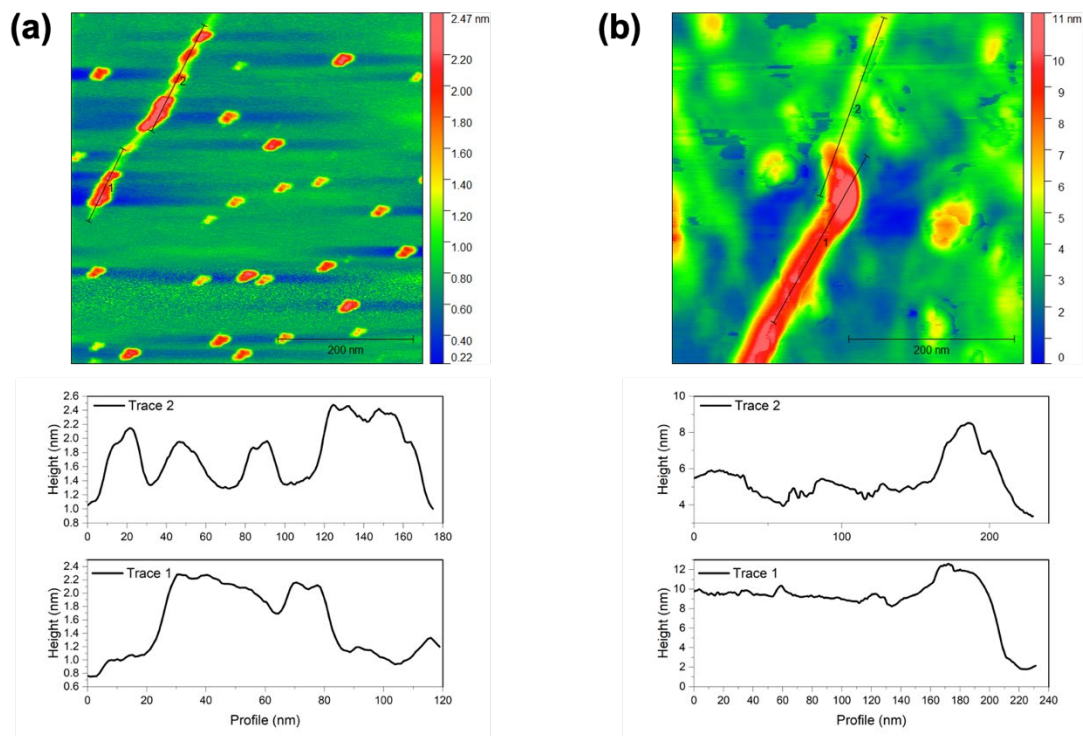
Appendix Figure 28. PL emission (a) and excitation (b) spectra of 5-day MPO/H₂O₂/Cl⁻ degradation of GO without MPO, H₂O₂, and Cl⁻, respectively. The emission spectra in (a) were obtained with excitation at 325 nm. The excitation spectra in (b) were obtained at emission wavelength 440 nm.



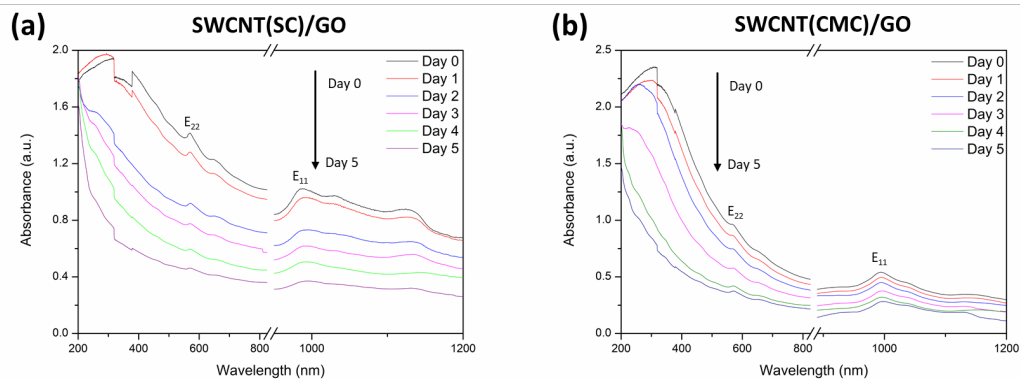
Appendix Figure 29. Visible PL emission (a, with 325 nm excitation) and excitation (b, at emission wavelength 400 nm) spectra of MPO/H₂O₂/Cl⁻ degradation without GO from Day 0 to Day 5. PL emission spectra (c) after 5-day MPO/H₂O₂/Cl⁻ degradation without GO with different excitation wavelengths ranging from 275 to 375 nm. (*) is water Raman peak.



Appendix Figure 30. PL emission spectra of MPO/H₂O₂/Cl⁻ degradation of GO after 5-day degradation (1), and control without GO (2). The emission spectra were obtained with excitation at 325 nm. Spectra were normalized based on the intensity of water Raman peaks. Spectrum 3 is the result after subtracting spectrum 2 from spectrum 1.



Appendix Figure 31. AFM images and line profiles of SWCNT(SC) (a) or SWCNT(CMC) (b) nanoscroll before degradation.



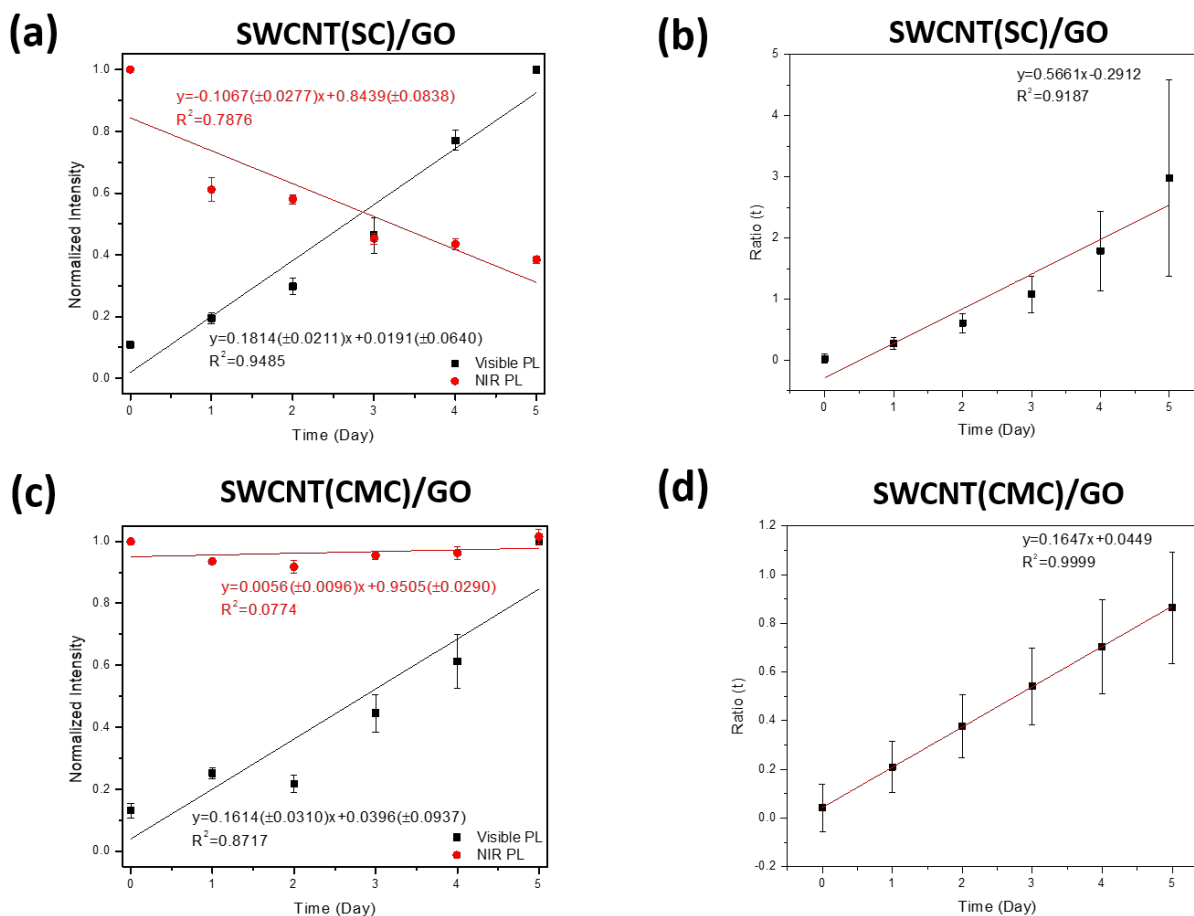
Appendix Figure 32. UV-vis-NIR absorption spectra of MPO/H₂O₂/Cl⁻ degradation of SWCNT(SC)/GO (a) or SWCNT(CMC)/GO (b) nanoscrolls from Day 0 to Day 5.

Additional Regression Analysis

Linear Regression Analysis

In addition to the method discussed in the main text, following are the other two methods to acquire the trendline between $Ratio(t)$ and Time (Day) by incorporating the uncertainty calculations for each data points before regression analysis.

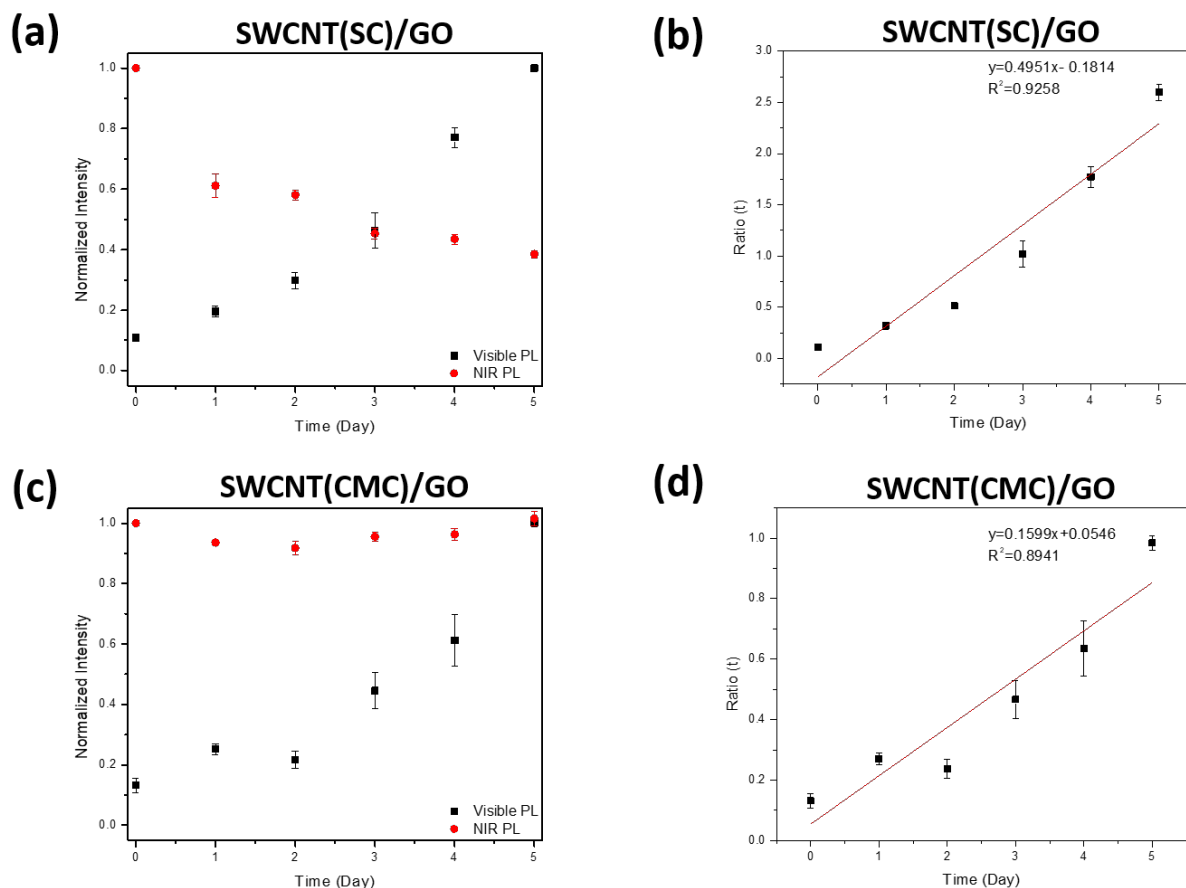
In the first method, $Ratio(t)$ (Appendix Figures 33 b and d) is still be calculated using Eq.3 while taking the uncertainty of the slopes and intercepts in both fitted lines (Appendix Figures 33 a and c) into consideration.



Appendix Figure 33. (a, b) Changes in the SWCNT(SC)/GO or (c, d) SWCNT(CMC)/GO nanoscrolls. (a, c) Normalized photoluminescence intensity and (b, d) ratio of intensity (Ratio) over 5-day MPO/H₂O₂/Cl⁻ degradation. The error bars represent standard deviations based on three replicate measurements.

In the second method, $Ratio(t)$ was calculated using Eq.4. The regression analysis results are shown in Appendix Figure 34.

$$Ratio(t) = \frac{I_{GO}^{normalized}(t)}{I_{SWCNT}^{normalized}(t)} \quad (4)$$

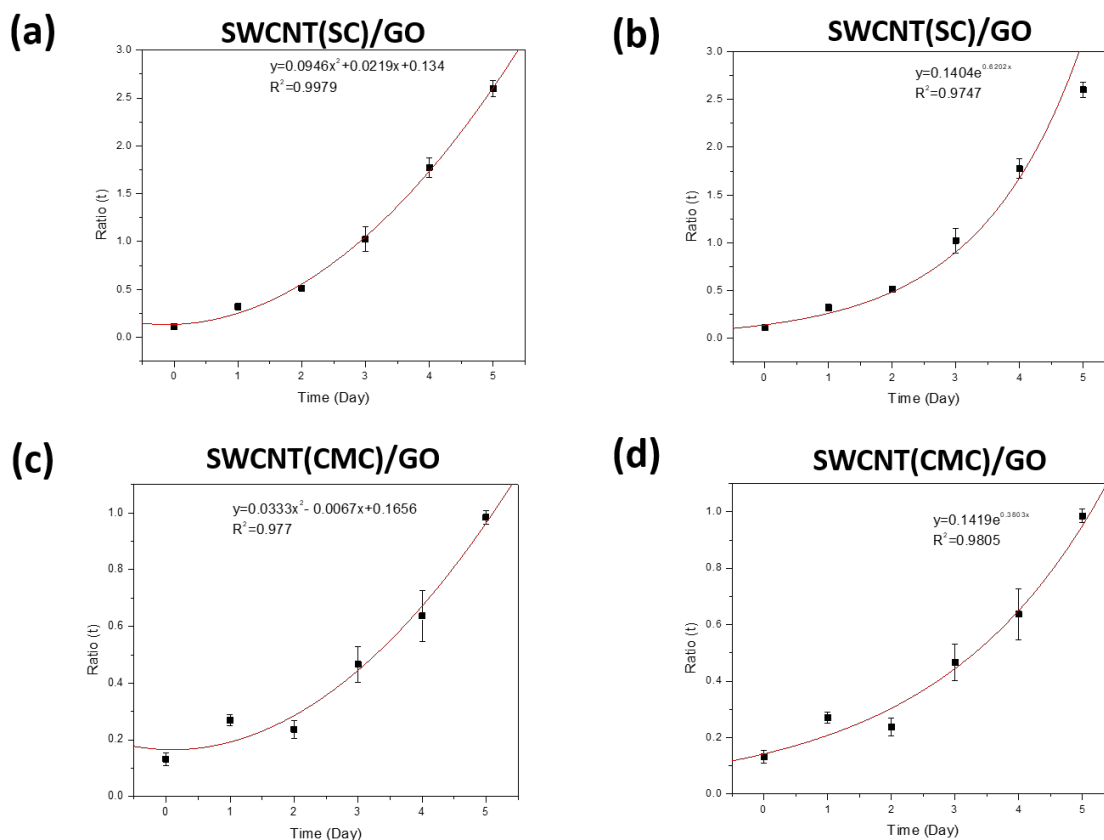


Appendix Figure 34. (a, b) Changes in the SWCNT(SC)/GO or (c, d) SWCNT(CMC)/GO nanoscrolls. (a, c) Normalized photoluminescence intensity and (b, d) ratio of intensity (Ratio) over 5-day MPO/H₂O₂/Cl⁻ degradation. The error bars represent standard deviations based on three replicate measurements.

Comparing the results using the above two methods (Appendix Figures 33 b and d vs. Appendix Figures 34 b and d), the error bars are generally lower for all the data points using the second method. The R² value of the fitted line is higher (Appendix Figure 34b vs Appendix Figure 33b) when using the second method for the SWCNT(SC)/GO system, while comparatively lower in terms of the SWCNT(CMC)/GO system (Appendix Figure 34d vs Appendix Figure 33d). Overall, the second method could be a potential better regression analysis approach without pre-fitting (Appendix Figures 33 a and c) both visible and NIR signals with linear regression models.

Non-Linear Regression Analysis

Two non-linear regression models, exponential and polynomial regression models, were chosen to further fit the data in Appendix Figures 34b and d, as shown in Appendix Figure 35. In terms of the SWCNT(SC)/GO system, the exponential model gives a higher R^2 value whereas the polynomial regression model fits better as to SWCN(CMC)/GO system. For both systems, both non-linear regression models provide a better fit in comparison with linear models.



Appendix Figure 35. Ratio of intensity (Ratio) over 5-day MPO/H₂O₂/Cl⁻ degradation using either polynomial (a, c) or exponential (b, d) regression models.

Appendix A.3 Composition and Structure of Fluorescent Graphene Quantum Dots Generated by Enzymatic Degradation of Graphene Oxide

This section contains supporting information for Chapter 4.1.

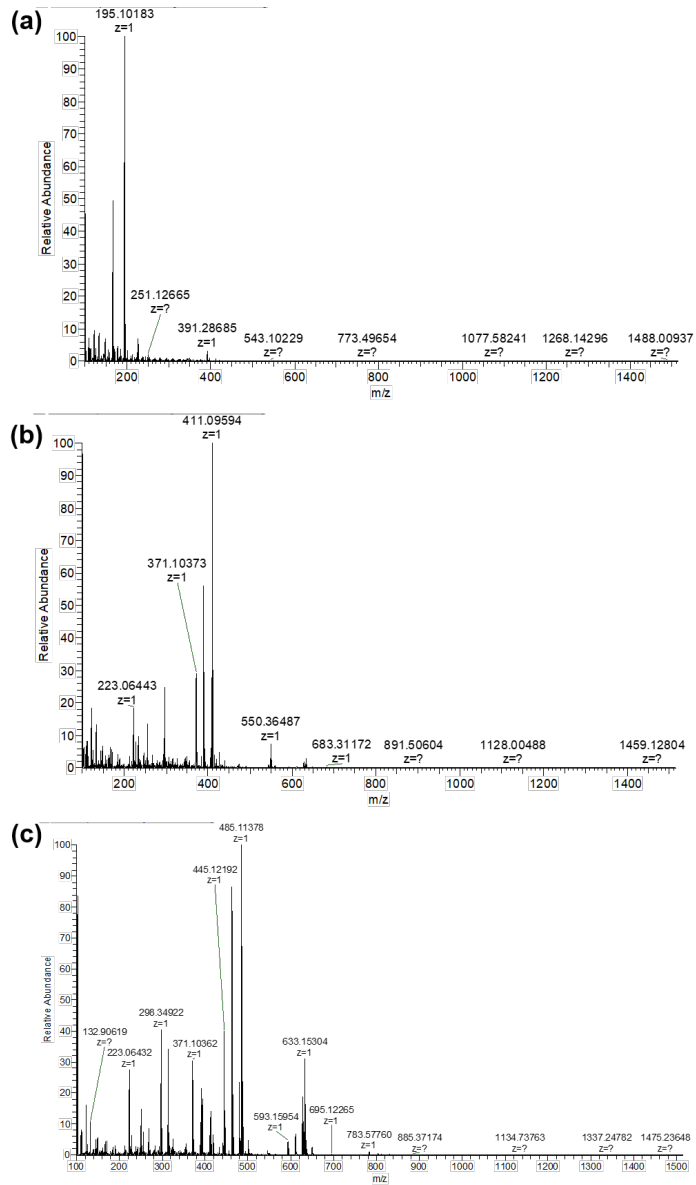
Additional Methodological Details

The samples for transmission electron microscopy (TEM, FEI Morgagni, 80 keV) were prepared by dropcasting 6 μL of 100 \times diluted solution on a lacey carbon grid and dried under ambient conditions overnight.

Raman spectra were acquired on an XploRA plus confocal Raman microscope (Horiba) with 638 nm laser (24 mW) operating at 10% power.

X-ray photoelectron spectroscopy (XPS) data were generated on a Thermo ESCALAB 250 Xi XPS using monochromated Al K α X-rays as the source. A 650- μm spot size was used and the samples were charge-compensated using an electron flood gun. Samples were prepared via repeated dropcasting onto copper tape until a thick black spot was generated.

Visible photoluminescence spectra were recorded using a Fluoromax-3 spectrometer (HORIBA Jobin Yvon) equipped with a xenon lamp light source and a photomultiplier tube detector. The slit width was set at 10 nm for all measurements.



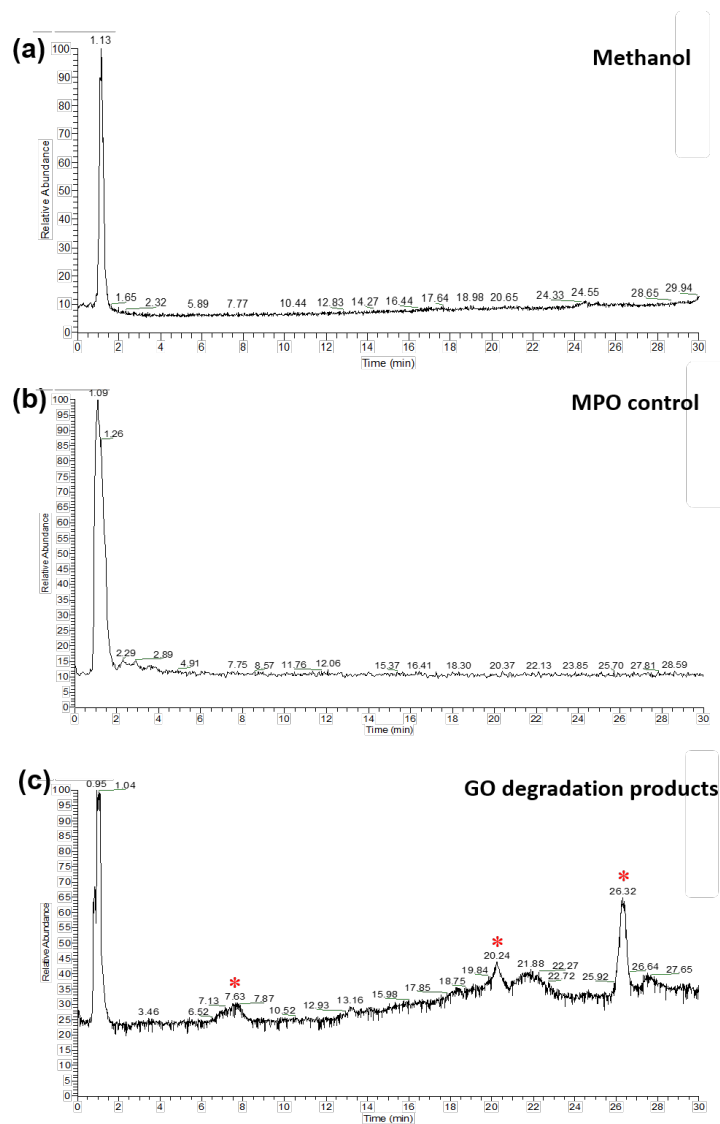
Appendix Figure 36. Positive-ion ESI mass spectra of chromatographic peaks at (a) 9.28 min, (b) 20.29 min, and (c) 26.35 min in Figure 4.2c.

Appendix Table 10. Potential PAHs generated by MPO/H₂O₂/Cl⁻ oxidation of GO (detected in the positive ionization mode).

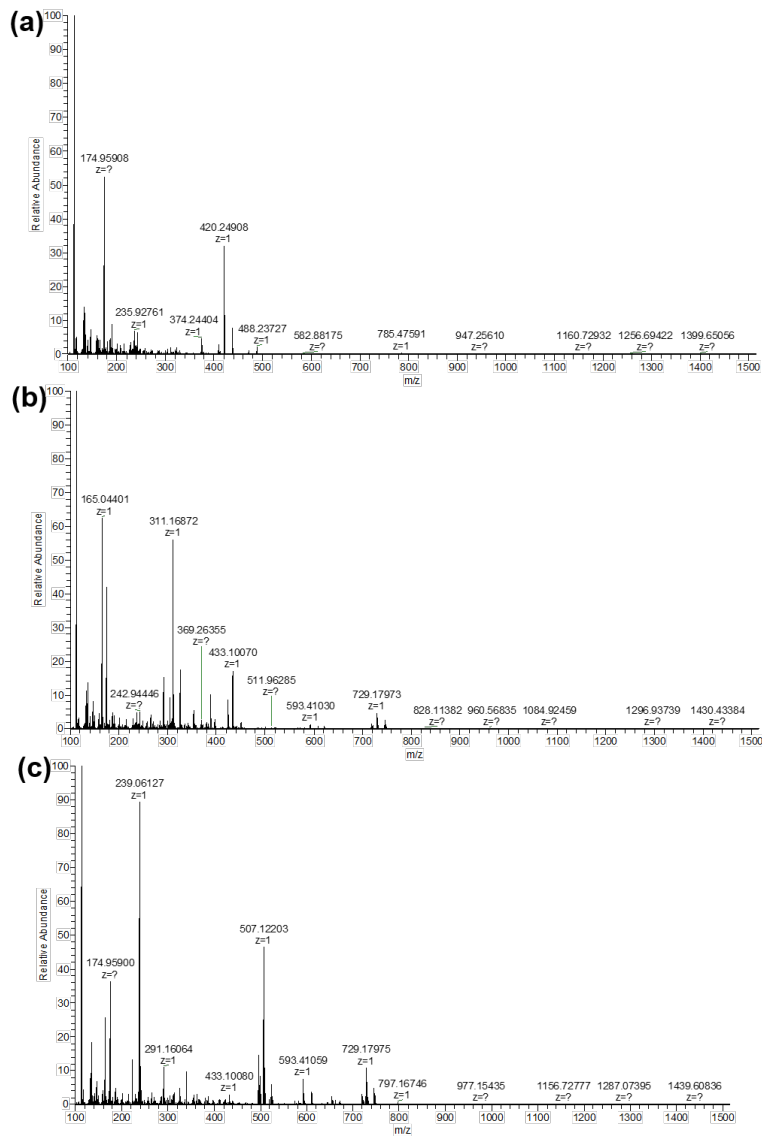
No.	Retention time (RT, min)	Mass to charge ratio (m/z)	Experimental M+1(0.5)/M (%)	Charge (z)	Chemical formula	RDB ^a	Mass error (ppm)	Theoretical M+1(0.5)/M (%)
1	9.28	195.10183	11.58	1	[C ₁₁ H ₁₄ O ₃ + H] ⁺	5	1.33	11.90
2		178.56805	18.44	2	[C ₂₃ H ₁₄ O ₃ + H + NH ₄] ²⁺	17	1.97	24.88
3		203.14358	14.45	1	[C ₁₄ H ₁₈ O + H] ⁺	6	2.65	15.14
4		176.06534	15.37	2	[C ₂₁ H ₁₈ O ₅ + 2H] ²⁺	13	2	22.71
5		149.02369	8.07	1	[C ₈ H ₄ O ₃ + H] ⁺	7	2.48	8.65
6		187.57338	16.74	2	[C ₂₃ H ₁₆ O ₄ + H + NH ₄] ²⁺	16	2.13	24.88
7		245.07968	13.65	1	[C ₁₄ H ₁₂ O ₄ + H] ⁺	9	-4.71	15.14
8		255.10281	28.13	2	[C ₂₀ H ₂₆ O ₁₃ + 2NH ₄] ²⁺	8	1.23	21.63
9					[C ₂₃ H ₃₄ O ₁₁ + H + Na] ²⁺	7	-1.94	24.88
10					[C ₃₂ H ₂₈ O ₆ + 2H] ²⁺	19	4.86	34.61
11		222.18599	14.16	1	[C ₁₄ H ₂₀ O + NH ₄] ⁺	5	3.37	15.14
12	20.29	389.11433	29.28	1	[C ₂₅ H ₁₈ O ₃ + Na] ⁺	17	-1.25	27.04
13					[C ₂₂ H ₂₂ O ₄ + K] ⁺	12	-1.64	23.79
14		234.54734	28.66	2	[C ₃₀ H ₁₀ O ₅ + H + NH ₄] ²⁺	26	1.61	32.45
15		190.07172	5.74	1	[C ₇ H ₈ O ₅ + NH ₄] ⁺	4	3.79	7.57
16		321.20659	15.5	1	[C ₁₉ H ₂₈ O ₄ + H] ⁺	6	1.73	20.55
17		473.06586	28.34	1	[C ₂₉ H ₁₂ O ₇ + H] ⁺	24	0.59	31.37
18		319.22741	16.53	1	[C ₂₀ H ₃₀ O ₃ + H] ⁺	6	2	21.63
19		545.38242	31.11	1	[C ₃₁ H ₅₄ O ₆ + Na] ⁺	5	2.13	33.53
20					[C ₃₃ H ₅₂ O ₆ + H] ⁺	8	-2.28	35.69
21	26.35	485.11378	39.93	1	[C ₃₃ H ₁₈ O ₃ + Na] ⁺	25	-2.13	35.69
22					[C ₃₀ H ₂₂ O ₄ + K] ⁺	20	-2.45	32.45
23		463.13242	38.01	1	[C ₃₃ H ₁₈ O ₃ + H] ⁺	25	-0.97	35.69
24					[C ₂₈ H ₂₄ O ₄ + K] ⁺	17	3.89	30.28
25					[C ₃₁ H ₂₀ O ₃ + Na] ⁺	22	4.22	33.53
26		445.12192	36.41	1	[C ₃₃ H ₁₆ O ₂ + H] ⁺	26	-0.87	35.69
27					[C ₂₈ H ₂₂ O ₃ + K] ⁺	18	4.19	30.28
28					[C ₃₁ H ₁₈ O ₂ + Na] ⁺	23	4.54	33.53
29		371.10362	26.52	1	[C ₂₅ H ₁₆ O ₂ + Na] ⁺	18	-1.7	27.04
30					[C ₂₂ H ₂₀ O ₃ + K] ⁺	13	-2.11	23.79
31		480.15851	37.7	1	[C ₃₃ H ₁₈ O ₃ + NH ₄] ⁺	25	-1.9	35.69
32		251.04363	36.14	2	[C ₂₅ H ₁₈ O ₁₀ + H + Na] ²⁺	17	1.52	27.04
33					[C ₂₇ H ₁₆ O ₁₀ + 2H] ²⁺	20	-3.27	29.20
34		413.26845	25.83	1	[C ₂₆ H ₃₆ O ₄ + H] ⁺	9	-0.45	28.12
35		325.06396	53.19	2	[C ₄₅ H ₂₂ O ₃ + H + K] ²⁺	35	0.91	48.67

36				$[\text{C}_{48}\text{H}_{18}\text{O}_2 + \text{H} + \text{Na}]^{2+}$	40	1.14	51.92
37				$[\text{C}_{50}\text{H}_{16}\text{O}_2 + 2\text{H}]^{2+}$	43	-2.56	54.08
38				$[\text{C}_{45}\text{H}_{10}\text{O}_4 + 2\text{NH}_4]^{2+}$	41	3.63	48.67
39				$[\text{C}_{40}\text{H}_{28}\text{O}_4 + 2\text{K}]^{2+}$	27	4.37	43.26
40				$[\text{C}_{43}\text{H}_{24}\text{O}_3 + \text{K} + \text{Na}]^{2+}$	32	4.61	46.51
41				$[\text{C}_{46}\text{H}_{20}\text{O}_2 + 2\text{Na}]^{2+}$	37	4.84	49.75
42	501.08783	37.17	1	$[\text{C}_{36}\text{H}_{14}\text{O}_2 + \text{Na}]^+$	30	-1.54	38.94
43				$[\text{C}_{33}\text{H}_{18}\text{O}_3 + \text{K}]^+$	25	-1.84	35.69
44	161.05999	8.16	1	$[\text{C}_{10}\text{H}_8\text{O}_2 + \text{H}]^+$	7	1.76	10.82
45	271.55722	36.94	2	$[\text{C}_{29}\text{H}_{16}\text{O}_{10} + \text{H} + \text{NH}_4]^{2+}$	22	-1.86	31.37
46				$[\text{C}_{27}\text{H}_{18}\text{O}_{10} + \text{NH}_4 + \text{Na}]^{2+}$	19	2.57	29.20
47	547.08393	37.93	1	$[\text{C}_{26}\text{H}_{20}\text{O}_{12} + \text{Na}]^+$	17	-1.4	28.12
48				$[\text{C}_{35}\text{H}_{14}\text{O}_7 + \text{H}]^+$	29	4.94	37.86
49	455.31517	25.22	1	$[\text{C}_{29}\text{H}_{42}\text{O}_4 + \text{H}]^+$	9	-0.91	31.37
50				$[\text{C}_{27}\text{H}_{44}\text{O}_4 + \text{Na}]^+$	6	4.37	29.20
51	783.5776	50.14	1	$[\text{C}_{48}\text{H}_{78}\text{O}_8 + \text{H}]^+$	10	0.83	51.92
52				$[\text{C}_{46}\text{H}_{80}\text{O}_8 + \text{Na}]^+$	7	3.9	49.75

^a RDB = ring double bond.



Appendix Figure 37. LC-MS total ion liquid chromatograms (TIC) in negative ionization mode of (a) pure methanol, (b) MPO control, and (c) after 5-day MPO/H₂O₂/Cl⁻ degradation of GO. Note: the red * symbol in panel (b) indicates the peak subjected to chemical formula screening.

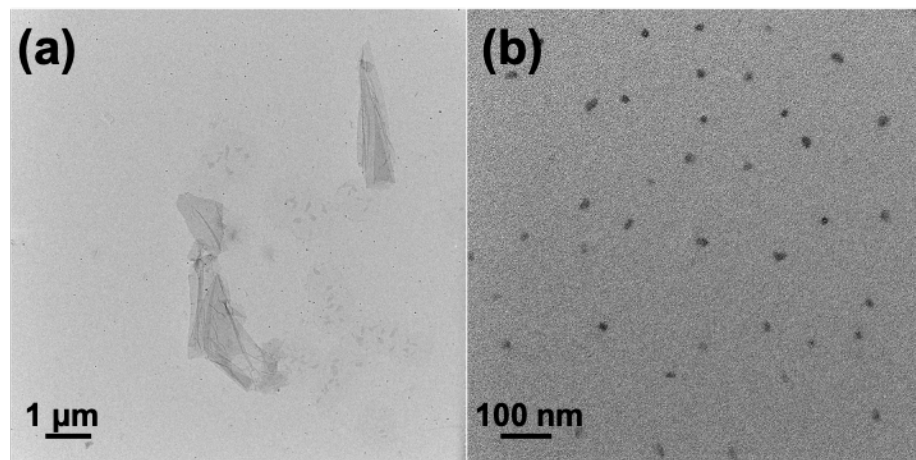


Appendix Figure 38. Negative-ion ESI mass spectra of chromatographic peaks at (a) 7.63 min, (b) 20.24 min, and (c) 26.32 min in Appendix Figure 34c.

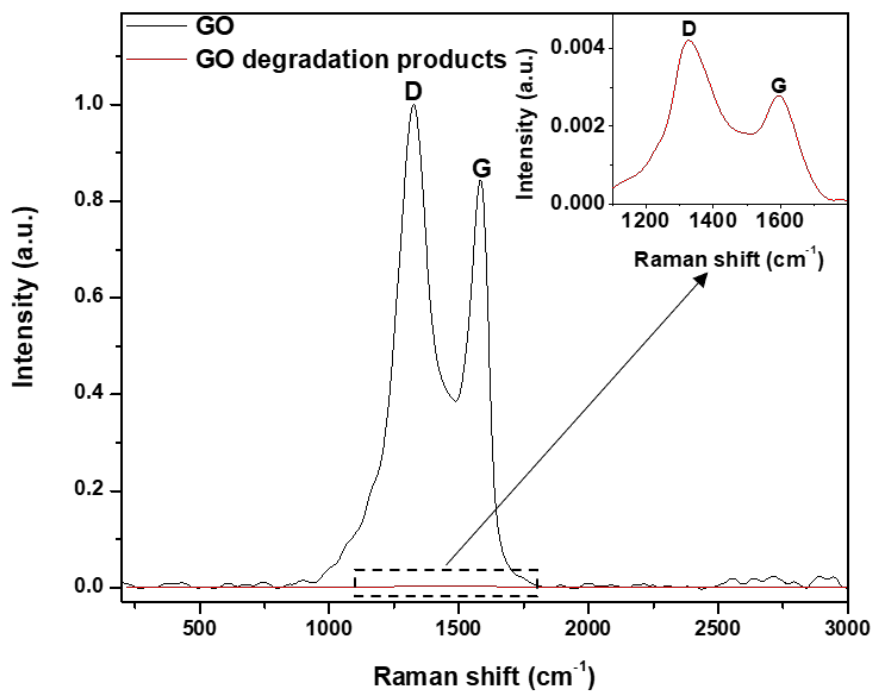
Appendix Table 11. Potential PAHs generated by MPO/H₂O₂/Cl⁻ oxidation of GO (detected in the negative ionization mode).

No	Retention time (RT, min)	Mass charge ratio (m/z)	Experimental M+1/M (%)	Charge (z)	Chemical formula	RDB ^a	Mass error (ppm)	Theoretical M+1/M (%)
1	7.63	323.22255	20.15	1	[C ₁₉ H ₃₂ O ₄ - H] ⁻	4	2.678	20.55
2	20.24	423.07266	29.11	1	[C ₂₂ H ₁₆ O ₉ - H] ⁻	15	3.79	23.79
3		379.155	20.66	1	[C ₂₃ H ₂₄ O ₅ - H] ⁻	12	2.64	24.88
4		593.4103	43.11	1	[C ₃₉ H ₅₈ O ₂ + Cl] ⁻	11	-2.84	42.18
5		719.15092	63.08	1	[C ₅₀ H ₂₄ O ₆ - H] ⁻	39	2.79	54.08
6	26.32	507.12203	41.18	1	[C ₃₄ H ₂₀ O ₅ - H] ⁻	25	-1.32	36.77
7		729.17975	63.35	1	[C ₅₀ H ₃₀ O ₄ + Cl] ⁻	36	-4.06	54.08
8		433.1008	32.03	1	[C ₂₉ H ₁₈ O ₂ + Cl] ⁻	21	4.19	31.37
9		661.39863	43.82	1	[C ₄₂ H ₅₈ O ₄ + Cl] ⁻	14	-4.81	45.43
10		583.38198	43.43	1	[C ₃₂ H ₅₆ O ₉ - H] ⁻	5	-3.56	34.61
11		575.11011	36.82	1	[C ₃₁ H ₂₄ O ₉ + Cl] ⁻	20	-0.39	33.53
12					[C ₃₇ H ₂₀ O ₇ - H] ⁻	28	-4.21	40.02

^a RDB = ring double bond.

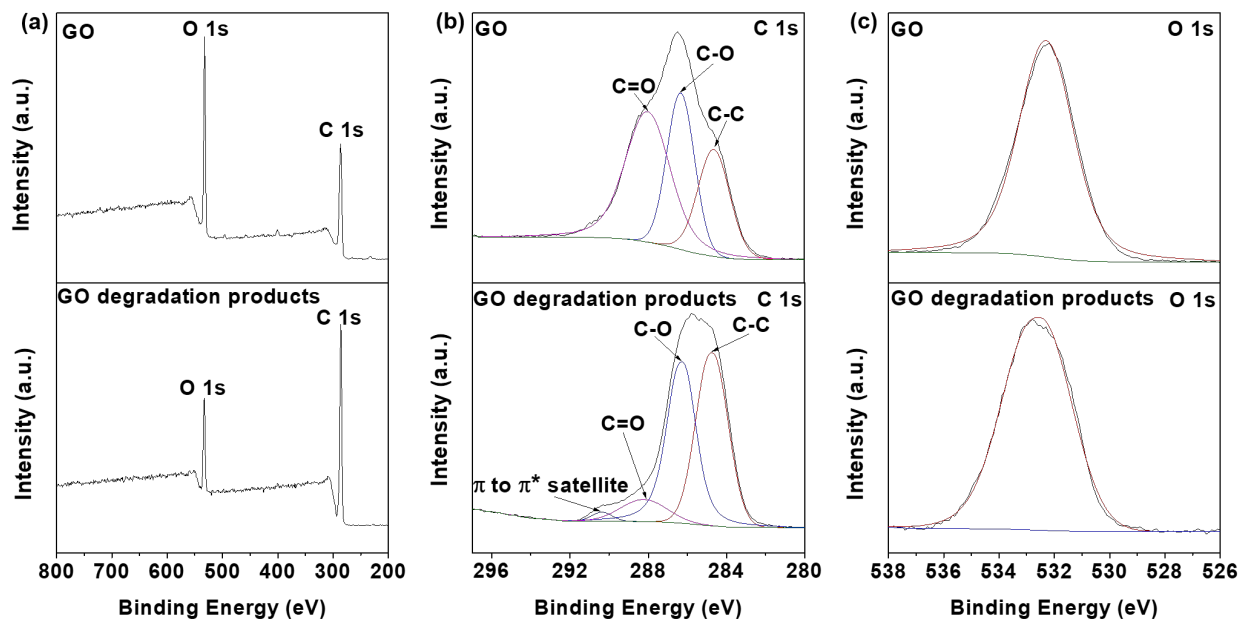


Appendix Figure 39. TEM images of (a) GO and (b) GO after 5-day MPO/H₂O₂/Cl⁻ degradation. Adapted with permission from S1. Copyright 2020 American Chemical Society.

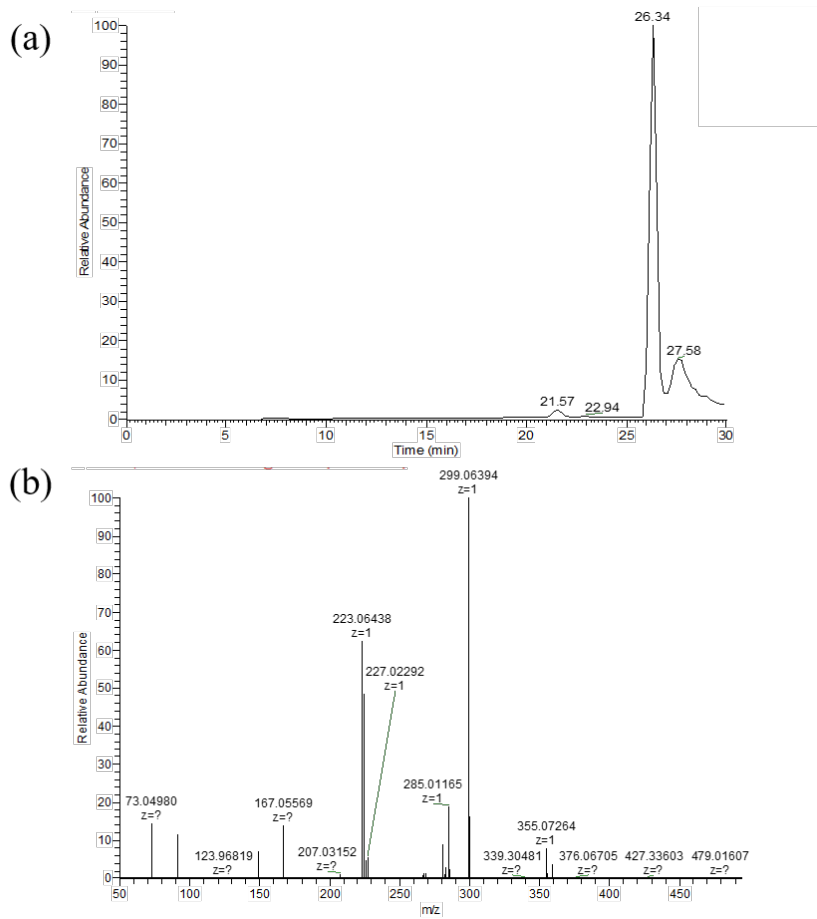


Appendix Figure 40. Raman spectra of GO in the initial state and after 5-day MPO/H₂O₂/Cl⁻ degradation.

The expanded inset show the D and G peaks of GO degradation products.

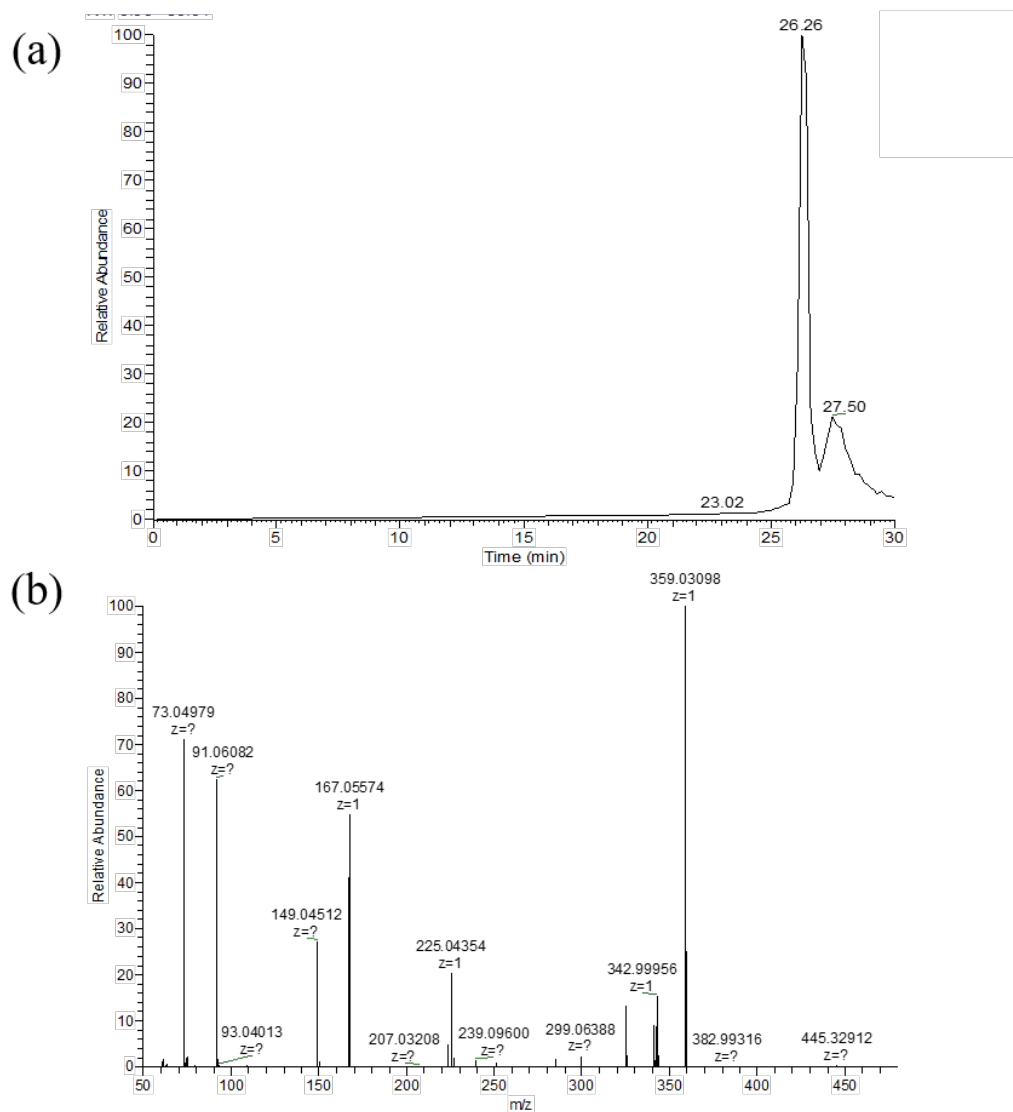


Appendix Figure 41. (a) XPS survey, (b) high-resolution carbon 1s and (c) high-resolution oxygen 1s spectra of GO (top) and GO after 5-day MPO/H₂O₂/Cl⁻ degradation (bottom).

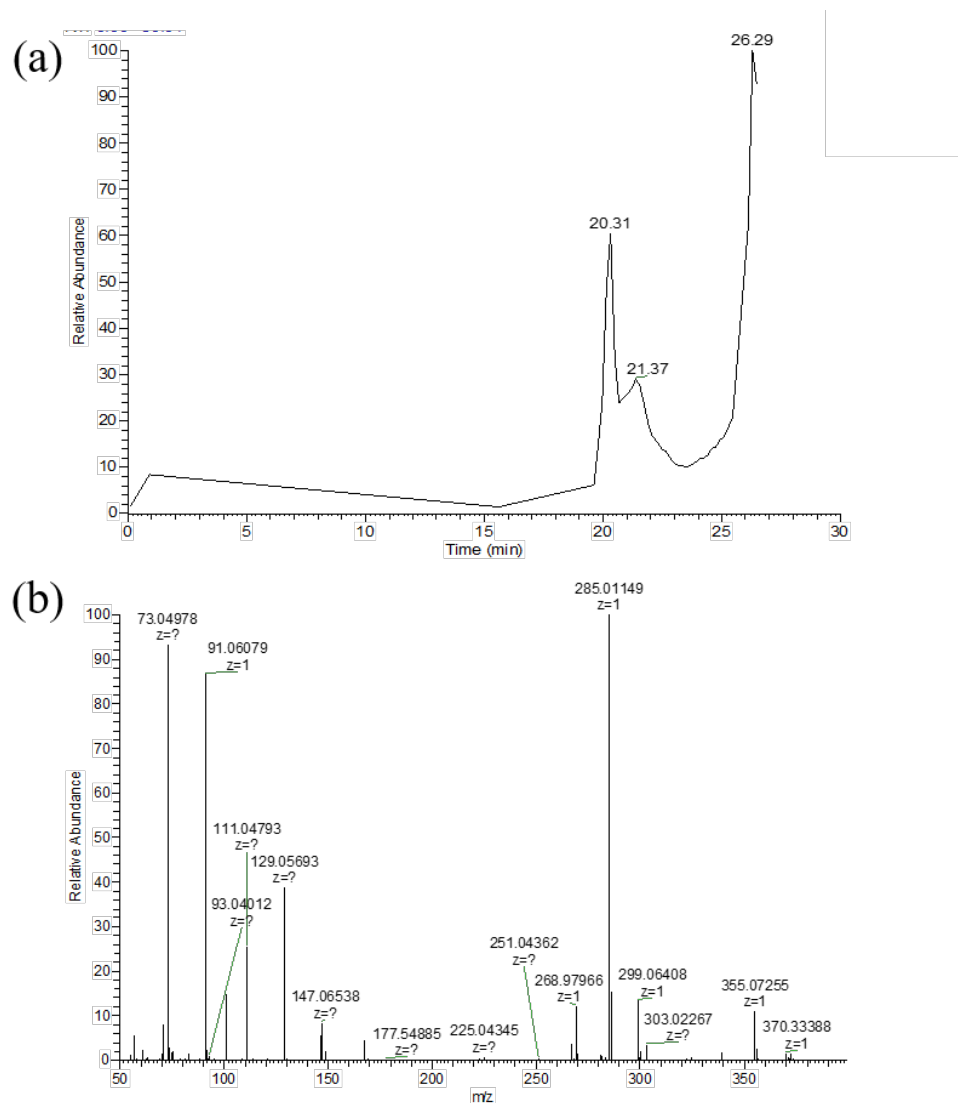


Appendix Figure 42. (a) LC-MS/MS ion chromatogram showing the product ion profile and (b) LC-MS/MS product ion spectrum of the precursor ion m/z 463.13 in Appendix Table 10.

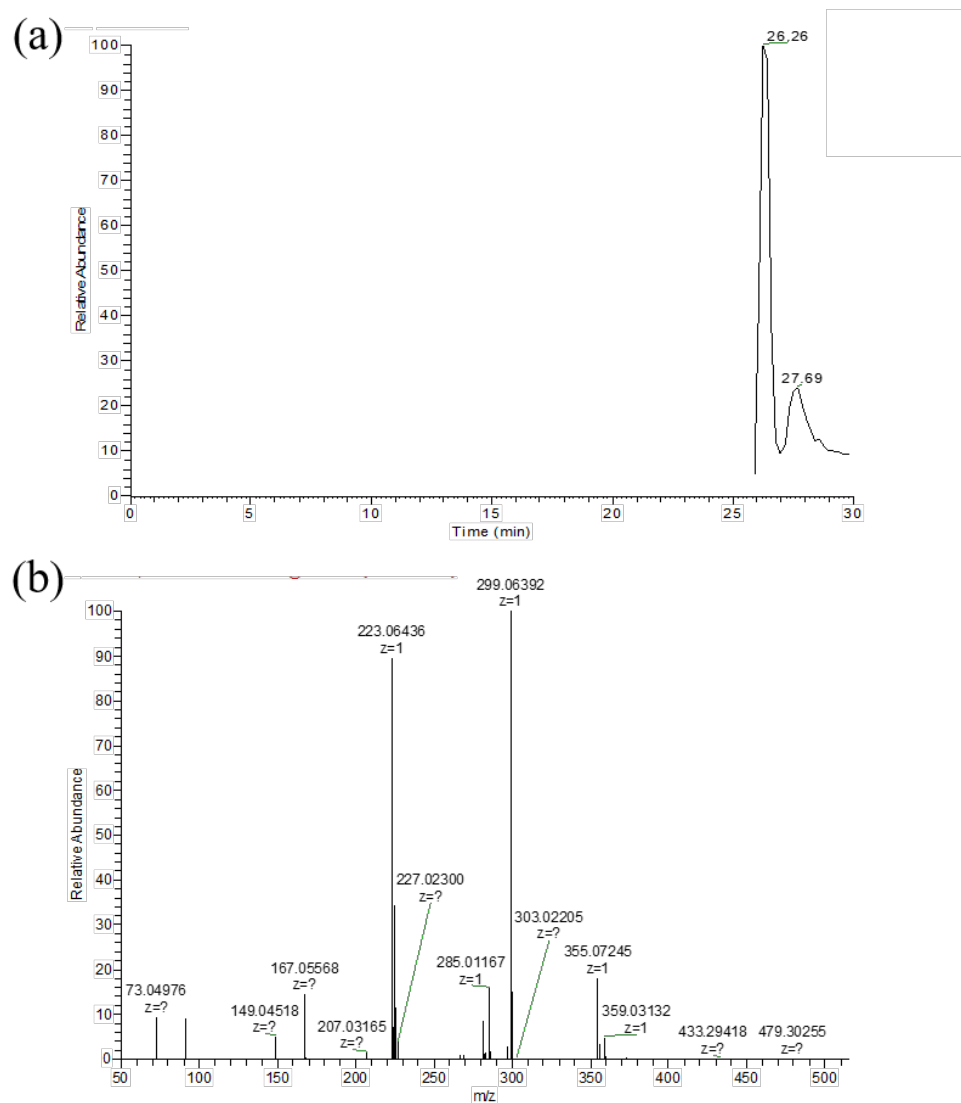
It should be noted that as the MS/MS data were acquired using data dependent MS/MS acquisition mode, the chromatograms in Appendix Figures 42(a)-53(a) are therefore not displayed across the full LC retention time domain. ^{S2, S3}



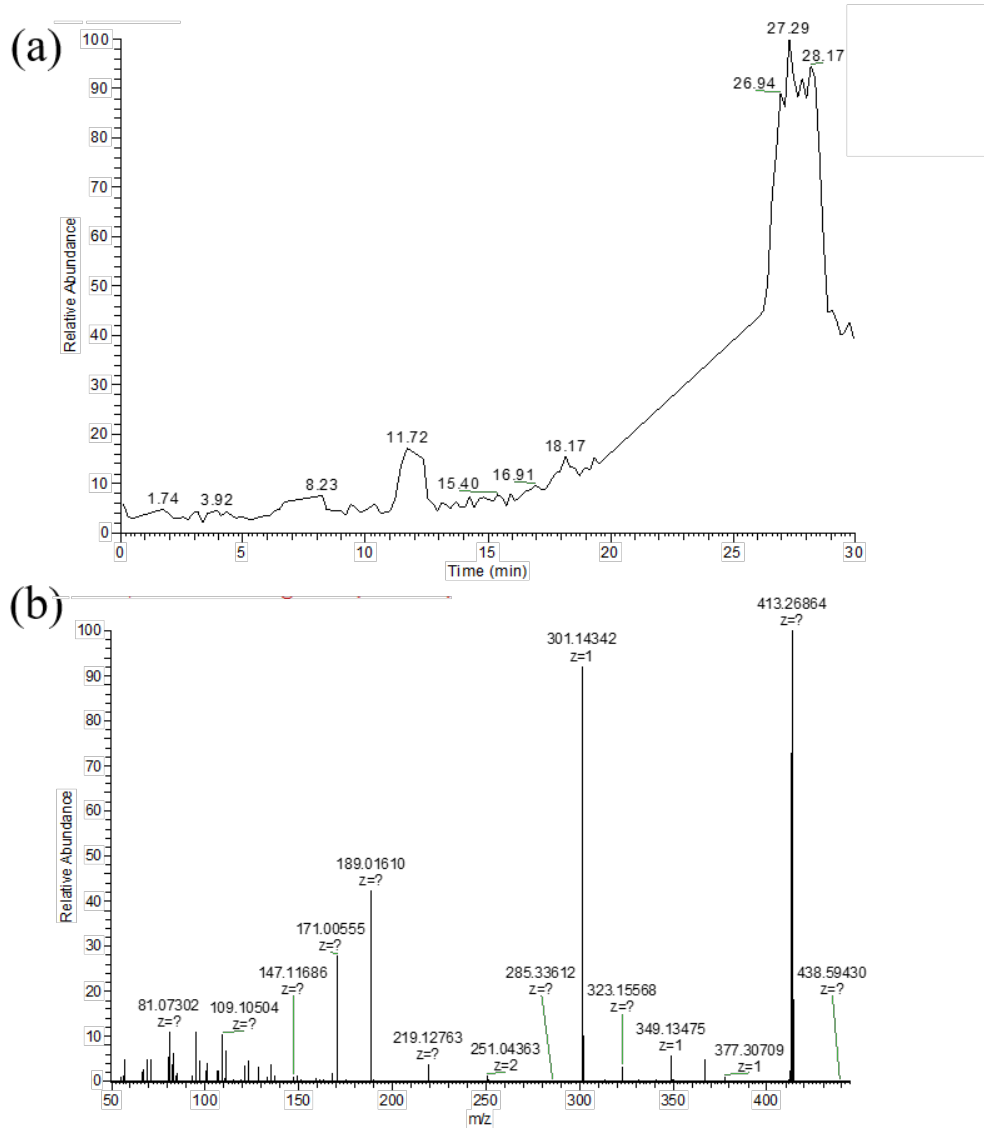
Appendix Figure 43. (a) LC-MS/MS ion chromatogram showing the product ion profile and (b) LC-MS/MS product spectrum of the precursor ion m/z 445.12 in Appendix Table 10.



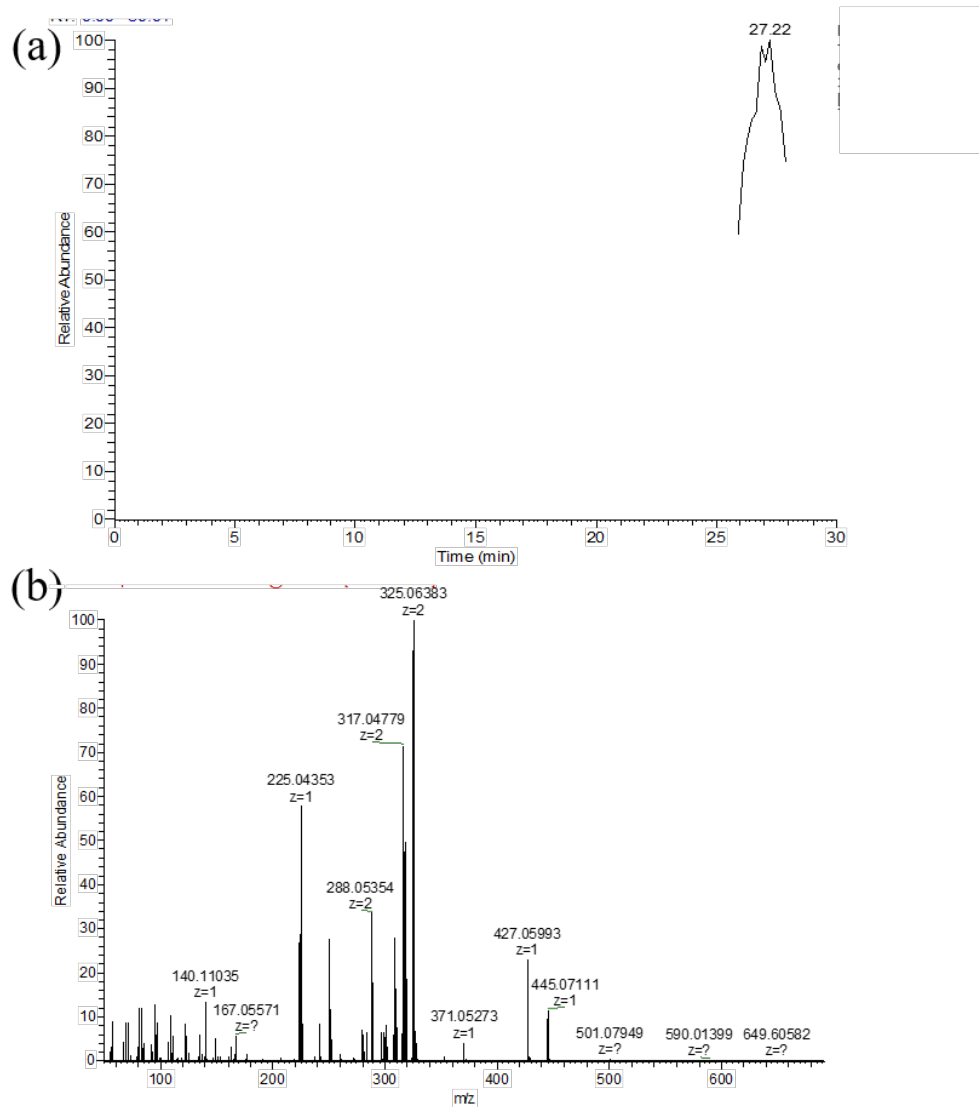
Appendix Figure 44. (a) LC-MS/MS ion chromatogram showing the product ion profile and (b) LC-MS/MS product spectrum of the precursor ion m/z 371.10 in Appendix Table 10.



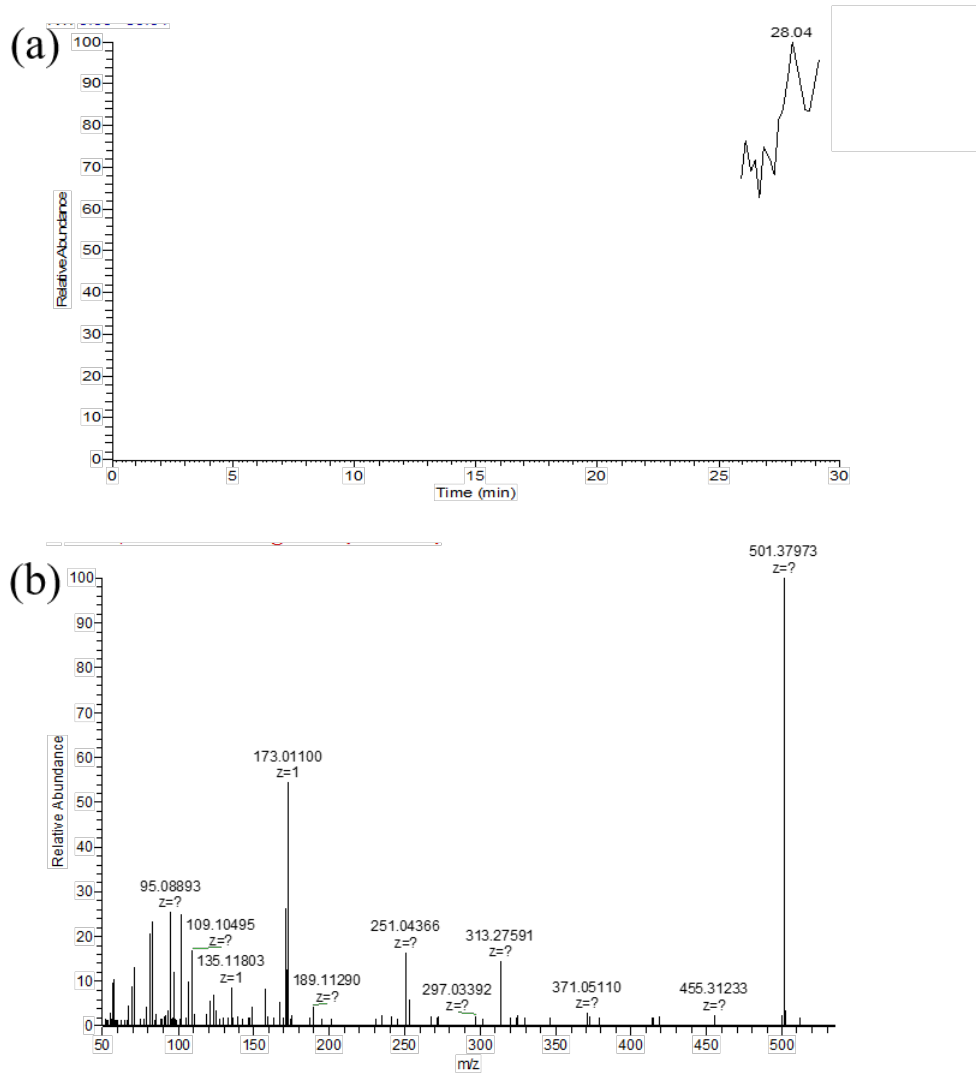
Appendix Figure 45. (a) LC-MS/MS ion chromatogram showing the product ion profile and (b) LC-MS/MS product spectrum of the precursor ion m/z 480.16 in Appendix Table 10.



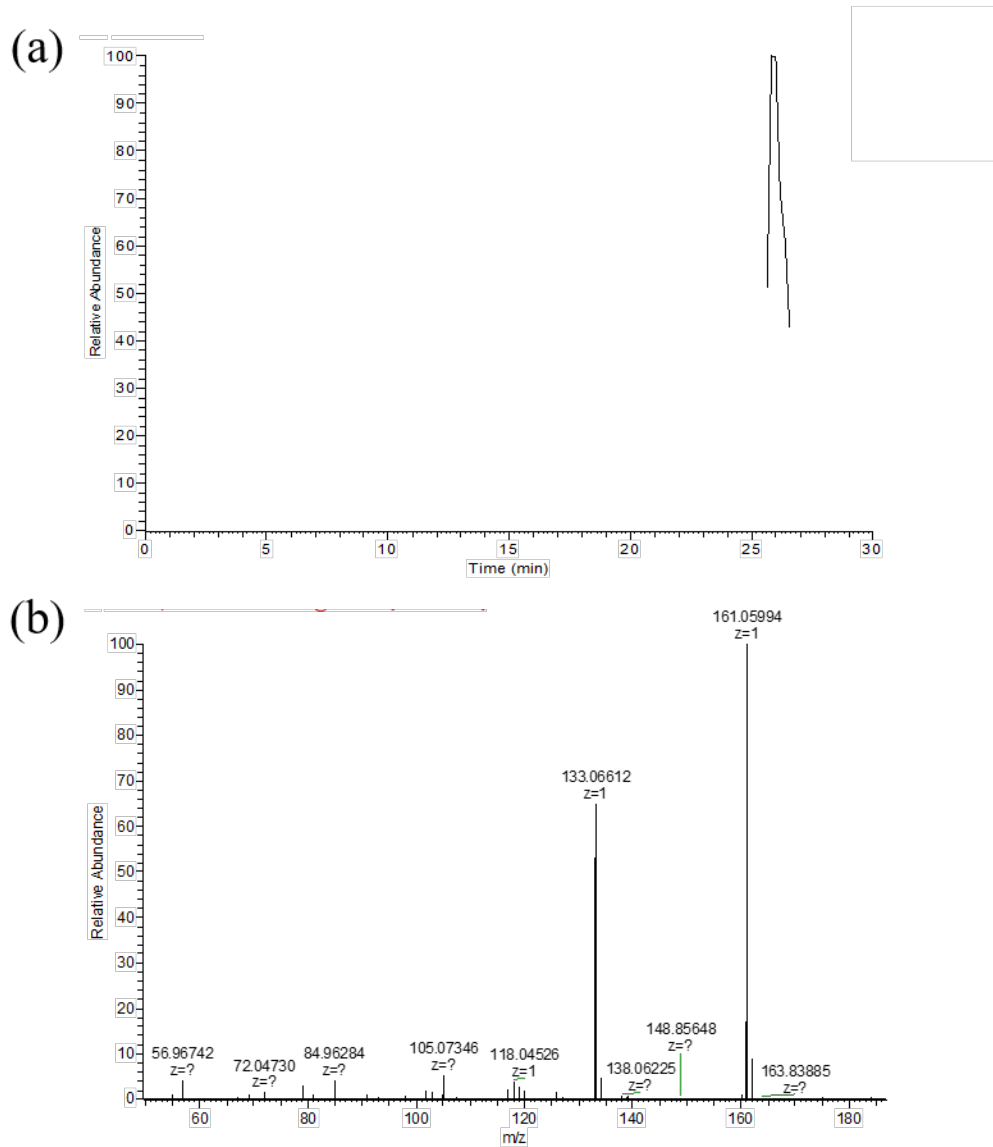
Appendix Figure 46. (a) LC-MS/MS ion chromatogram showing the product ion profile and (b) LC-MS/MS product spectrum of the precursor ion m/z 413.27 in Appendix Table 10.



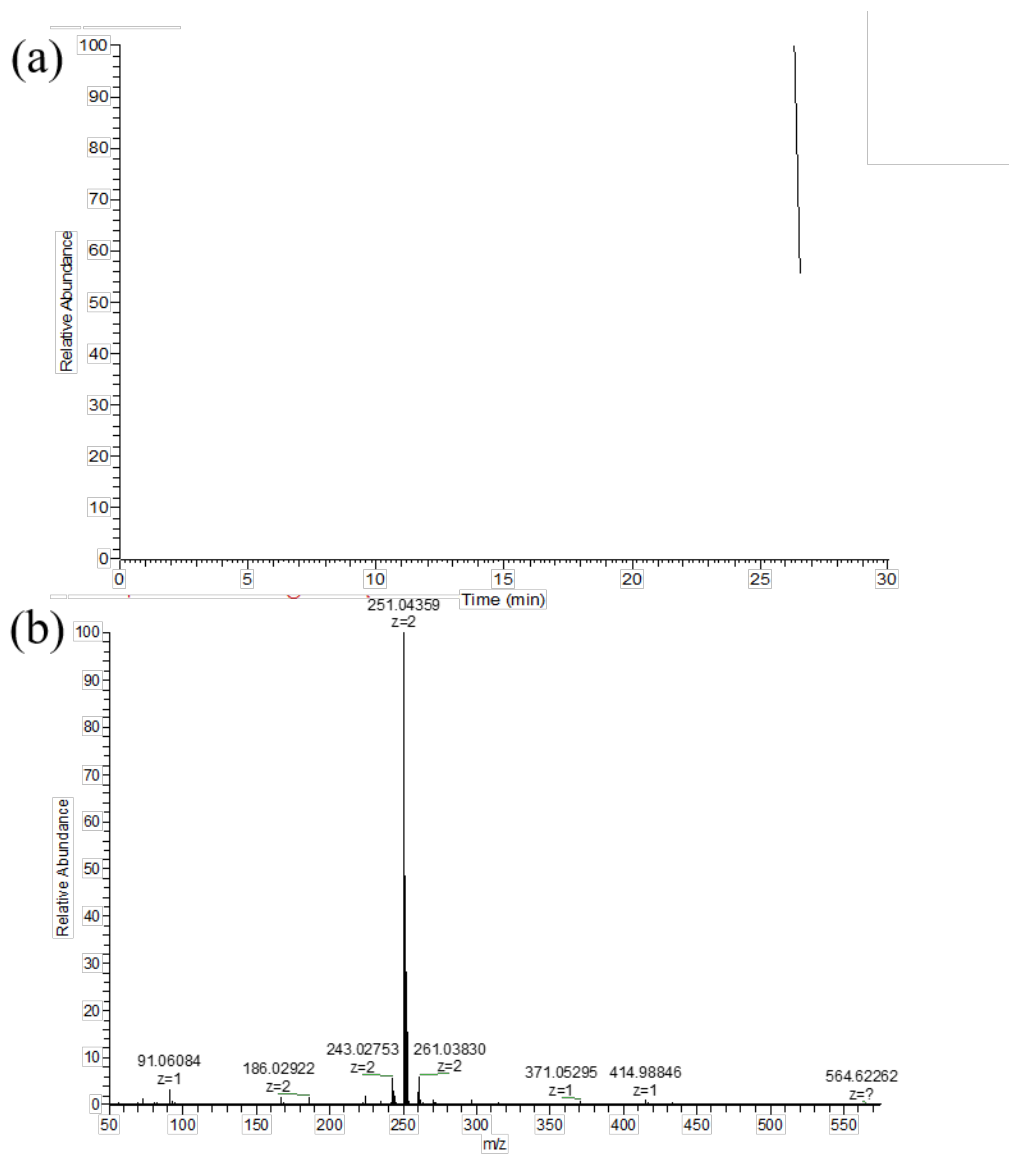
Appendix Figure 47. (a) LC-MS/MS ion chromatogram showing the product ion profile and (b) LC-MS/MS product spectrum of the precursor ion m/z 325.06 in Appendix Table 10.



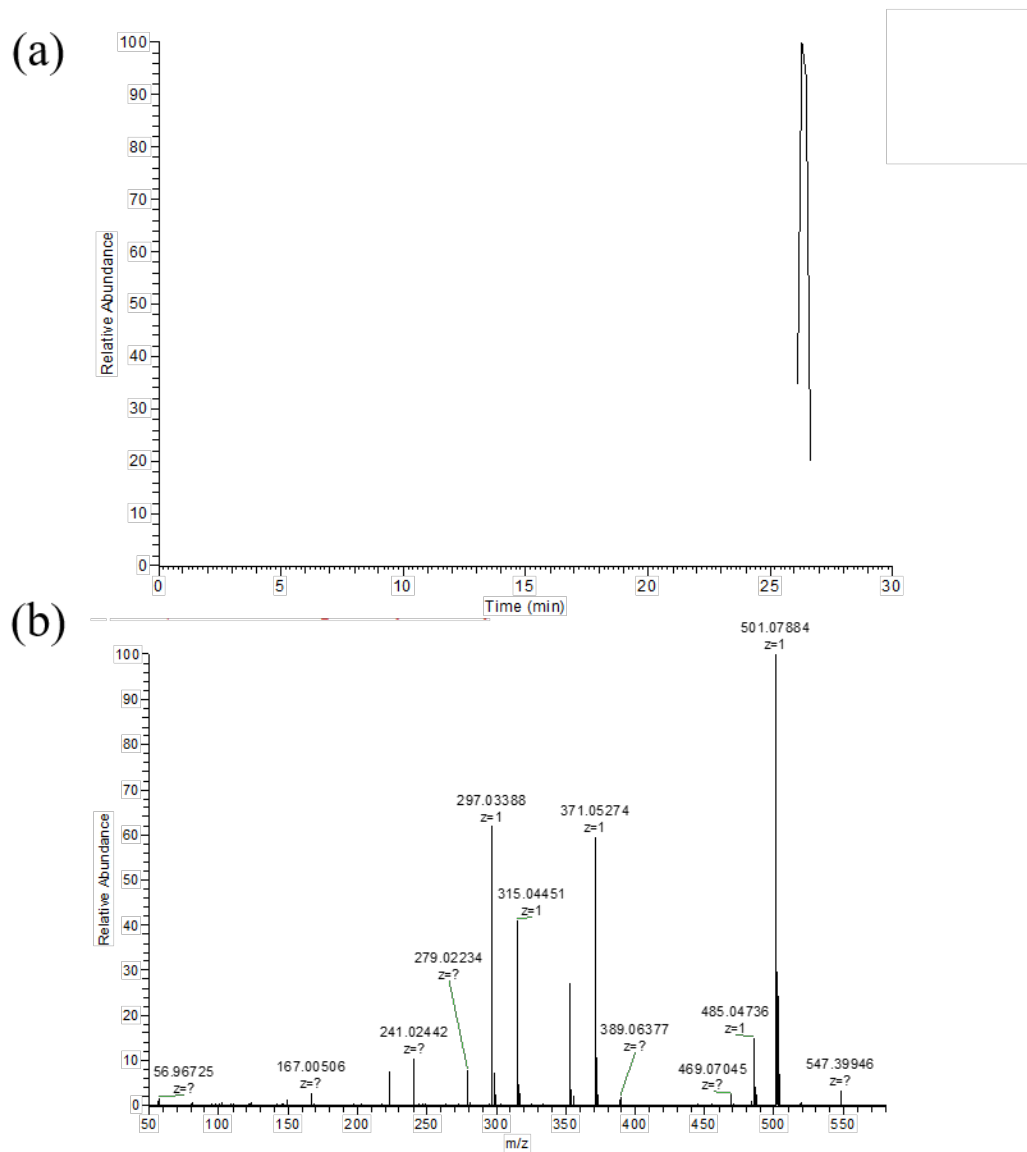
Appendix Figure 48. (a) LC-MS/MS ion chromatogram showing the product ion profile and (b) LC-MS/MS product spectrum of the precursor ion m/z 501.09 in Appendix Table 10.



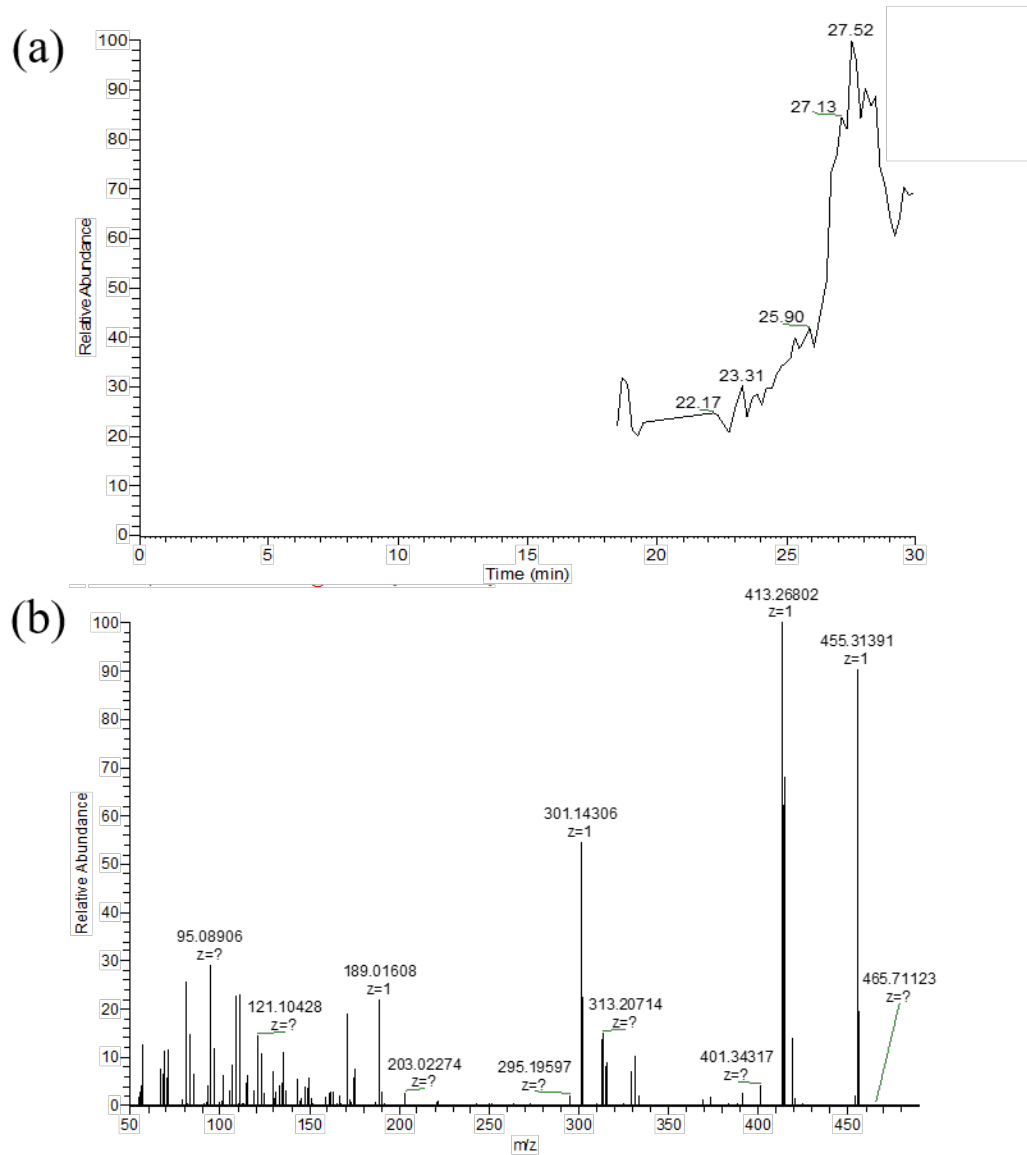
Appendix Figure 49. (a) LC-MS/MS ion chromatogram showing the product ion profile and (b) LC-MS/MS product spectrum of the precursor ion m/z 161.06 in Appendix Table 10.



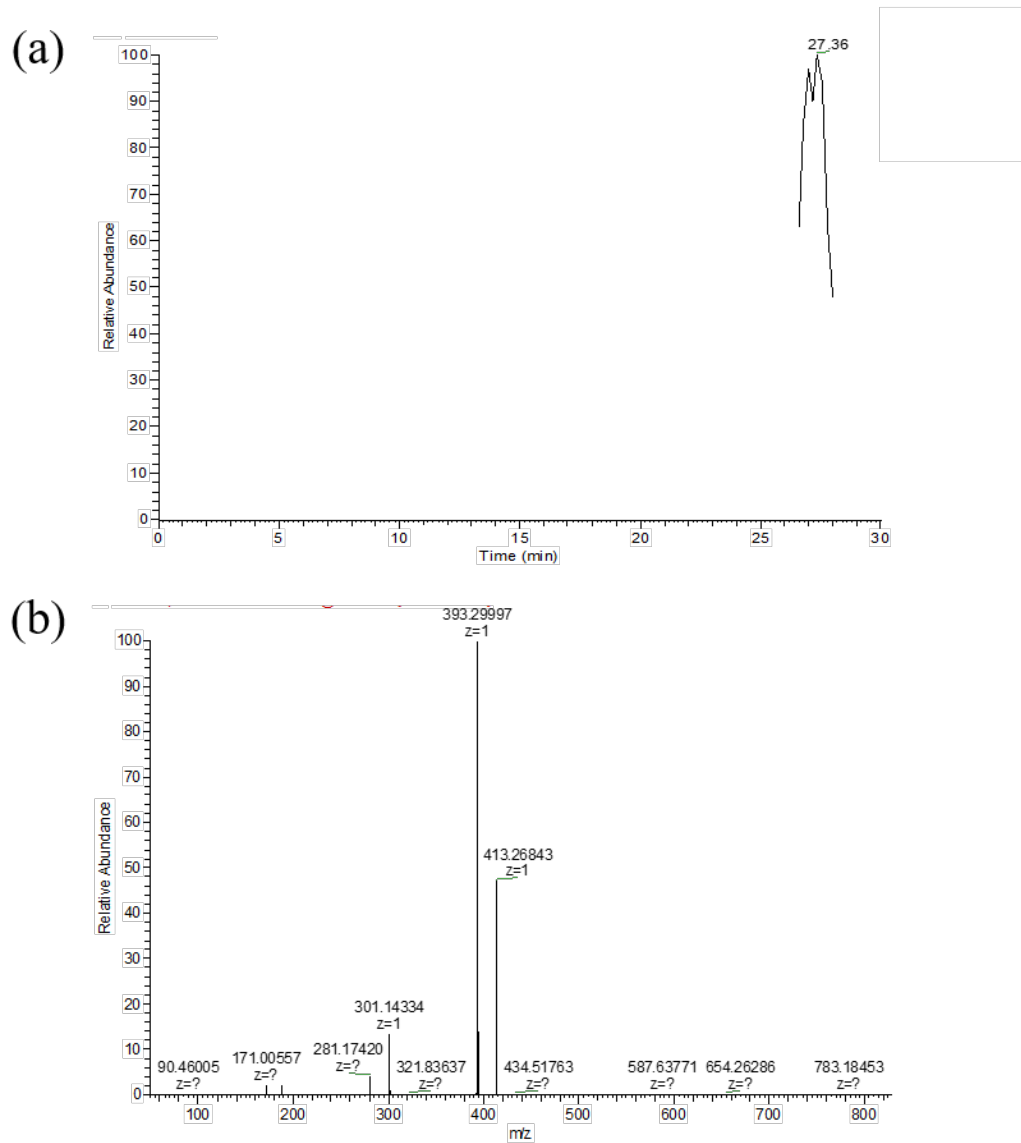
Appendix Figure 50. (a) LC-MS/MS ion chromatogram showing the product ion profile and (b) LC-MS/MS product spectrum of the precursor ion m/z 271.55 in Appendix Table 10.



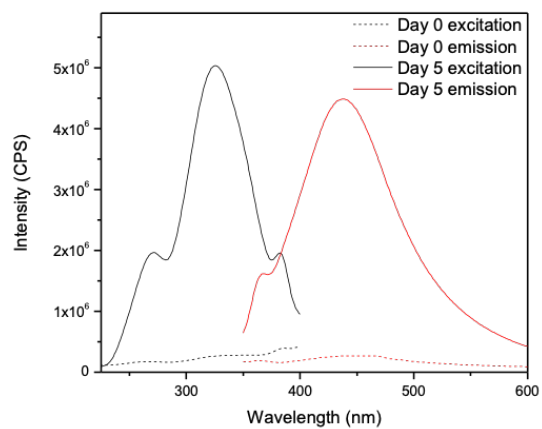
Appendix Figure 51. (a) LC-MS/MS ion chromatogram showing the product ion profile and (b) LC-MS/MS product spectrum of the precursor ion m/z 547.08 in Appendix Table 10.



Appendix Figure 52. (a) LC-MS/MS ion chromatogram showing product the ion profile and (b) LC-MS/MS product spectrum of the precursor ion m/z 455.31 in Appendix Table 10.



Appendix Figure 53. (a) LC-MS/MS ion chromatogram showing the product ion profile and (b) LC-MS/MS product spectrum of the precursor ion m/z 783.58 in Appendix Table 10.



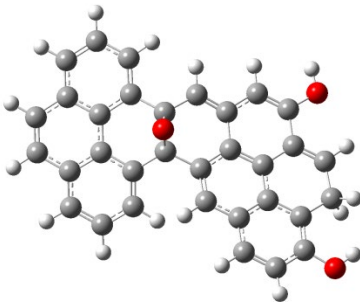
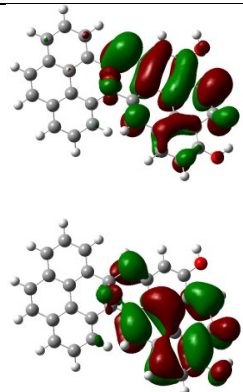
Appendix Figure 54. PL excitation (black line) and emission spectra (red line) of GO before (dashed line) and after (solid line) 5-day enzymatic degradation. The PL emission spectra were obtained with excitation at 325 nm. The excitation spectra were obtained at emission wavelength 440 nm.

Appendix Table 12. Comparison of PL emission under different excitations of GO after 5-day MPO-catalyzed degradation.

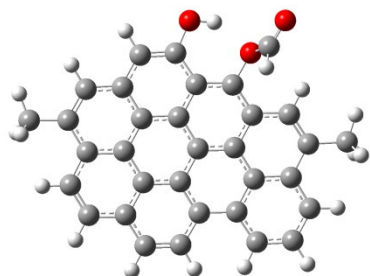
λ_{ex} (nm)	λ_{em} (nm)
275	450
300	439
325	440
350	452
375	461

More information about PL results in Appendix Figure 54 and Appendix Table 12 can be found in previous publication.^{S1}

Appendix Table 13. The calculated set of vertical excitations and fluorescence energies (in nm units) obtained at CAM-B3LYP/6-311+G(2d,p) level of theory for the molecular systems decorated with ester, ether (epoxide), and/or carbonyl groups considered in this work under solvation (water) condition. The labels A and B refer to $C_{33}H_{18}O_3$ and $C_{25}H_{18}O_{10}$ stoichiometries, respectively. For absorption transitions selective excitations with oscillator strengths f larger than 0.01 are indicated, with excitations in the (325 ± 21) nm range indicated in bold

System	Molecular Structure	Absorption Transition	Excitation		LUMO / HOMO Orbitals
			Energy / Oscillator Strength	Fluorescence Energy ^a	
A1		S0→S1	349.0 (0.3257)	440.6	
		S0→S2	320.4 (0.1704)		
		S0→S3	306.6 (0.1138)		
		S0→S4	297.4 (0.0142)		
		S0→S6	278.8 (0.0366)		

A2



S0→S1 401.5 (0.6801)

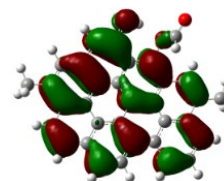
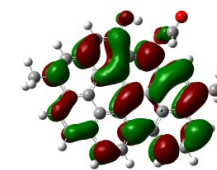
S0→S2 388.1 (0.1844)

S0→S3 **314.0** (0.6187)

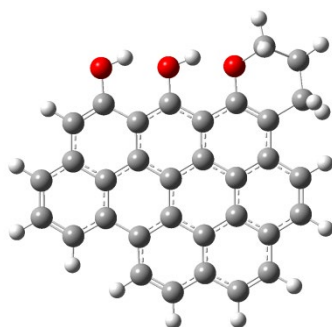
S0→S4 302.0 (0.3154)

S0→S5 280.7 (0.1419)

451.7



A3



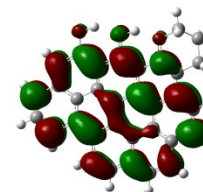
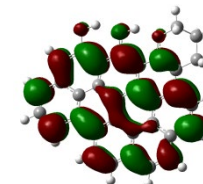
S0→S1 397.1 (0.2188)

S0→S2 381.3 (0.1301)

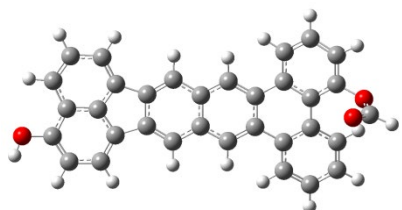
S0→S3 **311.7** (0.2554)S0→S5 **317.4** (0.0627)

S0→S7 276.8 (0.1785)

444.5



A4



S0→S1 360.6 (0.3687)

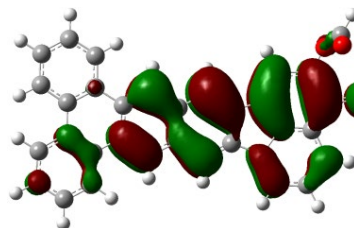
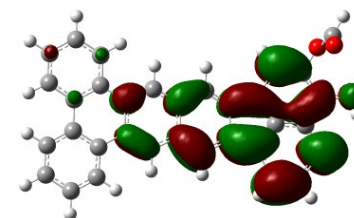
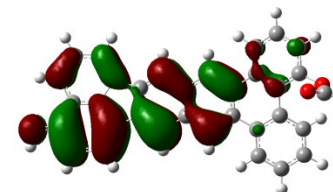
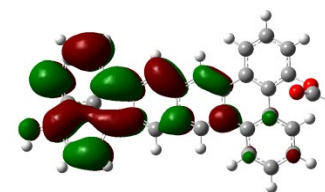
S0→S2 347.4 (0.0541)

S0→S3 **312.4** (0.8449)

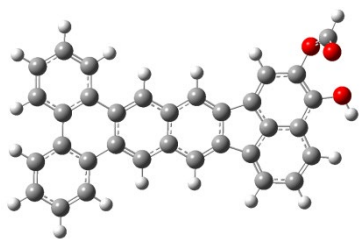
S0→S4 302.0 (0.5615)

S0→S7 281.0 (0.0339)

443.1



A5



S0→S1 362.2 (0.4148)

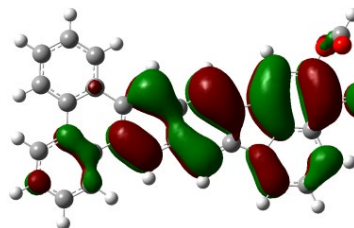
S0→S2 344.1 (0.0235)

S0→S3 **311.7** (0.6386)

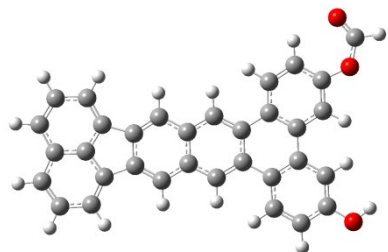
S0→S4 305.3 (0.7177)

S0→S6 273.7 (0.5372)

438.9



A6



S0→S1 355.5 (0.3083)

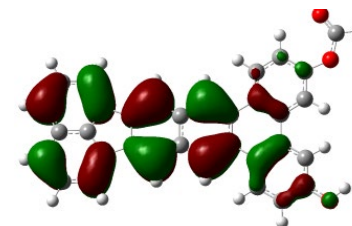
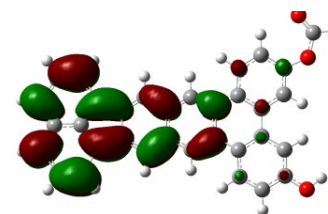
S0→S2 **327.0** (1.7714)

S0→S4 **305.2** (0.2268)

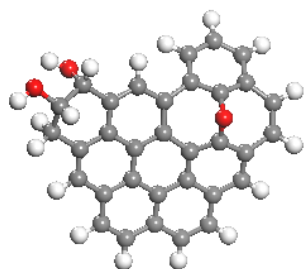
S0→S7 282.5 (0.0388)

S0→S9 265.9 (0.0209)

420.4



A7



S0→S1 369.9 (0.6308)

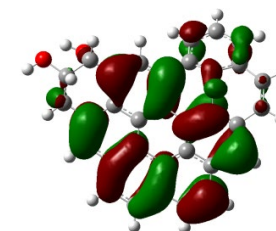
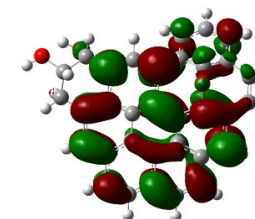
S0→S2 354.4 (0.1092)

S0→S3 359.0 (0.1143)

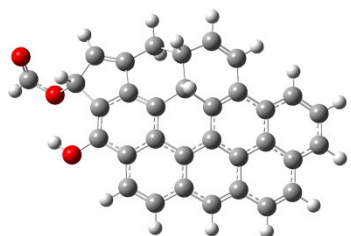
S0→S4 **308.1** (0.2408)

S0→S6 278.1 (0.0605)

419.3



A8



S0→S1 376.4 (0.2774)

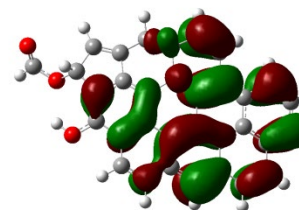
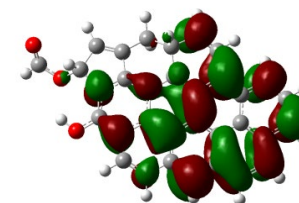
S0→S3 **319.9** (0.2905)

S0→S4 301.7 (0.0996)

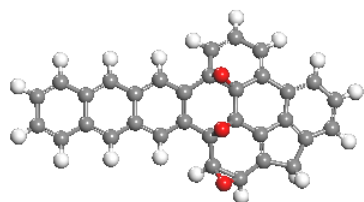
S0→S5 298.4 (0.1621)

S0→S8 270.15 (0.2340)

449.7



A9



S0→S1 350.88 (0.0459)

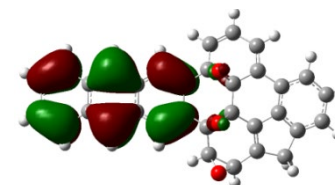
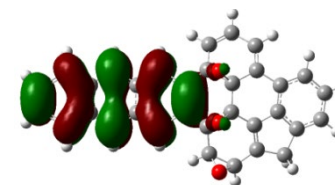
S0→S2 **326.8** (0.3155)

S0→S3 310.4 (0.0036)

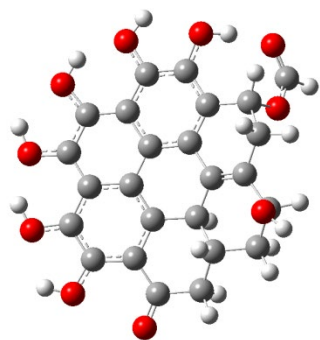
S0→S4 287.1 (0.0448)

S0→S5 299.96 (0.0066)

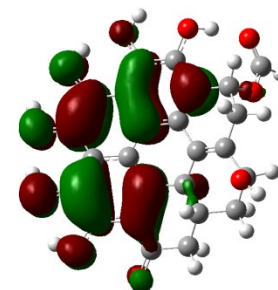
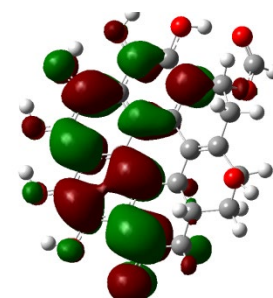
435.6



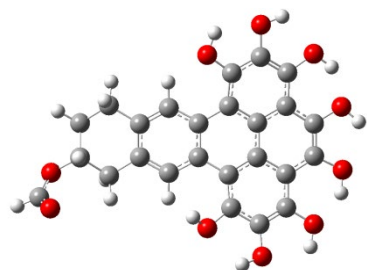
B1



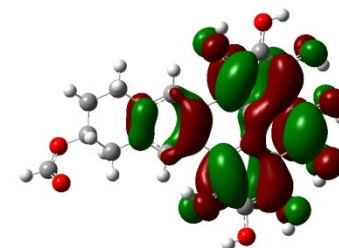
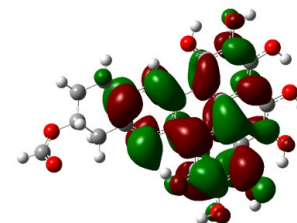
S0→S1	359.6 (0.0740)	455.2
S0→S2	341.0 (0.2515)	
S0→S4	304.6 (0.1769)	
S0→S6	277.7 (0.2598)	
S0→S7	269.4 (0.2183)	



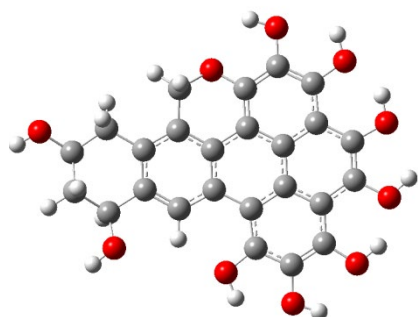
B2



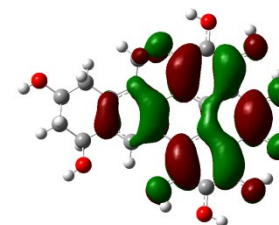
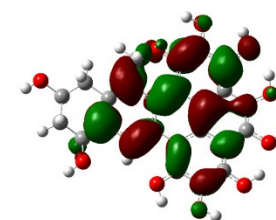
S0→S1	343.6 (0.0612)	423.2
S0→S2	327.5 (0.1768)	
S0→S3	288.4 (0.1865)	
S0→S4	273.6 (0.4688)	
S0→S7	266.5 (0.3121)	



B3



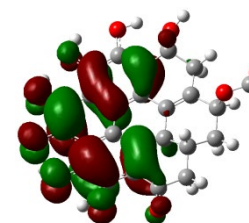
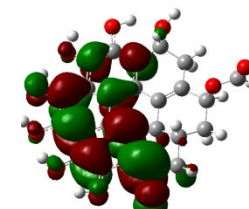
S0→S1	346.8 (0.0765)	423.0
S0→S2	331.5 (0.1725)	
S0→S3	287.8 (0.1619)	
S0→S6	274.4 (0.4488)	
S0→S7	264.6 (0.3078)	



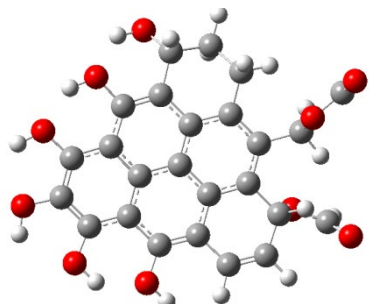
B4



S0→S1	357.6 (0.0634)	461.7
S0→S2	341.4 (0.2191)	
S0→S3	315.5 (0.2169)	
S0→S5	305.6 (0.1310)	
S0→S6	276.8 (0.2580)	



B5



S0→S1

S0→S2

344.6 (0.1334)

S0→S3

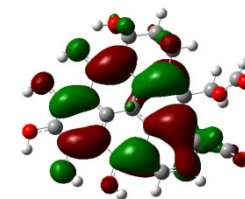
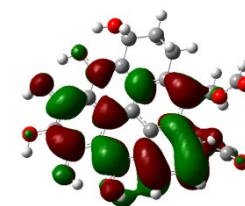
296.5 (0.0460)

S0→S4

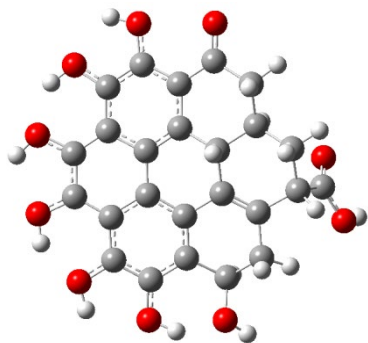
S0→S5

S0→S6

430.2



B6



S0→S1

358.2 (0.0525)

S0→S2

351.5 (0.5259)

S0→S3

314.7 (0.2101)

S0→S4

314.6 (0.2100)

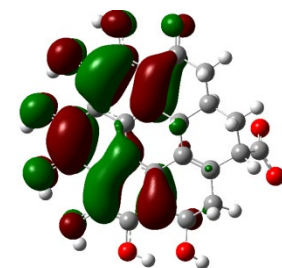
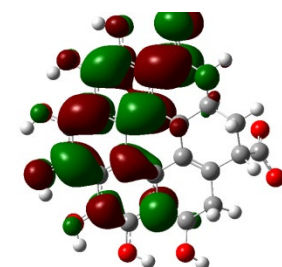
S0→S5

301.4 (0.0502)

S0→S6

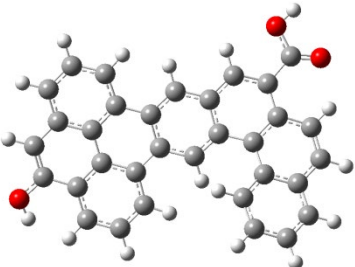
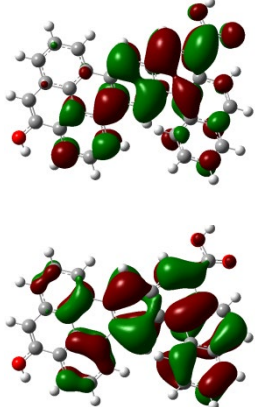
278.2 (0.2473)

461.7

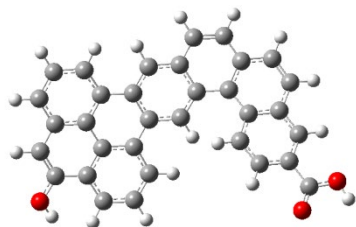


^a fluorescence transition corresponds to $\pi^* \rightarrow \pi$ transition in agreement with previous findings.^{S4, S5}

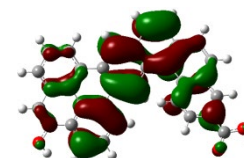
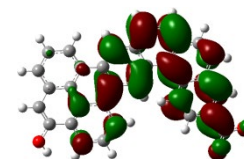
Appendix Table 14. The calculated set of vertical excitations and fluorescence energies (in nm units) obtained at CAM-B3LYP/6-311+G(2d,p) level of theory under solvation (water) condition for the case of structures decorated with OH and COOH groups. The labels C and D refer to C₃₃H₁₈O₃ and C₂₅H₁₈O₁₀ stoichiometries, respectively. For absorption transitions selective excitations with oscillator strengths f larger than 0.01 are indicated, with excitations in the (325 ± 21) nm range indicated in bold.

System	Molecular Structure	Absorption Transition	Excitation		LUMO Orbitals	HOMO
			Energy	Fluorescence Energy		
C1		S0→S2	341.1 (0.0971)		435.7	
		S0→S3	315.4 (0.5410)			
		S0→S4	308.0 (0.2097)			
		S0→S7	278.9 (0.1181)			
		S0→S6	277.5 (0.1504)			

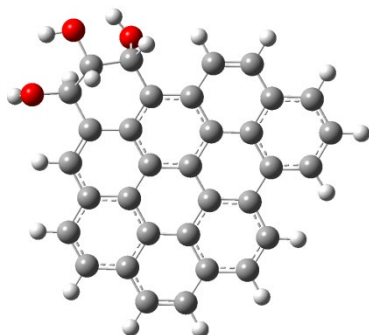
C2



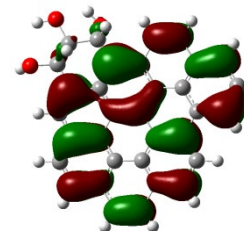
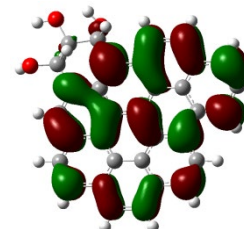
S0→S2	339.1 (0.0457)	
S0→S3	301.7 (0.7880)	421.6
S0→S4	306.4 (0.4149)	
S0→S6	285.3 (0.1249)	

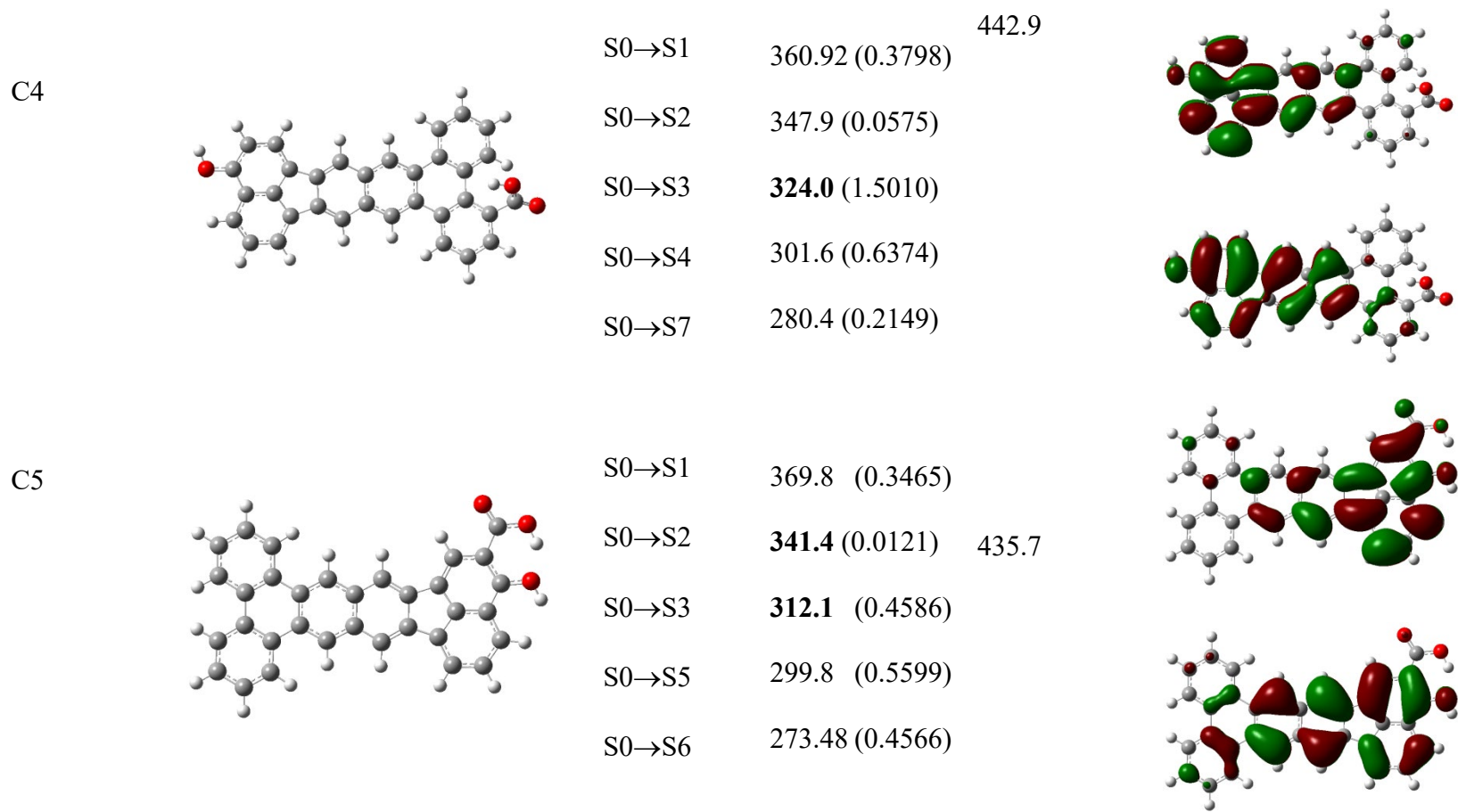


C3

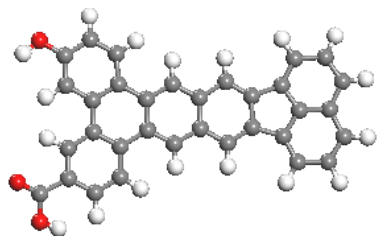


S0→S2	375.4 (0.1571)	
S0→S3	295.6 (0.4560)	427.5
S0→S4	307.7 (0.4502)	
S0→S5	293.45 (0.0395)	
S0→S6	278.1 (0.5785)	

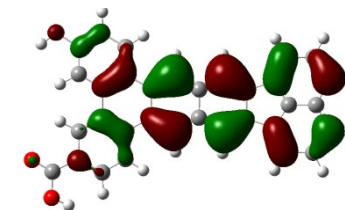
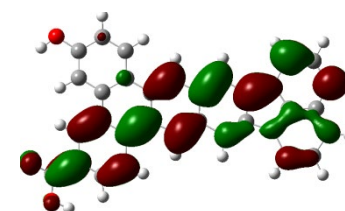




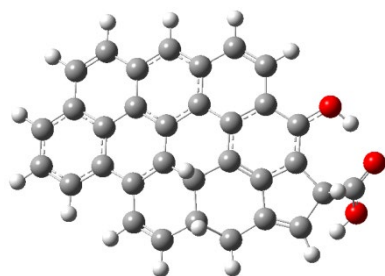
C6



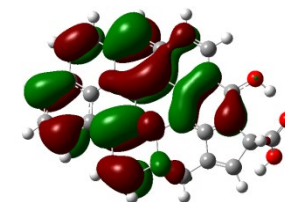
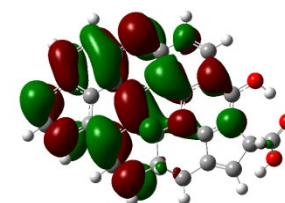
S0→S1	364.5 (0.3845)	422.8
S0→S2	344.9 (0.0621)	
S0→S3	318.1 (1.3181)	
S0→S4	302.7 (0.3249)	
S0→S6	287.4 (0.3293)	



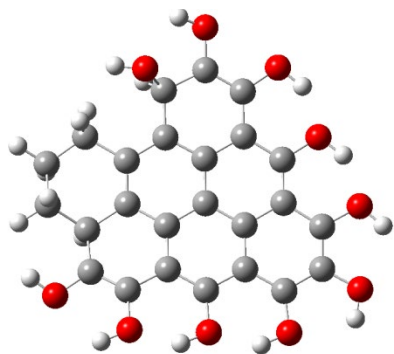
C7



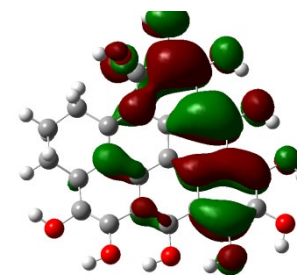
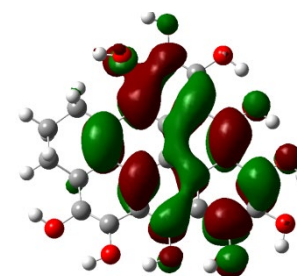
S0→S1	375.7 (0.2693)	450.2
S0→S3	320.1 (0.3278)	
S0→S4	306.9 (0.0874)	
S0→S5	300.2 (0.1821)	
S0→S6	288.3 (0.2815)	



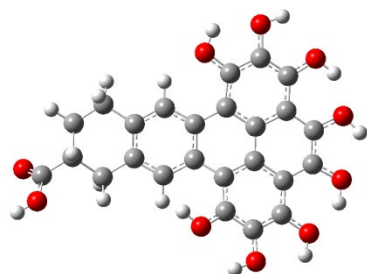
D1



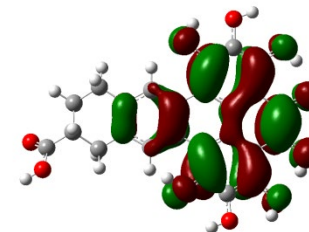
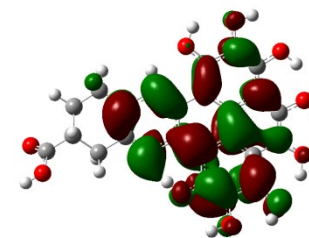
S0→S1	348.2 (0.2525)	419.6
S0→S3	329.2 (0.0652)	
S0→S4	290.8 (0.0683)	
S0→S6	283.4 (0.0489)	



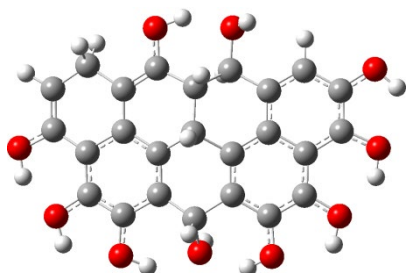
D2



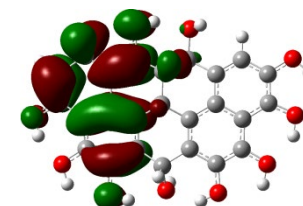
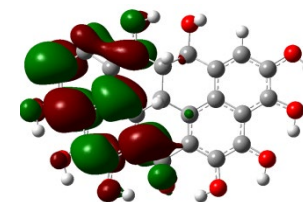
S0→S1	343.3 (0.0609)	423.2
S0→S2	327.2 (0.1770)	
S0→S3	288.1 (0.1861)	
S0→S4	273.5 (0.4724)	
S0→S6	278.1 (0.0261)	



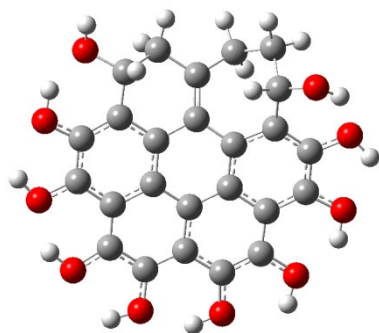
D3



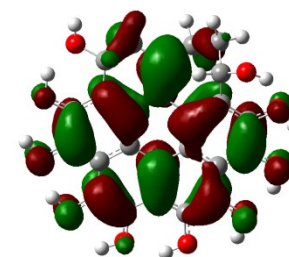
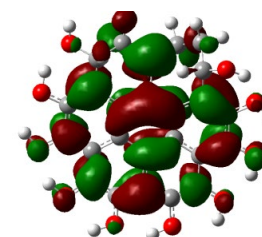
S0→S1	325.6 (0.1341)	428.5
S0→S2	307.2 (0.0708)	
S0→S3	300.3 (0.0677)	
S0→S4	298.4 (0.0180)	
S0→S5	269.0 (0.2881)	



D4



S0→S1	387.3 (0.1278)	456.6
S0→S3	310.8 (0.5529)	
S0→S4	288.8 (0.0423)	
S0→S5	286.0 (0.0148)	
S0→S6	277.1 (0.1926)	

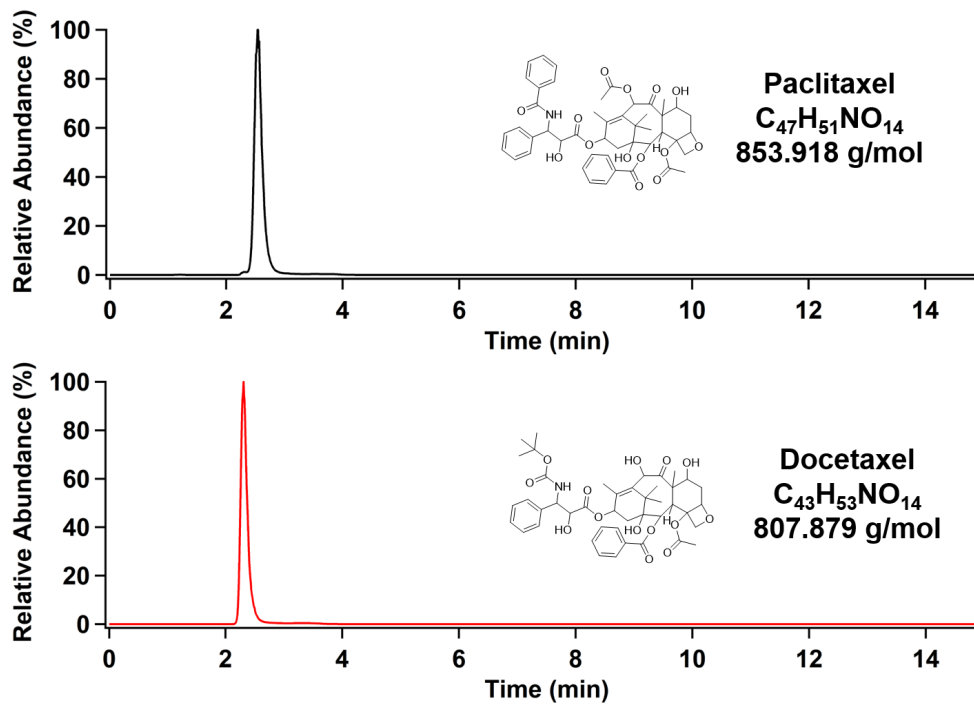


References

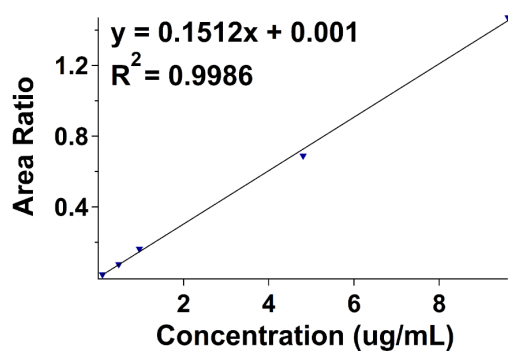
- S1. He, X.; White, D. L.; Kapralov, A. A.; Kagan, V. E.; Star, A. Photoluminescence Response in Carbon Nanomaterials to Enzymatic Degradation. *Anal. Chem.* **2020**, *92*, 12880-12890.
- S2. Barbier Saint Hilaire, P.; Rousseau, K.; Seyer, A.; Dechaumet, S.; Damont, A.; Junot, C.; Fenaille, F. Comparative Evaluation of Data Dependent and Data Independent Acquisition Workflows Implemented on an Orbitrap Fusion for Untargeted Metabolomics. *Metabolites* **2020**, *10*, 158.
- S3. Krasny, L.; Huang, P. H. Data-independent acquisition mass spectrometry (DIA-MS) for proteomic applications in oncology. *Mol. Omics* **2021**, *17*, 29-42.
- S4. Pu, L. Fluorescence of organic molecules in chiral recognition. *Chem. Rev.* **2004**, *104*, 1687-1716.
- S5. Improta, R.; Barone, V. Absorption and fluorescence spectra of uracil in the gas phase and in aqueous solution: A TD-DFT quantum mechanical study. *J. Am. Chem. Soc.* **2004**, *126*, 14320-14321.

Appendix A.4 Quantitative Analysis of Drug Loading and Release in Carbon Nanodelivery System

This section contains supporting information for Chapter 4.2.



Appendix Figure 55. LC-MS chromatogram of paclitaxel and docetaxel with associated chemical structure and molecular weight.



Appendix Figure 56. Calibration plot for the quantification of paclitaxel.

Appendix B Publications

- (1) He, X.; Sorescu, D. C.; Star, A. Composition and Structure of Fluorescent Graphene Quantum Dots Generated by Enzymatic Degradation of Graphene Oxide. *J. Phys. Chem. C* **2021**, 125, 24, 13361-13369.
- (2) Zeng, Z.; Sorescu, D. C.; White, D. L.; Hwang, S. I.; Shao, W.; He, X.; Schulte, Z. M.; Rosi, N. L.; Star, A. Heterogenous Growth of UiO-66-NH₂ on Oxidized Single-Walled Carbon Nanotubes to Form “Beads-on-a-String” Composites. *ACS Appl. Mater. Interfaces* **2021**, 13, 15482-15489.
- (3) He, X.; Kevlishvili, I.; Murcek, K.; Liu P.; Star, A. $[2\pi + 2\pi]$ Photocycloaddition of Enones to Single-Walled Carbon Nanotubes Creates Fluorescent Quantum Defects. *ACS Nano* 2021, 15, 4833-4844.
- (4) Shao, W.; Shurin, M. R.; Wheeler, S. E.; He, X.; Star, A. Rapid Detection of SARS-CoV-2 Antigens using High Purity Semiconducting Single-Walled Carbon Nanotube-based Field-Effect Transistor. *ACS Appl. Mater. Interfaces* 2021, 13, 10321-10327.
- (5) He, X.; White, D. L.; Kapralov, A. A.; Kagan, V. E.; Star, A. Photoluminescence Response in Carbon Nanomaterials to Enzymatic Degradation. *Anal. Chem.* 2020, 92, 19, 12880-12890.
- (6) White, D. L.; Lystrom, L.; He, X.; Burkert, S. C.; Kilin, D. S.; Kilina, S.; Star, A. Synthesis of Holey Graphene Nanoparticle Compounds. *ACS Appl. Mater. Interfaces* 2020, 12, 36513-36522.
- (7) Burkert, S. C.; Shurin, G. V.; White, D. L.; He, X.; Kapralov, A. A.; Kagan, V. E.; Shurin, M.

- R.; Star, A. Targeting myeloid regulators by paclitaxel-loaded enzymatically degradable nanocups. *Nanoscale* **2018**, *10*, 17990-18000.
- (8) Ge, T.; Hua, Z.; He, X.; Lv, J.; Chen, H.; Zhang, L.; Yao, H.; Liu, Z.; Lin, C.; Shi, J. On the Mesopore-Free Synthesis of Single-Crystalline Hierarchically Structured ZSM-5 Zeolites in a Quasi-Solid-State System. *Chem. Eur. J.* **2016**, *22*, 7895-7905.
- (9) He, X.; Ge, T.; Hua, Z.; Zhou, J.; Lv, J.; Zhou, J.; Liu, Z.; Shi, J. Mesopore-Free Synthesis of Hierarchically Structured Zeolites with Variable Si/Al Ratios via a Steam-Assisted Crystallization Process. *ACS Appl. Mater. Interfaces* **2016**, *8*, 7118-7124.
- (10) Ge, T.; Hua, Z.; He, X.; Zhu, Y.; Ren, W.; Chen, L.; Zhang, L.; Chen, H.; Lin, C.; Yao, H.; Shi, J. One-pot synthesis of hierarchically structured ZSM-5 zeolites using single micropore-templating. *Chinese J. Catal.* **2015**, *36*, 866-873.
- (11) Han, C.; Pi, Y.; An, Q.; Mai, L.; Xie, J.; Xu, X.; Xu, L.; Zhao, Y.; Niu, C.; Khan, A. M.; He, X. Substrate-Assisted Self-Organization of Radial β -AgVO₃ Nanowire Clusters for High Rate Rechargeable Lithium Batteries. *Nano Lett.* **2012**, *12*, 4668-4673.

Bibliography

1. Geim, A. K.; Novoselov, K. S., The rise of graphene. *Nature Materials* **2007**, *6* (3), 183-191.
2. Nikolaev, P.; Bronikowski, M. J.; Bradley, R. K.; Rohmund, F.; Colbert, D. T.; Smith, K. A.; Smalley, R. E., Gas-phase catalytic growth of single-walled carbon nanotubes from carbon monoxide. *Chemical Physics Letters* **1999**, *313* (1), 91-97.
3. Resasco, D. E.; Alvarez, W. E.; Pompeo, F.; Balzano, L.; Herrera, J. E.; Kitiyanan, B.; Borgna, A., A Scalable Process for Production of Single-walled Carbon Nanotubes (SWNTs) by Catalytic Disproportionation of CO on a Solid Catalyst. *Journal of Nanoparticle Research* **2002**, *4* (1), 131-136.
4. Graupner, R., Raman spectroscopy of covalently functionalized single-wall carbon nanotubes. *Journal of Raman Spectroscopy* **2007**, *38* (6), 673-683.
5. Chen, D.; Feng, H.; Li, J., Graphene Oxide: Preparation, Functionalization, and Electrochemical Applications. *Chemical Reviews* **2012**, *112* (11), 6027-6053.
6. Zhu, Y.; Murali, S.; Cai, W.; Li, X.; Suk, J. W.; Potts, J. R.; Ruoff, R. S., Graphene and Graphene Oxide: Synthesis, Properties, and Applications. *Advanced Materials* **2010**, *22* (35), 3906-3924.
7. Cote, L. J.; Kim, F.; Huang, J., Langmuir–Blodgett Assembly of Graphite Oxide Single Layers. *Journal of the American Chemical Society* **2009**, *131* (3), 1043-1049.
8. Paredes, J. I.; Villar-Rodil, S.; Solís-Fernández, P.; Martínez-Alonso, A.; Tascón, J. M. D., Atomic Force and Scanning Tunneling Microscopy Imaging of Graphene Nanosheets Derived from Graphite Oxide. *Langmuir* **2009**, *25* (10), 5957-5968.
9. Kudin, K. N.; Ozbas, B.; Schniepp, H. C.; Prud'homme, R. K.; Aksay, I. A.; Car, R., Raman Spectra of Graphite Oxide and Functionalized Graphene Sheets. *Nano Letters* **2008**, *8* (1), 36-41.
10. Lee, V.; Whittaker, L.; Jaye, C.; Baroudi, K. M.; Fischer, D. A.; Banerjee, S., Large-Area Chemically Modified Graphene Films: Electrophoretic Deposition and Characterization by Soft X-ray Absorption Spectroscopy. *Chemistry of Materials* **2009**, *21* (16), 3905-3916.
11. Ganguly, A.; Sharma, S.; Papakonstantinou, P.; Hamilton, J., Probing the Thermal Deoxygenation of Graphene Oxide Using High-Resolution In Situ X-ray-Based Spectroscopies. *The Journal of Physical Chemistry C* **2011**, *115* (34), 17009-17019.

12. Gao, W.; Alemany, L. B.; Ci, L.; Ajayan, P. M., New insights into the structure and reduction of graphite oxide. *Nature Chemistry* **2009**, *1* (5), 403-408.
13. Mattevi, C.; Eda, G.; Agnoli, S.; Miller, S.; Mkhoyan, K. A.; Celik, O.; Mastrogiovanni, D.; Granozzi, G.; Garfunkel, E.; Chhowalla, M., Evolution of Electrical, Chemical, and Structural Properties of Transparent and Conducting Chemically Derived Graphene Thin Films. *Advanced Functional Materials* **2009**, *19* (16), 2577-2583.
14. Lee, D. W.; De Los Santos V, L.; Seo, J. W.; Felix, L. L.; Bustamante D, A.; Cole, J. M.; Barnes, C. H. W., The Structure of Graphite Oxide: Investigation of Its Surface Chemical Groups. *The Journal of Physical Chemistry B* **2010**, *114* (17), 5723-5728.
15. Zhang, W.; Carravetta, V.; Li, Z.; Luo, Y.; Yang, J., Oxidation states of graphene: Insights from computational spectroscopy. *The Journal of Chemical Physics* **2009**, *131* (24), 244505.
16. Cai, W.; Piner, R. D.; Stadermann, F. J.; Park, S.; Shaibat, M. A.; Ishii, Y.; Yang, D.; Velamakanni, A.; An, S. J.; Stoller, M.; An, J.; Chen, D.; Ruoff, R. S., Synthesis and Solid-State NMR Structural Characterization of ^{13}C -Labeled Graphite Oxide. *Science* **2008**, *321* (5897), 1815.
17. Si, Y.; Samulski, E. T., Synthesis of Water Soluble Graphene. *Nano Letters* **2008**, *8* (6), 1679-1682.
18. Casabianca, L. B.; Shaibat, M. A.; Cai, W. W.; Park, S.; Piner, R.; Ruoff, R. S.; Ishii, Y., NMR-Based Structural Modeling of Graphite Oxide Using Multidimensional ^{13}C Solid-State NMR and ab Initio Chemical Shift Calculations. *Journal of the American Chemical Society* **2010**, *132* (16), 5672-5676.
19. Bagri, A.; Mattevi, C.; Acik, M.; Chabal, Y. J.; Chhowalla, M.; Shenoy, V. B., Structural evolution during the reduction of chemically derived graphene oxide. *Nature Chemistry* **2010**, *2* (7), 581-587.
20. Acik, M.; Lee, G.; Mattevi, C.; Pirkle, A.; Wallace, R. M.; Chhowalla, M.; Cho, K.; Chabal, Y., The Role of Oxygen during Thermal Reduction of Graphene Oxide Studied by Infrared Absorption Spectroscopy. *The Journal of Physical Chemistry C* **2011**, *115* (40), 19761-19781.
21. Sudesh; Kumar, N.; Das, S.; Bernhard, C.; Varma, G. D., Effect of graphene oxide doping on superconducting properties of bulk MgB_2 . *Superconductor Science and Technology* **2013**, *26* (9), 095008.
22. Li, Z.; Chen, F.; Yuan, L.; Liu, Y.; Zhao, Y.; Chai, Z.; Shi, W., Uranium(VI) adsorption on graphene oxide nanosheets from aqueous solutions. *Chemical Engineering Journal* **2012**, *210*, 539-546.

23. Dresselhaus, M. S.; Jorio, A.; Hofmann, M.; Dresselhaus, G.; Saito, R., Perspectives on Carbon Nanotubes and Graphene Raman Spectroscopy. *Nano Letters* **2010**, *10* (3), 751-758.
24. Zhao, Y.; Burkert, S. C.; Tang, Y.; Sorescu, D. C.; Kapralov, A. A.; Shurin, G. V.; Shurin, M. R.; Kagan, V. E.; Star, A., Nano-Gold Corking and Enzymatic Uncorking of Carbon Nanotube Cups. *J. Am. Chem. Soc.* **2015**, *137* (2), 675-684.
25. Burkert, S. C.; Star, A., Corking Nitrogen-Doped Carbon Nanotube Cups with Gold Nanoparticles for Biodegradable Drug Delivery Applications. *Current Protocols in Chemical Biology* **2015**, *7* (4), 249-262.
26. Maiti, D.; Tong, X.; Mou, X.; Yang, K., Carbon-Based Nanomaterials for Biomedical Applications: A Recent Study. *Frontiers in Pharmacology* **2019**, *9* (1401).
27. Hui, Y. Y.; Chang, H.-C.; Dong, H.; Zhang, X., *Carbon nanomaterials for bioimaging, bioanalysis, and therapy*. John Wiley & Sons: 2019.
28. Shin, S. R.; Shin, C.; Memic, A.; Shadmehr, S.; Miscuglio, M.; Jung, H. Y.; Jung, S. M.; Bae, H.; Khademhosseini, A.; Tang, X., Aligned carbon nanotube-based flexible gel substrates for engineering biohybrid tissue actuators. *Advanced functional materials* **2015**, *25* (28), 4486-4495.
29. Martínez, L. M. T.; Kharissova, O. V.; Kharisov, B. I., *Handbook of ecomaterials*. **2019**.
30. Azizi-Lalabadi, M.; Hashemi, H.; Feng, J.; Jafari, S. M., Carbon nanomaterials against pathogens; the antimicrobial activity of carbon nanotubes, graphene/graphene oxide, fullerenes, and their nanocomposites. *Advances in Colloid and Interface Science* **2020**, *284*, 102250.
31. Schleh, C.; Rothen-Rutishauser, B.; Kreyling, W. G., The influence of pulmonary surfactant on nanoparticulate drug delivery systems. *European Journal of Pharmaceutics and Biopharmaceutics* **2011**, *77* (3), 350-352.
32. Kapralov, A. A.; Feng, W. H.; Amoscato, A. A.; Yanamala, N.; Balasubramanian, K.; Winnica, D. E.; Kisin, E. R.; Kotchey, G. P.; Gou, P.; Sparvero, L. J.; Ray, P.; Mallampalli, R. K.; Klein-Seetharaman, J.; Fadeel, B.; Star, A.; Shvedova, A. A.; Kagan, V. E., Adsorption of Surfactant Lipids by Single-Walled Carbon Nanotubes in Mouse Lung upon Pharyngeal Aspiration. *ACS Nano* **2012**, *6* (5), 4147-4156.
33. Kumar, A.; Dhawan, A., *Nanoparticle-Protein Corona: Biophysics to Biology*. Royal Society of Chemistry: 2019; Vol. 40.
34. Breznica, P.; Koliqi, R.; Daka, A., A review of the current understanding of nanoparticles protein corona composition. *Med Pharm Rep* **2020**, *93* (4), 342-350.

35. Bhattacharya, K.; Andón, F. T.; El-Sayed, R.; Fadeel, B., Mechanisms of carbon nanotube-induced toxicity: Focus on pulmonary inflammation. *Advanced Drug Delivery Reviews* **2013**, *65* (15), 2087-2097.
36. Castranova, V.; Schulte, P. A.; Zumwalde, R. D., Occupational Nanosafety Considerations for Carbon Nanotubes and Carbon Nanofibers. *Accounts of Chemical Research* **2013**, *46* (3), 642-649.
37. Bianco, A., Graphene: Safe or Toxic? The Two Faces of the Medal. *Angewandte Chemie International Edition* **2013**, *52* (19), 4986-4997.
38. Schinwald, A.; Murphy, F. A.; Jones, A.; MacNee, W.; Donaldson, K., Graphene-Based Nanoplatelets: A New Risk to the Respiratory System as a Consequence of Their Unusual Aerodynamic Properties. *ACS Nano* **2012**, *6* (1), 736-746.
39. Kostarelos, K.; Novoselov, K. S., Exploring the Interface of Graphene and Biology. *Science* **2014**, *344* (6181), 261.
40. Kotchey, G. P.; Allen, B. L.; Vedala, H.; Yanamala, N.; Kapralov, A. A.; Tyurina, Y. Y.; Klein-Seetharaman, J.; Kagan, V. E.; Star, A., The enzymatic oxidation of graphene oxide. *ACS Nano* **2011**, *5* (3), 2098-108.
41. Zhou, X.; Zhang, Y.; Wang, C.; Wu, X.; Yang, Y.; Zheng, B.; Wu, H.; Guo, S.; Zhang, J., Photo-Fenton reaction of graphene oxide: a new strategy to prepare graphene quantum dots for DNA cleavage. *ACS Nano* **2012**, *6* (8), 6592-9.
42. Bai, H.; Jiang, W.; Kotchey, G. P.; Saidi, W. A.; Bythell, B. J.; Jarvis, J. M.; Marshall, A. G.; Robinson, R. A.; Star, A., Insight into the Mechanism of Graphene Oxide Degradation via the Photo-Fenton Reaction. *J Phys Chem C Nanomater Interfaces* **2014**, *118* (19), 10519-10529.
43. Kurapati, R.; Russier, J.; Squillaci, M. A.; Treossi, E.; Menard-Moyon, C.; Del Rio-Castillo, A. E.; Vazquez, E.; Samori, P.; Palermo, V.; Bianco, A., Dispersibility-Dependent Biodegradation of Graphene Oxide by Myeloperoxidase. *Small* **2015**, *11* (32), 3985-94.
44. Witko-Sarsat, V.; Rieu, P.; Descamps-Latscha, B.; Lesavre, P.; Halbwachs-Mecarelli, L., Neutrophils: molecules, functions and pathophysiological aspects. *Laboratory investigation; a journal of technical methods and pathology* **2000**, *80* (5), 617-53.
45. Hampton, M. B.; Kettle, A. J.; Winterbourn, C. C., Inside the neutrophil phagosome: oxidants, myeloperoxidase, and bacterial killing. *Blood* **1998**, *92* (9), 3007-17.
46. Kagan, V. E.; Konduru, N. V.; Feng, W.; Allen, B. L.; Conroy, J.; Volkov, Y.; Vlasova, II; Belikova, N. A.; Yanamala, N.; Kapralov, A.; Tyurina, Y. Y.; Shi, J.; Kisin, E. R.; Murray, A. R.; Franks, J.; Stolz, D.; Gou, P.; Klein-Seetharaman, J.; Fadeel, B.; Star,

- A.; Shvedova, A. A., Carbon nanotubes degraded by neutrophil myeloperoxidase induce less pulmonary inflammation. *Nat Nanotechnol* **2010**, *5* (5), 354-9.
47. Vlasova, I.; Sokolov, A. V.; Chekanov, A. V.; Kostevich, V. A.; Vasil'ev, V. B., Myeloperoxidase-induced biodegradation of single-walled carbon nanotubes is mediated by hypochlorite. *Bioorganicheskaya khimiya* **2011**, *37* (4), 510-21.
48. Mukherjee, S. P.; Gliga, A. R.; Lazzaretto, B.; Brandner, B.; Fielden, M.; Vogt, C.; Newman, L.; Rodrigues, A. F.; Shao, W.; Fournier, P. M.; Toprak, M. S.; Star, A.; Kostarelos, K.; Bhattacharya, K.; Fadeel, B., Graphene oxide is degraded by neutrophils and the degradation products are non-genotoxic. *Nanoscale* **2018**, *10* (3), 1180-1188.
49. Kagan, V. E.; Konduru, N. V.; Feng, W.; Allen, B. L.; Conroy, J.; Volkov, Y.; Vlasova, I. I.; Belikova, N. A.; Yanamala, N.; Kapralov, A.; Tyurina, Y. Y.; Shi, J.; Kisin, E. R.; Murray, A. R.; Franks, J.; Stolz, D.; Gou, P.; Klein-Seetharaman, J.; Fadeel, B.; Star, A.; Shvedova, A. A., Carbon nanotubes degraded by neutrophil myeloperoxidase induce less pulmonary inflammation. *Nature Nanotechnology* **2010**, *5* (5), 354-359.
50. Zhao, Y.; Burkert, S. C.; Tang, Y.; Sorescu, D. C.; Kapralov, A. A.; Shurin, G. V.; Shurin, M. R.; Kagan, V. E.; Star, A., Nano-gold corking and enzymatic uncorking of carbon nanotube cups. *J Am Chem Soc* **2015**, *137* (2), 675-84.
51. Usai, C.; Diaspro, A., Fluorescence: General Aspects. In *Encyclopedia of Biophysics*, Roberts, G. C. K., Ed. Springer Berlin Heidelberg: Berlin, Heidelberg, 2013; pp 826-832.
52. Nollet, L. M.; Toldra, F., UV-Visible Absorption, Fluorescence, and Chemiluminescence Spectroscopy. In *Handbook of Food Analysis-Two Volume Set*, CRC Press: 2015; pp 1417-1432.
53. Fluorescence Spectroscopy Principles. *Principles and Applications of Fluorescence Spectroscopy* **2007**, 88-114.
54. SádeČká, J.; TóThoVá, J., Fluorescence spectroscopy and chemometrics in the food classification-a review. *Czech Journal of Food Sciences* **2007**, *25* (4), 159-173.
55. Essig, S.; Marquardt, C. W.; Vijayaraghavan, A.; Ganzhorn, M.; Dehm, S.; Hennrich, F.; Ou, F.; Green, A. A.; Sciascia, C.; Bonaccorso, F.; Bohnen, K. P.; Löhneysen, H. v.; Kappes, M. M.; Ajayan, P. M.; Hersam, M. C.; Ferrari, A. C.; Krupke, R., Phonon-Assisted Electroluminescence from Metallic Carbon Nanotubes and Graphene. *Nano Letters* **2010**, *10* (5), 1589-1594.
56. Robertson, J.; O'Reilly, E. P., Electronic and atomic structure of amorphous carbon. *Physical Review B* **1987**, *35* (6), 2946-2957.

57. Mathioudakis, C.; Kopidakis, G.; Kelires, P. C.; Patsalas, P.; Gioti, M.; Logothetidis, S., Electronic and optical properties of a-C from tight-binding molecular dynamics simulations. *Thin Solid Films* **2005**, *482* (1), 151-155.
58. Chen, C. W.; Robertson, J., Nature of disorder and localization in amorphous carbon. *Journal of Non-Crystalline Solids* **1998**, *227-230*, 602-606.
59. Heitz, T.; Godet, C.; Bourée, J. E.; Dré villon, B.; Conde, J. P., Radiative and nonradiative recombination in polymerlike $\text{C}:\text{H}$ films. *Physical Review B* **1999**, *60* (8), 6045-6052.
60. Trauzettel, B.; Bulaev, D. V.; Loss, D.; Burkard, G., Spin qubits in graphene quantum dots. *Nature Physics* **2007**, *3* (3), 192-196.
61. Güttinger, J.; Frey, T.; Stampfer, C.; Ihn, T.; Ensslin, K., Spin States in Graphene Quantum Dots. *Physical Review Letters* **2010**, *105* (11), 116801.
62. Ritter, K. A.; Lyding, J. W., The influence of edge structure on the electronic properties of graphene quantum dots and nanoribbons. *Nature Materials* **2009**, *8* (3), 235-242.
63. Ma, L.; Wang, J.; Ding, F., Strain-Induced Orientation-Selective Cutting of Graphene into Graphene Nanoribbons on Oxidation. *Angewandte Chemie International Edition* **2012**, *51* (5), 1161-1164.
64. Son, Y.-W.; Cohen, M. L.; Louie, S. G., Energy Gaps in Graphene Nanoribbons. *Physical Review Letters* **2006**, *97* (21), 216803.
65. Eda, G.; Lin, Y.-Y.; Mattevi, C.; Yamaguchi, H.; Chen, H.-A.; Chen, I. S.; Chen, C.-W.; Chhowalla, M., Blue Photoluminescence from Chemically Derived Graphene Oxide. *Advanced Materials* **2010**, *22* (4), 505-509.
66. Weisman, R. B.; Bachilo, S. M., Dependence of Optical Transition Energies on Structure for Single-Walled Carbon Nanotubes in Aqueous Suspension: An Empirical Kataura Plot. *Nano Letters* **2003**, *3* (9), 1235-1238.
67. Weisman, R. B., Fluorimetric characterization of single-walled carbon nanotubes. *Analytical and Bioanalytical Chemistry* **2010**, *396* (3), 1015-1023.
68. Wu, B.; Geng, D.; Liu, Y., Evaluation of metallic and semiconducting single-walled carbon nanotube characteristics. *Nanoscale* **2011**, *3* (5), 2074-2085.
69. Yang, D.; Li, L.; Wei, X.; Wang, Y.; Zhou, W.; Kataura, H.; Xie, S.; Liu, H., Submilligram-scale separation of near-zigzag single-chirality carbon nanotubes by temperature controlling a binary surfactant system. *Science Advances* **2021**, *7* (8), eabe0084.

70. Bisker, G.; Dong, J.; Park, H. D.; Iverson, N. M.; Ahn, J.; Nelson, J. T.; Landry, M. P.; Kruss, S.; Strano, M. S., Protein-targeted corona phase molecular recognition. *Nature Communications* **2016**, *7* (1), 10241.
71. Iizumi, Y.; Yudasaka, M.; Kim, J.; Sakakita, H.; Takeuchi, T.; Okazaki, T., Oxygen-doped carbon nanotubes for near-infrared fluorescent labels and imaging probes. *Scientific Reports* **2018**, *8* (1), 6272.
72. Ma, X.; Hartmann, N. F.; Baldwin, J. K. S.; Doorn, S. K.; Htoon, H., Room-temperature single-photon generation from solitary dopants of carbon nanotubes. *Nature Nanotechnology* **2015**, *10* (8), 671-675.
73. He, X.; Htoon, H.; Doorn, S. K.; Pernice, W. H. P.; Pyatkov, F.; Krupke, R.; Jeantet, A.; Chassagneux, Y.; Voisin, C., Carbon nanotubes as emerging quantum-light sources. *Nature Materials* **2018**, *17* (8), 663-670.
74. Miyauchi, Y.; Iwamura, M.; Mouri, S.; Kawazoe, T.; Ohtsu, M.; Matsuda, K., Brightening of excitons in carbon nanotubes on dimensionality modification. *Nature Photonics* **2013**, *7* (9), 715-719.
75. Ghosh, S.; Bachilo, S. M.; Simonette, R. A.; Beckingham, K. M.; Weisman, R. B., Oxygen Doping Modifies Near-Infrared Band Gaps in Fluorescent Single-Walled Carbon Nanotubes. *Science* **2010**, *330* (6011), 1656.
76. Piao, Y.; Meany, B.; Powell, L. R.; Valley, N.; Kwon, H.; Schatz, G. C.; Wang, Y., Brightening of carbon nanotube photoluminescence through the incorporation of sp³ defects. *Nature Chemistry* **2013**, *5* (10), 840-845.
77. Gross, J. H., *Mass spectrometry: a textbook*. Springer Science & Business Media: 2006.
78. De Hoffmann, E.; Charette, J.; Stroobant, V., *Mass spectrometry: Principles and applications*. 1997.
79. Dorfs, D.; Krahn, R.; Falqui, A.; Manna, L.; Giannini, C.; Zanchet, D., 1.08 - Quantum Dots: Synthesis and Characterization. In *Comprehensive Nanoscience and Technology*, Andrews, D. L.; Scholes, G. D.; Wiederrecht, G. P., Eds. Academic Press: Amsterdam, 2011; pp 219-270.
80. Shuster, J.; Reith, F.; Southam, G., Applications of Transmission Electron Microscopy in Geomicrobiology. In *Analytical Geomicrobiology: A Handbook of Instrumental Techniques*, Alessi, D. S.; Veeramani, H.; Kenney, J. P. L., Eds. Cambridge University Press: Cambridge, 2019; pp 166-186.
81. Iijima, S., Helical microtubules of graphitic carbon. *Nature* **1991**, *354* (6348), 56-58.

82. Bachilo, S. M.; Strano, M. S.; Kittrell, C.; Hauge, R. H.; Smalley, R. E.; Weisman, R. B., Structure-assigned optical spectra of single-walled carbon nanotubes. *Science* **2002**, *298* (5602), 2361-6.
83. O'Connell, M. J.; Bachilo, S. M.; Huffman, C. B.; Moore, V. C.; Strano, M. S.; Haroz, E. H.; Rialon, K. L.; Boul, P. J.; Noon, W. H.; Kittrell, C.; Ma, J.; Hauge, R. H.; Weisman, R. B.; Smalley, R. E., Band gap fluorescence from individual single-walled carbon nanotubes. *Science* **2002**, *297* (5581), 593-6.
84. Ghosh, S.; Bachilo, S. M.; Simonette, R. A.; Beckingham, K. M.; Weisman, R. B., Oxygen Doping Modifies Near-Infrared Band Gaps in Fluorescent Single-Walled Carbon Nanotubes. *Science* **2010**, *330* (6011), 1656-1659.
85. Zhang, Y.; Valley, N.; Brozena, A. H.; Piao, Y. M.; Song, X. P.; Schatz, G. C.; Wang, Y. H., Propagative Sidewall Alkylcarboxylation that Induces Red-Shifted Near-IR Photoluminescence in Single-Walled Carbon Nanotubes. *Journal of Physical Chemistry Letters* **2013**, *4* (5), 826-830.
86. Piao, Y. M.; Meany, B.; Powell, L. R.; Valley, N.; Kwon, H.; Schatz, G. C.; Wang, Y. H., Brightening of carbon nanotube photoluminescence through the incorporation of sp(3) defects. *Nature Chemistry* **2013**, *5* (10), 840-845.
87. Iizumi, Y.; Yudasaka, M.; Kim, J.; Sakakita, H.; Takeuchi, T.; Okazaki, T., Oxygen-doped carbon nanotubes for near-infrared fluorescent labels and imaging probes. *Sci Rep* **2018**, *8* (1), 6272.
88. Chiu, C. F.; Saidi, W. A.; Kagan, V. E.; Star, A., Defect-Induced Near-Infrared Photoluminescence of Single-Walled Carbon Nanotubes Treated with Polyunsaturated Fatty Acids. *Journal of the American Chemical Society* **2017**, *139* (13), 4859-4865.
89. Lin, C. W.; Bachilo, S. M.; Zheng, Y.; Tsedev, U.; Huang, S. N.; Weisman, R. B.; Belcher, A. M., Creating fluorescent quantum defects in carbon nanotubes using hypochlorite and light. *Nature Communications* **2019**, *10*.
90. Deng, S.; Zhang, Y.; Brozena, A. H.; Mayes, M. L.; Banerjee, P.; Chiou, W.-A.; Rubloff, G. W.; Schatz, G. C.; Wang, Y., Confined propagation of covalent chemical reactions on single-walled carbon nanotubes. *Nature Communications* **2011**, *2* (1), 382.
91. Kwon, H.; Furmanchuk, M.; Kim, M.; Meany, B.; Guo, Y.; Schatz, G. C.; Wang, Y. H., Molecularly Tunable Fluorescent Quantum Defects. *Journal of the American Chemical Society* **2016**, *138* (21), 6878-6885.
92. Maeda, Y.; Takehana, Y.; Yamada, M.; Suzuki, M.; Murakami, T., Control of the photoluminescence properties of single-walled carbon nanotubes by alkylation and subsequent thermal treatment. *Chem Commun (Camb)* **2015**, *51* (70), 13462-5.

93. Maeda, Y.; Kuroda, K.; Tambo, H.; Murakoshi, H.; Konno, Y.; Yamada, M.; Zhao, P.; Zhao, X.; Nagase, S.; Ehara, M., Influence of local strain caused by cycloaddition on the band gap control of functionalized single-walled carbon nanotubes. *RSC Advances* **2019**, *9* (25), 13998-14003.
94. Brozena, A. H.; Leeds, J. D.; Zhang, Y.; Fourkas, J. T.; Wang, Y., Controlled defects in semiconducting carbon nanotubes promote efficient generation and luminescence of trions. *ACS Nano* **2014**, *8* (5), 4239-47.
95. Kwon, H.; Kim, M.; Nutz, M.; Hartmann, N. F.; Perrin, V.; Meany, B.; Hofmann, M. S.; Clark, C. W.; Htoon, H.; Doorn, S. K.; Hoeghele, A.; Wang, Y. H., Probing Trions at Chemically Tailored Trapping Defects. *Acs Central Science* **2019**, *5* (11), 1786-1794.
96. Powell, L. R.; Piao, Y.; Wang, Y., Optical Excitation of Carbon Nanotubes Drives Localized Diazonium Reactions. *J Phys Chem Lett* **2016**, *7* (18), 3690-4.
97. Shiraki, T.; Shiraishi, T.; Juhasz, G.; Nakashima, N., Emergence of new red-shifted carbon nanotube photoluminescence based on proximal doped-site design. *Sci Rep* **2016**, *6*, 28393.
98. Zheng, Y.; Bachilo, S. M.; Weisman, R. B., Controlled Patterning of Carbon Nanotube Energy Levels by Covalent DNA Functionalization. *ACS Nano* **2019**, *13* (7), 8222-8228.
99. Powell, L. R.; Kim, M.; Wang, Y., Chirality-Selective Functionalization of Semiconducting Carbon Nanotubes with a Reactivity-Switchable Molecule. *Journal of the American Chemical Society* **2017**, *139* (36), 12533-12540.
100. Wu, X. J.; Kim, M.; Kwon, H.; Wang, Y. H., Photochemical Creation of Fluorescent Quantum Defects in Semiconducting Carbon Nanotube Hosts. *Angewandte Chemie-International Edition* **2018**, *57* (3), 648-+.
101. Zheng, Y.; Bachilo, S. M.; Weisman, R. B., Photoexcited Aromatic Reactants Give Multicolor Carbon Nanotube Fluorescence from Quantum Defects. *ACS Nano* **2020**, *14* (1), 715-723.
102. Luo, H.-B.; Wang, P.; Wu, X.; Qu, H.; Ren, X.; Wang, Y., One-Pot, Large-Scale Synthesis of Organic Color Center-Tailored Semiconducting Carbon Nanotubes. *ACS Nano* **2019**, *13* (7), 8417-8424.
103. Brozena, A. H.; Kim, M.; Powell, L. R.; Wang, Y., Controlling the optical properties of carbon nanotubes with organic colour-centre quantum defects. *Nature Reviews Chemistry* **2019**, *3* (6), 375-392.
104. Shiraki, T.; Miyauchi, Y.; Matsuda, K.; Nakashima, N., Carbon Nanotube Photoluminescence Modulation by Local Chemical and Supramolecular Chemical Functionalization. *Accounts of Chemical Research* **2020**, *53* (9), 1846-1859.

105. He, X. W.; Hartmann, N. F.; Ma, X. D.; Kim, Y.; Ihly, R.; Blackburn, J. L.; Gao, W. L.; Kono, J.; Yomogida, Y.; Hirano, A.; Tanaka, T.; Kataura, H.; Htoon, H.; Doorn, S. K., Tunable room-temperature single-photon emission at telecom wavelengths from sp(3) defects in carbon nanotubes. *Nature Photonics* **2017**, *11* (9), 577-+.
106. Akizuki, N.; Aota, S.; Mouri, S.; Matsuda, K.; Miyauchi, Y., Efficient near-infrared up-conversion photoluminescence in carbon nanotubes. *Nat Commun* **2015**, *6*, 8920.
107. Ma, X. D.; Hartmann, N. F.; Baldwin, J. K. S.; Doorn, S. K.; Htoon, H., Room-temperature single-photon generation from solitary dopants of carbon nanotubes. *Nature Nanotechnology* **2015**, *10* (8), 671-675.
108. Kwon, H.; Kim, M.; Meany, B.; Piao, Y.; Powell, L. R.; Wang, Y., Optical Probing of Local pH and Temperature in Complex Fluids with Covalently Functionalized, Semiconducting Carbon Nanotubes. *The Journal of Physical Chemistry C* **2015**, *119* (7), 3733-3739.
109. Hartmann, N. F.; Velizhanin, K. A.; Haroz, E. H.; Kim, M.; Ma, X. D.; Wang, Y. H.; Htoon, H.; Doorn, S. K., Photoluminescence Dynamics of Aryl sp(3) Defect States in Single-Walled Carbon Nanotubes. *Acs Nano* **2016**, *10* (9), 8355-8365.
110. Sykes, M. E.; Kim, M.; Wu, X.; Wiederrecht, G. P.; Peng, L.; Wang, Y.; Gosztola, D. J.; Ma, X., Ultrafast Exciton Trapping at sp³ Quantum Defects in Carbon Nanotubes. *ACS Nano* **2019**, *13* (11), 13264-13270.
111. Shaikh, S. R.; Edidin, M., Polyunsaturated fatty acids and membrane organization: elucidating mechanisms to balance immunotherapy and susceptibility to infection. *Chem Phys Lipids* **2008**, *153* (1), 24-33.
112. Astarita, G.; Kendall, A. C.; Dennis, E. A.; Nicolaou, A., Targeted lipidomic strategies for oxygenated metabolites of polyunsaturated fatty acids. *Biochim Biophys Acta* **2015**, *1851* (4), 456-68.
113. Raftery, D., Mass spectrometry in metabolomics : methods and protocols. **2014**.
114. Li, Y.; Osuna, S.; Garcia-Borràs, M.; Qi, X.; Liu, S.; Houk, K. N.; Lan, Y., Reactivity of Single-Walled Carbon Nanotubes in the Diels-Alder Cycloaddition Reaction: Distortion-Interaction Analysis along the Reaction Pathway. *Chemistry - A European Journal* **2016**, *22* (36), 12819-12824.
115. Mercuri, F.; Sgamellotti, A., First-principles investigations on the functionalization of chiral and non-chiral carbon nanotubes by Diels–Alder cycloaddition reactions. *Phys. Chem. Chem. Phys.* **2009**, *11* (3), 563-567.
116. Osuna, S. L.; Houk, K. N., Cycloaddition Reactions of Butadiene and 1,3-Dipoles to Curved Arenes, Fullerenes, and Nanotubes: Theoretical Evaluation of the Role of

- Distortion Energies on Activation Barriers. *Chemistry - A European Journal* **2009**, *15* (47), 13219-13231.
117. Lu, X.; Tian, F.; Wang, N.; Zhang, Q., Organic Functionalization of the Sidewalls of Carbon Nanotubes by Diels–Alder Reactions: A Theoretical Prediction. *Organic Letters* **2002**, *4* (24), 4313-4315.
118. Cao, Y.; Osuna, S.; Liang, Y.; Haddon, R. C.; Houk, K. N., Diels–Alder Reactions of Graphene: Computational Predictions of Products and Sites of Reaction. *Journal of the American Chemical Society* **2013**, *135* (46), 17643-17649.
119. Martínez, J. P.; Langa, F.; Bickelhaupt, F. M.; Osuna, S.; Solà, M., (4 + 2) and (2 + 2) Cycloadditions of Benzyne to C60 and Zig-Zag Single-Walled Carbon Nanotubes: The Effect of the Curvature. *The Journal of Physical Chemistry C* **2016**, *120* (3), 1716-1726.
120. Frisch, M. J. T., G. W.; Schlegel, H. B.; Scuseria, G. E.; Robb, M. A.; Cheeseman, J. R.; Scalmani, G.; Barone, V.; Petersson, G. A.; Nakatsuji, H.; Li, X.; Caricato, M.; Marenich, A. V.; Bloino, J.; Janesko, B. G.; Gomperts, R.; Mennucci, B.; Hratchian, H. P.; Ortiz, J. V.; Izmaylov, A. F.; Sonnenberg, J. L.; Williams; Ding, F.; Lipparini, F.; Egidi, F.; Goings, J.; Peng, B.; Petrone, A.; Henderson, T.; Ranasinghe, D.; Zakrzewski, V. G.; Gao, J.; Rega, N.; Zheng, G.; Liang, W.; Hada, M.; Ehara, M.; Toyota, K.; Fukuda, R.; Hasegawa, J.; Ishida, M.; Nakajima, T.; Honda, Y.; Kitao, O.; Nakai, H.; Vreven, T.; Throssell, K.; Montgomery Jr., J. A.; Peralta, J. E.; Ogliaro, F.; Bearpark, M. J.; Heyd, J. J.; Brothers, E. N.; Kudin, K. N.; Staroverov, V. N.; Keith, T. A.; Kobayashi, R.; Normand, J.; Raghavachari, K.; Rendell, A. P.; Burant, J. C.; Iyengar, S. S.; Tomasi, J.; Cossi, M.; Millam, J. M.; Klene, M.; Adamo, C.; Cammi, R.; Ochterski, J. W.; Martin, R. L.; Morokuma, K.; Farkas, O.; Foresman, J. B.; Fox, D. J., Gaussian 16 Rev. C.01, Wallingford, CT, 2016.
121. Perdew, J. P.; Burke, K.; Ernzerhof, M., Generalized Gradient Approximation Made Simple. *Physical Review Letters* **1996**, *77* (18), 3865-3868.
122. Grimme, S.; Antony, J.; Ehrlich, S.; Krieg, H., A consistent and accurate ab initio parametrization of density functional dispersion correction (DFT-D) for the 94 elements H-Pu. *The Journal of Chemical Physics* **2010**, *132* (15), 154104.
123. Marenich, A. V.; Cramer, C. J.; Truhlar, D. G., Universal Solvation Model Based on Solute Electron Density and on a Continuum Model of the Solvent Defined by the Bulk Dielectric Constant and Atomic Surface Tensions. *The Journal of Physical Chemistry B* **2009**, *113* (18), 6378-6396.
124. Hanwell, M. D.; Curtis, D. E.; Lonie, D. C.; Vandermeersch, T.; Zurek, E.; Hutchison, G. R., Avogadro: an advanced semantic chemical editor, visualization, and analysis platform. *Journal of Cheminformatics* **2012**, *4* (1), 17.

125. Avogadro: an open-source molecular builder and visualization tool. Version 1.2.0 <http://avogadro.cc/>.
126. Wei, X.; Tanaka, T.; Yomogida, Y.; Sato, N.; Saito, R.; Kataura, H., Experimental determination of excitonic band structures of single-walled carbon nanotubes using circular dichroism spectra. *Nature Communications* **2016**, *7* (1), 12899.
127. Torrens, O. N.; Zheng, M.; Kikkawa, J. M., Energy of K-Momentum Dark Excitons in Carbon Nanotubes by Optical Spectroscopy. *Physical Review Letters* **2008**, *101* (15), 157401.
128. Blackburn, J. L.; Holt, J. M.; Irurzun, V. M.; Resasco, D. E.; Rumbles, G., Confirmation of K-Momentum Dark Exciton Vibronic Sidebands Using ¹³C-labeled, Highly Enriched (6,5) Single-walled Carbon Nanotubes. *Nano Letters* **2012**, *12* (3), 1398-1403.
129. Koti, A. S. R.; Krishna, M. M. G.; Periasamy, N., Time-Resolved Area-Normalized Emission Spectroscopy (TRANES): A Novel Method for Confirming Emission from Two Excited States. *The Journal of Physical Chemistry A* **2001**, *105* (10), 1767-1771.
130. Fujimoto, K.; Shimizu, H.; Inouye, M., Unambiguous Detection of Target DNAs by Excimer-Monomer Switching Molecular Beacons. *The Journal of Organic Chemistry* **2004**, *69* (10), 3271-3275.
131. Iwamura, M.; Takeuchi, S.; Tahara, T., Real-Time Observation of the Photoinduced Structural Change of Bis(2,9-dimethyl-1,10-phenanthroline)copper(I) by Femtosecond Fluorescence Spectroscopy: A Realistic Potential Curve of the Jahn-Teller Distortion. *Journal of the American Chemical Society* **2007**, *129* (16), 5248-5256.
132. Woodward, R. B., Structure and the Absorption Spectra of α,β -Unsaturated Ketones. *Journal of the American Chemical Society* **1941**, *63* (4), 1123-1126.
133. Fieser, L. F.; Fieser, M.; Rajagopalan, S., ABSORPTION SPECTROSCOPY AND THE STRUCTURES OF THE DIOSTEROLS. *The Journal of Organic Chemistry* **1948**, *13* (6), 800-806.
134. Woodward, R. B., Structure and Absorption Spectra. III. Normal Conjugated Dienes. *Journal of the American Chemical Society* **1942**, *64* (1), 72-75.
135. Medishetty, R.; Tandiana, R.; Koh, L. L.; Vittal, J. J., Assembly of 3D Coordination Polymers from 2D Sheets by [2+2] Cycloaddition Reaction. *Chemistry – A European Journal* **2014**, *20* (5), 1231-1236.
136. Kancheva, P. B.; Delchev, V. B., Investigation of the mechanisms of photo-induced formation of cyclobutane dimers of cytosine and 2,4-diaminopyrimidine. *Journal of Molecular Modeling* **2016**, *22* (9), 230.

137. Sonoda, Y., Solid-state [2+2] photodimerization and photopolymerization of α,ω -diarylpolyene monomers: effective utilization of noncovalent intermolecular interactions in crystals. *Molecules (Basel, Switzerland)* **2010**, *16* (1), 119-148.
138. Fedorova, O. A.; Saifutiarova, A. E.; Gulakova, E. N.; Guskova, E. O.; Aliyev, T. M.; Shepel, N. E.; Fedorov, Y. V., The regioselective [2 + 2] photocycloaddition reaction of 2-(3,4-dimethoxystyryl)quinoxaline in solution. *Photochemical & Photobiological Sciences* **2019**, *18* (9), 2208-2215.
139. Sun, X.; Zaric, S.; Daranciang, D.; Welsher, K.; Lu, Y.; Li, X.; Dai, H., Optical Properties of Ultrashort Semiconducting Single-Walled Carbon Nanotube Capsules Down to Sub-10 nm. *Journal of the American Chemical Society* **2008**, *130* (20), 6551-6555.
140. He, X.; Gifford, B. J.; Hartmann, N. F.; Ihly, R.; Ma, X.; Kilina, S. V.; Luo, Y.; Shayan, K.; Strauf, S.; Blackburn, J. L.; Tretiak, S.; Doorn, S. K.; Htoon, H., Low-Temperature Single Carbon Nanotube Spectroscopy of sp^3 Quantum Defects. *ACS Nano* **2017**, *11* (11), 10785-10796.
141. El Seoud, O. A.; Baader, W. J.; Bastos, E. L., Practical Chemical Kinetics in Solution. *Encyclopedia of Physical Organic Chemistry* **2016**, 1-68.
142. Schöppler, F.; Mann, C.; Hain, T. C.; Neubauer, F. M.; Privitera, G.; Bonaccorso, F.; Chu, D.; Ferrari, A. C.; Hertel, T., Molar Extinction Coefficient of Single-Wall Carbon Nanotubes. *The Journal of Physical Chemistry C* **2011**, *115* (30), 14682-14686.
143. Sanchez, S. R.; Bachilo, S. M.; Kadria-Vili, Y.; Lin, C.-W.; Weisman, R. B., (n,m)-Specific Absorption Cross Sections of Single-Walled Carbon Nanotubes Measured by Variance Spectroscopy. *Nano Letters* **2016**, *16* (11), 6903-6909.
144. Kühn, H.; Wiesner, R.; Rathmann, J.; Schewe, T., Formation of ketodienoic fatty acids by the pure pea lipoxygenase-1. *Eicosanoids* **1991**, *4* (1), 9-14.
145. Cai, W.; Fan, H.; Ding, D.; Zhang, Y.; Wang, W., Synthesis of Z-alkenes via visible light promoted photocatalytic E \rightarrow Z isomerization under metal-free conditions. *Chemical Communications* **2017**, *53* (96), 12918-12921.
146. Roothaan, C. C. J., New Developments in Molecular Orbital Theory. *Reviews of Modern Physics* **1951**, *23* (2), 69-89.
147. Because the geometries of open-shell singlet diradicals cannot be successfully located in our geometry optimizations after multiple attempts, h., geometry optimizations of the diradical intermediates were performed at triplet state. Single point energies were then computed as an open shell singlet.

148. Vlasova, II; Kapralov, A. A.; Michael, Z. P.; Burkert, S. C.; Shurin, M. R.; Star, A.; Shvedova, A. A.; Kagan, V. E., Enzymatic oxidative biodegradation of nanoparticles: Mechanisms, significance and applications. *Toxicol Appl Pharmacol* **2016**, *299*, 58-69.
149. Bhattacharya, K.; Sacchetti, C.; El-Sayed, R.; Fornara, A.; Kotchey, G. P.; Gaugler, J. A.; Star, A.; Bottini, M.; Fadeel, B., Enzymatic ‘stripping’ and degradation of PEGylated carbon nanotubes. *Nanoscale* **2014**, *6* (24), 14686-14690.
150. Burkert, S. C.; Shurin, G. V.; White, D. L.; He, X.; Kapralov, A. A.; Kagan, V. E.; Shurin, M. R.; Star, A., Targeting myeloid regulators by paclitaxel-loaded enzymatically degradable nanocups. *Nanoscale* **2018**, *10* (37), 17990-18000.
151. Chen, M.; Qin, X.; Zeng, G., Biodegradation of Carbon Nanotubes, Graphene, and Their Derivatives. *Trends in Biotechnology* **2017**, *35* (9), 836-846.
152. Cao, L.; Meziani, M. J.; Sahu, S.; Sun, Y. P., Photoluminescence properties of graphene versus other carbon nanomaterials. *Acc Chem Res* **2013**, *46* (1), 171-80.
153. Chiu, C. F.; Barth, B. A.; Kotchey, G. P.; Zhao, Y.; Gogick, K. A.; Saidi, W. A.; Petoud, S.; Star, A., Enzyme-catalyzed oxidation facilitates the return of fluorescence for single-walled carbon nanotubes. *J Am Chem Soc* **2013**, *135* (36), 13356-64.
154. Chiu, C. F.; Dar, H. H.; Kapralov, A. A.; Robinson, R. A. S.; Kagan, V. E.; Star, A., Nanoemitters and innate immunity: the role of surfactants and bio-coronas in myeloperoxidase-catalyzed oxidation of pristine single-walled carbon nanotubes. *Nanoscale* **2017**, *9* (18), 5948-5956.
155. Huang, J.; Milton, A.; Arnold, R. D.; Huang, H.; Smith, F.; Panizzi, J. R.; Panizzi, P., Methods for measuring myeloperoxidase activity toward assessing inhibitor efficacy in living systems. *J Leukoc Biol* **2016**, *99* (4), 541-8.
156. Querol, M.; Chen, J. W.; Bogdanov, A. A., Jr., A paramagnetic contrast agent with myeloperoxidase-sensing properties. *Org Biomol Chem* **2006**, *4* (10), 1887-95.
157. Rodriguez, E.; Nilges, M.; Weissleder, R.; Chen, J. W., Activatable magnetic resonance imaging agents for myeloperoxidase sensing: mechanism of activation, stability, and toxicity. *J Am Chem Soc* **2010**, *132* (1), 168-77.
158. Breckwoldt, M. O.; Chen, J. W.; Stangenberg, L.; Aikawa, E.; Rodriguez, E.; Qiu, S.; Moskowitz, M. A.; Weissleder, R., Tracking the inflammatory response in stroke in vivo by sensing the enzyme myeloperoxidase. *Proc Natl Acad Sci USA* **2008**, *105* (47), 18584-9.
159. Hajnsek, M.; Schiffer, D.; Harrich, D.; Koller, D.; Verient, V.; Palen, J. v. d.; Heinzle, A.; Binder, B.; Sigl, E.; Sinner, F.; Guebitz, G. M., An electrochemical sensor for fast

- detection of wound infection based on myeloperoxidase activity. *Sensors and Actuators B: Chemical* **2015**, *209*, 265-274.
160. Borgmann, S. J. A.; Chemistry, B., Electrochemical quantification of reactive oxygen and nitrogen: challenges and opportunities. **2009**, *394* (1), 95-105.
 161. Calas-Blanchard, C.; Catanante, G.; Noguier, T., Electrochemical Sensor and Biosensor Strategies for ROS/RNS Detection in Biological Systems. **2014**, *26* (6), 1277-1286.
 162. Simões, E. F. C.; Leitão, J. M. M.; da Silva, J. C. G. E. J. M. A., Carbon dots prepared from citric acid and urea as fluorescent probes for hypochlorite and peroxyxynitrite. **2016**, *183* (5), 1769-1777.
 163. Yu, C.; Wu, Y.; Zeng, F.; Wu, S., A fluorescent ratiometric nanosensor for detecting NO in aqueous media and imaging exogenous and endogenous NO in live cells. *Journal of Materials Chemistry B* **2013**, *1* (33), 4152-4159.
 164. Yin, B.; Deng, J.; Peng, X.; Long, Q.; Zhao, J.; Lu, Q.; Chen, Q.; Li, H.; Tang, H.; Zhang, Y. J. A., Green synthesis of carbon dots with down-and up-conversion fluorescent properties for sensitive detection of hypochlorite with a dual-readout assay. **2013**, *138* (21), 6551-6557.
 165. Wang, Q.; Tan, C.; Cai, W. J. A., A targetable fluorescent sensor for hypochlorite based on a luminescent europium complex loaded carbon nanotube. **2012**, *137* (8), 1872-1875.
 166. Uusitalo, L. M.; Hempel, N., Recent advances in intracellular and in vivo ROS sensing: focus on nanoparticle and nanotube applications. *Int J Mol Sci* **2012**, *13* (9), 10660-79.
 167. Liu, X.; Han, Z.; Li, F.; Gao, L.; Liang, G.; Cui, H. J. A. a. m.; interfaces, Highly chemiluminescent graphene oxide hybrids bifunctionalized by N-(aminobutyl)-N-(ethylisoluminol)/horseradish peroxidase and sensitive sensing of hydrogen peroxide. **2015**, *7* (33), 18283-18291.
 168. Zan, X.; Fang, Z.; Wu, J.; Xiao, F.; Huo, F.; Duan, H., Freestanding graphene paper decorated with 2D-assembly of Au@Pt nanoparticles as flexible biosensors to monitor live cell secretion of nitric oxide. *Biosensors and Bioelectronics* **2013**, *49*, 71-78.
 169. Yeh, T.-Y.; Wang, C.-I.; Chang, H.-T. J. T., Photoluminescent C-dots@ RGO for sensitive detection of hydrogen peroxide and glucose. **2013**, *115*, 718-723.
 170. Doussineau, T.; Schulz, A.; Lapresta-Fernandez, A.; Moro, A.; Korsten, S.; Trupp, S.; Mohr, G. J., On the design of fluorescent ratiometric nanosensors. *Chemistry* **2010**, *16* (34), 10290-9.
 171. Yoon, S. M.; Kim, S. J.; Shin, H. J.; Benayad, A.; Choi, S. J.; Kim, K. K.; Kim, S. M.; Park, Y. J.; Kim, G.; Choi, J. Y.; Lee, Y. H., Selective oxidation on metallic carbon nanotubes by halogen oxoanions. *J Am Chem Soc* **2008**, *130* (8), 2610-6.

172. Wu, C. H., Studies of the equilibrium and thermodynamics of the adsorption of Cu(2+) onto as-produced and modified carbon nanotubes. *Journal of colloid and interface science* **2007**, *311* (2), 338-46.
173. Kotchey, G. P.; Gaugler, J. A.; Kapralov, A. A.; Kagan, V. E.; Star, A., Effect of antioxidants on enzyme-catalysed biodegradation of carbon nanotubes. *J Mater Chem B* **2013**, *1* (3), 302-309.
174. Kotchey, G. P.; Hasan, S. A.; Kapralov, A. A.; Ha, S. H.; Kim, K.; Shvedova, A. A.; Kagan, V. E.; Star, A., A natural vanishing act: the enzyme-catalyzed degradation of carbon nanomaterials. *Acc Chem Res* **2012**, *45* (10), 1770-81.
175. Sannino, A.; Demitri, C.; Madaghiele, M., Biodegradable Cellulose-based Hydrogels: Design and Applications. *Materials* **2009**, *2* (2), 353-373.
176. Schurz, J., A bright future for cellulose. *Progress in Polymer Science* **1999**, *24* (4), 481-483.
177. Wang, B.; Du, X.; Wang, M.; Gong, W.; Anzai, J. i. J. E. A. I. J. D. t. F.; Electroanalysis, P. A. o., A Facile Preparation of H₂O₂ Sensors Using Layer-by-Layer Deposited Thin Films Composed of Poly (ethyleneimine) and Carboxymethyl Cellulose as Matrices for Immobilizing Hemin. **2008**, *20* (9), 1028-1031.
178. Shibraen, M. H. A.; Yagoub, H.; Wang, Z.; Yang, S. In *Influence of Operational Parameters on Layer-by-layer Assembled Cellulose Derivatives Thin Film*, 2nd Annual International Conference on Advanced Material Engineering (AME 2016), Atlantis Press: 2016.
179. Bachilo, S. M.; Strano, M. S.; Kittrell, C.; Hauge, R. H.; Smalley, R. E.; Weisman, R. B., Structure-Assigned Optical Spectra of Single-Walled Carbon Nanotubes. *Science* **2002**, *298* (5602), 2361.
180. Hilmer, A. J.; McNicholas, T. P.; Lin, S.; Zhang, J.; Wang, Q. H.; Mendenhall, J. D.; Song, C.; Heller, D. A.; Barone, P. W.; Blankschtein, D.; Strano, M. S., Role of adsorbed surfactant in the reaction of aryl diazonium salts with single-walled carbon nanotubes. *Langmuir* **2012**, *28* (2), 1309-21.
181. Heinecke, J. W.; Li, W.; Daehnke, H. L., 3rd; Goldstein, J. A., Dityrosine, a specific marker of oxidation, is synthesized by the myeloperoxidase-hydrogen peroxide system of human neutrophils and macrophages. *The Journal of biological chemistry* **1993**, *268* (6), 4069-77.
182. Harms, G. S.; Pauls, S. W.; Hedstrom, J. F.; Johnson, C. K. J. J. o. F., Fluorescence and Rotational Dynamics of Dityrosine. **1997**, *7* (4), 283-292.

183. Martin, S. F.; Wood, A. D.; McRobbie, M. M.; Mazilu, M.; McDonald, M. P.; Samuel, I. D. W.; Herrington, C. S., Fluorescence spectroscopy of an in vitro model of human cervical precancer identifies neoplastic phenotype. *International Journal of Cancer* **2007**, *120* (9), 1964-1970.
184. Ansari, M. A.; Erfanzadeh, M.; Mohajerani, E., Mechanisms of Laser-Tissue Interaction: II. Tissue Thermal Properties. *J Lasers Med Sci* **2013**, *4* (3), 99-106.
185. Orecchioni, M.; Bedognetti, D.; Sgarrella, F.; Marincola, F. M.; Bianco, A.; Delogu, L. G., Impact of carbon nanotubes and graphene on immune cells. *Journal of Translational Medicine* **2014**, *12* (1), 138.
186. Gallagher, R.; Collins, S.; Trujillo, J.; McCredie, K.; Ahearn, M.; Tsai, S.; Metzgar, R.; Aulakh, G.; Ting, R.; Ruscelli, F.; Gallo, R., Characterization of the continuous, differentiating myeloid cell line (HL-60) from a patient with acute promyelocytic leukemia. *Blood* **1979**, *54* (3), 713-733.
187. Ye, R.; Xiang, C.; Lin, J.; Peng, Z.; Huang, K.; Yan, Z.; Cook, N. P.; Samuel, E. L. G.; Hwang, C.-C.; Ruan, G.; Ceriotti, G.; Raji, A.-R. O.; Martí, A. A.; Tour, J. M., Coal as an abundant source of graphene quantum dots. *Nature Communications* **2013**, *4* (1), 2943.
188. Liu, F.; Jang, M.-H.; Ha, H. D.; Kim, J.-H.; Cho, Y.-H.; Seo, T. S., Facile Synthetic Method for Pristine Graphene Quantum Dots and Graphene Oxide Quantum Dots: Origin of Blue and Green Luminescence. *Advanced Materials* **2013**, *25* (27), 3657-3662.
189. Wang, S.; Cole, I. S.; Zhao, D.; Li, Q., The dual roles of functional groups in the photoluminescence of graphene quantum dots. *Nanoscale* **2016**, *8* (14), 7449-7458.
190. Kungl, A. J.; Landl, G.; Visser, A. J. W. G.; Breitenbach, M.; Kauffmann, H. F., l-Dityrosine: A time-resolved fluorescence investigation. *Journal of Fluorescence* **1992**, *2* (1), 63-73.
191. Chang, N.; Lu, Y.; Mao, J.; Yang, J.; Li, M.; Zhang, S.; Liu, Y., Ratiometric fluorescence sensor arrays based on quantum dots for detection of proteins. *Analyst* **2016**, *141* (6), 2046-2052.
192. Huang, C.; Jia, T.; Tang, M.; Yin, Q.; Zhu, W.; Zhang, C.; Yang, Y.; Jia, N.; Xu, Y.; Qian, X., Selective and Ratiometric Fluorescent Trapping and Quantification of Protein Vicinal Dithiols and in Situ Dynamic Tracing in Living Cells. *Journal of the American Chemical Society* **2014**, *136* (40), 14237-14244.
193. Han, J.; Zhang, C.; Liu, F.; Liu, B.; Han, M.; Zou, W.; Yang, L.; Zhang, Z., Upconversion nanoparticles for ratiometric fluorescence detection of nitrite. *Analyst* **2014**, *139* (12), 3032-3038.

194. Dong, X.; Xing, G.; Chan-Park, M. B.; Shi, W.; Xiao, N.; Wang, J.; Yan, Q.; Sum, T. C.; Huang, W.; Chen, P., The formation of a carbon nanotube–graphene oxide core–shell structure and its possible applications. *Carbon* **2011**, *49* (15), 5071-5078.
195. Li, Y.; Yang, T.; Yu, T.; Zheng, L.; Liao, K., Synergistic effect of hybrid carbon nanotube–graphene oxide as a nanofiller in enhancing the mechanical properties of PVA composites. *Journal of Materials Chemistry* **2011**, *21* (29), 10844-10851.
196. Wimalasiri, Y.; Zou, L., Carbon nanotube/graphene composite for enhanced capacitive deionization performance. *Carbon* **2013**, *59*, 464-471.
197. Zhang, C.; Ren, L.; Wang, X.; Liu, T., Graphene Oxide-Assisted Dispersion of Pristine Multiwalled Carbon Nanotubes in Aqueous Media. *The Journal of Physical Chemistry C* **2010**, *114* (26), 11435-11440.
198. White, B.; Banerjee, S.; O'Brien, S.; Turro, N. J.; Herman, I. P., Zeta-Potential Measurements of Surfactant-Wrapped Individual Single-Walled Carbon Nanotubes. *The Journal of Physical Chemistry C* **2007**, *111* (37), 13684-13690.
199. Kim, Y.-K.; Min, D.-H., Preparation of scrolled graphene oxides with multi-walled carbon nanotube templates. *Carbon* **2010**, *48* (15), 4283-4288.
200. Ishibashi, A.; Nakashima, N., Strong Chemical Structure Dependence for Individual Dissolution of Single-Walled Carbon Nanotubes in Aqueous Micelles of Biosurfactants. *Bulletin of the Chemical Society of Japan* **2006**, *79* (2), 357-359.
201. Riou, I.; Bertoncini, P.; Bizot, H.; Mevellec, J. Y.; Buléon, A.; Chauvet, O., Carboxymethylcellulose/Single Walled Carbon Nanotube Complexes. *Journal of Nanoscience and Nanotechnology* **2009**, *9* (10), 6176-6180.
202. Salavagione, H. J.; Díez-Pascual, A. M.; Lázaro, E.; Vera, S.; Gómez-Fatou, M. A., Chemical sensors based on polymer composites with carbon nanotubes and graphene: the role of the polymer. *Journal of Materials Chemistry A* **2014**, *2* (35), 14289-14328.
203. Choi, J. H.; Strano, M. S., Solvatochromism in single-walled carbon nanotubes. **2007**, *90* (22), 223114.
204. Giraldo, J. P.; Landry, M. P.; Kwak, S. Y.; Jain, R. M.; Wong, M. H.; Iverson, N. M.; Ben-Naim, M.; Strano, M. S., A Ratiometric Sensor Using Single Chirality Near-Infrared Fluorescent Carbon Nanotubes: Application to In Vivo Monitoring. *Small* **2015**, *11* (32), 3973-84.
205. Dai, L.; Chang, D. W.; Baek, J.-B.; Lu, W., Carbon Nanomaterials for Advanced Energy Conversion and Storage. *Small* **2012**, *8* (8), 1130-1166.
206. Zhang, J.; Xia, Z.; Dai, L., Carbon-based electrocatalysts for advanced energy conversion and storage. *Science Advances* **2015**, *1* (7), e1500564.

207. Loh, K. P.; Ho, D.; Chiu, G. N. C.; Leong, D. T.; Pastorin, G.; Chow, E. K.-H., Clinical Applications of Carbon Nanomaterials in Diagnostics and Therapy. *Advanced Materials* **2018**, *30* (47), 1802368.
208. Fadeel, B.; Bussy, C.; Merino, S.; Vázquez, E.; Flahaut, E.; Mouchet, F.; Evariste, L.; Gauthier, L.; Koivisto, A. J.; Vogel, U.; Martín, C.; Delogu, L. G.; Buerki-Thurnherr, T.; Wick, P.; Beloin-Saint-Pierre, D.; Hischier, R.; Pelin, M.; Candotto Carniel, F.; Tretiach, M.; Cesca, F.; Benfenati, F.; Scaini, D.; Ballerini, L.; Kostarelos, K.; Prato, M.; Bianco, A., Safety Assessment of Graphene-Based Materials: Focus on Human Health and the Environment. *ACS Nano* **2018**, *12* (11), 10582-10620.
209. Kobayashi, N.; Izumi, H.; Morimoto, Y., Review of toxicity studies of carbon nanotubes. *J Occup Health* **2017**, *59* (5), 394-407.
210. Madannejad, R.; Shoaie, N.; Jahanpeyma, F.; Darvishi, M. H.; Azimzadeh, M.; Javadi, H., Toxicity of carbon-based nanomaterials: Reviewing recent reports in medical and biological systems. *Chemico-Biological Interactions* **2019**, *307*, 206-222.
211. Kotchey, G. P.; Hasan, S. A.; Kapralov, A. A.; Ha, S. H.; Kim, K.; Shvedova, A. A.; Kagan, V. E.; Star, A., A natural vanishing act: the enzyme-catalyzed degradation of carbon nanomaterials. *Acc Chem Res* **2012**, *45* (10), 1770-1781.
212. Vlasova, I. I.; Kapralov, A. A.; Michael, Z. P.; Burkert, S. C.; Shurin, M. R.; Star, A.; Shvedova, A. A.; Kagan, V. E., Enzymatic oxidative biodegradation of nanoparticles: Mechanisms, significance and applications. *Toxicology and Applied Pharmacology* **2016**, *299*, 58-69.
213. Kurapati, R.; Russier, J.; Squillaci, M. A.; Treossi, E.; Ménard-Moyon, C.; Del Rio-Castillo, A. E.; Vazquez, E.; Samori, P.; Palermo, V.; Bianco, A., Dispersibility-Dependent Biodegradation of Graphene Oxide by Myeloperoxidase. *Small* **2015**, *11* (32), 3985-3994.
214. Haritash, A. K.; Kaushik, C. P., Biodegradation aspects of Polycyclic Aromatic Hydrocarbons (PAHs): A review. *Journal of Hazardous Materials* **2009**, *169* (1), 1-15.
215. He, X.; White, D. L.; Kapralov, A. A.; Kagan, V. E.; Star, A., Photoluminescence Response in Carbon Nanomaterials to Enzymatic Degradation. *Analytical Chemistry* **2020**, *92* (19), 12880-12890.
216. Zhou, X.; Zhang, Y.; Wang, C.; Wu, X.; Yang, Y.; Zheng, B.; Wu, H.; Guo, S.; Zhang, J., Photo-Fenton Reaction of Graphene Oxide: A New Strategy to Prepare Graphene Quantum Dots for DNA Cleavage. *ACS Nano* **2012**, *6* (8), 6592-6599.
217. Shinde, D. B.; Pillai, V. K., Electrochemical Resolution of Multiple Redox Events for Graphene Quantum Dots. *Angewandte Chemie International Edition* **2013**, *52* (9), 2482-2485.

218. Li, H.; He, X.; Kang, Z.; Huang, H.; Liu, Y.; Liu, J.; Lian, S.; Tsang, C. H. A.; Yang, X.; Lee, S.-T., Water-Soluble Fluorescent Carbon Quantum Dots and Photocatalyst Design. *Angewandte Chemie International Edition* **2010**, *49* (26), 4430-4434.
219. Bai, H.; Jiang, W.; Kotchey, G. P.; Saidi, W. A.; Bythell, B. J.; Jarvis, J. M.; Marshall, A. G.; Robinson, R. A. S.; Star, A., Insight into the Mechanism of Graphene Oxide Degradation via the Photo-Fenton Reaction. *The Journal of Physical Chemistry C* **2014**, *118* (19), 10519-10529.
220. Allen, B. L.; Kotchey, G. P.; Chen, Y.; Yanamala, N. V. K.; Klein-Seetharaman, J.; Kagan, V. E.; Star, A., Mechanistic Investigations of Horseradish Peroxidase-Catalyzed Degradation of Single-Walled Carbon Nanotubes. *J Am Chem Soc* **2009**, *131* (47), 17194-17205.
221. Huang, J.; Smith, F.; Panizzi, J. R.; Goodwin, D. C.; Panizzi, P., Inactivation of myeloperoxidase by benzoic acid hydrazide. *Archives of Biochemistry and Biophysics* **2015**, *570*, 14-22.
222. Russo, C.; Apicella, B.; Ciajolo, A., Blue and green luminescent carbon nanodots from controllable fuel-rich flame reactors. *Scientific Reports* **2019**, *9* (1), 14566.
223. Furche, F.; Ahlrichs, R., Adiabatic time-dependent density functional methods for excited state properties. *J. Chem. Phys.* **2002**, *117* (16), 7433-7447.
224. Scalmani, G.; Frisch, M. J.; Mennucci, B.; Tomasi, J.; Cammi, R.; Barone, V., Geometries and properties of excited states in the gas phase and in solution: Theory and application of a time-dependent density functional theory polarizable continuum model. *J. Chem. Phys.* **2006**, *124* (9), 094107.
225. Casida, M. E., Time-dependent density-functional theory for molecules and molecular solids. *Journal of Molecular Structure: THEOCHEM* **2009**, *914* (1), 3-18.
226. Frisch, M. J.; Trucks, G. W.; Schlegel, H. B.; Scuseria, G. E.; Robb, M. A.; Cheeseman, J. R.; Scalmani, G.; Barone, V.; Petersson, G. A.; Nakatsuji, H.; Li, X.; Caricato, M.; Marenich, A. V.; Bloino, J.; Janesko, B. G.; Gomperts, R.; Mennucci, B.; Hratchian, H. P.; Ortiz, J. V.; Izmaylov, A. F.; Sonnenberg, J. L.; Williams; Ding, F.; Lipparini, F.; Egidi, F.; Goings, J.; Peng, B.; Petrone, A.; Henderson, T.; Ranasinghe, D.; Zakrzewski, V. G.; Gao, J.; Rega, N.; Zheng, G.; Liang, W.; Hada, M.; Ehara, M.; Toyota, K.; Fukuda, R.; Hasegawa, J.; Ishida, M.; Nakajima, T.; Honda, Y.; Kitao, O.; Nakai, H.; Vreven, T.; Throssell, K.; Montgomery Jr., J. A.; Peralta, J. E.; Ogliaro, F.; Bearpark, M. J.; Heyd, J. J.; Brothers, E. N.; Kudin, K. N.; Staroverov, V. N.; Keith, T. A.; Kobayashi, R.; Normand, J.; Raghavachari, K.; Rendell, A. P.; Burant, J. C.; Iyengar, S. S.; Tomasi, J.; Cossi, M.; Millam, J. M.; Klene, M.; Adamo, C.; Cammi, R.; Ochterski, J. W.; Martin, R. L.; Morokuma, K.; Farkas, O.; Foresman, J. B.; Fox, D. J. *Gaussian 16 Rev. C.01*, Wallingford, CT, 2016.

227. Yanai, T.; Tew, D. P.; Handy, N. C., A new hybrid exchange–correlation functional using the Coulomb-attenuating method (CAM-B3LYP). *Chemical Physics Letters* **2004**, *393* (1), 51-57.
228. Tomasi, J.; Mennucci, B.; Cammi, R., Quantum Mechanical Continuum Solvation Models. *Chemical Reviews* **2005**, *105* (8), 2999-3094.
229. Cancès, E.; Mennucci, B.; Tomasi, J., A new integral equation formalism for the polarizable continuum model: Theoretical background and applications to isotropic and anisotropic dielectrics. *J. Chem. Phys.* **1997**, *107* (8), 3032-3041.
230. Harms, G. S.; Pauls, S. W.; Hedstrom, J. F.; Johnson, C. K., Fluorescence and Rotational Dynamics of Dityrosine. *Journal of Fluorescence* **1997**, *7* (4), 283-292.
231. Heinecke, J. W.; Li, W.; Daehnke, H. L.; Goldstein, J. A., Dityrosine, a specific marker of oxidation, is synthesized by the myeloperoxidase-hydrogen peroxide system of human neutrophils and macrophages. *Journal of Biological Chemistry* **1993**, *268* (6), 4069-4077.
232. Cazier, H.; Malgorn, C.; Fresneau, N.; Georgin, D.; Sallustrau, A.; Chollet, C.; Tabet, J.-C.; Campidelli, S.; Pinault, M.; Mayne, M.; Taran, F.; Dive, V.; Junot, C.; Fenaille, F.; Colsch, B., Development of a Mass Spectrometry Imaging Method for Detecting and Mapping Graphene Oxide Nanoparticles in Rodent Tissues. *Journal of the American Society for Mass Spectrometry* **2020**, *31* (5), 1025-1036.
233. Chen, S.; Xiong, C.; Liu, H.; Wan, Q.; Hou, J.; He, Q.; Badu-Tawiah, A.; Nie, Z., Mass spectrometry imaging reveals the sub-organ distribution of carbon nanomaterials. *Nature Nanotechnology* **2015**, *10* (2), 176-182.
234. Liu, Q.; Cheng, M.; Wang, J.; Jiang, G., Graphene Oxide Nanoribbons: Improved Synthesis and Application in MALDI Mass Spectrometry. *Chemistry – A European Journal* **2015**, *21* (14), 5594-5599.
235. Jing, Z.; Hao-Yang, W.; Yin-Long, G., Amino Acids Analysis by MALDI Mass Spectrometry Using Carbon Nanotube as Matrix. *Chinese Journal of Chemistry* **2005**, *23* (2), 185-189.
236. Hu, Q.; Meng, X.; Choi, M. M. F.; Gong, X.; Chan, W., Elucidating the structure of carbon nanoparticles by ultra-performance liquid chromatography coupled with electrospray ionisation quadrupole time-of-flight tandem mass spectrometry. *Analytica Chimica Acta* **2016**, *911*, 100-107.
237. Cech, N. B.; Enke, C. G., Practical implications of some recent studies in electrospray ionization fundamentals. *Mass Spectrometry Reviews* **2001**, *20* (6), 362-387.
238. Wang, C.; Wang, M.; Han, X., Applications of mass spectrometry for cellular lipid analysis. *Molecular BioSystems* **2015**, *11* (3), 698-713.

239. Kruve, A.; Kaupmees, K.; Liigand, J.; Oss, M.; Leito, I., Sodium adduct formation efficiency in ESI source. *Journal of Mass Spectrometry* **2013**, *48* (6), 695-702.
240. Kruve, A.; Kaupmees, K., Adduct Formation in ESI/MS by Mobile Phase Additives. *Journal of the American Society for Mass Spectrometry* **2017**, *28* (5), 887-894.
241. Gao, X.; Jang, J.; Nagase, S., Hydrazine and Thermal Reduction of Graphene Oxide: Reaction Mechanisms, Product Structures, and Reaction Design. *The Journal of Physical Chemistry C* **2010**, *114* (2), 832-842.
242. Demarque, D. P.; Crotti, A. E. M.; Vessecchi, R.; Lopes, J. L. C.; Lopes, N. P., Fragmentation reactions using electrospray ionization mass spectrometry: an important tool for the structural elucidation and characterization of synthetic and natural products. *Natural Product Reports* **2016**, *33* (3), 432-455.
243. Neta, P.; Simón-Manso, Y.; Liang, Y.; Stein, S. E., Loss of H₂ and CO from protonated aldehydes in electrospray ionization mass spectrometry. *Rapid Communications in Mass Spectrometry* **2014**, *28* (17), 1871-1882.
244. Moon, I. K.; Lee, J.; Ruoff, R. S.; Lee, H., Reduced graphene oxide by chemical graphitization. *Nat Commun* **2010**, *1* (1), 73.
245. Shin, H.-J.; Kim, K. K.; Benayad, A.; Yoon, S.-M.; Park, H. K.; Jung, I.-S.; Jin, M. H.; Jeong, H.-K.; Kim, J. M.; Choi, J.-Y.; Lee, Y. H., Efficient Reduction of Graphite Oxide by Sodium Borohydride and Its Effect on Electrical Conductance. *Advanced Functional Materials* **2009**, *19* (12), 1987-1992.
246. Ambrosi, A.; Pumera, M., Electrochemically Exfoliated Graphene and Graphene Oxide for Energy Storage and Electrochemistry Applications. *Chemistry – A European Journal* **2016**, *22* (1), 153-159.
247. Newman, L.; Lozano, N.; Zhang, M.; Iijima, S.; Yudasaka, M.; Bussy, C.; Kostarelos, K., Hypochlorite degrades 2D graphene oxide sheets faster than 1D oxidised carbon nanotubes and nanohorns. *npj 2D Materials and Applications* **2017**, *1* (1), 39.
248. Morgan, K. M.; Ellis, J. A.; Lee, J.; Fulton, A.; Wilson, S. L.; Dupart, P. S.; Dastoori, R., Thermochemical Studies of Epoxides and Related Compounds. *The Journal of Organic Chemistry* **2013**, *78* (9), 4303-4311.
249. Yoon, S.-M.; Kim, S. J.; Shin, H.-J.; Benayad, A.; Choi, S. J.; Kim, K. K.; Kim, S. M.; Park, Y. J.; Kim, G.; Choi, J.-Y.; Lee, Y. H., Selective Oxidation on Metallic Carbon Nanotubes by Halogen Oxoanions. *J Am Chem Soc* **2008**, *130* (8), 2610-2616.
250. Wu, C.-H., Studies of the equilibrium and thermodynamics of the adsorption of Cu²⁺ onto as-produced and modified carbon nanotubes. *Journal of Colloid and Interface Science* **2007**, *311* (2), 338-346.

251. de Poorter, B.; Meunier, B., Catalytic epoxidation of aliphatic terminal olefins with sodium hypochlorite. *Tetrahedron Letters* **1984**, 25 (18), 1895-1896.
252. Gómez-Navarro, C.; Weitz, R. T.; Bittner, A. M.; Scolari, M.; Mews, A.; Burghard, M.; Kern, K., Electronic Transport Properties of Individual Chemically Reduced Graphene Oxide Sheets. *Nano Letters* **2007**, 7 (11), 3499-3503.
253. Feng, H.; Cheng, R.; Zhao, X.; Duan, X.; Li, J., A low-temperature method to produce highly reduced graphene oxide. *Nat Commun* **2013**, 4 (1), 1539.
254. Eda, G.; Lin, Y.-Y.; Mattevi, C.; Yamaguchi, H.; Chen, H.-A.; Chen, I.-S.; Chen, C.-W.; Chhowalla, M., Blue Photoluminescence from Chemically Derived Graphene Oxide. *Advanced Materials* **2010**, 22 (4), 505-509.
255. Cox, E. G.; Bragg, W. H., The crystalline structure of benzene. *Proceedings of the Royal Society of London. Series A, Containing Papers of a Mathematical and Physical Character* **1932**, 135 (827), 491-498.
256. Ruiz-Morales, Y., HOMO–LUMO Gap as an Index of Molecular Size and Structure for Polycyclic Aromatic Hydrocarbons (PAHs) and Asphaltenes: A Theoretical Study. I. *The Journal of Physical Chemistry A* **2002**, 106 (46), 11283-11308.
257. Adkins, E. M.; Miller, J. H., Towards a taxonomy of topology for polynuclear aromatic hydrocarbons: linking electronic and molecular structure. *Physical Chemistry Chemical Physics* **2017**, 19 (41), 28458-28469.
258. Wei, K.; Liao, F.; Huang, H.; Shao, M.; Lin, H.; Liu, Y.; Kang, Z., Simple Semiempirical Method for the Location Determination of HOMO and LUMO of Carbon Dots. *The Journal of Physical Chemistry C* **2021**.
259. World Health Organization. Regional Office for, E., *WHO guidelines for indoor air quality: selected pollutants*. World Health Organization. Regional Office for Europe: Copenhagen, 2010.
260. Humans, I. W. G. o. t. E. o. C. R. t., Some non-heterocyclic polycyclic aromatic hydrocarbons and some related exposures. *IARC Monogr Eval Carcinog Risks Hum* **2010**, 92, 1-853.
261. Bauer, A. K.; Velmurugan, K.; Plöttner, S.; Siegrist, K. J.; Romo, D.; Welge, P.; Brüning, T.; Xiong, K.-N.; Käfferlein, H. U., Environmentally prevalent polycyclic aromatic hydrocarbons can elicit co-carcinogenic properties in an in vitro murine lung epithelial cell model. *Archives of Toxicology* **2018**, 92 (3), 1311-1322.
262. Pan, S.; Sardesai, N. P.; Liu, H.; Li, D.; Rusling, J. F., Assessing DNA damage from enzyme-oxidized single-walled carbon nanotubes. *Toxicology Research* **2013**, 2 (6), 375-378.

263. Geier, M. C.; Chlebowski, A. C.; Truong, L.; Massey Simonich, S. L.; Anderson, K. A.; Tanguay, R. L., Comparative developmental toxicity of a comprehensive suite of polycyclic aromatic hydrocarbons. *Archives of Toxicology* **2018**, *92* (2), 571-586.
264. Sowada, J.; Lemoine, L.; Schön, K.; Hutzler, C.; Luch, A.; Tralau, T., Toxification of polycyclic aromatic hydrocarbons by commensal bacteria from human skin. *Archives of Toxicology* **2017**, *91* (6), 2331-2341.
265. Xue, W.; Warshawsky, D., Metabolic activation of polycyclic and heterocyclic aromatic hydrocarbons and DNA damage: A review. *Toxicology and Applied Pharmacology* **2005**, *206* (1), 73-93.
266. Incardona, J. P.; Day, H. L.; Collier, T. K.; Scholz, N. L., Developmental toxicity of 4-ring polycyclic aromatic hydrocarbons in zebrafish is differentially dependent on AH receptor isoforms and hepatic cytochrome P4501A metabolism. *Toxicology and Applied Pharmacology* **2006**, *217* (3), 308-321.
267. Agency for Toxic Substances and Disease Registry (ATSDR). 1995. Toxicological profile for Polycyclic Aromatic Hydrocarbons (PAHs). Atlanta, G. U. S. D. o. H. a. H. S.